Dissertation

submitted to the

Combined Faculty of Natural Sciences and Mathematics

of the *Ruperto-Carola Heidelberg University, Germany*

for the degree of

Doctor of Natural Sciences

Put forward by

Valentin Titus Tenorth

born in *Bottrop*

Oral examination: 10.02.2021

Characterizing Dark Matter at low and high Momentum Transfers

Referees:

1st: *Dr. Florian Goertz*

2nd: *Prof. Dr. Tilman Plehn*

Abstract

In this thesis we investigate theoretical frameworks for the characterization of dark matter and other new physics at colliders in combination with further experimental probes. To this end, we examine different theoretical approaches. Next-generation simplified models are the new benchmarks for LHC-based dark matter searches. We analyze and compare two commonly used instances of this class of models, namely a two-Higgs-doublet model extended with either a scalar or pseudoscalar mediator to the dark sector. We focus on the signatures in $t\bar{t}$ resonance, mono-Z and mono-h searches. Those show an interesting interplay and distinguished signatures in the two models. Turning to more model-independent approaches, in addition to the dark matter searches, we investigate a new search channel for the rare Higgs decay to a Z boson and a photon, using effective field theory. This decay could still exhibit significant contributions from physics beyond the standard model. The proposed $t\bar{t}$-associated production channel has the potential to discover this decay already at the HL-LHC. This would set strong constraints on so-far weakly tested modifications of the Higgs interactions. Back to dark matter, we examine the extended dark matter effective field theory. This framework allows the combination of various dark matter searches across different energy scales, in a model-independent and theoretically consistent quantum field theory, while providing a valid collider phenomenology. We perform parameter scans of increasing complexity taking all relevant constraints into account, and identify new viable parameter regions. Those non-trivial regions arise because of the more comprehensive framework, and are potentially testable in upcoming collider surveys. To further show the flexibility of this approach we apply slightly more specific versions to particular phenomenological interesting cases: di-fermion plus missing energy signatures at (future) colliders, and the excess in low-energy electron recoil events announced by the XENON1T collaboration.

Zusammenfassung

In dieser Dissertation untersuchen wir mehrere theoretische Ansätze für die Charakterisierung dunkler Materie und anderer neuer Physik an Teilchenbeschleunigern in Kombination mit weiteren Experimenten. Die neue Generation von vereinfachten Modellen ist der heutige Standard für Suchen nach dunkler Materie am LHC. Wir vergleichen zwei typische Realisierungen dieser Modelle, nämlich solche mit zwei Higgs-Doubletts und einem weiteren skalaren, oder pseudoskalaren, Mediator zum dunklen Sektor. Dabei konzentrieren wir uns auf mögliche Signaturen in Suchen nach $t\bar{t}$ Resonanzen, mono-h, oder mono-Z, welche ein interessantes Zusammenspiel und signifikante Unterschiede in den beiden Modellen aufweisen. Danach wenden wir uns modelunabhängigeren Methoden zu. Zusätzlich zu den dunkle Materie Suchen analysieren wir mit Hilfe effektiver Feldtheorie einen neuen Kanal für die Messung des seltenen Higgszerfalls in ein Z Boson und ein Photon, da dieser signifikante Beiträge von Physik jenseits des Standardmodells aufweisen könnte. Mit Hilfe der vorgeschlagenen Suche in $t\bar{t}$-assoziierter Higgsproduktion ist die Entdeckung dieses Zerfalls bereits am HL-LHC möglich. Eine solche Messung würde zudem starke Grenzen an bisher nur schwer zu testenden Modifikationen der Higgskopplungen setzen. Zurück zu dunkler Materie, hier beschreiben wir detailliert die erweiterte effektive Feldtheorie für dunkle Materie. Dieser Ansatz stellt eine theoretisch konsistente Quantenfeldtheorie dar und ermöglicht die komobinierte Analyse einer Vielzahl von Experimenten über mehrere Energieskalen hinweg, sowie eine valide Phänomenologie an Teilchenbeschleunigern. Durch stetig verfeinerte Tests des allgemeinen Parameterraumes unter Einbeziehung aller relevanten Einschränkungen, können wir in diesem Bereiche identifizieren, die in einfacheren Beschreibungen bereits ausgeschlossen sind. Diese erlaubten Regionen werden durch den hier berücksichtigten, vollständigen Satz von Operatoren ermöglicht und können zum Teil in zukünftigen LHC-Experimenten getested werden. Um darüber hinaus die Flexibilität dieses Ansatzes zu demonstrieren, verwenden wir leicht erweiterte Versionen um zwei phänomenologisch interessante Fälle zu beschreiben: Signaturen aus zwei Fermionen und fehlender transversaler Energie in (zukünftigen) Beschleunigern, und den Exzess im Rückstoßspektrum niederenergetischer Elektronen, den die XENON1T Kollaboration beobachtet hat.

Contents

Publications

The results presented in this thesis are based on the authors publications listed below:

I G. Arcadi, A. Bally, F. Goertz, K. Tame-Narvaez, V. T. Tenorth and S. Vogl, *EFT Interpretation of XENON1T Electron Recoil Excess: Neutrinos and Dark Matter*, accepted for publication by Physical Review D, [arXiv:2007.08500]

II T. Alanne, G. Arcadi, F. Goertz, V. T. Tenorth and S. Vogl, *Model-independent constraints with extended dark matter EFT*, JHEP **10** (2020), 172, [arXiv:2006.07174]

III G. Arcadi, G. Busoni, T. Hugle and V. T. Tenorth, *Comparing 2HDM + Scalar and Pseudoscalar Simplified Models at LHC*, JHEP **06** (2020), 098, [arXiv:2001.10540]

IV F. Goertz, E. Madge, P. Schwaller and V. T. Tenorth, *Discovering the $h \to Z\gamma$ decay in $t\bar{t}$ associated production*, Phys. Rev. D **102** (2020) no.5, 053004, [arXiv:1909.07390]

V F. Goertz, K. Tame-Narvaez and V. T. Tenorth, *Di-jet/e^+e^-+ MET to Probe Z_2-Odd Mediators to the Dark Sector*, Eur. Phys. J. C **79** (2019) no.10, 860, [arXiv:1906.08007]

The following publications were prepared during the authors PhD studies but are not included in this thesis:

VI J. L. Diaz-Cruz, U. J. Saldana-Salazar, K. M. Tame-Narvaez and V. T. Tenorth, *Natural 2HDMs without FCNCs*, [arXiv:2010.05923]

VII M. Bauer, M. Klassen and V. T. Tenorth, *Universal properties of pseudoscalar mediators in dark matter extensions of 2HDMs*, JHEP **07** (2018), 107, [arXiv:1712.06597]

Chapter 1

Introduction

Since its first mention in the early 30s of the last century [1–4], dark matter (DM) has turned from an "overdensity" in the Coma Cluster to one of the leading interests of fundamental physical research. Despite the overwhelming progress in the field, and the large number of robust astrophysical and cosmological observations, the underlying nature of DM remains unknown. Nevertheless, our understanding of physics at the smallest and largest scales has grown enormously in the last 90 years. This knowledge has culminated in the formulation of two standard models, one for particle physics (SM), and one for cosmology (ΛCDM).

The SM is formulated as a Quantum Field Theory (QFT), and its field content has been completed with the discovery of the Higgs boson at the LHC in 2012 [5, 6]. The agreement of the data with the SM predictions is shown in recent precision measurements [7, 8]. The dynamics of elementary particles are described by a Lagrangian with its operators respecting Poincare invariance and the non-trivial local gauge group $G_{SM} = SU(3)_c \times SU(2)_L \times U(1)_Y$. The bosonic force carriers related to these gauge symmetries in addition to the elementary fermionic matter states make up the field content of the SM. It features 18 free low-energy parameters which have to be determined by experiments. Besides the great success of the SM in laboratory experiments, several problems remain unsolved. In this thesis we focus on ways to probe the nature of DM.

The ΛCDM model is based on Einsteins field equations, and describes the evolution of our universe since the Big Bang with only six free parameters. Among other observations it is shaped by high precision measurements of the cosmic microwave background (CMB) from the WMAP [9, 10] to the Planck mission [11, 12]. Those reveal the composition of todays universe to be 69 % dark energy, 26 % DM, and only 5 % baryonic matter described by the SM [13, 14]. The main constituents gave rise to the model's name: Λ for a cosmological constant describing dark energy, and CDM for cold dark matter, where cold means non-relativistic.

Besides its impact on the CMB power spectrum, via forming gravitational wells in the plasma in the early universe, DM also leaves an imprint in many other observations. Examples reach from the well-known flattening of galactic rotation curves [15] over the observation of galaxy cluster mergers showing a clear separation of the gravitational potential and ordinary matter [16] (including the famous "bullet cluster" [17]). In addition, DM is the crucial component in simulations of large scale structure formation [18–20] in order for them to agree with observations [21, 22]. Therefore, evidence for the existence of DM reaches from galactic to cosmological scales. This makes DM a fascinating field of research connecting a broad range of observations and scientific findings. From all these observations, some necessary characteristics of a DM theory can be derived [23], however, an experimentally confirmed, fundamental explanation is still missing.

All this evidence provides excellent motivations and guidance for designing and performing experiments. In the absence of new particles found at the LHC or other high-precision-physics

experiments DM is among the clearest observational hints for BSM physics. While there are trials of non-particle explanations, e.g. modified gravity [24], the aforementioned cluster merges strongly suggests the existence particle-like DM with a very high confidence. However, neither the DM mass, nor its interaction strength with SM particles can be determine by those mergers. Hence, the range of proposed candidates is potentially broader than the range of evidence for DM. The proposed candidates reach from axion-like particles, with masses $\sim 10^{-20}$ eV, to (solarmass) primordial black holes, with masses $\gtrsim M_\odot \sim 10^{66}$ eV. Reviews of (particle) DM and proposed candidates can for instance be found in Refs. [25–31].

Among the proposed candidates, new elementary particles are probably the most discussed option. While those still span a huge range, we will focus on "weakly interacting massive particles" (WIMPs). They are (among others) motivated by the finding that a particle with its mass, and its interaction strength to SM fields, both related to the electroweak scale can "naturally" end up with the correct relic abundance. To this end, the simple thermal freeze out mechanism is considered. This is also the main DM production mechanism considered throughout this thesis. Here, the DM decouples (or "freezes out") from the thermal SM bath, when its average interaction rate drops below the expansion rate of the universe. This is the so-called "WIMP-miracle", or more appropriately "coincidence" (or "number crunsh"). Such a particle is not only rather easy to include in many theories for physics beyond the SM (BSM), but also served as a guideline for several new experiments. Experiments searching for DM are performed in various ways and especially at very different energy scales, or better momentum transfers. Combining and consistently describing those experiments in a manner which is as general as possible is a theoretical challenge for which different solutions have been raised.

Let us first briefly look at the three main search strategies that are currently explored to discover WIMP-like DM. Starting with the lowest momentum transfer, direct detection (DD) experiments aim to observe the recoil of a nucleus caused by a DM particle; for an introduction to DD see e.g. Ref. [32]. Since these recoil events are very rare, a low-background environment and a dense detector medium are needed. The leading exclusion limits are obtained with liquid xenon detectors, e.g. XENON1T [33], PandaX [34], or LUX [35]. The second approach is called indirect detection (ID), which searches for potential SM remnants of DM annihilations or decays. The most promising indicators are gamma-ray lines, or an excess of antimatter detectable via telescopes, e.g. H.E.S.S. [36], or satellite-based particle detectors, e.g. Fermi-LAT [37–39]. Promising search regions are those with a high DM density, like dwarf galaxies, galaxy cluster, and the center of the Milky Way; for reviews see e.g. Refs. [40, 41]. Finally there are collider searches, which aim to directly produce DM in high-energy particle collisions; see e.g. Ref. [42] for a review. As DM has no electric charge, it evades the detectors at colliders. For detection, it has to be produced in association with a visible, highly energetic SM particle leading to so-called mono-X events. The DM particle would then manifest itself via momentum imbalance as missing transverse energy ($\not{E}_T$). The LHC experiments, ATLAS [43] and CMS [44], are looking for an excess of mono-X events over the SM background [45, 46].

While in principle those searches are independent of the exact model used to describe DM, collider searches in particular need theoretical benchmarks to identify interesting kinematic regions, and to optimize the search strategy and data analyses. Those benchmark models also allow the characterization of a potential discovery, and the consistent comparison with the non-collider searches. This is especially relevant since even in case of a $\not{E}_T$ signal at the LHC experiments, it is not unequivocally possible to relate this to DM. A simple reason for this is that at the LHC, all electrically-neutral particles with a lifetime longer $\mathcal{O}(10^{-8}\,\text{s})$ leave the detectors, and are counted as $\not{E}_T$, while a proper DM candidate has to be stable over the

lifetime of the universe. Therefore, combining results from several experiments is necessary to determine all properties and aspects of the DM candidate. For simplicity we will always refer to invisible states in this work as DM, even if the cosmological properties are not those of single-component DM.

In the end, there is of course a deeper motivation to develop adequate models for DM than computing cross sections. The aim of particle physics is to develop a more fundamental theory of nature, and DM is currently one of the most promising and clearest hints towards that.

In the pre-LHC era, phenomenological studies were dominated by complex models, such as supersymmetry, composite Higgs, and others. Those models are designed to address the hierarchy problem, and therefore, feature states close to the EW scale, which could have been discovered in the early LHC runs. Their non-discovery lead to simpler and more model-independent approaches to cover a higher variety of potential BSM realizations, especially in the case of DM searches. The dark matter effective field theory (DMEFT) was initially used to this end, and to allow comparisons of DD and collider searches. There, only one state is added to the SM field content: the DM candidate, which is a singlet under the SM gauge groups in the simplest realizations. Additional states belonging to more complex dark sectors are assumed to be heavy, and are integrated out. Hence, the interactions of DM with SM fields are parametrized via effective operators, typically of dimension six. Visible states needed for the mono-X signatures are obtained via initial state radiation (ISR). This setup allows for relatively model-independent comparisons of different searches with a small parameter space, spanned by the Wilson coefficients and the DM mass; more details are given in Sec. 3.1. Nevertheless, it was soon realized that the critical assumption for the validity of effective field theories (EFT) gets potentially violated at the LHC. In fact the momentum transfer in LHC collisions can be of the same order as the masses of the states integrated out. In this case, the kinematics predicted in the DMEFT can differ significantly from models where the mediator is taken into account explicitly due to on-shell effects [47–55]. Therefore, the general applicability of the DMEFT for LHC searches is (at least) questionable.

To capture the effects of on-shell mediators, the so-called simplified models were developed; see e.g. Refs. [56–59] for reviews. Those consider not only the DM candidate but also a mediating particle as a propagating degree of freedom. Several ways to realize such simplified models have been proposed for different types of DM, and especially for different spins of the mediator. Also how the interactions with the SM are implemented can differ, still simplified models share some common advantages. They capture the kinematics in particle collisions correctly, need only a rather small set of parameters, and allow additional observables to be included, for instance resonance searches for the mediator. On the other hand, they exhibit several drawbacks, for example the implied coupling structure typically does not respect gauge invariance. This leads to unitarity violation in several processes directly related to DM searches, like the mono-Z cross section $\sigma(gg \to Za) \sim \ln^4(s)$. Due to the log-dependence on the center of mass energy, $\sqrt{s}$, simplified models do not break down at energies available at the LHC, but the energy dependence indicates the presence of additional contributions to this processes in every gauge-invariant completion. Hence, in these interesting and relevant channels additional states cannot be fully decoupled in general and could change the DM phenomenology. A simple way to recover gauge-invariance would be via mixing the mediator with one of the SM bosons. However, those interactions are strongly constrained by other, non-DM observables, like Higgs-signal strength measurements, and exclude the parameter space of potential interest for mono-X searches. This lack of viable theoretical completions renders predictions of simplified models potentially unreliable, see e.g. [45, 60–74]. From a positive viewpoint, this might hint

towards a more complex and therefore more interesting new physics sector with impacts on DM searches, and potentially accessible in near-future experiments. In fact, there is no reason for the dark sector to consist only of a minimal particle content.

While these are mainly theoretically driven arguments, there are also experimental or phenomenological motivations to go beyond simplified models. The simplicity of the these models might render them too strongly constrained and prevent taking interesting channels into account. Even though featuring a richer phenomenology than DMEFTs, they are associated with a limited set of experimental signatures. In addition, the sensitivity reach of mono-X searches is dominated by the mono-jet channel. Similar to the DMEFT the visible states originate from ISR, and jets have the strongest interaction of those states. However, even mono-jet searches are often sub-dominant compared to DD and resonance searches for the mediator, especially for vector mediators. Therefore, the experimental collaborations are interested in theoretically consistent models, which allow for a richer phenomenology and so far unexplored channels for DM searches at the LHC.

The main topic of this thesis is to investigate two approaches aiming for a more sophisticated description of DM searches. First, two established examples of so-called next-generation simplified models are investigated in detail: a two-Higgs-doublet model (2HDM) plus an additional scalar (S) or pseudoscalar (PS) singlet mediator. These models are new benchmark scenarios for the LHC collaborations. They overcome many drawbacks of the simplified models mentioned above with the price of a more complex field and parameter content, and an increase in model dependency. We will place the focus on three specific collider signatures and their interplay to constrain and potentially distinguish the two models.

The second half is dedicated to a detailed analysis of a new approach, the extended dark matter effective field theory (eDMEFT). It features a mediator as propagating degree of freedom, and accounts for additional new physics by consistently including effective operators keeping a high level of flexibility and model-independence. The framework is faced with various constraints in general parameter scans, and applied to two more specific scenarios to show its broad applicability.

In detail, this thesis is structured as follows. We discuss and compare the important benchmark scenarios of a 2HDM plus a scalar or a pseudoscalar mediator in Chapter 2. After introducing the two models and their potentials in Sec. 2.1, we narrow the parameter space with a list of general constraints in Sec. 2.2. In Sec. 2.3 we derive and compare the reach of three dedicated collider channels for both models, namely $t\bar{t}$ resonances, mono-Z and mono-h. Those limits are derived for the first time in the 2HDM+S. We discuss how to distinguish the two models by the ratio of their signal strengths in different channels, and summarize in Sec. 2.4.

To set the stage for the second approach towards a model-independent interpretation of DM searches, we examine EFTs in Chapter 3. They can provide relatively model-independent classifications of experimental results to discover new physics. Starting with a brief introduction of general EFT concepts in Sec. 3.1, we take a small detour to a non-DM related analysis. Precision measurements of the Higgs sector are a key test of the SM. In case of an observed deviation, they can reveal BSM contributions hidden in other channels, or otherwise can severely constrain them. To this end, in Sec. 3.2 we explore the potential to discover the decay of a SM Higgs to a Z boson and a photon in $t\bar{t}$-associated production. Projected limits can be used to constrain new physics contributions. Afterwards the theoretical background for the eDMEFT is introduced in Sec. 3.3.

The phenomenology of the eDMEFT is explored in great detail in Chapter 4. We start

with the case of a scalar mediator, and qualitatively discuss DM and collider related limits in Secs. 4.1.1 and 4.1.2. In Sec. 4.1.3 we show how simplified models are naturally captured by the eDMEFT in a gauge-invariant way. In addition, they are extended with additional operators to open up parameter space, and finally a generic parameter scan is performed, taking all discussed bounds into account. In Sec. 4.2 the analysis is repeated for a pseudoscalar mediator, which features crucial phenomenological differences. To further show the flexibility of the eDMEFT, we investigate two more specific scenarios. First, the case of a mediator charged under a $\mathbb{Z}_2$ symmetry is investigated in Sec. 4.3. The setup there is motivated by the smallness of the first-generation fermion masses and can give rise to interesting collider signatures. Second, we characterize the excess of low-energy electron recoil events recently announced by the XENON1T collaboration in a variant of the eDMEFT containing two $\mathbb{Z}_2$ charged mediators in Sec. 4.4. Those mediators give rise to neutrino-electron scattering which significantly improves the fit. The severe experimental constraints can be avoided by appropriately chosen parameters and non-trivial mechanisms.

In Chapter 5 we finally summarize our findings and conclude.

Chapter 2

2HDM plus Scalar or Pseudoscalar

The search for DM is one of the major topics of the LHC program, and the requirements for modeling DM have evolved over time. In fact, further-improved approaches have become necessary due to the of problems the DMEFT and simplified models which are discussed in the introduction.

In this chapter we investigate in detail two instances belonging to the next generation of simplified models for DM and compare them with each other. Criteria for these are listed in Ref. [45], as follows:

- theoretically consistent extension of a simplified model used by the LHC collaborations;
- generality to be potentially used in more complete theoretical frameworks;
- phenomenology versatile enough to encourage comparison of different experimental signals and searches in unexplored channels;
- interest beyond the DM community to identify other (in)direct constraints.

Two notable examples of models satisfying this criteria are the 2HDM+S and 2HDM+PS [60, 61, 64, 66, 72]. Here a 2DHM is extended either by a $\mathcal{CP}$-even scalar S or $\mathcal{CP}$-odd pseudoscalar P mediating between the SM and the dark sector. Since they are singlets under the SM gauge groups, they allow for a renormalizable coupling with a fermionic gauge singlet DM candidate χ. The coupling to the SM is realized in a second step, where a portal is created by mass mixing of the spin-0 singlet with the state of the second Higgs doublet, which shares its $\mathcal{CP}$-property. Hence, all interactions are invariant under the SM gauge group.

Beyond these theoretical advantages, the typical hierarchy of constraints from mono-X searches in simplified models, where X originates from ISR [61, 75],

$$\text{mono-jet} > \text{mono-photon} > \text{mono-}Z/W^{\pm} > \text{mono-}h$$

can be broken up. That is because in the 2HDM+S and 2HDM+PS the mono-Z, and mono-h cross sections can be resonantly enhanced [61,76]. This is in particular interesting, as constraints from mono-jet searches are not expected to improve significantly in the near future. The reason for this is that they are already limited by systematic uncertainties and therefore do not benefit from only increasing the total accumulated luminosity [61, 77, 78]. On the contrary, mono-Z/h searches are expected to improve significantly in the near-future LHC runs; thus it is worth to investigate frameworks where they can lead to relevant constraints. In addition, the 2HDM+S and 2HDM+PS provide a broad variety of collider signals beyond simple missing energy signatures; see e.g. Refs. [45, 60, 61, 64–69].

It is important to note that, even as the 2HDM+S/PS are UV complete, in the sense that all couplings are renormalizable and respect gauge invariance, they should be interpreted more

as minimal benchmark models for LHC searches than full models. Therefore, the presence of further BSM states is possible and not a contradiction.

While the 2HDM+PS was already used by the LHC collaborations, e.g. first by CMS in the mono-h analysis in [79], a dedicated collider study for the 2HDM+S was missing prior to our work in [80]. In addition, we work out similarities, and distinguishing features of the two models.

This chapter closely follows Ref. [80] and studies various signatures, namely $t\bar{t}$ resonances, mono-Z and mono-h, particularly relevant for the 2HDM+S and PS. Although these signatures are present in both models, there can be sizable differences in the expected signal rates. This opens the possibility of discriminating between the models in case of a future signal detection. To this end we characterize similarities and differences in the two approaches by deriving limits from current LHC data, and in case of the mono-Z channel, also from projections for future HL-LHC runs.

We start with comprehensively describing the models in Sec. 2.1, focusing on their scalar potentials in the Higgs and flavor basis and the relevant parameter space. Then we will give an overview of experimental and theoretical constraints applied in general to 2HDMs and DM models in Sec. 2.2. Those provide a guideline to narrow the extended parameter space for the final LHC analyses. The main findings are presented in Sec. 2.3 with the analysis of the three LHC signatures mentioned above, for the two models under consideration. We compare the sensitivity reach of the channels among each other and among the models to point out how they could be distinguished in case of an observation. Finally, we summarize and discuss our findings in Sec. 2.4.

2.1 Model Setup

The two models under consideration feature an extended scalar sector with non-trivial potentials. In the first part of this section those and the related parameter spaces are introduced and homogenized. We then turn to the Yukawa interactions and discuss branching ratios of the spin-0 states. These will become relevant for interpretations of the following analyses.

While a full review of 2HDMs is beyond the scope of this thesis and done in e.g. [81–83], we focus on features regarding the analyses of mono-X searches and give the theoretical background to simplify the following phenomenological discussions.

2.1.1 Scalar Potential

We start with a discussion of the scalar potentials of both models, and the applied symmetries in order to simplify them. Besides introducing the notation, simplified versions of the potential are given at the end.

In the most general form the scalar potentials of the two models can be written as

$$V(\Phi_1, \Phi_2, P) = V_{\text{2HD}}(\Phi_1, \Phi_2) + V_P(P) + V_{P\text{2HD}}(\Phi_1, \Phi_2, P), \tag{2.1}$$

$$V(\Phi_1, \Phi_2, S) = V_{\text{2HD}}(\Phi_1, \Phi_2) + V_S(S) + V_{S\text{2HD}}(\Phi_1, \Phi_2, S), \tag{2.2}$$

where V_{2HD} denotes the known potential for two SU(2) Higgs doublets and will be briefly reviewed hereafter. The potentials V_S and V_P involve the scalar and pseudoscalar singlet self-interactions, while $V_{S\text{2HD}}$ and $V_{P\text{2HD}}$ contain their interactions with the two doublets. Both will be explained in more detail below.

2HDM We point out basic properties of the generic 2HDM scalar potential relevant for our analysis. The two $SU(2)$-doublets (Φ_1, Φ_2) can be defined as

$$\Phi_i = \begin{pmatrix} \Phi_i^+ \\ \frac{1}{\sqrt{2}}\left(v_i + \rho_i + i\eta_i\right) \end{pmatrix}, \tag{2.3}$$

where Φ_i^+ is the charged scalar component, $\rho_{1,2}$ are even, and $\eta_{1,2}$ odd under $\mathcal{CP}$-transformation, but all are not necessarily mass eigenstates. The vacuum expectation values (vevs) $v_{1,2}$ are usually parametrized in terms of

$$\tan\beta = \frac{v_2}{v_1}, \qquad \text{with} \qquad v_1^2 + v_2^2 = v^2 \approx (246\,\text{GeV})^2, \tag{2.4}$$

where $\tan\beta$ is in general a basis-dependent quantity. Choosing a specific scalar basis for the Yukawa sector relates it to physical parameters [84, 85].

The most general potential for two doublets reads

$$\begin{aligned} V_{\text{2HD}}(\Phi_1,\Phi_2) =& M_{11}^2\Phi_1^\dagger\Phi_1 + M_{22}^2\Phi_2^\dagger\Phi_2 + \left[M_{12}^2\Phi_2^\dagger\Phi_1 + \text{h.c.}\right] \\ &+ \tfrac{1}{2}\lambda_1(\Phi_1^\dagger\Phi_1)^2 + \tfrac{1}{2}\lambda_2(\Phi_2^\dagger\Phi_2)^2 \\ &+ \lambda_3(\Phi_1^\dagger\Phi_1)(\Phi_2^\dagger\Phi_2) + \lambda_4(\Phi_2^\dagger\Phi_1)(\Phi_1^\dagger\Phi_2) \\ &+ \left[\tfrac{1}{2}\lambda_5(\Phi_2^\dagger\Phi_1)^2 + \left\{\lambda_6(\Phi_1^\dagger\Phi_1) + \lambda_7(\Phi_2^\dagger\Phi_2)\right\}(\Phi_1^\dagger\Phi_2) + \text{h.c.}\right], \end{aligned} \tag{2.5}$$

where in general the coefficients $\lambda_{5,6,7}$ and M_{12}^2 can be complex. They and both vevs are taken to be real to ensure $\mathcal{CP}$ conservation of the potential and vacuum [86, 87].

As the doublets carry identical charges under the SM gauge group, we have the freedom to choose a specific basis in terms of which to write the potential. A generic SU(2) change of basis,

$$\begin{pmatrix}\Phi_1\\ \Phi_2\end{pmatrix} \;\rightarrow\; \begin{pmatrix}\Phi_1'\\ \Phi_2'\end{pmatrix} = U\begin{pmatrix}\Phi_1\\ \Phi_2\end{pmatrix}, \tag{2.6}$$

where U is an SU(2) matrix, will result in a potential giving the same physical results but with different coefficients for the new operators. Note that in our case, where all potential coefficients are real, the freedom reduces to SO(2) rotations.

We will use this to change between the flavor and the Higgs basis [84, 87]. In the Higgs basis doublets will be labeled with (Φ_h, Φ_H). It is defined such that only one doublet develops a vev and is identified with SM Higgs doublet. The rotation to the Higgs basis and the resulting doublets are given by

$$\begin{aligned} \Phi_h &= \cos\beta\,\Phi_1 + \sin\beta\,\Phi_2 = \begin{pmatrix} G^+ \\ \frac{1}{\sqrt{2}}(v + \hat{\rho}_1 + iG^0) \end{pmatrix}, \\ \Phi_H &= -\sin\beta\,\Phi_1 + \cos\beta\,\Phi_2 = \begin{pmatrix} H^+ \\ \frac{1}{\sqrt{2}}(\hat{\rho}_2 + i\hat{\rho}_3) \end{pmatrix}, \end{aligned} \tag{2.7}$$

where the SM Goldstone bosons $G^\pm$, G^0, and the charged scalars $H^\pm$ are already mass eigenstates. The $\mathcal{CP}$-even scalars $\hat{\rho}_{1,2}$, on the other hand, are linear combinations of the SM

Higgs boson, h, the additional 2HDM scalar, H, and, in the case of the 2HDM+S, the singlet mediator S. Instead, $\hat{\rho}_3$ is $\mathcal{CP}$-odd and related to the 2HDM pseudoscalar A and, in the case of the 2HDM+PS, is a linear combination with P. We will discuss the mass eigenstates and the mass ordering separately for both cases further below.

The potential from Eq. (2.5) transforms to

$$\begin{aligned}\hat{V}_{\text{2HD}}(\Phi_h,\Phi_H) =&\hat{M}^2_{hh}\Phi_h^\dagger\Phi_h + \hat{M}^2_{HH}\Phi_H^\dagger\Phi_H + \left[\hat{M}^2_{hH}\Phi_H^\dagger\Phi_h + \text{h.c.}\right]\\ &+ \tfrac{1}{2}\hat{\lambda}_h(\Phi_h^\dagger\Phi_h)^2 + \tfrac{1}{2}\hat{\lambda}_H(\Phi_H^\dagger\Phi_H)^2\\ &+ \hat{\lambda}_3(\Phi_h^\dagger\Phi_h)(\Phi_H^\dagger\Phi_H) + \hat{\lambda}_4(\Phi_H^\dagger\Phi_h)(\Phi_h^\dagger\Phi_H)\\ &+ \left[\tfrac{1}{2}\hat{\lambda}_5(\Phi_H^\dagger\Phi_h)^2 + \left\{\hat{\lambda}_6(\Phi_h^\dagger\Phi_h) + \hat{\lambda}_7(\Phi_H^\dagger\Phi_H)\right\}\Phi_H^\dagger\Phi_h + \text{h.c.}\right],\end{aligned} \tag{2.8}$$

due to choosing the coefficients of Eq. (2.5) to be real, all parameters are real. The minimization conditions of the scalar potential simplify in the Higgs basis, where only one doublet develops a vev, to

$$M^2_{hh} = -\tfrac{1}{2}\hat{\lambda}_h v^2 \quad \text{and} \quad M^2_{hH} = -\tfrac{1}{2}\hat{\lambda}_6 v^2. \tag{2.9}$$

$\mathbb{Z}_2$-Symmetry and Alignment Limit As we will see in the discussion of the Yukawa couplings in the next section, to ensure the absence of flavor changing neutral currents (FCNCs) typically a discrete $\mathbb{Z}_2$ symmetry is imposed, under which the doublets transform as $\Phi_1 \to +\Phi_1$ and $\Phi_2 \to -\Phi_2$.

When applied to the scalar potential in Eq. (2.5), this symmetry is slightly relaxed by allowing for the soft breaking term proportional to M^2_{12}, as it is needed to obtain the desired mass spectrum. Therefore, we set

$$\lambda_6 = \lambda_7 = 0. \tag{2.10}$$

The potential with this restriction will be referred to as the flavor basis, as each Φ_i interacts with a specific fermion flavor, see Sec. 2.1.2.

So far, precision measurements of the Higgs couplings done by the ATLAS and CMS collaborations show no deviations from the SM predictions, and restrict the Higgs to interact very similar to the SM predictions [7, 8]. In order to avoid these strong bounds, the original papers [60, 61, 64, 66] and experimental searches [46, 79] using the 2HDM+S/PS exploit the alignment limit, where the light $\mathcal{CP}$-even scalar part of the two doublets h has SM-like couplings to fermions and gauge bosons. This limit can be ensured by a specific choice of the potential coefficients [88]

$$\lambda_1 = \lambda_2 = \lambda_3 + \lambda_4 + \lambda_5. \tag{2.11}$$

With this choice, transferring the potential parameters from the flavor to the Higgs basis is particularly easy, as $\lambda_i = \hat{\lambda}_i$ for $i = \{1, h\}$, $\{2, H\}$, 3, 4, 5 and in particular $\hat{\lambda}_6 = \hat{\lambda}_7 = 0$. We note that $c_{\beta-\alpha} \propto \hat{\lambda}_6 = 0$, where α is the mixing angle of the $\mathcal{CP}$-even scalars, and this condition is typically used to denote the alignment limit.

Applying these two assumptions, the Higgs basis potential in Eq. (2.8) simplifies to

$$\begin{aligned}\hat{V}_{\text{2HD}}(\Phi_h,\Phi_H) =&\hat{M}^2_{hh}\Phi_h^\dagger\Phi_h + \hat{M}^2_{HH}\Phi_H^\dagger\Phi_H\\ &+ \tfrac{1}{2}\lambda_1\left[(\Phi_h^\dagger\Phi_h)^2 + (\Phi_H^\dagger\Phi_H)^2\right] + \lambda_3(\Phi_h^\dagger\Phi_h)(\Phi_H^\dagger\Phi_H)\\ &+ \lambda_4(\Phi_H^\dagger\Phi_h)(\Phi_h^\dagger\Phi_H) + \tfrac{1}{2}\lambda_5\left[(\Phi_H^\dagger\Phi_h)^2 + \text{h.c.}\right],\end{aligned} \tag{2.12}$$

where we made use of the minimization conditions from Eq. (2.9). We will now turn to the implications of the two considered scenarios with an additional singlet.

Pseudoscalar Extension The 2HDM+PS specific parts of the potential from Eq. (2.1) are given by [60, 61, 80]

$$V_P(P) = \tfrac{1}{2} M_{PP}^2 P^2 + \tfrac{1}{4}\lambda_P P^4, \tag{2.13}$$

$$V_{P2\mathrm{HD}}(\Phi_1,\Phi_2,P) = \lambda_{P1}(\Phi_1^\dagger\Phi_1)P^2 + \lambda_{P2}(\Phi_2^\dagger\Phi_2)P^2 + \mu_{P12} P\left(i\Phi_1^\dagger\Phi_2 + \mathrm{h.c.}\right). \tag{2.14}$$

Rewriting these in the Higgs basis leads to

$$\hat{V}(\Phi_h,\Phi_H,P) = \hat{V}_{2\mathrm{HD}}(\Phi_h,\Phi_H) + V_P(P) + \hat{V}_{P2\mathrm{HD}}(\Phi_h,\Phi_H,P), \tag{2.15}$$

where $\hat{V}_{2\mathrm{HD}}$ is discussed in Eqs. (2.8) and (2.12). While V_P does not change under the $SU(2)$ transformation, the interactions with the new defined doublets are given by

$$\begin{aligned}\hat{V}_{P2\mathrm{HD}}(\Phi_h,\Phi_H,P) =& \hat{\lambda}_{HHP}(\Phi_H^\dagger\Phi_H)P^2 + \hat{\lambda}_{hhP}(\Phi_h^\dagger\Phi_h)P^2 \\ &+ \hat{\lambda}_{hHP}\, P^2\left(\Phi_h^\dagger\Phi_H + \mathrm{h.c.}\right) + \mu_{P12}\, P\left(i\Phi_h^\dagger\Phi_H + \mathrm{h.c.}\right),\end{aligned} \tag{2.16}$$

with μ_{P12} staying unchanged and the coefficients transforming as

$$\begin{aligned}\hat{\lambda}_{HHP} &= \sin^2\beta\,\lambda_{P1} + \cos^2\beta\,\lambda_{P2}, \\ \hat{\lambda}_{hhP} &= \cos^2\beta\,\lambda_{P1} + \sin^2\beta\,\lambda_{P2}, \\ \hat{\lambda}_{hHP} &= \sin\beta\cos\beta\,(\lambda_{P2} - \lambda_{P1}).\end{aligned} \tag{2.17}$$

When written in the Higgs basis and with the alignment conditions in Eq. (2.11) applied, the mass matrix of the 2HDM+PS is block diagonal and includes two parts. The first one is a diagonal block containing two zero eigenvalues corresponding to the massless SM Goldstone bosons G^0, $G^\pm$, and the squared masses M_h^2, M_H^2, $M_{H^\pm}^2$ of the $\mathcal{CP}$-even mass eigenstates. The second one is a two-dimensional block made up of the $\mathcal{CP}$-odd states $\hat{\rho}_3$ and P. Diagonalizing it via their mixing angle

$$\sin 2\theta = \frac{2\,v\,\mu_{P12}}{M_A^2 - M_a^2}, \tag{2.18}$$

gives rise to the physical mass eigenstates a and A with masses M_a^2 and M_A^2. According to Refs. [61, 64], we concentrate on $M_a < M_A$ and small mixing, such that a denotes the more singlet-like state.

Together with the alignment conditions in Eq. (2.11), the original set of parameters $\lambda_{1,2,3,4,5}$, M_{11}^2, M_{22}^2, M_{12}^2, M_{PP}^2, and μ_{P12} can be expressed in terms of M_h, M_H, $M_{H^\pm}$, M_A, M_a, $\sin\theta$, $\tan\beta$, and v.

Scalar Extension For the 2HDM+S, the singlet specific parts of the potential in Eq. (2.2) in the most general expression, are given by

$$V_S(S) = \tfrac{1}{2} M_{SS}^2 S^2 + \tfrac{1}{3}\mu_S S^3 + \tfrac{1}{4}\lambda_S S^4, \tag{2.19}$$

$$\begin{aligned}V_{S2\mathrm{HD}}(\Phi_1,\Phi_2,S) =& \mu_{S1}(\Phi_1^\dagger\Phi_1)S + \mu_{S2}(\Phi_2^\dagger\Phi_2)S + \mu_{S12}S\left(\Phi_2^\dagger\Phi_1 + \mathrm{h.c}\right) \\ &+ \tfrac{1}{2}\lambda_{S1}(\Phi_1^\dagger\Phi_1)S^2 + \tfrac{1}{2}\lambda_{S2}(\Phi_2^\dagger\Phi_2)S^2 + \tfrac{1}{2}\lambda_{S12}S^2\left(\Phi_2^\dagger\Phi_1 + \mathrm{h.c}\right),\end{aligned} \tag{2.20}$$

where all coefficients are taken to be real to ensure $\mathcal{CP}$ conservation. The λ_{S12} term vanishes due to the assumed $\mathbb{Z}_2$ symmetry of the Higgs doublets. Extending this $\mathbb{Z}_2$ symmetry to S by choosing $S \to -S$, in the potentials (2.19) and (2.20), the terms μ_S, μ_{S1}, and μ_{S2} would be forbidden. However, they would be allowed in the case of the softly broken $\mathbb{Z}_2$. Since all these terms would only affect the scalar trilinear and quartic interactions, they would have a negligible impact on the phenomenology discussed in this work. Consequently, and in line with the 2HDM+PS definitions in Ref. [61], we will not include them in our analysis. While later on we are interested in a specific trilinear vertex, states from both doublets are required to generate the relevant effect; see Sec. 2.3.3.

A similar procedure as in the 2HDM+PS would be possible to mix the $\mathcal{CP}$-even scalars. However, we take another approach here, which further simplifies the potential. We make the additional assumption that the scalar potential in Eq. (2.2) features a $\mathbb{Z}_2^S$ symmetry under which only S is odd, which is spontaneously broken by the vev of the singlet. Therefore, all linear and cubic terms vanish independently of the basis choice for the doublets [64, 72]. Therefore in the Higgs basis, the singlet part of the potential

$$\hat{V}(\Phi_h, \Phi_H, S) = \hat{V}_{\text{2HD}}(\Phi_h, \Phi_H) + V_S(S) + \hat{V}_{S\text{2HD}}(\Phi_h, \Phi_H, S), \tag{2.21}$$

with $\hat{V}_{\text{2HD}}$ given in Eq. (2.12), simplifies to

$$\begin{aligned}\hat{V}_{S\text{2HD}}(\Phi_h, \Phi_H, S) =& \tfrac{1}{2}\hat{\lambda}_{HHS}(\Phi_H^\dagger \Phi_H)S^2 + \tfrac{1}{2}\hat{\lambda}_{hhS}(\Phi_h^\dagger \Phi_h)S^2 \\ &+ \tfrac{1}{2}\hat{\lambda}_{hHS}S^2\left(\Phi_h^\dagger \Phi_H + \text{h.c}\right),\end{aligned} \tag{2.22}$$

where the coefficients transform according to Eq. (2.17). To reach the alignment limit, the additional requirement

$$\hat{\lambda}_{hhS} = 0 \tag{2.23}$$

is needed to avoid mixing of the SM Higgs and S.

In the alignment limit the mass matrix of the 2HDM+S is made of a diagonal block containing two zero eigenvalues, corresponding to the SM Goldstone bosons G^0, $G^\pm$, and the squared masses M_h^2, $M_{H^\pm}^2$, M_A^2, plus a two-dimensional block. Diagonalizing this block of the $\mathcal{CP}$-even states $\hat{\rho}_2$ and S, via a rotation with the mixing angle

$$\sin 2\theta = \frac{2\hat{\lambda}_{hHS}\, v\, v_S}{M_{S_1}^2 - M_{S_2}^2}, \tag{2.24}$$

leads to the two mass eigenstates S_1 and S_2 with masses $M_{S_{1,2}}$. Again, we will concentrate on the case $M_{S_2} < M_{S_1}$ and small mixing, such that S_2 is more singlet-like. With the alignment conditions in Eq. (2.11) one can exchange the parameters $\hat{\lambda}_{1,2,3,4,5}$, M_{11}^2, M_{22}^2, M_{12}^2, M_{SS}^2, and $\hat{\lambda}_{hHS}$ for M_h, M_{S_1}, $M_{H^\pm}$, M_A, M_{S_2}, $\sin\theta$, $\tan\beta$, and v. The additional alignment condition from Eq. (2.23) sets $\hat{\lambda}_{hhS}$, while $\hat{\lambda}_{HHS}$ and λ_S remain free. This limit has the additional advantage that the λ_i do not change in an uncontrolled way when varying $\tan\beta$.

To facilitate a reasonable comparison between the 2HDM+PS and 2HDM+S and to avoid variations with $\tan\beta$, we set

$$\hat{\lambda}_{HHS} = 0 \qquad \text{and} \qquad \hat{\lambda}_{hhP} = \hat{\lambda}_{HHP} = \hat{\lambda}_{hHP} = 0, \tag{2.25}$$

Model	ϵ_d	ϵ_u	ϵ_l
Type I	$\cot\beta$	$\cot\beta$	$\cot\beta$
Type II	$-\tan\beta$	$\cot\beta$	$-\tan\beta$
Type X	$\cot\beta$	$\cot\beta$	$-\tan\beta$
Type Y	$-\tan\beta$	$\cot\beta$	$\cot\beta$

Table 2.1: Values of the Yukawa scaling factors $\epsilon_{u,d,l}$ which correspond to models with discrete $\mathbb{Z}_2$ symmetries.

for the rest of the chapter. The parameters $\lambda_{P,S}$ are set to zero as they are not relevant for the considered signatures.

Finally, applying all restrictions simplifies the potentials significantly to

$$\hat{V}(\Phi_h, \Phi_H, P) = \hat{V}_{\text{2HD}}(\Phi_h, \Phi_H) + \mu_{P12}\, P \left(i\Phi_h^\dagger \Phi_H + \text{h.c.} \right), \tag{2.26}$$

$$\hat{V}(\Phi_h, \Phi_H, S) = \hat{V}_{\text{2HD}}(\Phi_h, \Phi_H) + \hat{\lambda}_{hHS}\, S^2 \left(\Phi_h^\dagger \Phi_H + \text{h.c.} \right), \tag{2.27}$$

with the restricted 2HDM potential $\hat{V}_{\text{2HD}}$ given in Eq. (2.12).

2.1.2 Yukawa Sector

For the collider phenomenology the interactions of the additional spin-0 states with SM fermions are essential. Therefore, we investigate possible Yukawa structures of the two models, which simultaneously avoid observational constraints.

In full generality, the Yukawa interactions of the SM fermions with the two Higgs doublets can be expressed as

$$\mathcal{L}_{\text{Yukawa}} = -\sum_{n=1,2} \left(\left(Y_n^u\right)^{ij} \bar{Q}_L^i \widetilde{\Phi}_n u_R^j + \left(Y_n^d\right)^{ij} \bar{Q}_L^i \Phi_n d_R^j + \left(Y_n^\ell\right)^{ij} \bar{L}_L^i \Phi_n \ell_R^j + \text{h.c.} \right). \tag{2.28}$$

Here Q_L, and L_L denote the left-handed quark and lepton doublets. The right-handed singlets for the leptons, up-, and down-quarks are denoted by ℓ_R, u_R, and d_R, respectively, and $\widetilde{\Phi}_n = \epsilon \Phi_n^*$ with ϵ the two-dimensional antisymmetric tensor. Diagonalizing the fermion mass matrices does in general not simultaneously diagonalize the Yukawa matrix anymore, because each fermion gets two mass contributions. This can give rise to flavor-changing neutral currents (FCNCs), which are strongly constrained by experiments.

The typical approach to avoid FCNCs at tree-level in 2HDMs is to introduce a $\mathbb{Z}_2$ symmetry in the Yukawa sector, which can be the same as the one in the scalar sector. The charges are assigned to the right-handed singlets, such that only one of the two doublets $\Phi_{1,2}$ is allowed to couple to a certain fermion flavor, and it goes under the name of natural flavor conservation (NFC) [89, 90]. There are four possible assignments of the $\mathbb{Z}_2$ charges, which result in different types of 2HDMs.

Another way to see how FCNCs can be avoided is by rewriting Eq. (2.28) in the Higgs basis

$$\mathcal{L}_{\text{Yukawa}} = -\sum_{n=h,H} \left(\left(\hat{Y}_n^u\right)^{ij} \bar{Q}_L^i \widetilde{\Phi}_n u_R^j + \left(\hat{Y}_n^d\right)^{ij} \bar{Q}_L^i \Phi_n d_R^j + \left(\hat{Y}_n^\ell\right)^{ij} \bar{L}_L^i \Phi_n \ell_R^j + \text{h.c.} \right). \tag{2.29}$$

Here Φ_h corresponds to the SM Higgs doublet and the corresponding Yukawa matrices $Y_h^{u,d,l}$ have to be the SM ones. The matrices of the second doublet are then assumed to be proportional

to them, namely

$$\hat{Y}_h^i \equiv Y_{\text{SM}}^i \qquad \text{and} \qquad \hat{Y}_H^i = \epsilon_i Y_{\text{SM}}^i, \tag{2.30}$$

with the scaling factors ϵ_i and $i = u,\, d,\, \ell$. This Yukawa structure satisfies NFC, and is called the Aligned Yukawa model [91–97]. In special cases, this structure can correspond to one of the $\mathbb{Z}_2$ symmetric Yukawa assignments, where the ϵ_i satisfy the relationships shown in Table 2.1. We will concentrate on these cases in the following. Since we will only consider values of $0.3 \leq \tan\beta \leq 3$, our results will be valid for all Yukawa types included in Table 2.1.

The presence of the charged scalar $H^\pm$ allows for FCNC at loop level, which enables limits to be set on $\tan\beta$, and the charged scalar mass. These also hold in the alignment limit that is weakly constrained by many other Higgs physics observables: see Sec. 2.2.1.

The additional fermionic DM candidate, χ, is assumed to be a singlet under the SM gauge groups. It therefore, couples only to the singlet mediators via

$$\mathcal{L}_{\text{S-DM}} = -y_\chi^S\, S\, \bar{\chi}\chi, \qquad \text{or} \qquad \mathcal{L}_{\text{P-DM}} = -iy_\chi^P\, P\, \bar{\chi}\gamma^5\chi, \tag{2.31}$$

in the 2HDM+S, or 2HDM+PS respectively. The DM couples to SM fields due to the mass mixing of the SU(2) singlets S or P and the spin-0 state of doublet with similar $\mathcal{CP}$-parity, as discussed above.

2.1.3 Branching Ratios

The resonant production of mono-Z/h in the 2HDM+S/PS relies on the decay structures of the additional spin-0 states. To get an initial feeling for interesting parameter regions we compute and compare their branching ratios (BR) in both models. This will also be helpful for the later interpretation of the obtained collider limits.

The plots of the BRs for the four neutral states are shown in Fig. 2.1 to Fig. 2.4 and will be discussed consecutively hereafter. We use the parameter values given further below in Eq. (2.43), and fix $M_A = 500\,\text{GeV}$ and $\tan\beta = 1$. Due to the choice that $\tan\beta = 1$, our findings and their interpretations are applicable to all four types of 2HDMs. Analytic expressions for the dominant decay widths of all spin-0 states are given in App. A.

As mentioned above, in the alignment limit studied here, the couplings of h to SM fields remain unchanged. However, its total decay width can be significantly enhanced in the presence of kinematically available additional decay channels, where the most relevant ones are pairs of the mediators a or S_2. Even for mediator masses above half of the Higgs mass, the three body decays $a\chi\bar{\chi}$ or $S_2\chi\bar{\chi}$ can be sizeable and even dominate the Higgs width for small DM masses, as the dominant SM decay to $b\bar{b}$ features a small Yukawa coupling. This is shown in Fig. 2.1. For brevity only the new decays and the two dominating SM decays are plotted, as the other decays behave identically.

The BRs of the light mediators a and S_2 shown in Fig. 2.2 depict similar behavior in both models. In the mass region relevant for mono-X searches, the decay to $\chi\bar{\chi}$ is kinematically allowed. There the decay to DM dominates the width for $y_\chi = \mathcal{O}(1)$, even if the channel to $t\bar{t}$ is accessible. Therefore, here we chose a higher value of m_χ to show the non-trivial decay channels in the low M_{a/S_2} region. Decays to SM particles arise from mixing with the corresponding doublet state and are therefore suppressed by $\sin^2\theta$. We note that in the 2HDM+PS the BRs to $t\bar{t}$ and gluons are slightly bigger than in the 2HDM+S.

While for the heavy scalars, H and S_1, and pseudoscalar, A, the dominant decay is the one to $t\bar{t}$ in both models, the subleading decays including a Z or a Higgs boson behave contrarily,

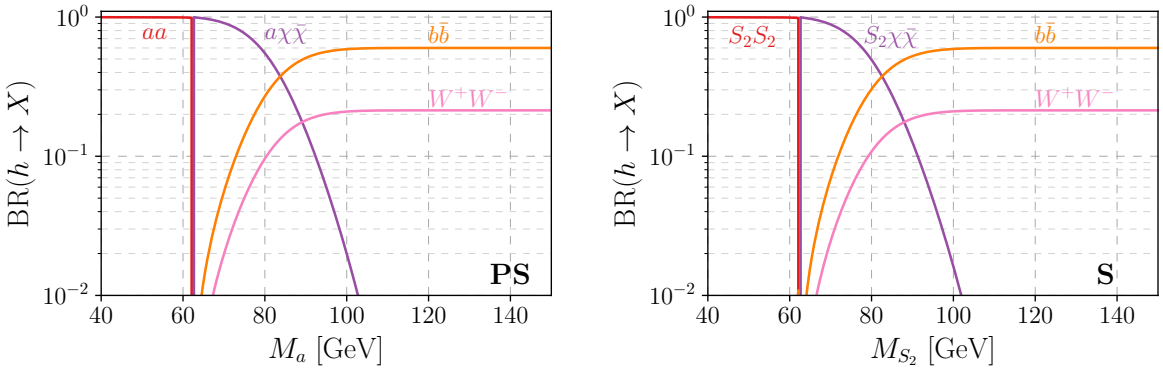

Figure 2.1: Dominant branchings ratios (BRs) of the SM Higgs-like scalar h as function of the mediator mass M_{a,S_2} for $\tan\beta = 1$, $m_\chi = 10\,\text{GeV}$, $M_{H/S_1} = 500\,\text{GeV}$ and other parameters as in Eq. (2.43) in the 2HDM+PS (left) and 2HDM+S (right). For brevity only the two dominant SM decays are shown. The other decays behave identically.

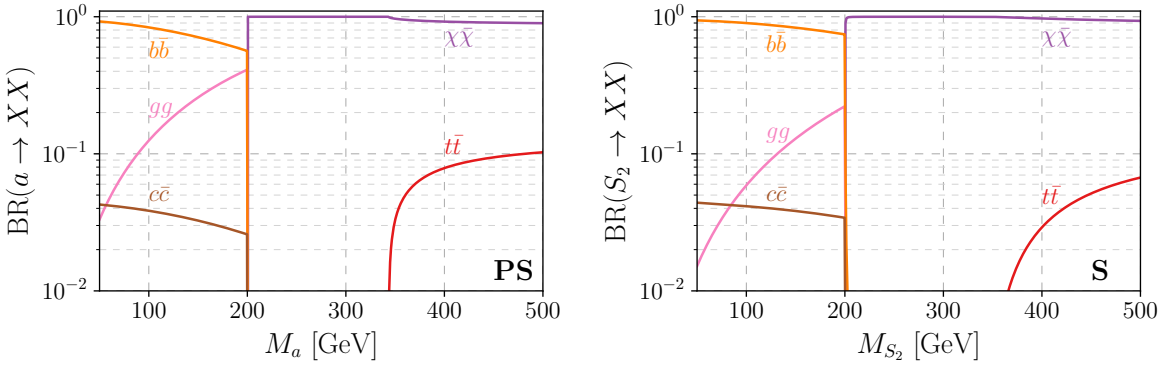

Figure 2.2: Dominant BRs of the light pseudoscalar a in the 2HDM+PS (left) and the light scalar S_2 in the 2HDM+S (right) as function of their masses for $\tan\beta = 1$, $m_\chi = 100\,\text{GeV}$, $M_{H/S_1} = 500\,\text{GeV}$ and other parameters as in Eq. (2.43).

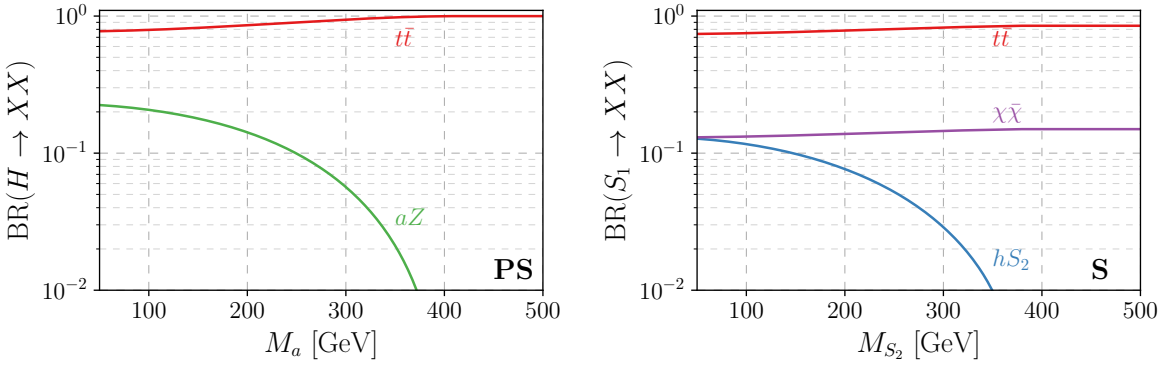

Figure 2.3: Dominant BRs of the heavy scalar H in the 2HDM+PS (left) and S_1 in the 2HDM+S (right) for $\tan\beta = 1$, $M_{H/S_1} = 500\,\text{GeV}$, $m_\chi = 10\,\text{GeV}$ and other parameters as in Eq. (2.43).

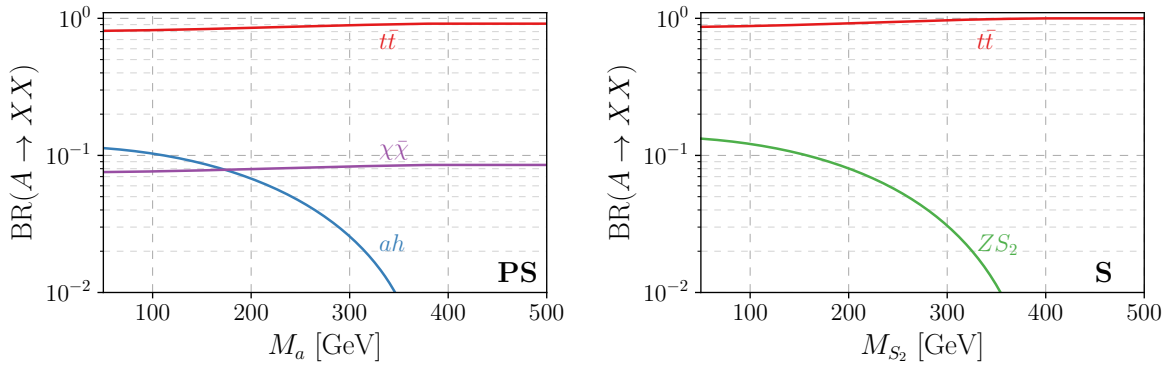

Figure 2.4: Dominant BRs of the heavy pseudoscalar A in the 2HDM+PS (left) and 2HDM+S (right) for $\tan\beta = 1$, $M_A = 500\,\text{GeV}$, $m_\chi = 10\,\text{GeV}$ and other parameter as in Eq. (2.43).

shown in Figs. 2.3 and 2.4. The heavy pseudoscalar A in the 2HDM+S and the heavy scalar H in the 2HDM+PS decay to the ZS_2, or Za final state respectively, which enables the resonant enhancement of mono-Z production as discussed in detail below. It is important to note, that the BR($H \to Za$) in the 2HDM+PS is bigger by roughly a factor of two with respect to BR($A \to ZS_2$) in the 2HDM+S, due to the smaller decay width of scalars to top-quarks, and the resultant smaller total width and larger BR. In the 2HDM+S, the heavy scalar S_1 has BRs of $\mathcal{O}(10\%)$ to hS_2, decreasing with M_{S_2}, and $\chi\bar{\chi}$ via mixing with S_2. In the 2HDM+PS the heavy pseudoscalar A features analogue decays to ah and to $\chi\bar{\chi}$ with BRs of similar size. In both models the former decays enable resonant production of mono-h final states.

With the proper defined models at hand and first insights into their behavior, we turn now to various general constraints, which further narrow down the parameter space.

2.2 General Constraints

In this section we give a brief overview of various constraints on 2HDMs relevant for the studied cases mainly from non-collider experiments. Those constraints serve as a guideline to narrow down the parameter space introduced above, such that the remaining parts can be tested in the dedicated collider analyses in Sec. 2.2.3. The DM properties of the 2HDM+S/PS are also discussed.

2.2.1 Theory and Precision Requirements

First, we briefly review theoretical requirements and precision tests, which will lead to simplifying assumptions, for instance the mass-degenerated limit, and a lower bound on the masses of the spin-0 states.

Perturbativity and Unitarity Theoretical limits on the coefficients of the scalar potentials are obtained by requiring perturbativity, unitarity and being bounded from below; for a general discussion for 2HDMs see [83, 98–101]. Those bounds can be approximately summarized by $\hat{\lambda}_i \lesssim \mathcal{O}(1)$.

In case of the 2HDM+S details and exact expressions for those bounds can be found in e.g. [72, 80]. There are also scattering processes of the type $\phi_i\phi_j \to \phi_k\phi_l$ taken into account for the perturbative limit. We note, that bounds on the quartic couplings can be re-expressed in terms of upper limits on the mass splittings between the scalar eigenstates; see e.g. [72, 76].

Specific unitarity constraints for the 2HDM+PS rely on the amplitudes of the processes aa, aA, $AA \to W^+W^-$ and have been studied in [74]. Requiring perturbativity on top of unitarity strengthens the limit on the scalar masses down to $M_{A,H,H^\pm} \lesssim \mathcal{O}(\text{TeV})$ for sizable mixing, which is needed to generate the desired collider signatures [45, 61].

Electroweak Precision Tests It can be shown that the scalar potential for the 2HDM+S in Eq. (2.2) and (2.21) breaks the custodial symmetry [102–107], in particular the λ_4, λ_5 and λ_{hHS} terms. This leads to contributions to EW precision observables. The most relevant observable is the ρ parameter, which receives a contribution of

$$\begin{aligned}\Delta\rho = \frac{1}{(4\pi)^2\, v^2}\Big[&F\big(M^2_{H^\pm}, M^2_A\big) + c^2_\theta\, F\big(M^2_{H^\pm}, M^2_{S_1}\big) + s^2_\theta\, F\big(M^2_{H^\pm}, M^2_{S_2}\big) \\ &- c^2_\theta\, F\big(M^2_A, M^2_{S_1}\big) - s^2_\theta\, F\big(M^2_A, M^2_{S_2}\big)\Big],\end{aligned} \tag{2.32}$$

where

$$F(x,y) \equiv \frac{x+y}{2} - \frac{x\,y}{x-y}\,\log\Big(\frac{x}{y}\Big). \tag{2.33}$$

One can verify that $\Delta\rho = 0$ for $M_A = M_{H^\pm}$ [64].

A similar relation holds for the 2HDM+PS potential in Eq. (2.1) and (2.15). With the replacements $M_A \to M_H$, $M_{S_1} \to M_A$, and $M_{S_2} \to M_a$, Eq. (2.32) leads to $\Delta\rho = 0$ for $M_H = M_{H^\pm}$. This leads us to the assumption of mass-degeneracy: $M_A = M_{H^\pm} = M_{H,S_1}$, where EW precision constraints are automatically fulfilled in both models. We will adopt this assumption for the rest of the chapter.

As soon as a small mass splitting between the scalars of the second doublet appears, limits from EW precision can become very constraining. This implies $M_{S_1} \sim M_A \sim M_{H^\pm}$ and $0 \le \theta \lesssim \pi/4$ for the 2HDM+S and $M_A \sim M_H \sim M_{H^\pm}$ and $0 \le \theta \lesssim \pi/4$ for the 2HDM+PS. Our choice of $M_{S_1} > M_{S_2}$ in the 2HDM+S, and $M_A > M_a$ in the 2HDM+PS, is motivated by the fact that for a resonant enhancement of mono-Z and mono-h a mass hierarchy between the (pseudo)scalars is required. For more details on EW precision constraints for these models, see [61, 64].

Flavor As explained above, we are considering specific realizations of the 2HDM in which flavor violating processes are forbidden at tree level through suitable assignments of the couplings of the SM fermions to the two Higgs doublets. Nevertheless, FCNCs can be induced at loop level. A comprehensive discussion of the possible bounds has been performed in [108]. Among them, the most relevant bounds come from $b \to s$ transitions, in particular the $B \to X_s\gamma$ process, whose rate is mostly sensitive to $\tan\beta$ and $M_{H^\pm}$. Those transitions mostly constrain 2HDMs featuring $\tan\beta$ enhanced interactions of the BSM scalars with down-type quarks, namely types II and Y, see Tab. 2.1. For them, a lower bound of $M_{H^\pm} > 570\,\text{GeV}$ can be derived, which is weakly sensitive to the value of $\tan\beta$.

Additional constraints, from $B_s \to \mu^+\mu^-$ and $B \to K\mu^+\mu^-$ processes, affect models of type II for moderate to high values of $\tan\beta$. Models of type I and X have $\tan\beta$ suppressed

interactions with quarks, and are only constrained in a small region of the parameter space for $\tan\beta \lesssim 2$.

Using the relations imposed by EWPT and requirements on the scalar potential, the bound on $M_{H^\pm}$ can be translated into bounds for the masses of the other BSM scalars, see also e.g. [109, 110]. It is worth to note that flavor bounds are typically sensitive to further BSM contributions, which could relax them significantly. Therefore, we will also include smaller scalar masses in our scans.

2.2.2 Astrophysical Constraints

Astrophysical and cosmological observations define the properties of a valid DM candidate, and set strong limits on its interaction strength with SM particles. In this section we briefly review how those requirements can be realized in the models under consideration.

Direct Detection The DD prospects are very different for the two models. In the 2HDM+S, the DM generates spin-independent (SI) interactions with nucleons due to t-channel exchanges of the scalar mediators at tree level. This is described by the operator [64, 72]

$$\mathcal{L}_N = c_N\, \mathcal{O}_1^N = c_N\, \bar{\chi}\chi\, \bar{N}N, \tag{2.34}$$

where

$$c_N = y_\chi s_\theta c_\theta\, \frac{m_N}{v} \left(\frac{1}{M_{S_1}^2} - \frac{1}{M_{S_2}^2}\right) \left(\epsilon_u f_{T_u}^N + \epsilon_d \sum_{q=d,s} f_{T_q}^N + \frac{2}{9}\frac{2\epsilon_u + \epsilon_d}{3}\, f_{T_g}^N\right). \tag{2.35}$$

The coefficients ϵ_q are given in Table 2.1, and the coefficients $f_{T_i}^N$ can be found in [111]. Such an interaction is well within the reach of current detectors for $y_\chi, \tan\beta \sim \mathcal{O}(1)$, $s_\theta\, c_\theta \sim \mathcal{O}(0.3)$ and $M_{S_i} \sim \mathcal{O}(\text{TeV})$, apart from the regions where negative interference effects become important [72], see also Sec. 4.1.1. In the following section on collider searches we focus on light DM where DD is insensitive, therefore acting as a complementary search.

In the case of the 2HDM+PS, the DM-nucleon interaction from tree-level exchange of the pseudoscalar mediators leads to spin-dependent (SD) cross sections, and is described by the operator [111]

$$\mathcal{L}_N = \tilde{c}_N\, \mathcal{O}_4^N = \tilde{c}_N\, \bar{\chi} i\gamma^5 \chi\; \bar{N} i\gamma^5 N, \tag{2.36}$$

where the effective coefficient $\tilde{c}_N$ is given in e.g. [112, 113]. In the non-relativistic limit [114–120], this operator reduces to

$$\mathcal{L}_N \equiv 4\, \tilde{c}_N\, (\vec{s}_\chi \cdot \vec{q})(\vec{s}_N \cdot \vec{q}), \tag{2.37}$$

where $\vec{s}_\chi$, $\vec{s}_N$ are the DM and nucleon spins, respectively, while $\vec{q}$ is the momentum transfer. The corresponding cross section is hence suppressed by the fourth power of the momentum transfer, and experimentally relevant only for very light masses of the mediators [112, 113, 121]. At one-loop level, SI nucleon-DM interactions emerge which are within the reach of next generation detectors like XENONnT and DARWIN [121–127]; see also Sec. 4.2.1.

Indirect Detection and Relic Density Adopting the WIMP paradigm, the DM relic density as well as eventual ID signals rely on the DM annihilation processes. The case of the 2HDM+S has been studied in e.g. [64]; see also Sec. 4.1.1 for a related discussion. The possible annihilation channels are $f\bar{f}$, S_1S_1, S_1S_2, S_2S_2, H^+H^-, $H^\pm W^\mp$, AA, AZ, S_1h, and S_2h, where f denotes all SM fermions with $m_f < m_\chi$. All these annihilation channels are characterized by p-wave suppressed cross sections. While it is still possible to achieve the correct relic density in special kinematic regions, for example around the resonances $m_\chi \sim M_{S_i}/2$, or $m_\chi \gtrsim M_{S_i}$, we do not expect measurable ID signals due to the p-wave suppression.

The phenomenology related to ID and the relic density for the 2HDM+PS has been discussed in [45, 110, 123, 124]. In the alignment limit, the DM abundance is determined by the kinematically accessible annihilation processes among $f\bar{f}$, hA, HA, $H^\pm W^\mp$, HZ, aa, aA, and AA. While the annihilation channels into two pseudoscalars are p-wave suppressed, the other chanels have s-wave dominated cross sections, and are also relevant for ID; see also Sec. 4.2.1. Nevertheless, the aa channel can be relevant for the relic density, especially for very light a. We note that despite the s-wave enhancement, the correct relic density can typically only be obtained for rather tuned parameters, for example in the resonance region $m_\chi \sim M_a/2$.

With respect to ID, the s-wave nature is crucial to obtain a possible signal due to the much smaller DM velocity at present, compared to the early universe. Possible signals are mostly accounted by the $b\bar{b}$, $t\bar{t}$ and ha channels, where the last one gives rise to four fermion signatures like $b\bar{b}b\bar{b}$. For heavy DM, the hA, HZ and $H^\pm W^\mp$ final states may play a role as well, while the other channels are negligible. However, no dedicated studies for DM annihilations into a gauge and a Higgs boson exist so far. As discussed in [45], FERMI-LAT bounds [128] on the $b\bar{b}$ and $t\bar{t}$ channels can probe DM masses from 190 GeV up to around 400 GeV, therefore offering a complementary approach to collider searches.

2.2.3 Collider Searches

The extended scalar spectrum of 2HDMs is subject to a broad variety of collider searches. Resulting constraints have recently been summarized in [129]. In the considered limits of mass-degeneracy and alignment, many of those vanish, e.g. from searches for $A/H \to hZ$. Exemplarily, we study the recently updated $A/H \to t\bar{t}$ search from CMS in more detail in the next section, as it is among the most relevant searches for the $\tan\beta$ range under consideration.

Here we will comment on searches related to DM, namely for Higgs-to-invisible, $t\bar{t} + \not{E}_T$, and mono-jets, and check their constraints on the parameter space. The mono-Z and mono-h final states are discussed in detail in the following section, because they lead to the most stringent and interesting limits for the 2HDM+S/PS.

Higgs-to-invisible As discussed in Sec. 2.1.3, even in the alignment limit the light states a or S_2 represent a new dominant decay channel for the SM-like Higgs if $M_h \gtrsim 2M_{a/S_2}$. For light DM, the three-body final state $a/S_2\,\chi\bar{\chi}$ can also be relevant, even above the kinematic threshold quoted above, as shown in Fig. 2.1. As a and S_2 dominantly decay to DM, Higgs-to-invisible searches are sensitive to those decays. Such an analysis performed by ATLAS [130] in various production mechanisms gives

$$\mathrm{BR}(h \to \mathrm{inv}) < 0.26 \ \ \left(0.17^{+0.07}_{-0.05}\right) \tag{2.38}$$

for the observed (expected) upper limit on the Higgs-to-invisible branching ratio at 95% confidence level. Using the decay widths from Sec. 2.1.3, we find a lower bound of $M_{a/S_2} \gtrsim$

100 GeV for $m_\chi = 10\,\text{GeV}$ with a mild residual dependence on the degenerated masses of the heavy Higgs and couplings. Therefore, we start the parameter scans in the following section at $M_{a/S_2} = 100\,\text{GeV}$.

We note that a stronger limit has been reported in [131, 132] after this analysis, which does not qualitatively change our findings.

$t\bar{t} + \not{E}_T$ New spin-0 mediators with large invisible widths can be searched for in the $t\bar{t} + \not{E}_T$ and $b\bar{b} + \not{E}_T$ channels. The most recent experimental searches have been reported in [133, 134]. Their results have been interpreted in simplified DM models. As long as $M_a \ll M_A$, they can be applied to the 2HDM+PS by applying the scaling relation [45, 61]

$$\frac{\sigma(pp \to t\bar{t} + \not{E}_T)_{\text{2HDM+PS}}}{\sigma(pp \to t\bar{t} + \not{E}_T)_{\text{DM-simp}}} = \left(\frac{y_\chi \sin\theta}{g_\chi\, g_q\, \tan\beta}\right)^2 . \tag{2.39}$$

A similar relation applies for $b\bar{b} + \not{E}_T$ with the replacement of $\tan\beta$ according to Table 2.1. As discussed in Ref. [45], in analogous manner the limits of [133, 134] can be applied to the 2HDM+S, as long as there is a substantial mass splitting between the BSM scalars. In the case where the new scalars have comparable masses, the $\not{E}_T$ spectrum features distortions with respect to the simplified models. Hence, more refined procedures to map the experimental limits on the models under consideration should be applied. However, in Ref. [46] it was shown that the $t\bar{t} + \not{E}_T$ exclusions are sub-dominant for the 2HDM+PS. Therefore, we do not derive explicit bounds from those searches.

Mono-jet Similarly to heavy flavors+$\not{E}_T$ searches, experimental constraints from mono-jet searches are typically interpreted in simplified models. In the limit where the second doublet is decoupled in mass, the kinematic distribution of mono-jet events are essentially the same for simplified models and the 2HDM+S/PS, with respect to the singlet-like states. The second doublet can be effectively decoupled in the mono-jet production, since the jets originate from ISR, and the additional states have no significant effects there. Experimental limits can be applied to our setups by using scaling relations analogous to Eq. (2.39).

As mono-jet events provide the strongest bounds among ISR signatures [75], we explicitly checked promising points with the CheckMATE [135] implementation of the ATLAS search in [77], and found no excluded points for $\tan\beta = 1$ in either models. This agrees with findings for the 2HDM+PS in [61], where mono-jet sets a limit of roughly $\tan\beta < 0.5$ for maximal mixing of $\sin\theta = 1/\sqrt{2}$. However, this region is already excluded by other constraints and therefore we do not investigate this further.

The recent ATLAS mono-jet search [136] with $139\,\text{fb}^{-1}$ of data was not taken into account as it was published after the original analysis. For the 2HDM+PS, an analysis with this data is performed in [137]. The authors find significant contributions of the mono-jet search to the overall sensitivity, especially for $M_A \sim 800\,\text{GeV}$, or $\sin\theta = 1/\sqrt{2}$. They find no new exclusions at 95% confidence level in the mass-degenerated limit.

2.3 Comparison of LHC Signatures

After reviewing constraints relevant in general for 2HDMs and DM models, and describing their impact on the parameter space of the two models, we will now turn to LHC signatures of

particular interest for the 2HDM+S/PS. By dedicated collider simulations, we obtain limits for the leftover parameter space and discuss how the searches and models compare to each other. While $t\bar{t}$ resonance searches are relevant for many theories with extended scalar sectors, the 2HDM+S/PS were designed to be sensitive to the mono-Z/h channels [45, 61]. As we will show, the simultaneous discussion of mono-Z and mono-h provides the potential to distinguish between the two models. Combined the three considered searches are complementary to each other.

Before turning to the actual simulations and their results, we briefly discuss topics in common to all three processes. We give an analytic description of the resonant production mechanism, which will become useful for interpreting our findings, as well as a summary of the studied parameter space and the program chain used for the signal generation.

Resonant Production As discussed above and in Ref. [45], a desired feature of the 2HDM+S/PS is the resonantly enhanced production of mono-h and mono-Z signals. In the narrow width approximation, the production cross section for a spin-0 s-channel resonance S, with mass M and total decay width Γ_{tot}, subsequently decaying into a final state X, can schematically be written as [138]

$$\sigma(pp \to S \to X) = \frac{1}{Ms} \frac{\Gamma(S \to X)}{\Gamma_{\text{tot}}} \sum_i \mathcal{K}_i \, C_i \, \Gamma(S \to i), \tag{2.40}$$

where s is the squared center of mass energy. The sum runs over all possible partonic initial states i, for example quark-(anti)quark and gluon pairs in proton-proton collisions. The corresponding k-factors $\mathcal{K}_i$ include higher-order QCD corrections. The weight factors C_i that account for the proton parton distribution function (PDF) and color factors are defined as

$$C_{gg} = \frac{\pi^2}{8} \int_{M^2/s}^1 \frac{\mathrm{d}x}{x} \, g(x) \, g\left(\frac{M^2}{sx}\right), \tag{2.41}$$

$$C_{q\bar{q}} = \frac{4\pi^2}{9} \int_{M^2/s}^1 \frac{\mathrm{d}x}{x} \left[q(x) \, \bar{q}\left(\frac{M^2}{sx}\right) + q\left(\frac{M^2}{sx}\right) \bar{q}(x) \right], \tag{2.42}$$

with $q(x)$, $\bar{q}(x)$ and $g(x)$ being the PDFs of the corresponding quark, anti-quark or gluon, respectively, and x is the conventional Bjorken scaling variable. Note that to derive the results in the following, we do not rely on this approximation. Since it helps to understand the features of the exclusion limits discussed below, we verified its validity in the relevant parameter space.

In general, the two main production mechanisms for the states from the second doublet are gluon fusion and $b\bar{b}$ initial state. We show the production cross sections of H/S_1 and A as a function of their masses for gluon fusion ($b\bar{b}$ initial state) production in the left (right) panel of Fig. 2.5 for $\sin\theta = 0$. For $\tan\beta = 1$, the gluon fusion production cross sections are about 100 times larger than that of $b\bar{b}$ initial states. Only for $\tan\beta \gg 3$ in 2HDMs of types II and Y, does $b\bar{b}$-initial state production become important. Therefore, in our considered parameter space of $0.3 \leq \tan\beta \leq 3$, we can safely neglect it, such that the results hold for all types of 2HDMs. The lower limit is motivated by the fact that the widths should be significantly smaller than the masses together with the exclusions shown below. The production cross section of the pseudoscalars is larger compared to the scalar ones due to their $\mathcal{CP}$ structure, shown in Fig. 2.5 and e.g. [110, 139]. In the 2HDM+S, the S_1 production gets modified through the mixing with S_2. In the 2HDM+PS, the production of A gets accordingly modified by a. We focus here on small mixing angles causing differences smaller than 10%.

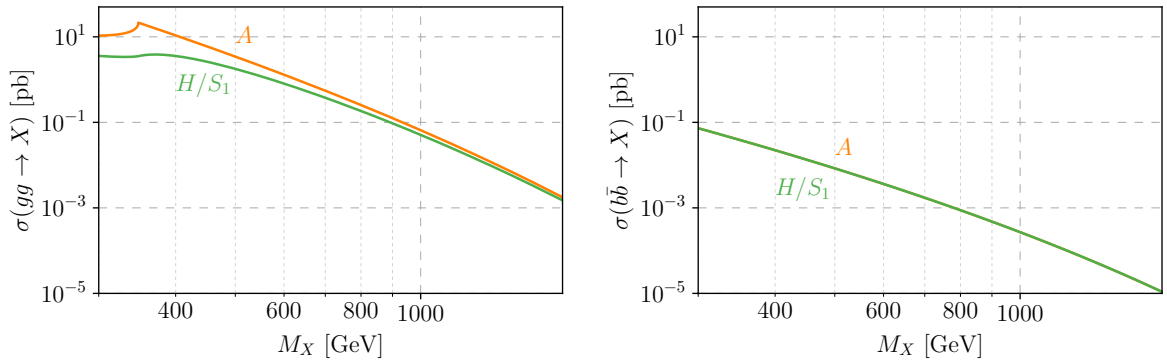

Figure 2.5: Production cross sections for the heavy scalar H/S_1 and pseudoscalar A through gluon fusion (left) and $b\bar{b}$ initial state (right) as function of their mass M_X in the 2HDM+PS/S as given in Eq. (2.40). The plot depicts the case of $\tan\beta = 1$ and $\sin\theta = 0$.

Parameter Overview For a better overview, we summarize our choice of values and ranges for the free parameters of the two models. They are motivated by various constraints discussed above and used for the Monte Carlo simulations and other examples throughout this chapter

$$\begin{aligned} M_A = M_{H^\pm} = M_{H/S_1} &\in [200,\, 1500]\,\text{GeV} \\ M_{a,S_2} &\in [100,\, 500]\,\text{GeV} \\ y_\chi^S = y_\chi^P &= 1 \\ m_\chi &= 10\,\text{GeV} \\ \sin\theta &= 0.3 \\ \tan\beta &\in [0.3,\, 3]. \end{aligned} \tag{2.43}$$

Signal Generation The parton-level signal events for the mono-Z and mono-h processes are simulated with MadGraph5_aMC@NLO [140–144] at next-to-leading order (NLO) in QCD with the recommended 263000 PDF set (NNPDF3.0) [145] provided through LHAPDF6 [146]. For the parton-showering we use the MadGraph built-in Pythia 8.2 [147] package. Where needed, a fast detector simulation is applied with the help of Delphes 3.4.2 [148], using the provided CMS card as the ATLAS card showed problems in the muon reconstruction efficiency. The final cuts and selection criteria are implemented in MadAnalysis 5 [149, 150].

The correct implementation of the program chain and analysis is checked in detail by reproducing the mono-Z and mono-h exclusion limits for the 2HDM+PS presented in [45, 46].

2.3.1 $t\bar{t}$ Resonances

We start with searches for $t\bar{t}$ resonances since they are a powerful tool to test models with extended scalar sectors in general, and the 2HDM+S/PS in particular. These searches lead to strong exclusions nearly independent of the additional singlet. If the masses of the additional spin-0 particles exceed the top-threshold, $M_{H/S_1,A} > 2\,m_t$, they dominantly decay into a pair of top quarks, see Sec. 2.1.3. While S_2 and a in the upper mass region could also decay to $t\bar{t}$, their production and decay rates are suppressed by $\sin^2\theta$, hence leading to no exclusion limits, as a consequent we concentrate on H, S_1 and A.

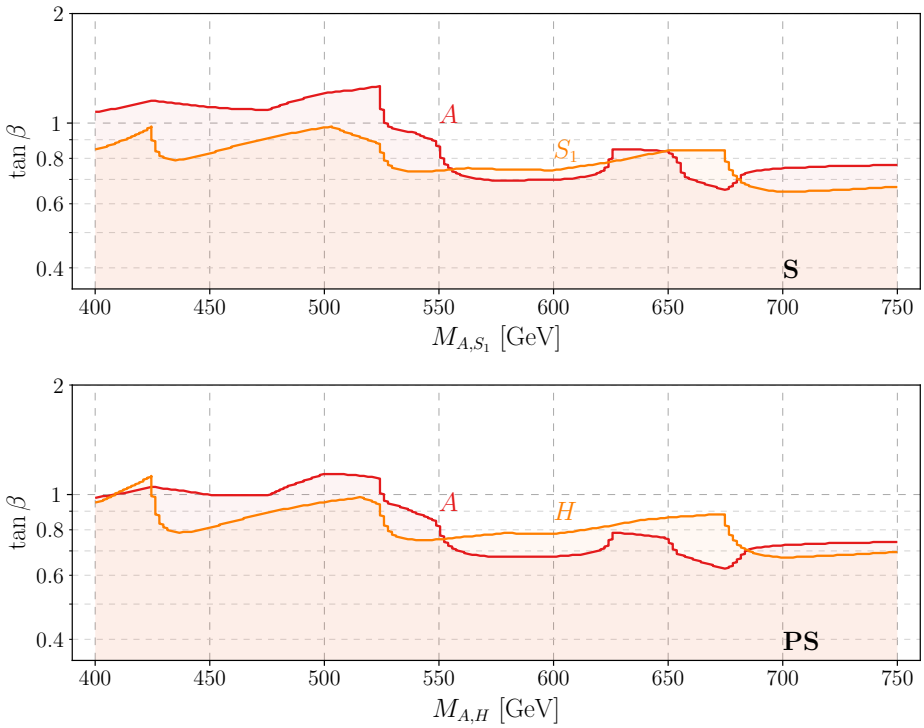

Figure 2.6: Shaded regions indicate the 2σ observed exclusion limits from $t\bar{t}$ resonance searches by CMS [151] in the $M_{A,H/S_1}$–$\tan\beta$ plane for the 2HDM+S (top) and 2HDM+PS (bottom). The parameters are fixed to $M_{a/S_2} = 400\,\text{GeV}$ and the values from Eq. (2.43), besides breaking the mass-degeneracy as described in the text. The limits derived from searches for the scalar (pseudoscalar) resonances H/S_1 (A) are given in orange (red).

One aspect complicating the analysis, is that the signal processes interfere non-trivially with the SM background and themselves, if various mediators are considered simultaneously. This was described and taken into account by the ATLAS analysis in [152]. There, the results are interpreted in a 2HDM of type II, for the case in which only one mediator contributes to the signal[1] as well as for the mass-degenerate case where both mediators contribute simultaneously. As the latter case gives significantly stronger constraints, deriving exclusions for a single mediator serves as a conservative estimate. The most recent results for $\sqrt{s} = 13\,\text{TeV}$ and an integrated luminosity of $35.9\,\text{fb}^{-1}$ are provided by CMS in [151]. The limits are presented in terms of simplified models with either a scalar or a pseudoscalar mediator with Yukawa-like couplings to tops and in the hMSSM. Here, a $1.9\,\sigma$ "signal-like deviation" is observed that would fit to a pseudoscalar with mass of around 400 GeV. Therefore, limits in that mass range are not significantly stronger than the ones from the previous ATLAS analysis with $\sqrt{s} = 8\,\text{TeV}$, but reach further in mass.

The additional light state a/S_2 can have a non-trivial impact on the limit due to interference effects, see Sec. 7.1 in [45]. However, this effect is expected to be small for our choice of the mixing angle, $\sin\theta = 0.3$. A detailed analysis of the impact of interference and combining

[1] Physically, this could for example correspond to a limit where one mediator is much heavier.

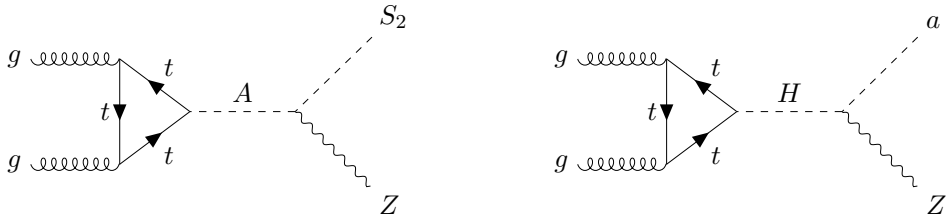

Figure 2.7: Feynman diagrams for the resonant production of a mono-Z signal via gluon fusion production in the chosen mass hierarchy for the 2HDM+S (left) and 2HDM+PS (right).

the limits for the two heavy states is beyond the scope of this thesis. Instead, we recast the stronger CMS limits for single mediators to our parameter space, interpolating between the different total width to mass ratios given in Ref. [151]. This can be seen as breaking the assumption of mass-degeneracy, and taking one spin-0 state to be much heavier than the other, which then does not contribute to the $t\bar{t}$ production. In the end we combine the limits from the two cases in each model. As commented above in the context of [152], this can bee seen as a conservative estimate, since the bounds get significantly stronger by taking the contribution of both mass-degenerate states H/S_1 and A into account.

The limits are shown in Fig. 2.6 in the $M_{A,H/S_1}$–$\tan\beta$ plane for the 2HDM+S (top) and 2HDM+PS (bottom). We choose the setting in Eq. (2.43) with $M_{a/S_2} = 400\,\text{GeV}$, and loosen the assumption of mass-degeneracy. Due to changes of the total width a mild dependency on the mass of the light state remains, which is shown in Fig. 2.13 and 2.14 for $\tan\beta = 1$.

With the effective coupling approximation for the dominant gluon fusion production in Eqs. (2.40) and [153], it can be understood that pseudoscalar resonances provide stronger constraints than scalar resonances. This is because the decay widths of pseudoscalars to quarks and gluons are bigger than those of scalars, in the mass range $M_A > 2m_t$, see Sec. 2.1.3 [154].

In the 2HDM+S, the couplings of the heavy scalar S_1 to quarks are reduced due to the mixing with the singlet S_2, while couplings of A are unaltered. As a consequence, the exclusions for S_1 reach up to $\tan\beta = 1$, while the exclusion for A exceed $\tan\beta = 1$ for $M_{A,S_1} \lesssim 550\,\text{GeV}$. In the 2HDM+PS instead, the stronger constrained pseudoscalar A mixes with the singlet a, slightly weakening the exclusions for it, while the couplings of H remain unchanged. This leads to similar constraints from $t\bar{t}$ searches for A and H in this model, which are overall slightly weaker than the ones for the 2HDM+S. Nevertheless, in both models, for masses of the heavy Higgs around 500 GeV, $t\bar{t}$ resonance searches provide a strong lower limit on $\tan\beta$ and essentially exclude values of $\tan\beta \lesssim 1$. The similarity of the (combined) exclusions in the two models is caused by coincidences in theory and experimental data.

2.3.2 Mono-Z

The mono-Z final state offers a very promising new channel for DM searches, which could be used in simplified models only to a small extend. We will show that mono-Z contributes already very competitive constraints in the models under consideration. To estimate its future prospects, we rescale the current exclusions to the high luminosity phase of the LHC (HL-LHC). In addition, Ref. [76] showed that the mono-Z signature is a general feature for 2HDMs extended by pseudoscalar mediated DM, and that its relevance does not rely on the concrete realization. Searches for mono-Z in the cleanest final state, where the Z boson decays

leptonically[2], are performed by ATLAS and CMS in Refs. [155–157][3].

To generate a strong mono-Z signal, the heavy neutral doublet component which does not mix with the additional singlet has to be produced as a s-channel resonance. This state, meaning the scalar H in the 2HDM+PS and the pseudoscalar A in the 2HDM+S, can decay to a Z boson and the light state a or S_2, respectively. These further decay to $\chi\bar{\chi}$ with a high branching ratio, as shown in Fig. 2.2. The Feynman diagrams for this processes are shown in Fig. 2.7 for the dominant gluon fusion production. For a better understanding of the following results, we briefly discuss the $\not{E}_T$ spectrum of the signal process.

$\not{E}_T$ Spectrum The maximum value of the missing transverse energy $\not{E}_T$ can be obtained from kinematics and is given by [61]

$$\not{E}_T^{\max} = \frac{\sqrt{\lambda(M_{A,H},\, M_{S_2,a},\, M_Z)}}{2\, M_{A,H}}, \tag{2.44}$$

where $\lambda(m_1, m_2, m_3)$ is given in Eq. (A.17) and the first (second) subscript is used for the 2HDM+S (PS). The missing energy spectrum is given by

$$\frac{1}{N}\frac{dN}{d\not{E}_T} = \frac{\not{E}_T}{2\not{E}_T^{\max}\sqrt{\left(\not{E}_T^{\max}\right)^2 - \not{E}_T^2}}, \tag{2.45}$$

which is a monotonic increasing function in $\not{E}_T$ up to $\not{E}_T^{\max}$. However, detector smearing effects are expected to increase the maximum value of $\not{E}_T$ to $\not{E}_T^{\max,\,\mathrm{D}} > \not{E}_T^{\max}$. he resulting distribution is expected to be peaked close to $\not{E}_T = \not{E}_T^{\max}$, instead of having its endpoint there.

Example $\not{E}_T$ spectra are shown in Fig. 2.8 for the mono-Z final state after applying a detector simulation and using the same binning as in [155]. We plot the 2HDM+PS and the decay $Z \to e^+e^-$ for two assignments of the pseudoscalar masses, namely $M_a = 250\,\mathrm{GeV}$, $M_A = 700\,\mathrm{GeV}$ (solid line) and $M_a = 150\,\mathrm{GeV}$, $M_A = 400\,\mathrm{GeV}$ (dotted line). For the first (second) case, the spectra peaks around $\not{E}_T^{\max} \approx 300\,(160)\,\mathrm{GeV}$ as given in Eq. (2.44). Events populating higher bins are due to detector effects. For comparison we also show the predicted smoothly falling SM backgrounds and the observed number of events as provided in [155]. The $\not{E}_T$ spectra for $Z \to \mu^+\mu^-$ and the 2HDM+S are nearly identical.

Backgrounds As shown in Fig. 2.8, the main background[4] for mono-Z searches is the irreducible ZZ production, where one Z decays to neutrinos. Another important, though in principle reducible background is WZ production, where one lepton from the W-decay escapes detection, or a τ decays hadronically such that the W appears as $\not{E}_T$. Minor contributions to the background, especially in the lower $\not{E}_T$-bins, come from Z+jet processes with poor $\not{E}_T$ reconstruction and non-resonant $\ell\ell$ production. The backgrounds and their uncertainties are estimated from simulations and data-driven methods. For details see [155, 157] and references therein. For both the electron and muon final states, the uncertainty on the total number of background events is dominated by systematic uncertainties, especially from the Z+jets and ZZ in gluon fusion processes.

[2] Here and in the following leptons denote electrons and muons.

[3] We note that the CMS results in [157] were published after the original analysis had been performed and we quote them for completeness.

[4] Not to get confused by the logarithmic stacking.

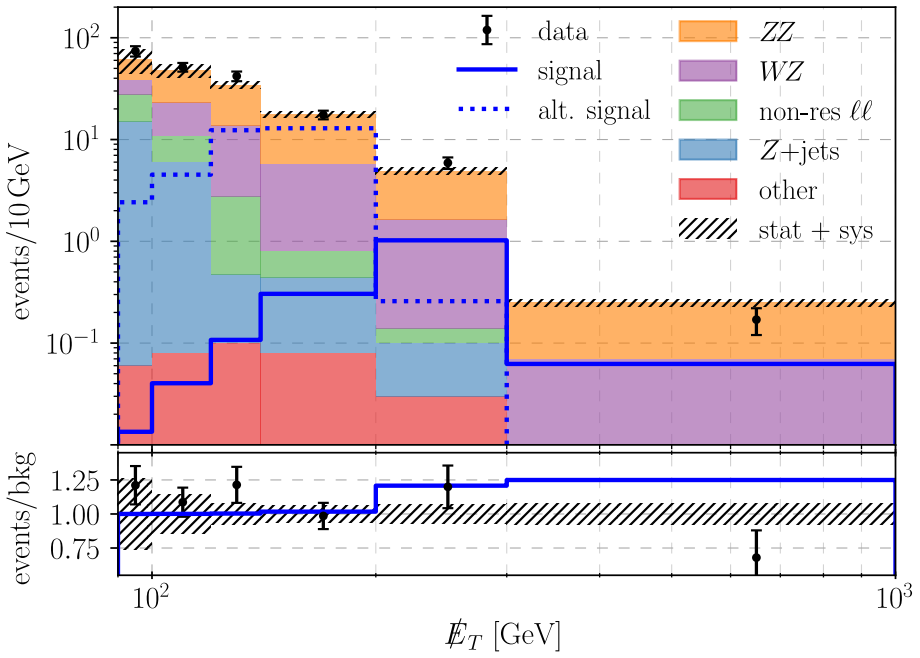

Figure 2.8: Top panel: $\not{E}_T$ spectra for $gg \to e^+e^-\chi\bar{\chi}$ in the 2HDM+PS for $M_a = 250\,\text{GeV}$, $M_A = 700\,\text{GeV}$ (solid line) and $M_a = 150\,\text{GeV}$, $M_A = 400\,\text{GeV}$ (dotted line), while the other parameters are set to the values given in Eq. (2.43). The expected SM backgrounds and observed events are taken from [155], and shown in different colors with their combined uncertainty displayed as a hatched region on top.
Lower panel: The observed events (points with error-bars) and signal plus background expectation (solid line) both as ratio to the background expectation, together with the background uncertainty (hatched region).

Current Constraints To determine constraints on the models, we use the ATLAS results in [155] as they are also used by the LHC-DMWG, and are easier to reproduce than the (slightly stronger) results obtained by CMS in [156, 157]. To be explicit, for our exclusion bounds we use the expected number of background events b and the corresponding uncertainty σ_b from [155], together with our simulated event numbers s for various parameter points. The sensitivity for the i-th bin is given by [45, 158]

$$Z_i = \sqrt{2\left((s+b)\ln\left[\frac{(s+b)(b+\sigma_b^2)}{b^2+(s+b)\sigma_b^2}\right] - \frac{b^2}{\sigma_b^2}\ln\left[1+\frac{s\,\sigma_b^2}{b\,(b+\sigma_b^2)}\right]\right)}\,, \tag{2.46}$$

which can be seen as a likelihood-inspired generalization of standard definition $Z = s/\sqrt{b+\sigma_b}$ [158]. The values for the Z_i are added up quadratically to find the square of the overall sensitivity Z^2. One expects to exclude parameter points with $Z > 2\,(5)$ at $2\,(5)\sigma$ confidence level. The expected limits, see Fig. 2.9, obtained in this way, are very similar to the observed ones in [46]. Therefore we can use the expected mono-Z exclusion limits for comparisons with the observed $t\bar{t}$ and mono-h limits in Sec. 2.3.4.

The constraints from mono-Z searches are similar in shape and reach for both models as shown in Fig. 2.9. This can be understood with help of the approximation for resonant

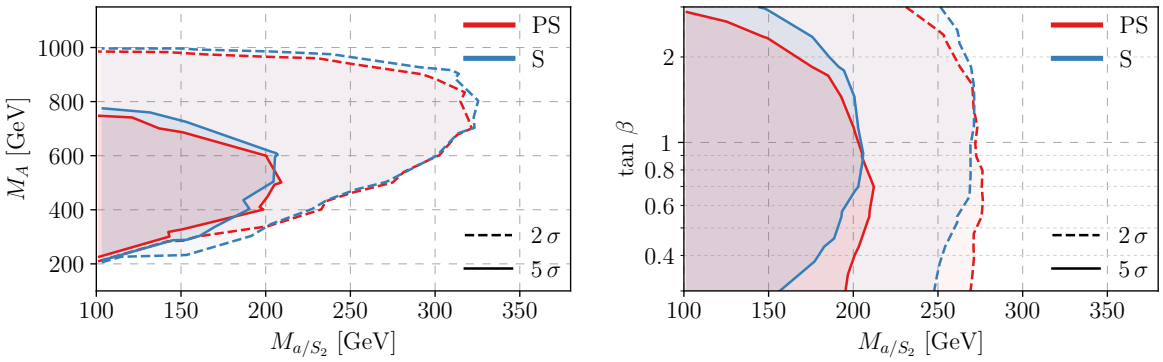

Figure 2.9: $2\,\sigma$ (dashed) and $5\,\sigma$ (solid) exclusion limits from mono-Z searches in the M_{a/S_2}–M_A (left) and M_{a/S_2}–$\tan\beta$ plane (right) for the 2HDM+S (blue) and PS (red). In both plots we use the parameters as given in Eq. (2.43) with $\tan\beta = 1$ for the left one and $M_A = 500\,\text{GeV}$ for the right one.

production in Eq. (2.40) and its corresponding discussion, see also Fig. 2.7 for the dominant Feynman diagrams. In the 2HDM+S, first the heavy pseudoscalar A gets produced, which subsequently decays to a Z boson and the light mediator S_2. In the 2HDM+PS, by contrast, after producing the scalar H in the s-channel, it decays to the light pseudoscalar a and a Z. The light mediator decays nearly exclusively to DM in both models, see Fig. 2.2. For the relevant masses, the production cross section of the pseudoscalar in the 2HDM+S, is bigger by a factor of two than that of a scalar. Since the branching ratio for the mono-Z final state

$$\text{BR}(A \to S_2 Z) \approx \text{BR}(H \to aZ)/2 \approx 0.1, \tag{2.47}$$

is bigger in the 2HDM+PS by a factor of approximately two, it is understood that the total cross section is similar in both models. The difference in the branching ratios is related to the different decay widths of scalars and pseudoscalars to top quarks, which dominate the total width, as mentioned in Sec. 2.1.3.

The general features of the excluded region from the mono-Z search shown in Fig. 2.9 can be understood by considering the kinematic behavior and the change in couplings. In the M_{a/S_2}–M_A plane three different features become visible. First, the "diagonal" lower bound to the exclusion region is due to the fact that for $M_A \lesssim M_{a/S_2} + M_Z$ the resonant production is not allowed with on-shell a/S_2. Second, the upper bound of the exclusion limit stems from the heavy Higgs being harder to produce the heavier it is. Third, a heavier M_{a/S_2} leaves less energy available for the Z, so the Z production gets kinematically suppressed, thereby smoothing out the transition between the first two features. In the M_{a/S_2}–$\tan\beta$ plane, the exclusion limit weakens with growing values of $\tan\beta$ is because the top coupling scales like $1/\tan\beta$ and is essential for the production of the intermediate heavy Higgs via gluon fusion, see Fig. 2.7. According to Eq. (2.40), for values of $\tan\beta < 1$, the production rate of the heavy resonances increases but the BR to the required final states $S_2 Z$, or aZ respectively, gets simultaneously suppressed. Therefore, in the 2HDM+PS, with the higher BR the constraints weaken more gradually.

Projected Sensitivity With the detailed background data of the experimental analysis [155] at hand, we estimate the reach of the HL-LHC for four distinct scenarios. We assume values for

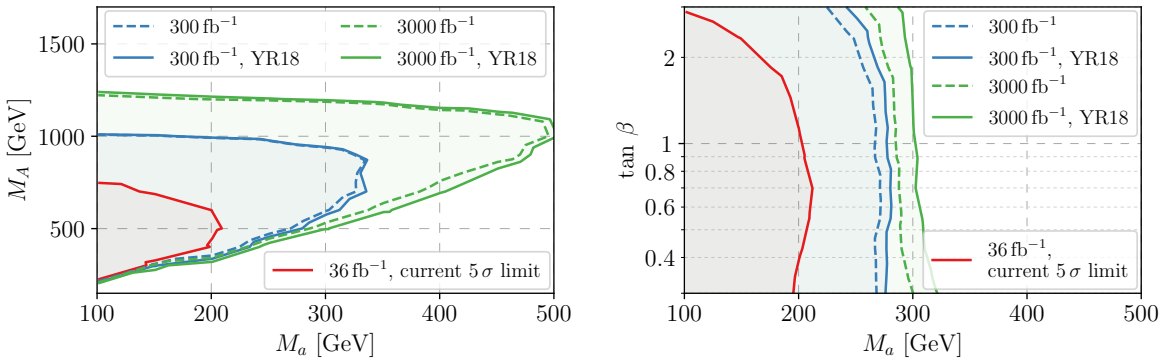

Figure 2.10: Current $5\,\sigma$ exclusion limits for the 2HDM+PS (in red) and projected limits for the high-luminosity LHC (in blue and green) from mono-Z searches in the M_a–M_A (left) and M_a–$\tan\beta$ plane (right) with $M_A = 500\,\text{GeV}$. The 2HDM+S limits are nearly identical and therefore not shown. The dashed lines correspond to a scenario without any improvement in the systematic uncertainties, whereas the solid lines assume a reduction by 50 %, called the YR18 scenario. For the other parameters, the numerical values used are identical to Fig. 2.9.

the integrated luminosity of $\mathcal{L} = 300\,\text{fb}^{-1}$ and $3000\,\text{fb}^{-1}$. In both cases, we study the effect of a projected reduction of the systematic uncertainties by 50%, called YR18 scenario [159, 160].

For the sake of simplicity and as the current bounds in Fig. 2.9 are very similar for both models under consideration, we only show the projections for the 2HDM+PS in Fig. 2.10. From there, one can see that the rise in integrated luminosity will lead to a substantial gain in sensitivity. In the final stage it will be possible to test values of M_a up to 500 GeV and to simultaneously improve the reach in M_A by roughly a factor of two. The saturation in the right panel of Fig. 2.10 is due to the kinematical limit of $M_A < M_a + M_Z$. In contrast to that, the influence of improving the systematic uncertainties will likely be small even in the quite optimistic YR18 scenario.

2.3.3 Mono-h

The final channel we consider is mono-h, since its additional information might reveal further details about the dark sector. In the case under consideration it could allow to distinguish the two models with collider measurements.

The progress in Higgs reconstruction can also be used for DM searches via the mono-h channel, as is can be resonantly enhanced in the 2HDM+S/PS. Here, the roles of the heavy scalar and pseudoscalar are switched between the two models, compared to the mono-Z case. This is also shwon in the corresponding Feynmann diagrams in Figs. 2.7 and 2.11. The limits are slightly weaker than those from mono-Z, but show different behavior in the two models.

The most recent searches for mono-h with $h \to b\bar{b}$ by the ATLAS and CMS collaborations can be found in [79, 161], where the 2HDM+PS got used for the first time in an experimental analysis by CMS. Furthermore, in [162] CMS performed a first combined search, taking decays of h to $b\bar{b}$, $\gamma\gamma$, $\tau^+\tau^-$, W^+W^- and ZZ into account The exclusions are dominated by the $b\bar{b}$ channel, which justifies focusing on this channel. In analogy to the LHC-DMWG in [45], we take a conservative approach by comparing the binned $h + \not{E}_T$ cross sections from our

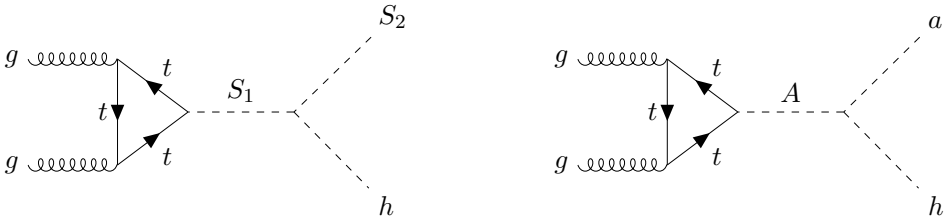

Figure 2.11: Feynman diagrams for the resonant production of a mono-h signal via gluon fusion production in the chosen mass hierarchy for the 2HDM+S (left) and 2HDM+PS (right).

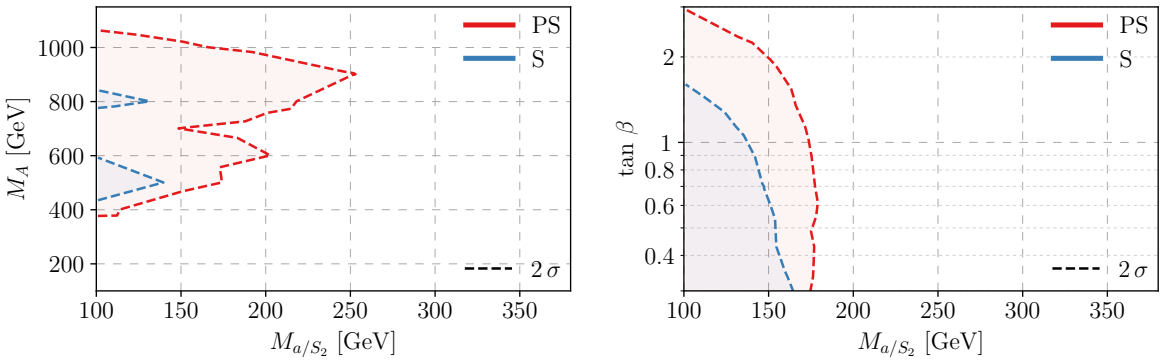

Figure 2.12: $2\,\sigma$ exclusion limits from mono-h searches in M_{a/S_2}–M_A (left) and M_{a/S_2}–$\tan\beta$ plane (right) for the 2HDM+S (blue) and PS (red). In both plots we use the parameters as given in Eq. (2.43) with $\tan\beta = 1$ for the left one and $M_A = 500\,\text{GeV}$ for the right one.

simulations to the model-independent upper limits derived by ATLAS in [161]. While the CMS data in [79] can be extrapolated to our parameter choice for the 2HDM+PS, it cannot be easily extended to the 2HDM+S. We confirmed that they are similar in reach, so we continue with the ATLAS results.

Backgrounds The main backgrounds for mono-h with $h \to b\bar{b}$ searches are $t\bar{t}$ and vector boson plus multiple jet production. See Refs. [79, 161] for a more detailed discussion of the backgrounds and their uncertainty estimates. Minor contributions arise from single top, diboson, SM Higgs plus $V(\to \nu\bar{\nu})$ and multijet processes. In the case of the $t\bar{t}$ background, a bottom quark from a top decay can be misidentified as a Higgs boson, in combination with another b-tagged jet, while the $\not{E}_T$ originates from neutrinos. Similarly, decays of vector bosons also produce $\not{E}_T$ via neutrinos or missed charged leptons, and jets can mimic a Higgs. To estimate those backgrounds, control regions with isolated leptons and extended Monte-Carlo simulations are used [79, 161].

Current Constraints The observed events do not significantly deviate from the expected SM background. Thus model-independent upper limits on the $h(\to b\bar{b}) + \not{E}_T$ cross section per $\not{E}_T$-bin are placed in Ref. [161], which we will use in the following in analogy to [45]. In [161], only one $\not{E}_T$ bin is used at a time to minimize the model dependency. This implies that the

derived limits can be seen as conservative estimates. Furthermore in [161], the dependency of the limits and of the acceptance times efficiency on variations of the event kinematics within a given bin is calculated for several parameter points of a 2HDM+Z' benchmark model. The least stringent limits and the smallest acceptance are given. This also leads to a conservative estimate for the exclusion limits of the 2HDM+S/PS, which are shown in Fig. 2.12. Similarly to the mono-Z exclusion in Fig. 2.9, the exclusion limits weaken in each model for larger $\tan\beta$, M_A and M_{a/S_2}.

The other most prominent feature in the M_{a/S_2}–M_A plane is the dip in the exclusion limit around $M_A \sim 700\,\text{GeV}$, shown in the left panel of Fig. 2.12. It originates from a binning effect due to the large $\not{E}_T$-bins used in the ATLAS analysis. The simulated data shows that for $M_A > 700\,\text{GeV}$ a significantly higher fraction of signal events reach $\not{E}_T > 350\,\text{GeV}$ and therefore end up in the stronger constrained bin with $\not{E}_T = 350 - 500\,\text{GeV}$. This effect compensates the decrease in production cross section caused by increasing the mediator mass, which is the dominant effect for $M_A = 600 - 700\,\text{GeV}$, and leads to a comparably strong or even stronger limit for $M_A \sim 900\,\text{GeV}$. The fact that more events are found in the bin with $\not{E}_T = 350 - 500\,\text{GeV}$, can also be understood in the light of the discussion of the $\not{E}_T$ spectrum around Fig. 2.8. The $\not{E}_T$ spectrum does not qualitatively change by replacing Z with h. For values of $M_A > 700\,\text{GeV}$, the peak of the $\not{E}_T$-spectrum starts to shift above the upper bin limit at 350 GeV because the peak is located slightly below $M_A/2$.

In contrast to the mono-Z searches, the exclusions limits from mono-h differ significantly between the 2HDM+S and 2HDM+PS. The bound on the light pseudoscalar mass M_a is stronger by an approximate factor of two compared to the bound on the corresponding light scalar mass M_{S_2}. This is due to the fact that the resonant production of mono-h events in the 2HDM+S requires the heavy scalar, S_1, in the intermediate state, rather than the heavy pseudoscalar, A, and the gluon fusion production cross section is smaller for scalars, see Eq. (2.40) and Fig. 2.5. Opposite to the mono-Z case, the branching ratios relevant for mono-h are similar in both models, see Sec. 2.1.3,

$$\text{BR}(S_1 \to S_2 h) \approx \text{BR}(A \to a h) \approx 0.1. \tag{2.48}$$

Therefore, the 2HDM+PS is expected to have a higher mono-h cross section in the resonant region, and overall stronger exclusion bounds, as the kinematics do not differ significantly from one model to the other.

2.3.4 Combination

Finally, we summarize our results by comparing all derived limits for the two models individually in the M_{a/S_2}–M_A and M_{a/S_2}–$\tan\beta$ plane in Fig. 2.13 and Fig. 2.14, respectively. We include the results from searches for Higgs-to-invisible, $t\bar{t}$ resonances, mono-Z and mono-h as discussed above. Limits of DD on the 2HDM+S, or from ID for the 2HDM+PS, are avoided by choosing a small value for m_χ.

The differences between the pseudoscalar and scalar model in the single searches have been discussed in the corresponding sections above, so here we focus on how the different constraints compare to each other within one model. Starting with the 2HDM+PS in the M_a–M_A plane for $\tan\beta = 1$, we can see that the dominant limit comes from mono-Z searches, shown in the left panel of Fig. 2.13. Those exclude light mediators with masses up to $M_a \sim 320\,\text{GeV}$ and heavy Higgs masses between 200 and 1000 GeV. For $M_A \gtrsim 1\,\text{TeV}$, the mono-$h$ search leads to slightly stronger bounds up to $M_a \lesssim 200\,\text{GeV}$. Higgs-to-invisible searches exclude masses

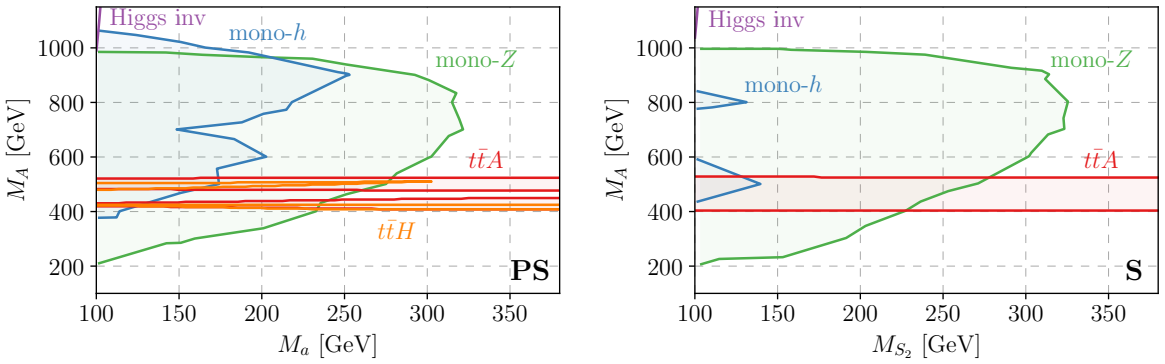

Figure 2.13: Overview of the $2\,\sigma$ exclusion limits from searches for mono-h, mono-Z, $t\bar{t}$ resonances and Higgs-to-invisible in the M_{a/S_2}–M_A plane for the 2HDM+PS (left) and 2HDM+S (right); see text for details. In both plots we use the parameters given in Eq. (2.43) and set $\tan\beta = 1$. Limits from ID and DD vanish for an appropiate choice of m_χ.

of the singlet-like pseudoscalar, a, below $\sim 100\,\text{GeV}$ with a mild dependency on $M_{S_1/H}$, see Eqs. (A.1) and (A.26). In contrast, $t\bar{t}$ resonance searches are nearly independent of M_a and can exclude narrow slices of the heavy Higgs masses around $M_A \sim 400$ and $500\,\text{GeV}$.

A similar structure holds true for the 2HDM+S especially for the mono-Z and Higgs-to-invisible searches, shown in the right panel of Fig. 2.13. In contrast to the 2HDM+PS, the limits from mono-h are significantly weaker compared to the ones from mono-Z and thus are never the strongest, as explained in Sec. 2.3.3. Furthermore, the $t\bar{t}$ limits exclude a larger band of heavy Higgs masses from 400 to $500\,\text{GeV}$. This is a reflection of slightly stronger limits compared to the pseudoscalar model, with the limits changing from just below to just above $2\,\sigma$.

For the M_{a/S_2}–$\tan\beta$ plane with fixed $M_A = 500\,\text{GeV}$, depicted in Fig. 2.14, we obtain similar limits for both models, except for the mono-h limit being weaker in the 2HDM+S. As in the M_a–M_A plane, the dominant limit is given by mono-Z searches, specifically for $\tan\beta \gtrsim 1$. They begin to weaken for values of $\tan\beta$ around three. While these limits, for $0.3 \lesssim \tan\beta \lesssim 3$ apply to 2HDMs of all Yukawa sector types, for $\tan\beta \gtrsim 3$ the $b\bar{b}$ production mode starts to become relevant for type II and Y. This leads to stronger limits for those types, while for type I and X $b\bar{b}$ production never becomes stronger than gluon fusion, and limits will continue to weaken for larger $\tan\beta$ values. The $t\bar{t}$ resonance searches provide a limit of $\tan\beta \gtrsim 1$ being slightly stronger in the 2HDM+S and nearly independent of the light mediator mass. Therefore this is the strongest limit for $M_{a/S_2} > 270\,\text{GeV}$.

Finally, another interesting aspect which is accessible via the comparison plots is the question of how to distinguish the two models. To this end, the weaker mono-h limits for the 2HDM+S can be useful. This sensitivity discrepancy in the mono-h channel could be exploited to distinguish between the 2HDM+PS and 2HDM+S, since the ratio of the signal strength in mono-Z and mono-h is characteristic for each model. So if signals would be detected in both channels, their signal strength ratio could be used to discriminate between the two models at the LHC.

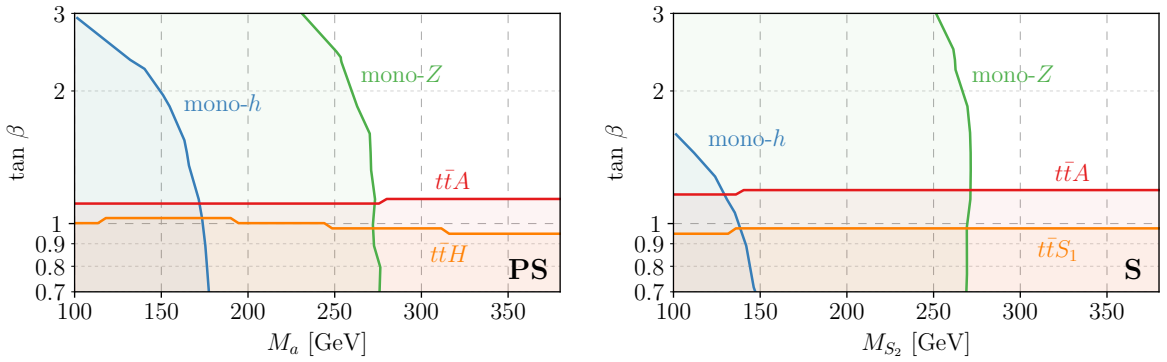

Figure 2.14: Overview on the $2\,\sigma$ exclusion limits from searches for mono-h, mono-Z, $t\bar{t}$ resonances and Higgs-to-invisible in the M_{a/S_2}–$\tan\beta$ plane for the 2HDM+PS (left) and 2HDM+S (right); see text for details. In both plots we use the parameters given in Eq. (2.43) and set $M_A = 500\,\text{GeV}$. Limits from ID and DD vanish for an appropiate choice of m_χ.

2.4 Summary

Next generation simplified models are the new benchmarks used by the ATLAS and CMS collaborations to interpret experimental results in the context of DM searches. In this chapter, we investigated two notable examples of those, the 2HDM+S and 2HDM+PS, focusing on their collider phenomenology in $t\bar{t}$ resonance, mono-Z and mono-h searches. An analysis of the 2HDM+S collider phenomenology, and the explicit comparison was performed for the first time in Ref. [80], where this discussion is based on.

These models feature an extended scalar sector, with a second Higgs doublet, and an additional singlet mediator to the dark sector. They differ from the previous generation of simplified DM models by tending to generate a richer collider phenomenology while restoring gauge invariance in a minimal setup. In particular, the mono-Z and mono-h cross sections can be resonantly enhanced via an intermediate s-channel exchange of a state from the second doublet. Its subsequent decay to a SM boson, in association with the additional singlet decaying to DM, leads to the desired final state.

We started by reviewing principal constraints on the two models. They serve as guidance to select appropriate ranges for the various parameters, which are then further tested with the specific collider searches. Some constraints, for instance those from DD and ID, are mostly complementary to collider searches, because they tend to require different mass spectra, and can be avoided by choosing a small value for m_χ. Others, as flavor and EW precision observables as well as perturbativity and unitarity considerations, are relevant for our signatures. Those lead to a few assumptions that reduce the dimensions of the parameter space. These assumptions have been established by the experimental collaborations [45], and ensure that the relevant constraints are avoided, while obtaining potential observable signals. In addition, these assumptions simplify the comparison between the two models and the different experimental signatures. These assumptions are essentially the mass-degeneracy of the heavy scalars, motivated by bounds from EW precision observables, together with the Higgs alignment limit. Motivated by precision measurements of the Higgs couplings to be SM-like the alignment limit simplifies the Higgs sector by turning one of the doublets into the SM Higgs doublet.

Thus, most constraints from Higgs physics are avoided. Moreover, while we have described four possible Yukawa sectors for the 2HDM, our results are universal due to the considered parameter range.

Using the data provided by different LHC analyses, we then derived limits for the 2HDM+S and 2HDM+PS arising from $t\bar{t}$ resonance, mono-Z and mono-h signatures and discussed how they compare to each other and between the two models. We found that the mono-Z limits are in general the most constraining ones, while the limits from $t\bar{t}$ resonances are nearly independent on the additional singlet and essentially excluding values of $\tan\beta < 1$ for a wide range of mediator masses. A lower bound of $\sim 100\,\text{GeV}$ for the additional singlet mass is given by Higgs-to-invisible searches, thus providing a natural starting point for this parameter in our scans.

We found that in principle the two models could be distinguished at a collider from the ratio of their signal strengths in the mono-Z and mono-h signatures. Also, the absence or appearance of mono-jet events, which are sub-dominant in the considered models, would give further insights into the general nature of the dark sector. Depending on the DM mass, other, mostly astrophysical, probes are powerful tools to discriminate between the two models, too. While the DD cross section is several orders of magnitude higher in the 2HDM+S, the ones related to ID signals are significantly stronger in the 2HDM+PS. These differences are caused by the $\mathcal{CP}$ properties of the light mediators. Therefore, detecting one of these two astrophysical signatures would give a clear indication towards the nature of the mediator to the dark sector and would discriminate between the 2HDM+S and 2HDM+PS. However, the exact realization of the dark sector cannot be investigated there, such that different realizations of the DM – SM interaction would still be possible. In this case, collider studies could help to further investigate the inner workings of the dark sector, since they allow for more precise and controlled tests.

Chapter 3

EFT Approaches to New Physic Searches

The next generation simplified models studied in the previous chapter feature renormalizable couplings and a relatively rich structure of new low-energy states. If new states are significantly above the electro-weak scale, an EFT approach often offers a more suitable characterization. Here, the particle content is less specified than in full models, but via higher-dimensional operators effects of non-minimal new physics can be captured in a relatively generic way. This approach will be the focus of the second part of this thesis.

Although this work focuses on phenomenological aspects of DM theories, it is worth summarizing arguments for the use EFTs and some of their general features. Note that only an incomplete list of EFT properties is presented, as not all are relevant for our purposes and are laid out in great detail in Refs. [163–173]. We will start in this chapter by introducing various aspects and concepts of EFTs, in particular how they can be used to investigate physics beyond the SM. We then discuss examples of EFT analyses directly related to BSM and DM.

The main aim of using EFTs is to systematically separate effects related to different scales, such that in the EFT only the scale of interest remains. Therefore, EFTs systematically exploit the assumption that physics on small length scales can only have a limited effect on observables related to larger scales. While this behavior is intuitively clear and to some extent made progress in physics possible in the first place, in the context of QFTs some subtleties emerge.

For example, in QFTs which are supposed to be valid up to arbitrarily high energies therefore called "UV-complete", some loop calculations seem to break this principle. There the momentum integral runs up to infinity and at first sight might be sensitive to states related to the highest energy scales. Since those scales are not experimentally accessible and the associated physics is unknown, computing low-energy observables would become (nearly) impossible. For example, the SM cross sections for low-energy processes would depend on the exact theory of quantum gravity associated to the Planck scale. However, UV-contributions, such as those loops, appear as point-like interactions in the infra-red (IR) regime, and therefore can be emulated by including new local operators in the Lagrangian. There they either contribute to low energy parameters, e.g. the electron mass; or add an in general infinite series of higher-dimensional operators suppressed by powers of the high scale, Λ, which would render predictions impossible. Both cases turn out to be non-problematic. Regardless of the UV-theory the low-energy parameters have to be determined by experiments. The predictability is restored by truncating the operator series at some order of $1/\Lambda$. The desired accuracy of the EFT prescripts the number of higher-dimensional operators that should be included. These in turn determine the number of low-energy parameters that need to be measured to enable predictions.

In a different formulation, physical theories described by QFTs are typically not complete up to arbitrarily high energy.[1] At best the theory is an EFT valid up to some cutoff scale Λ [165].

[1] Possible exceptions of this are theories which feature a reliably predicted UV fix point, such that they do not necessarily have a cutoff, for instance QCD at high energies.

This "scale of ignorance" is often a physical scale, such as the mass of a new particle, which is not explicitly taken into account, or has even not been discovered yet. When interpreted in this way, many well-known theories can be seen as EFTs [165, 168].

Following these arguments, EFTs provide a modern, more physical perspective on renormalization, going beyond the systematic cancellations of infinities. Higher-dimensional interactions, often called "non-renormalizable", always contribute at some level of precision and contain information about the physics at the cutoff scale. Their effects are simply numerically suppressed if the cutoff is much larger than the typical energies achieved in experiments, E. Hence, EFTs are "automatically" renormalizable at low energies, provided that the cutoff scale Λ is large [165, 174].

A key tool to restore predictability of EFTs is power counting. Each operator in the Lagrangian is explicitly assigned with a power of an expansion parameter, in high-energy physics, this is typically E/Λ. Observable quantities are calculated in a perturbative expansion of this parameter, and the order is adopted according to the problem at hand and the required accuracy. The validity of the EFT breaks down when its expansion parameter is $\mathcal{O}(1)$ and the perturbative expansion diverges. In that case, one has to develop a new EFT, explicitly including further states. Besides these more theoretical reasons, EFTs are a strong tool for two main purposes: calculational to improve predictions of a given UV theory at low energies, and conceptual to systematically characterize systems with several, separated scales [164]. While their capability to improve calculations in various theories is discussed in e.g. Refs. [163–168,173], we focus here on their conceptual capability to characterize BSM and DM scenarios. For the purpose of this thesis (and BSM searches in general), EFTs offer an efficient method to set relatively model-independent constraints on unknown new physics sectors, and to combine results from different experimental searches.

In this chapter, we start with a brief review of general approaches for constructing EFTs in Sec. 3.1. We also discuss BSM related examples, and provide an example of how to match a UV-theory to a corresponding EFT. The following Sec. 3.2 proposes $t\bar{t}$-associated production as a new channel for a measurement of the yet undetected Higgs decay to a Z boson and a photon. Potential deviations from the SM prediction can be parametrized in terms of effective operators. Future measurements could set limits on a so-far weakly constrained combination of effective operators. The last Sec. 3.3 introduces the theoretical background of the eDMEFT. We discuss the Lagrangians for a scalar and a pseudoscalar mediator, before their phenomenology is studied in detail in the following chapter.

3.1 General Concepts

In this section we will give a short summary of two different approaches for constructing an EFT, and we will show how to match a UV-complete theory to it. In addition two BSM related examples are given focusing on results needed in the following section.

While a physical problem that one wants to describe with an EFT can feature several scales, they can usually be considered one at a time. Then in the EFT, only one scale remains, thus for simplicity we will consider only examples with two well separated scales in the UV.

3.1.1 Construction

There are two general approaches to constructing an EFT for solving a given low energy problem. One approach is to start with a known high energy theory which features separated

scales[2]. Then, the heavy fields (or highly energetic modes to be more precise) are systematically integrated out, since they are not present at low energies where one wishes to perform the computations. We sketch the procedure of the so-called "top-down" approach here and come back to it in more hands-on examples in Secs. 3.1.3 and 3.3.2 about matching concrete UV theories.

The other approach, called "bottom-up", is more focused on the degrees of freedom available at the low energy. Here, the effective operators are constructed from low-energy degrees of freedom following the steps described below. This approach is especially helpful to describe new physics, when the full theory at high energies is unknown, e.g. historically Fermis theory of weak interactions. It allows the interpretation and parametrization of experimental results in a general, rather model-independent way in terms of the fields present at the accessible energy scale. Even if it is not possible to unambiguously extrapolate to the full theory in the absence of direct production of new states, one can learn about it by considering best-fit values for the EFT operators.

Top-Down If a given QFT features a large fundamental scale M, typically associated with the mass of a heavy particle or a characteristic (euclidean) momentum transfer, observables at experimentally accessible low energies $E \ll M$ can be calculated in an EFT. This EFT, valid at low energies, can be obtained from the full theory by the following steps [165, 175]:

- Dividing the fields ϕ of the QFT with respect to a fixed cutoff $\Lambda < M$ into low-energy Fourier modes, ϕ_L, with frequencies $\omega_L < \Lambda$ and high-energy ones ϕ_H, with $\omega_H > \Lambda$ such that $\phi = \phi_L + \phi_H$.[3]

  Due to this construction, correlation functions for energies $E \ll \Lambda$, which we want to correctly capture in the EFT, can only depend on ϕ_L. The generating functional of this theory is given by

  $$Z[J_L] = \int \mathcal{D}\phi_L \, \mathcal{D}\phi_H \, e^{iS[\phi_L,\phi_H]+i\int d^dx J_L(x)\phi_L(x)}, \tag{3.1}$$

  where $S(\phi_L, \phi_H) = \int d^dx \, \mathcal{L}(x)$ is the action of the QFT in d space-time dimensions.

- Integrating out the high-energy modes by computing the corresponding path integral

  $$e^{iS^\Lambda_{\text{eff}}(\phi_L)} \equiv \int \mathcal{D}\phi_H \, e^{iS[\phi_L,\phi_H]}, \tag{3.2}$$

  where $S^\Lambda_{\text{eff}}[\phi_L]$ is called the Wilsonian effective action and depends on the chosen cutoff Λ. This leads to the new generating functional

  $$Z[J_L] = \int \mathcal{D}\phi_L \, e^{iS^\Lambda_{\text{eff}}[\phi_L]+i\int d^dx J_L(x)\phi_L(x)}, \tag{3.3}$$

  where the high energy modes have been removed as dynamical degrees of freedom and it is therefore non-local at distances $\Delta x \sim 1/\Lambda$.

[2] While in general this could be any kind of scale, in particle physics usually energy scales are considered.

[3] We leave the concrete method of how to divide the fields into low- and high-energy modes open, as it does not affect the discussion.

- Expanding the non-local effective action in a sum of local operators consisting of the low energy fields $\mathcal{Q}_i^{(D)}(\phi_L)$, called Operator Product Expansion (OPE), yields

$$S_{\text{eff}}^{\Lambda}[\phi_L] = \int d^d x\, \mathcal{L}_{\text{eff}}^{\Lambda}(x) \qquad \text{with} \qquad \mathcal{L}_{\text{eff}}^{\Lambda}(x) = \sum_{D,i} g_i^{(D)} \mathcal{Q}_i^{(D)}\big(\phi_L(x)\big). \tag{3.4}$$

  The effective Lagrangian $\mathcal{L}_{\text{eff}}^{\Lambda}$ consists of an infinite series of all $\mathcal{Q}_i^{(D)}$ with mass dimensions D, which are allowed by the underlying symmetries. The $g_i^{(D)}$ are called Wilson coefficients and are of mass dimension $d-D$ as the action has to be dimensionless.

- Truncating the infinite series of operators at a required accuracy to enable predictability. To this end, an appropriate expansion parameter is needed, which keeps track of the important operators. Since M is assumed to be the only relevant scale in the QFT, we can rewrite

$$g_i^{(D)} = C_i\, M^{d-D}, \tag{3.5}$$

  where the dimensionless coefficients C_i are $\mathcal{O}(1)$ due to the criteria of naturalness. The operators are expected to scale as E^{D-d}. Therefore, in the validity range ($E \ll \Lambda < M$) the Lagrangian $\mathcal{L}_{\text{eff}}^{\Lambda}$ in Eq. (3.4) features the expansion parameter $E/M \ll 1$, and the different contributions scale as

$$C_i \left(\frac{E}{M}\right)^{D-d} \sim \begin{cases} \gg 1 & D < d \quad (\text{“relevant”}), \\ \mathcal{O}(1) \quad \text{for} & D = d \quad (\text{“marignal”}), \\ \ll 1 & D > d \quad (\text{“irrelevant”}). \end{cases} \tag{3.6}$$

  The first type of operators are named “relevant”, or “super-renormalazible”, because their importance grows for smaller energies. Operators of this type, for instance bare mass-terms, are typically forbidden by symmetries, and if not, could potentially lead to dangerous effects. The relevance of marginal operators, also named “renormalazible”, is independent of the energy. Those operators are usually considered in QFTs, for example in the SM. The “irrelevant” operators, also called “non-renormalizable”, vanish in the low-energy limit and are therefore often not considered. However, phenomenologically they are the most interesting interactions as they contain information about the physics at the cutoff scale $\Lambda \sim M$. For a demanded accuracy of order E/M, only a finite number of operators contribute, and predictability is restored [165, 173].

Bottom-Up As shown above, an EFT is completely defined by the effective action, S_{eff}. Therefore, S_{eff} can be used as starting point to construct an EFT since it is specified by defining the following three components [163]:

- Degrees of freedom, the minimum amount relevant for the problem at hand.
- Symmetries, first identify those that restrict the dynamics of the system and then include all invariant operators in the effective action. This results in an infinite series of operators, therefore a clear power counting is needed.
- Expansion parameters are an appropriately chosen small quantity and the key to handle the infinite series of effective operators. In particle physics, they are usually associated

with the ratio of the characteristic energy of an observable and the high scale. Each operator in the effective action can be associated with a power of the expansion parameter. Since observables are calculated via perturbation theory, the operator series can be truncated at a given order of accuracy. Therefore, only a finite amount of operators is left. This procedure ensures that the important, leading contributions to observables are kept.

This is close to the approach we choose in the following sections, where we identify the relevant degrees of freedom for a consistent DM phenomenology, and then construct the effective Lagrangian containing all valid operators.

3.1.2 Examples

While EFTs for many purposes exist, we will take a closer look at two examples of particular interest in BSM and DM searches, the standard model effective field theory (SMEFT) and the DMEFT.

SMEFT The absence of clear signs for states beyond the SM can be interpreted as a separation between the electro-weak (EW) and the new physics scale. This invites the use of an EFT for parameterizing experimental NP searches. Thereby we learn about physics at the high scale by either setting limits on it or by deviations from the $D=4$ SM predictions.

To this end, effective operators are built up from gauge-invariant combinations of the SM fields. Remarkably, at $D=5$ only the Weinberg-operator $\sim (LH)^2$ arises, which violates lepton number by two units and gives rise to a Majorana mass-term for neutrinos after EWSB [176]. The suppression scale in this case can be related to the mass of right-handed neutrinos for example.

At $D=6$, the SMEFT shows a richer phenomenology [177, 178]. Assuming baryon-number conservation (to forbid strongly constrained proton decays) and flavor-universality (to circumvent bounds from flavor physics), there are 59 independent operators. Those can be given in various bases; lists can for example be found in [178, 179]. At higher dimension, the number of operators grows rapidly [180, 181].

DMEFT Since DM cannot consist of the known SM particles and acts as an external state in experiments, its effects cannot be captured by any SMEFT variant. Therefore for describing its effects, it is straightforward to explicitly include it in the field content of an EFT following the "bottom-up" principle laid out above.

In so-called DMEFTs, the SM field content is extended by an additional degree of freedom χ, e.g. a fermion singlet. To model DM in various particle physics experiments, its interactions with the SM are parametrized by effective, higher-dimensional operators. Those are constructed as combinations of χ and the SM fields, which arise at $D=6$ for fermionic DM, and in the common notation do not respect the SM gauge symmetry. While SM fermions are often only considered, interactions with the SM gauge bosons are true $D=7$ operators, and are discussed e.g. in [58, 182–184]. For high-energy experiments but after EWSB, the effective Lagrangian can schematically be written as [47, 185–190]

$$\mathcal{L}_{\text{DMEFT}} = \sum_{i,j} \sum_{f} \frac{C_{ij}^{f}}{\Lambda^2} \left(\bar{f}\Gamma_i^f f\right)\left(\bar{\chi}\Gamma_j^\chi \chi\right), \tag{3.7}$$

where the sum runs over $f = u, d, s, c, b, t, e, \mu, \tau$ and includes all SM quarks and charged leptons. The matrices $\Gamma^f = \{1, \gamma^5, \gamma^\mu, \gamma^5\gamma^\mu, \sigma^{\mu\nu}\}$ and $\Gamma^\chi = \{\Gamma^f, \gamma^5\sigma^{\mu\nu}\}$ are chosen appropriately to form valid combinations of bilinear operators. The EFT in Eq. (3.7) is fully described by the DM mass, m_χ, and the Wilson coefficients, C_{ij}^f. The breaking of the SU(2) symmetry suggests a scaling of $C_{ij}^f = c_{ij}^f m_f/\Lambda$ for scalar operators [191].

While originally constructed for comparison of all DM searches, the validity at LHC was found to be questionable due to the high momentum transfers there [47–55]. In DD experiments the recoil energy is much smaller, and DMEFTs are used to calculate collision rates and give limits on the allowed interaction strength in a model-independent way. Those calculations are performed at the nuclear scale, such that nucleons instead of quark interactions are considered. Also, the heavy SM fields are integrated out, and the non-relativistic limit is taken [114–120].

3.1.3 Matching of UV theories

There are various ways to match a UV-complete theory to a corresponding EFT. In the "diagrammatic" approach, a specific process is calculated in the full theory and the EFT, taking diagrams up to a certain loop level into account. The Wilson coefficients are obtained by comparing the results order by order in perturbation theory. If loop-corrections are taken into account, EFTs offer a strong calculational tool to deal with largely separated scales. Logarithms of the large ratio of these scales, appearing in the perturbative expansion are handled by effectively splitting them into a high and a low energetic part. While the part above the matching scale is associated to the Wilson coefficients, the low energetic one is captured in the matrix elements of the effective operators. Then, the Wilson coefficients are derived at the high scale by the matching procedure. There, the corresponding large logarithms disappear in the calculations, since the matching is independent of the IR regime, where both theories are identical. By employing the renormalization group equations for the Wilson coefficients, they can be run down to the low scale. In this way, one is left with an EFT for the IR featuring only one scale. This combination allows to sum up the logarithms in all orders of perturbation theory. As this is more advanced and not needed for the phenomenology-driven analysis in the following, we do not persue it furter, and instead refer to Refs. [163, 164, 168, 174].

Here we show an approach using the equations of motion for the fields that should be integrated out. The effective Lagrangian is derived by solving them, and inserting the results in the Lagrangian of the UV theory. This approach is particularly easy for tree-level matching, and has been extended to one-loop level under the name of covariant-derivative-expansion [192–194], and applied to SMEFT [195–198]. To simplify the discussion and in analogy to [163, 164], we investigate a toy-model and stress that the findings can be extended to more complex theories.

We consider a UV-complete scalar theory in $d=4$ defined by the Lagrangian

$$\mathcal{L}_{\text{UV}} = \tfrac{1}{2}\partial_\mu\phi\partial^\mu\phi - \tfrac{1}{2}m^2\phi^2 + \tfrac{1}{2}\partial_\mu\Phi\partial^\mu\Phi - \tfrac{1}{2}M^2\Phi^2 - \tfrac{1}{2}\,b\,\phi^2\Phi, \tag{3.8}$$

with $m,\, b \ll M$. As discussed above, in the low-energy limit $E \ll M$, the field Φ cannot be an external degree of freedom, and the generating functional does not depend on it. Restoring powers of $\hbar$ for the moment, it is given by

$$Z[J] = \int \mathcal{D}\phi\, e^{iS_{\text{eff}}[\phi]/\hbar}\, e^{i\int d^4x J(x)\phi(x)/\hbar} \qquad \text{with} \qquad e^{iS_{\text{eff}}[\phi]/\hbar} \equiv \int \mathcal{D}\Phi\, e^{iS[\phi,\Phi]/\hbar}. \tag{3.9}$$

To simplify the calculation we expand $S_{\text{eff}} = S_{\text{eff}}^{(0)} + \hbar S_{\text{eff}}^{(1)} + \mathcal{O}(\hbar^2)$ in powers of $\hbar$. Here $S_{\text{eff}}^{(0)}$ includes all tree-level processes, while terms proportional to $\hbar^n$ correspond to n-loop

amplitudes. The leading contribution $S^{(0)}_{\text{eff}}$ can be calculated by making use of a saddle point approximation, leading to the simple expression [163]

$$S^{(0)}_{\text{eff}}[\phi] = S[\hat{\Phi}, \phi], \quad \text{where } \hat{\Phi}[\phi] \text{ is a solution of } \quad \frac{\delta S[\hat{\Phi}, \phi]}{\delta \hat{\Phi}} = 0. \tag{3.10}$$

In this particular example, the equation of motion for Φ

$$\left(\Box - M^2\right)\Phi = \tfrac{1}{2} b\, \phi^2 \tag{3.11}$$

is solved by

$$\hat{\Phi} = \frac{b}{2} \frac{1}{\Box - M^2}\, \phi^2 = \frac{b}{2} \left(\frac{1}{M^2} + \frac{\Box}{M^4} + \frac{\Box^2}{M^6} + \dots \right) \phi^2. \tag{3.12}$$

The expansion in $1/M^2$ is sensible because $\Box \sim E^2 \ll M^2$, and the truncation is related to the required accuracy. Inserting this result back into the original Lagrangian, we obtain the tree-level effective action

$$S^{(0)}_{\text{eff}}[\phi] = \int d^4x \left\{ \tfrac{1}{2} \partial_\mu \phi \partial^\mu \phi - \tfrac{1}{2} m^2 \phi^2 - \tfrac{1}{8} b^2 \phi^2 \left(\frac{3}{M^2} + \frac{4\Box}{M^4} + \dots \right) \phi^2 \right\}, \tag{3.13}$$

which describes the low-energy behavior up to a requested precision of $1/M^2$.

This example should serve as a justification of the simplified approach that we will use in Sec. 3.3.2. There, we solve the equations of motion, which are linearized in the heavy fields to consistently keep the lowest order of $1/M$, and we insert the solutions into the Lagrangian of the full theory. Accordingly, keeping also only operators with the lowest order of $1/M$ there, results in the effective Lagrangian. The Wilson coefficients of the general, "bottom-up" EFT are determined by comparing them to the coefficients generated via the matching. At tree-level there is no scale dependence to keep track of, which becomes important when matching at loop level [164].

Now that we have given an overview of general EFT characteristics, in the following sections we will use some of EFT properties in phenomenological motivated applications. A first example will be given in the context of a Higgs precision measurement, we will come back to DM models later. We will investigate a newly proposed channel with the potential to discover the decay of a Higgs to a Z boson and a photon. Modifications to this process can be parametrized by a combination of SMEFT operators, and the expected experimental sensitivity can be translated in bounds on this combination.

3.2 $h \to Z\gamma$: an example for SMEFT

A measurement of the yet undiscovered decay of the Higgs boson to a photon and a Z boson would provide a further consistency test of the SM. This channel also has the potential to unveil new physics potentially hidden in other observables [199–208], and is an example for a BSM search beyond DM. Moreover, it furnishes a promising channel to extract spin and parity properties of the Higgs boson [206, 209, 210].

Refined projections by the ATLAS and CMS collaborations have shown that even at the end of the HL-LHC program, with 3 ab^{-1}, a $5\,\sigma$ discovery of this decay will be challenging [211, 212],

and the sensitivity will still be driven by statistical uncertainties. After our analysis was finalized, the most recent ATLAS search in [213] using 139 fb^{-1} of data improved the upper limit on $\sigma(pp \to h \to Z\gamma)$ from 6.1 [214, 215] to 3.6 times the SM value. While $t\bar{t}$-associated production was taken into account as one Higgs production channel, its full potential was not exhausted, because no dedicated analysis has been performed.

In general, the $h \to \ell^+\ell^-\gamma$ channel[4] also offers the possibility to independently measure the spin [209, 210] and $\mathcal{CP}$ [206] properties of the Higgs, but the low signal to background ratio makes it difficult to extract angular correlations or asymmetries in the inclusive search. The Higgs $\mathcal{CP}$ properties in $t\bar{t}$-associated production in the $h \to \gamma\gamma$ decay channel have been investigated recently in [216, 217]. There, an upper limit on the $\mathcal{CP}$ mixing angle of 43° has been found.

In this section, the channel $pp \to t\bar{t}h$, $h \to Z\gamma \to \ell^+\ell^-\gamma$ is presented, which enhances the prospects of discovering the decay $h \to Z\gamma$, and of measuring the corresponding effective coupling. The $t\bar{t}h$-associated production has recently been observed by ATLAS [218, 219] and CMS [220], inviting the use of it for further studies. It profits in particular from the large top Yukawa coupling, such that the radiation of a Higgs from the $t\bar{t}$ state leads only to a modest suppression of the cross section compared to the main backgrounds. This provides a significantly enlarged signal-to-background ratio compared to other production channels like gluon fusion, where a loop-suppressed signal competes with tree-level backgrounds. Thereby, $t\bar{t}h$-associated production increases the prospects of measuring the spin and $\mathcal{CP}$ properties of the Higgs boson.

We will study both the expected significance for the channel under consideration at the high-luminosity LHC (HL-LHC), as well as examine potential constraints on the coefficient of the effective $hZ\gamma$ coupling. Finally, we will extend the analysis to potential future 27 TeV (HE-LHC) and 100 TeV pp colliders, for example the FCC_{hh}.

The results presented in this section follow Ref. [221]

SMEFT Setup We consider the SM augmented with the $D=6$ SMEFT operators[5]

$$\begin{aligned}
\mathcal{O}_{HW} &= \frac{ig}{m_W^2} \left(D^\mu H\right)^\dagger \sigma_i \left(D^\nu H\right) W^i_{\mu\nu}, \\
\mathcal{O}_{HB} &= \frac{ig'}{m_W^2} \left(D^\mu H\right)^\dagger \left(D^\nu H\right) B_{\mu\nu}, \\
\mathcal{O}_{\gamma} &= \frac{g'^2}{m_W^2} |H|^2 B_{\mu\nu} B^{\mu\nu},
\end{aligned} \tag{3.14}$$

relevant for the $h \to Z\gamma$ decay in leading approximation,[6] where H is the SM Higgs doublet, parametrized after electroweak symmetry breaking (EWSB) as $H = 1/\sqrt{2}(-i\varphi_1 - \varphi_2,\, v + h + i\varphi_3)^T$. Here, v denotes the vev $\langle H \rangle = 1/\sqrt{2}(0, v)^T$, which triggers EWSB, h is the physical Higgs boson, and $\varphi_{1,2,3}$ are the Goldstone modes.

This setup allows us to study deviations from the SM in a relatively model-independent way, under the assumption that there is a mass gap between the SM and the new states. After

[4] Here and in the following of the section, ℓ denotes electrons and muons.
[5] The complete set of SMEFT operators can be found in e.g. [178, 179].
[6] We do not take possible BSM effects in Higgs production into account, and neglect $\mathcal{CP}$-odd operators.

EWSB, the operators in Eq. (3.14) generate in particular the Lagrangian term

$$\mathcal{L} \supset \frac{c_{Z\gamma}}{v}\, h\, Z_{\mu\nu}\gamma^{\mu\nu}, \tag{3.15}$$

contributing to the $h \to Z\gamma$ decay at tree-level with

$$c_{Z\gamma} = -t_W \left[C_{HW} - C_{HB} + 8s_W^2 C_\gamma\right], \tag{3.16}$$

where $C_{HW,\,HB,\,\gamma}$ are the coefficients of the corresponding effective operators listed in Eq. (3.14) and $t_W \equiv \tan\theta_W$, $s_W \equiv \sin\theta_W$, with θ_W being the Weinberg angle. Analyses of the SMEFT coupling space show that the direction depicted in Eq. (3.16) is not strongly constrained such that significant BSM effects could be present [203, 222–224].

For the following analysis we define the ratio of the decay widths in the presence of effective operators and in the SM, see e.g. [202], as

$$\frac{\Gamma(h \to Z\gamma)}{\Gamma_{\text{SM}}(h \to Z\gamma)} \equiv \kappa_{Z\gamma}^2 \simeq 1 - 0.146\,\frac{4\pi}{\alpha c_W}\, c_{Z\gamma}, \tag{3.17}$$

where the second equality is valid for small $c_{Z\gamma}$. We will eventually study the constraints that can be set on $\kappa_{Z\gamma}$, and thus on the Wilson coefficient $c_{Z\gamma}$, from the process under consideration.

Signal Estimate The SM cross section for Higgs production in association with two top quarks at the LHC, with $\sqrt{s} = 14\,\text{TeV}$, including NLO QCD+EWK corrections is $\sigma(pp \to t\bar{t}h) = 613\,\text{fb}\,{}^{+6.0\%}_{-9.2\%}\,(\text{scale}) \pm 3.5\%\,(\text{PDF} + \alpha_s)$, and the relevant branching ratio amounts to $\text{BR}(h \to Z\gamma) = 1.54 \cdot 10^{-3}$ [225]. We consider the Z boson decaying to two leptons, $\ell = e, \mu$ with $\text{BR}(Z \to \ell^+\ell^-) = 0.067$ [226]. For the HL-LHC with $3\,\text{ab}^{-1}$ of integrated luminosity we thus expect $S_0 \approx 190$ signal events over all top decay channels.

For the signal to remain observable after selection cuts, the analysis has to be as inclusive as possible. On the one hand electrons, muons, and photons are reconstructed with high efficiencies. On the other hand, the number of events will be reduced by tagging $t\bar{t}h$-associated production and including isolation requirements to consider the probability of the $h \to Z\gamma$ overlapping with some of the top decay products. For a first estimate, we thus assume a selection efficiency of $(10 - 15)\,\%$ comparable to the experimental efficiency of the di-photon channel [227]. In the next section we will quantitatively confirm this estimate in an explicit analysis of the semi-leptonic top-decay channel. This would lead to roughly $S = (20 - 30)$ signal events per experiment.

Background Estimate The main irreducible background for the desired signal is $t\bar{t}Z$ production with radiation of a photon from initial or final states. At the 14 TeV LHC, the NLO QCD cross section with $p_{T,\gamma} > 10\,\text{GeV}$ and $|\eta_\gamma| < 4.0$ is $\sigma(pp \to t\bar{t}Z\gamma) = 9.3\,\text{fb}$. This is about ten times larger than the signal cross section resulting in $B_0 \approx 1870$.

Among the reducible backgrounds, we expect the dominant contribution from $pp \to tjjZ\gamma$ and $pp \to t\bar{t}Zj$ production, where j denotes a jet in the 5-flavor scheme including b-jets. The former background is only relevant when considering the semi-leptonic and fully-hadronic top decay channels. In the latter case, one jet is misidentified as a photon. Experimentally this can be estimated by loosening the photon identification, however we cannot simulate this reliably. Eventually, the best approach might be to float the background normalization to fit the data in the side-bands below and above the Higgs mass, m_h.

For the purpose of the present estimate we account for reducible backgrounds by simply increasing the irreducible background cross section by 50 % to obtain a more realistic sensitivity. The assumption about the reducible background contribution will be justified by explicit simulations in the next section. Including this factor and multiplying with the selection efficiency from above, we arrive at $(280 - 420)$ background events. Here we assumed that the efficiencies for the signal and background are comparable, as long as no cut on the $Z\gamma$ invariant mass spectrum around m_h is applied. Whether other backgrounds are relevant will depend on the $t\bar{t}$ decay channel, and on the analysis, but we expect them to be sub-leading and to have a smooth $m_{\gamma\ell\ell}$ invariant mass distribution.

Once the $\gamma\ell^+\ell^-$ invariant mass, $m_{\gamma\ell\ell}$, is restricted to a 10 GeV window around m_h, the background is reduced by another factor of ~ 15 (shown below) and we would obtain $B = (20 - 30) \approx S$. Therefore, we can conclude with a $4.5\,\sigma - 5.5\,\sigma$ sensitivity from a simple cut and count analysis. This can be further improved by fitting the invariant mass distribution with signal plus background, and background-only hypotheses. This potential to observe the $h \to \ell^+\ell^-\gamma$ channel in a low background environment is our main motivation to perform this study. In the next section we provide a detailed simulation for the semi-leptonic $t\bar{t}$-decay channel, to better understand how realistic the above estimate is.

3.2.1 Analysis

To get a robust estimate of the expected sensitivity at the HL-LHC with $\sqrt{s} = 14$ TeV and an integrated luminosity of $3\,\text{ab}^{-1}$, we perform an analysis with Monte Carlo simulations of the semi-leptonic top-pair decays ($t \to bjj$, $\bar{t} \to \bar{b}\ell^-\bar{\nu}_\ell$, or vice versa). The obtained selection efficiency is then used to estimate the sensitivity including all top-pair decay channels in the next paragraph.

We simulate the signal process $pp \to t\bar{t}h$ with MadGraph5_aMC@NLO [140, 141] at next-to-leading order (NLO) in QCD using the PDF4LHC15_nlo_30_pdfas PDF set [145], provided through LHAPDF6 [146]. Our value for the $t\bar{t}h$-production cross section is in good agreement with the results quoted above. For the parton-showering we use the MadGraph-build-in Pythia 8.2 [147] only allowing for the $h \to Z\gamma$ and $Z \to \ell^+\ell^-$ decays and rescaling the cross section with the corresponding branching ratios. A fast detector simulation is done with Delphes 3.4.2 [148] using the HL-LHC detector card.

We also simulate several background processes. The most relevant ones are: (i) the irreducible background $pp \to t\bar{t}\gamma Z$, $Z \to \ell^+\ell^-$. Without contributions from Higgs decays it gives a cross section of approximately 620 ab at NLO in QCD for $p_{T,\gamma} > 10$ GeV and $|\eta_\gamma| < 4$. (ii) The reducible background $pp \to tjj\gamma Z$, $Z \to \ell^+\ell^-$ with a LO cross section of 940 ab.

Other possible final states, such as $t\bar{t}jW^\pm\gamma$, $W^\pm b\bar{b}jZ\gamma$ and $t\bar{t}t\bar{t}\gamma$, have negligible cross sections in the selected region. These sum up to less than 10 % of the total background events. The $t\bar{t}Zj$ background is not simulated, as we cannot model the jet misidentification reliably. Instead, it is accounted for by increasing the total $t\bar{t}Z\gamma$ background by 20 % in our calculation of the significance [214].

We focus here on semi-leptonic $t\bar{t}$ decays since they are the most suitable for a cut-and-count analysis, and comment on the hadronic and leptonic decays in the next paragraph. In the parton shower by Pythia, all top decays are allowed to account for misidentification, e.g. τ's being mistagged as leptons and hence contributing to the semi-leptonic channel.

The reconstruction requirements for electrons (muons) in Delphes are $p_T > 15$ (10) GeV, $|\eta| < 2.47$ (2.7), and for photons $p_T > 5$ GeV, $|\eta| < 2.37$, and it is required to have no selected

leptons within a cone of $R = 0.3$. Jets are reconstructed with FastJet 3 [228] using the anti-k_t algorithm [229] with $R = 0.4$, and are considered to have $p_{T,j} > 25$ GeV and $|\eta| < 2.5$. In addition the following selection requirements[7] motivated by experimental analyses [214, 227] have to be fulfilled:

- Exactly three electrons and muons satisfying the reconstruction requirements
- Three or more jets, and $p_{T,j} > 30\,\text{GeV}$ for the first three jets in p_T
- Missing energy $\not{E}_T > 20\,\text{GeV}$
- At least one b-tagged jet
- At least one photon with $p_{T,\gamma} > 15\,\text{GeV}$
- Z-reconstruction: OSSF lepton pair with $76\,\text{GeV} < m_{\ell\ell} < 106\,\text{GeV}$
- Higgs-reconstruction: γ and Z candidate fulfill $120\,\text{GeV} < m_{\gamma\ell\ell} < 130\,\text{GeV}$

To reconstruct the Z boson, we require an opposite sign, same flavor (OSSF) lepton pair in the invariant mass range $76\,\text{GeV} < m_{\ell\ell} < 106\,\text{GeV}$ in the final state, to avoid contamination from top-decays. If more than one lepton pair fulfills this requirement, the one closer to the Z mass is chosen. This lepton pair together with the highest-p_T photon is used to reconstruct the Higgs mass. The invariant mass distribution of the $\gamma\ell^+\ell^-$ system before applying the $m_{\gamma\ell\ell}$ cut is shown in the top panel of Fig. 3.1. The signal clearly peaks at $m_{\gamma\ell\ell} = m_h = 125\,\text{GeV}$, and we see that by cutting on a window of $m_h \pm 5$ GeV, which is experimentally feasible [214, 215], we can obtain $S/B \gtrsim 1$. The numerical results for the signal and the two backgrounds are given in Table 3.1.

The selection efficiencies for the signal and background processes are defined as $\epsilon_N \equiv N_{\text{final}}/(N_{\text{initial}}\,\text{BR}_{\text{semi-lept}})$ with $N = S$, B_{irred}, B_{red}. The branching ratios of the semi-leptonic decay are $\text{BR}_{\text{semi-lept}} = \text{BR}(t\bar{t} \to b\bar{b}\ell\nu jj) = 0.288$ for the signal and irreducible background, and $\text{BR}_{\text{semi-lept}} = \text{BR}(t \to b\ell\nu) = 0.213$ for the $tjjZ\gamma$ background [226]. With the values from Table 3.1, we obtain $\epsilon_S = 0.14$, $\epsilon_{B_{\text{irred}}} = 0.0097$ and $\epsilon_{B_{\text{red}}} = 0.0027$. As to be expected, the reducible background has a smaller selection efficiency than the irreducible one, while $\epsilon_{B_{\text{irred}}} \approx \epsilon_S$ until Higgs-reconstruction.

Sensitivity Estimate In order to arrive at our final result for the expected significance and the anticipated constraint on $\kappa_{Z\gamma}$, we assume that the efficiencies for the semi-leptonic top-decay channel derived above also hold for the leptonic and hadronic channels. Due to the recent development in top-reconstruction using boosted decision trees, hadronic top-decays are identified with a high efficiency. The selection efficiency reported in [218–220, 230] is at least comparable to the leptonic channel, thus justifying our extrapolation from the semi-leptonic to the hadronic channel.

The reducible $pp \to tjjZ\gamma$ background is specific to the semi-leptonic and fully-hadronic channel. We therefore do not use the result of its simulation directly, but include it in the rescaling of the irreducible background. From the proper simulation of the process in the semi-leptonic channel, we find that the number of background events is increased by approximately 30 %, compared to the irreducible-background-only case. To be conservative we increase the irreducible background by 50 % in the following, also accounting for a 20 %

[7] Note that these cuts are mainly meant to select the signal and suppress other backgrounds, rather than separating it from the irreducible background.

Cut	S	$tt Z\gamma$	$tjj Z\gamma$
Initial	186	1862	2817
$N(l) = 3$	25	273	209
$N(j) \geq 3$, $p_{T,j} > 30\,\text{GeV}$	15	170	46
$\not{E}_T > 20\,\text{GeV}$	14	160	41
$N(b) \geq 1$	12	137	34
$N(\gamma) \geq 1$, $p_{T,\gamma} > 15\,\text{GeV}$	8.1	83	21
Z-reconstruction	7.6	80	21
Higgs-reconstruction	7.3	5.2	1.6

Table 3.1: Signal S and background events for two main processes $t\bar{t}\gamma Z$ and $tjj\gamma Z$ with $Z \to \ell^+\ell^-$ after each requirement to select the semi-leptonic channel for the HL-LHC with $\sqrt{s} = 14\,\text{TeV}$ and $3\,\text{ab}^{-1}$. For the backgrounds, a cut of $p_{T,\gamma} > 10\,\text{GeV}$ and $|\eta_\gamma| < 4$ is imposed at the generator level.

enhancement [214] from $t\bar{t}Zj$ contribution. We thus arrive at a total of $S = 186\,\epsilon_S \approx 25$ and $B = 1.5 \times 1862\,\epsilon_{B_{\text{irred}}} \approx 27$, including now realistic analysis cuts and losses due to overlapping final state particles. This result agrees well with our first estimate. Considering the statistical error of $\Delta B = \sqrt{B} \approx 5$, we thus expect to establish a signal from the total rate alone with a significance $S/\sqrt{B} \approx 5\,\sigma$ at a single experiment. Employing a more precise definition of the discovery significance given by $Z = \sqrt{2\,[(S+B)\,\log(1+S/B) - S]}$, results in a more conservative significance of $Z = 4.3$. This definition converges to $S/\sqrt{B}$ for $S \ll B$ [231]

We expect that the sensitivity can be further enhanced by performing a likelihood analysis of the peaked signal over the smoothly falling background, and thus a discovery should be feasible in this channel. An example is performed in Sec. 4.3, with details laid out in App. B. As this would add further experimental uncertainties which can only be estimated using a full detector simulation, we decided to stay conservative and not use shape information here.

27 and 100 TeV Colliders Next, we study the channel under consideration at a future 27 TeV (100 TeV) pp collider with $15\,\text{ab}^{-1}$ ($30\,\text{ab}^{-1}$) of integrated luminosity [232, 233]. Here the $t\bar{t}h$ production cross section amounts to 2.9 pb for $\sqrt{s} = 27\,\text{TeV}$ [212] and approximately 33 pb for 100 TeV [234], which were reproduced in our MadGraph simulations. The background of $t\bar{t}Z\gamma$ production features 46 fb (670 fb) at 27 TeV (100 TeV) with $p_{T,\gamma} > 10\,\text{GeV}$ and $|\eta_\gamma| < 4$. For simplicity and better comparability, we use a similar setting and the same reconstruction and selection requirements as for the HL-LHC. We note that these cuts are rather low for the higher center-of-mass energies, but a detailed study of potential future collider settings is beyond the scope of this section. In addition a moderate increase in cuts is expected to have only a mild influence on the obtained results. For the 100 TeV case, we use the FCC_{hh}-card provided through Delphes.

Considering again the $Z \to \ell^+\ell^-$ channel, we obtain the cut-flows shown in Table 3.2. The corresponding $m_{\gamma\ell\ell}$ spectra is shown in the middle and right panels of Fig. 3.1. For both scenarios, the same extrapolation to include all top-decay channels and an enhancement of the background by 50 % as for the HL-LHC, is performed motivated by our previous findings.

	27 TeV, 15 ab^{-1}		100 TeV, 30 ab^{-1}	
Cut	S	B	S	B
Initial	4.4k	47k	112k	1.3M
$N(l) = 3$	539	6.2k	16k	210k
$N(j) \geq 3$, $p_{T,j} > 30$ GeV	344	4.1k	12k	160k
$\not{E}_T > 20$ GeV	322	3.9k	11k	150k
$N(b) \geq 1$	276	3.3k	10k	140k
$N(\gamma) \geq 1$, $p_{T,\gamma} > 15$ GeV	180	2.0k	6.7k	84k
Z-reconstruction	166	1.9k	6.3k	82k
Higgs-reconstruction	160	101	6.1k	3.2k

Table 3.2: Number of signal S and background B events after each of the selection requirements at a 27 TeV or 100 TeV collider, with 3 ab^{-1} and 15 ab^{-1} of luminosity, respectively. For the background, a cut of $p_{T,\gamma} > 10$ GeV and $|\eta_\gamma| < 4$ is imposed at the generator level.

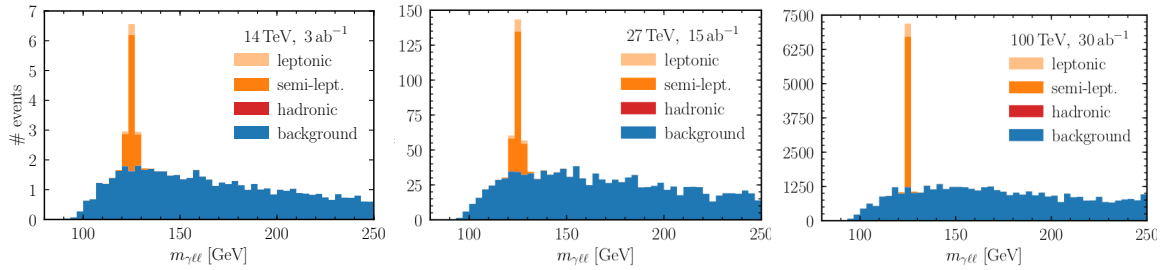

Figure 3.1: Invariant mass spectra for the signal process, stacked on the background distribution (blue) in the considered collider scenarios. The decays of the top-quark pair are separated in hadronic (red, not visible), semi-leptonic (orange) and leptonic (light orange).

3.2.2 Constraints on $\kappa_{Z\gamma}$

In the following, we want to examine the expected constraints that can be set on $\kappa_{Z\gamma}$ from the process under consideration. To that end, we first calculate the predicted number of events $N(\kappa_{Z\gamma}) = S(\kappa_{Z\gamma}) + B$, where $S(\kappa_{Z\gamma})$ is obtained from the SM value $S = 25$ by multiplying with $\kappa^2_{Z\gamma}$, see Eq. (3.17). We further assume the SM to be true and calculate how many standard deviations $\Delta N(\kappa_{Z\gamma})$ away the prediction $N(\kappa_{Z\gamma})$ is from $N(\kappa_{Z\gamma} = 1)$, which is the expected outcome of the experiment. Values of $\kappa_{Z\gamma}$ that lead to a discrepancy of more than n standard deviations are expected to be excluded with a significance of $n\sigma$. Following this procedure for the three considered collider scenarios, the expected 1σ (2σ) constraints on $\kappa_{Z\gamma}$ are thus obtained as

$$\begin{aligned} 14\,\text{TeV}: &\quad 0.86 \leq \kappa_{Z\gamma} \leq 1.14 \quad (0.71 \leq \kappa_{Z\gamma} \leq 1.29) \\ 27\,\text{TeV}: &\quad 0.97 \leq \kappa_{Z\gamma} \leq 1.03 \quad (0.94 \leq \kappa_{Z\gamma} \leq 1.06) \\ 100\,\text{TeV}: &\quad 0.995 \leq \kappa_{Z\gamma} \leq 1.005 \quad (0.991 \leq \kappa_{Z\gamma} \leq 1.009), \end{aligned} \tag{3.18}$$

and presented as red bars in Fig. 3.2.

At the envisaged future hadron colliders, a signal in this low background process could be established at a level well beyond $5\,\sigma$ using the definitions from above. The number of signal

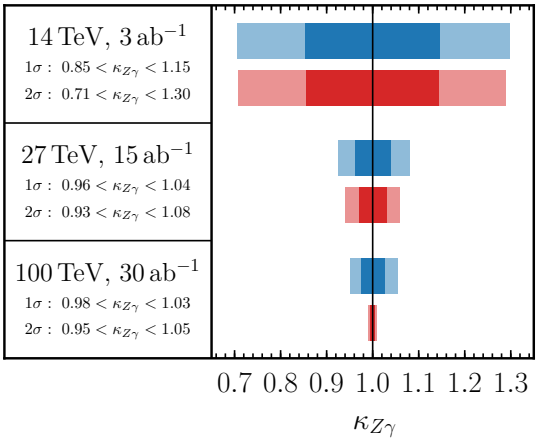

Figure 3.2: $1\,\sigma$ and $2\,\sigma$ limits on $\kappa_{Z\gamma}$, assuming the SM to be true, as obtained from our analysis. Shown are limits with statistical errors only (red) and including a 5 % systematic error from the theory uncertainty in the $t\bar{t}h$ cross section (blue). The numbers in the left column include the 5 % uncertainty.

events clearly allows the determination of the spin or the $\mathcal{CP}$ properties of the Higgs boson, and the performance of precision tests of the effective $hZ\gamma$ coupling at the 1 % level.

At this level of precision, it becomes necessary to take potential systematic errors into account. On the experimental, side there are $\mathcal{O}(1-5\,\%)$ uncertainties related to the lepton, photon and b-jet identification, which could be further reduced by fitting the sidebands of the spectra. Clearly a full experimental analysis is needed to assess these uncertainties and establish the estimated precision. On the theory side, the interpretation of the observed rate as a constraint on $\kappa_{Z\gamma}$ is affected by the uncertainty in $\sigma(pp \to t\bar{t}h)$, which is currently of order 10 % for the LHC. Anticipating progress there, we show in Fig. 3.2 the level of precision obtained, assuming a 5 % systematic error (blue bars) on the production cross section. The projected $1\,\sigma$ ($2\,\sigma$) constraints become

$$\begin{aligned} 14\,\text{TeV}: &\quad 0.85 \le \kappa_{Z\gamma} \le 1.15 \qquad (0.71 \le \kappa_{Z\gamma} \le 1.30) \\ 27\,\text{TeV}: &\quad 0.96 \le \kappa_{Z\gamma} \le 1.04 \qquad (0.93 \le \kappa_{Z\gamma} \le 1.08) \\ 100\,\text{TeV}: &\quad 0.98 \le \kappa_{Z\gamma} \le 1.03 \qquad (0.95 \le \kappa_{Z\gamma} \le 1.05). \end{aligned} \tag{3.19}$$

Our projected sensitivities to $\kappa_{Z\gamma}$ are comparable to those in other Higgs production channels, which are on the order of 10 % (3 − 4 %) at the HL-(HE-)LHC [212].

A further reduction of systematic errors could be achieved if ratios of couplings are considered, such as $\kappa_{Z\gamma}/\kappa_{\gamma\gamma}$ in $t\bar{t}$-associated production. Such ratios are very sensitive to potential new physics patterns. Additional charged fermions coupled to the Higgs, for example, have a stronger effect on $\kappa_{\gamma\gamma}$, since the W boson loop strongly dominates the $h \to Z\gamma$ rate in the SM.

Summary In this section we explored the prospects of discovering the decay of the Higgs to a Z boson plus a photon in $t\bar{t}$-associated production. Focusing the analysis on the semi-leptonic $t\bar{t}$-decay channel, we demonstrated that the considered production channel could lead to a $\sim 5\,\sigma$ discovery already at the HL-LHC. Beyond that, we showed in a concrete example how EFTs allow the interpretation of experimental findings in a general way, by deriving projected

bounds on the effective $hZ\gamma$ coupling. Establishing these limits on $\kappa_{Z\gamma}$ would provide a further contribution to determine the coefficients of the contributing SMEFT operators. Therefore, rather model-independent limits on new physics contributions could be set, and degeneracies in the SMEFT parameter space could be broken up.

At the HL-LHC and proposed pp colliders with 27 TeV and 100 TeV center-of-mass energies, we find $1\,\sigma$ constraints at the 15 %, 4 %, and 2 % level, respectively. The sensitivity is comparable to or even exceeds that of future lepton colliders [235–237]. Finally, the corresponding S/B ratios of $\mathcal{O}(1)$ could potentially allow for precise extractions of the spin and $\mathcal{CP}$ properties of the Higgs boson.

3.3 The Extended DM EFT

Now that we have discussing a new approach to a SM process, and how a precision measurement can potentially constrain SMEFT operators, in this section, a new EFT framework is introduced which is directly linked to BSM physics, namely DM.

The search for DM is tackled by a multitude of experiments operating at largely different energy scales. While DD experiments probe recoil energies in the keV range, the momentum transfer in LHC collisions can exceed the TeV scale. Combining results from such different types of experiments in a single, consistent, yet general framework with as little theory bias as possible, is important in order to make progress in resolving the nature of DM.

As outlined above, DD experiments are usually interpreted in an EFT consisting only of SM fields and a DM candidate, and limits are calculated as bounds on the Wilson coefficients, see e.g. in Sec. 2.2.2 and [47, 185–190]. Mediators between DM and the SM are typically assumed to have masses in the GeV-range, and thus can be safely removed as explicit degrees of freedom. On the other end of probed scales, LHC searches are typically only sensitive to mediator masses at or below the scale of reached momentum transfers, unless the model is very strongly coupled [238]. Thus, the DMEFT description becomes invalid [47–55]. As laid out in the discussion in Chapter 1, collider searches are commonly interpreted in terms of simplified models where the mediator is kept as a dynamical degree of freedom [56, 57, 239–244]. In common implementations, the mediator interacts with SM and DM fields by $D \leq 4$ operators, which are not required to be gauge-invariant and are thus not well-behaved at large energies. A further drawback of these models is that they are rather specific and do not allow for a general description of dark sectors. They also feature a rather limited set of mono-X observables and channels to obtain the relic density. In conclusion, the models suffers either from a lack of generality or, even worse, from a lack of validity.

To alleviate the above problems, in Ref. [245] a hybrid framework was proposed: the so-called extended dark matter effective field theory (eDMEFT). It offers a general setup for the joint interpretation of direct, indirect and various collider searches for DM. It overcomes drawbacks of other model-independent approaches to study the DM phenomenology, such as conventional DMEFT and simplified models. In the eDMEFT, the SM field content is enlarged by a SM-singlet fermion χ,[8] that is stable on cosmological scales and represents the DM candidate, and a (pseudo-)scalar mediator $\mathcal{S}$ ($\tilde{\mathcal{S}}$). The interactions of the mediator with SM fields are realized via higher-dimensional operators. As we will show in the next

[8] While it is also possible to consider scalar DM [245], we focus on fermionic DM, which is a common assumption. In addition, the collider phenomenology is expected to change only mildly [58], and scalar DM is potentially stronger constrained by DD [246].

chapter, in this framework the correct DM abundance can be achieved in several regions of the parameter space. Also, detectable collider cross sections can be obtained without relying on the problematic high-energy tail of kinematic distributions [50, 247], and with setting a cutoff safely above the EW scale.

In contrast to simplified models, the eDMEFT is a proper (order-by-order) renormalizable field theory, where gauge invariance stays intact, and correlations induced by it are included. In addition, stringent, model-dependent connections between different observables can be lifted, which arise in next-generation simplified models such as the 2HDM+S/PS [45, 61, 80], or realistic Z' models [63, 248]. The most general set of higher-dimensional operators allows the incorporation of effects from richer dark sectors, consisting of more than a DM state and a mediator. Interestingly, for fermionic DM, the leading corrections appear already at $D=5$.[9] Compared to the SMEFT, where contributions except the Weinberg operator for neutrino mass arise at $D \geq 6$ [177, 178, 225, 249], this leads to a significantly reduced number of free coefficients.

While including the mediator makes the theory valid at collider energies, the augmentation with $D=5$ operators accounts for the fact that the BSM sector is likely to be non-minimal. Indeed, there is no stringent reason for the latter to consist of only a few different particles, while the SM shows a complex structure. So it is conceivable that the dark sector is rather rich, while both DM and the mediator are significantly lighter than the remaining BSM states, e.g. if the mediator is a (pseudo-)Goldstone boson of a spontaneously broken global symmetry. This justifies the capture of BSM effects via higher-dimensional operators in the eDMEFT.

We will introduce the corresponding effective Lagrangians for a scalar in Sec. 3.3.1 and pseudoscalar mediator in Sec. 3.3.1 and discuss their basic features. A thorough investigation of their phenomenology is presented in Chapter 4, considering the predicted relic abundance as well as present and future constraints from collider, DD and ID searches.

3.3.1 Scalar Mediator

The eDMEFT for (Dirac) fermionic DM χ and a scalar mediator $\mathcal{S}$ is described, at $D \leq 5$, by the Lagrangian [245]

$$\begin{aligned}
\mathcal{L}_{\text{eff}}^{\mathcal{S}\chi} =& \mathcal{L}_{\text{SM}} + \tfrac{1}{2}\partial_\mu \mathcal{S} \partial^\mu \mathcal{S} - \tfrac{1}{2}\mu_S^2 \mathcal{S}^2 + \bar{\chi} i \partial\!\!\!/ \chi - m_\chi \bar{\chi}\chi \\
&+ \lambda'_{S1} v^3 \mathcal{S} - \frac{\lambda'_S}{2\sqrt{2}} v \mathcal{S}^3 - \frac{\lambda_S}{4} \mathcal{S}^4 - \lambda'_{HS}\, v |H|^2 \mathcal{S} - \lambda_{HS}\, |H|^2 \mathcal{S}^2 \\
&- y_S\, \mathcal{S}\, \bar{\chi}_L \chi_R - \frac{y_\chi^S\, \mathcal{S}^2 + y_\chi^H |H|^2}{\Lambda}\, \bar{\chi}_L \chi_R + \text{h.c.} \\
&- \frac{\mathcal{S}}{\Lambda} \left[c_{\lambda S}\, \mathcal{S}^4 + c_{HS}\, |H|^2 \mathcal{S}^2 + c_{\lambda H}\, |H|^4 \right] \\
&- \frac{\mathcal{S}}{\Lambda} \left[\left(Y_d^S\right)^{ij} \bar{Q}_L^i H d_R^j + \left(Y_u^S\right)^{ij} \bar{Q}_L^i \tilde{H} u_R^j + \left(Y_\ell^S\right)^{ij} \bar{L}_L^i H \ell_R^j + \text{h.c.} \right] \\
&- \frac{\mathcal{S}}{\Lambda} \left[C_{BB}^S\, B_{\mu\nu} B^{\mu\nu} + C_{WW}^S\, W^{I\mu\nu} W^I_{\mu\nu} + C_{GG}^S\, G^{a\mu\nu} G^a_{\mu\nu} \right],
\end{aligned} \tag{3.20}$$

where, $\mathcal{L}_{\text{SM}}$ is the renormalizable SM Lagrangian and $H = \frac{1}{\sqrt{2}}(0,\, v+\varphi)^T$ the SM Higgs doublet in the unitary gauge, with the vev $v = 246\,\text{GeV}$.

[9] The generalization to a vector mediator requires $D=6$ operators. We will leave a study of the very rich phenomenology for future work.

Moreover as before, Q_L, u_R and d_R (L_L and l_R) denote the left- and right-handed quarks (leptons), while the field-strength tensors of the SM gauge groups before EWSB are written as $B_{\mu\nu}$, $W^I_{\mu\nu}$ and $G^a_{\mu\nu}$. The generic mass-suppression scale of the higher-dimensional operators is parametrized by Λ, and each operator is associated with a coefficient that fixes its interaction strength. We note that Λ should not be included when counting the number of free parameters since it always appears in combination with the coefficients. We assume that $\mathcal{S}$ does not develop a vev and remain agnostic about the origin of the new physics scale. A stabilizing symmetry for χ forbids the $L\tilde{H}\chi_R$ term to prevent it from acting like a right handed neutrino.

Clearly this Lagrangian is not limited to a description of DM, and a scalar-singlet extended SMEFT forms a subset of the eDMEFT. While here the focus lies on the implications for DM, a recent study of the EFT for a pure scalar singlet extension can be found in Ref. [250], see also [251–255] for earlier works on the singlet-extended SMEFT.

In this section we will comment on the terms that will be most relevant for the phenomenology studied in the next section. There are already new physics contributions at $D \leq 4$. Of particular interest among them are the $\mathcal{S}\bar{\chi}\chi$ Yukawa term, coupling DM to the mediator, and the interactions between $\mathcal{S}$ and H. Together these interactions provide a minimal gauge-invariant connection between DM and the SM. In addition, there are numerous higher-dimensional operators that couple SM fields to the dark sector. These can be separated into three broad subgroups:

First, there are new physics extensions of the SM Yukawa sector that couple $\mathcal{S}$ to SM fermions in combination with H. Allowing the most general flavor structure leads to a large number of operators of this type. Unless stated otherwise, we will therefore assume the matrices $Y^S_{d,\,u,\,\ell}$ to be diagonal in the basis of SM Yukawa couplings

$$\begin{aligned}
\left(Y^S_u\right)^{ij} &\to \text{diag}\left(y^S_u,\, y^S_c,\, y^S_t\right) \\
\left(Y^S_d\right)^{ij} &\to \text{diag}\left(y^S_d,\, y^S_s,\, y^S_b\right) \\
\left(Y^S_\ell\right)^{ij} &\to \text{diag}\left(y^S_e,\, y^S_\mu,\, y^S_\tau\right)
\end{aligned} \tag{3.21}$$

in order to avoid the insurgence of dangerous flavor violation. Motivated by minimal-flavor-violation (MFV) [256], we further impose that our diagonal Yukawa-like matrices reproduce the hierarchy of the SM-fermion masses, and thus follow the relation $y^S_f \sim m_f/v$.

Next, the $\mathcal{S}^2\bar{\chi}\chi$ and $|H|^2\bar{\chi}\chi$ terms appear structurally very similar, but have very different phenomenological consequences. While the first mediates an additional interaction of DM with $\mathcal{S}$ that might change the dynamics within the new physics sector, the second term provides a direct link between DM and the SM circumventing the mediator $\mathcal{S}$ completely.

There are also effective couplings between $\mathcal{S}$ and the SM gauge bosons. Typically, interactions of this kind arise at the one-loop level in theories with additional matter fields, charged under the SM gauge group. With this general concept of UV completions in mind, we extract the loop factor and gauge coupling from the corresponding Wilson coefficients

$$\begin{aligned}
C^S_{GG} &= \frac{1}{16\pi^2}\, g_s^2\, c^S_G \\
C^S_{BB} &= \frac{1}{16\pi^2}\, g'^2\, c^S_B \\
C^S_{WW} &= \frac{1}{16\pi^2}\, g^2\, c^S_W.
\end{aligned} \tag{3.22}$$

In the parameter scans in the next section, we will typically use $c^S_{G,B,W}$, as they should naturally be of $\mathcal{O}(1)$. Moreover, for the phenomenological study presented in the next section, it is convenient to use the linear combinations that correspond to effective couplings with the physical states W^+W^-, ZZ, $Z\gamma$ and $\gamma\gamma$. They read

$$\begin{aligned} C^S_{W^+W^-} &= 2\, C^S_{WW} \\ C^S_{ZZ} &= c_W^2\, C^S_{WW} + s_W^2\, C^S_{BB} \\ C^S_{Z\gamma} &= 2\, c_W s_W \left(C^S_{WW} - C^S_{BB}\right) \\ C^S_{\gamma\gamma} &= s_W^2\, C^S_{WW} + c_W^2\, C^S_{BB}. \end{aligned} \tag{3.23}$$

Finally, DM could couple to the field-strength tensor of the hypercharge gauge boson via two $D=5$ interactions: $C_\mathrm{m}/\Lambda\ \bar{\chi}_L \sigma_{\mu\nu} \chi_R\, B^{\mu\nu}$, and $C_\mathrm{el}/\Lambda\ \bar{\chi}_L \sigma_{\mu\nu}\gamma_5 \chi_R\, B^{\mu\nu}$. Below the EW scale, they reduce to the well-known magnetic and electric dipole operators [257, 258]. This kind of operators are strongly constrained by DD experiments, and for $m_\chi = 100\,\mathrm{GeV}$ the non-observation of DM-nucleus scattering requires $C_{\mathrm{m(el)}}/\Lambda \lesssim 10^{-6}\,(10^{-9})\,\mathrm{GeV}^{-1}$ [259, 260]. For DM masses larger than a few GeV, this bounds exceed the sensitivity of other experimental probes by orders of magnitude. Thus, considering those operators in isolation rules out the parameter space preferred by the relic density [260]. For this reason, and since we are mainly interested in the phenomenology associated with the mediator $\mathcal{S}$, we do not include them in our analysis.

Higgs-Mediator Mixing Before illustrating the DM phenomenology for the eDMEFT with a scalar mediator in the next chapter, we briefly review a well known effect of $D=4$ operators, namely the Higgs-mediator mixing induced by the λ'_{HS} term.

After EWSB, the trilinear coupling λ'_{HS} induces an off-diagonal contribution in the scalar mass matrix which leads to mixing between the SM Higgs field, φ, and the mediator $\mathcal{S}$. This mixing can be described by a rotation matrix

$$\begin{pmatrix} h \\ S \end{pmatrix} = \begin{pmatrix} \cos\theta & \sin\theta \\ -\sin\theta & \cos\theta \end{pmatrix} \begin{pmatrix} \varphi \\ \mathcal{S} \end{pmatrix}, \tag{3.24}$$

where h and S denote the physical mass eigenstates. The mixing angle θ is defined by

$$\tan 2\theta = \frac{2\lambda'_{HS} v^2}{M^2_\varphi - M^2_\mathcal{S}}, \tag{3.25}$$

where M_φ and $M_\mathcal{S}$ denote the masses of the scalar fields in the absence of mixing. The masses of the physical states are then given by

$$m^2_{h/S} = \frac{M^2_\varphi + M^2_\mathcal{S}}{2} \pm \frac{M^2_\varphi - M^2_\mathcal{S}}{2\cos 2\theta}. \tag{3.26}$$

We identify h with the SM-like Higgs with $m_h = 125\,\mathrm{GeV}$ and do not make any assumptions about the ordering of the scalar mass eigenstates. The mixing in combination with the DM Yukawa y_S will generate a coupling between the dark and the SM sector described by the Lagrangians

$$\begin{aligned} \mathcal{L}^\mathrm{mix}_\mathrm{SM} &= (c_\theta h - s_\theta S) \left[\frac{2M_W^2}{v}\, W^+_\mu W^{-\mu} + \frac{M_Z^2}{v}\, Z^\mu Z_\mu - \sum_f \frac{m_f}{v}\, \bar{f} f \right], \\ \mathcal{L}^\mathrm{mix}_\mathrm{DM} &= -\,(s_\theta h + c_\theta S)\, y_S\, \bar{\chi}\chi, \end{aligned} \tag{3.27}$$

as well as a Lagrangian with trilinear couplings between the scalar fields

$$\mathcal{L}_{\text{scal}}^{\text{mix}} = -\frac{v}{2}\left[\kappa_{hhh}\, h^3 + \kappa_{hhS}\, h^2 S + \kappa_{hSS}\, h S^2 + \kappa_{SSS}\, S^3\right]. \tag{3.28}$$

The explicit results for the couplings k_{ijk} can be directly derived:

$$\begin{aligned}
\kappa_{hhh} &= 2\lambda_H c_\theta^3 + 2\lambda'_{HS} c_\theta^2 s_\theta + \tfrac{\lambda'_S}{\sqrt{2}} s_\theta^3 + \lambda_{HS} s_\theta s_{2\theta} \\
\kappa_{hhS} &= -2 s_\theta^3 \lambda_{HS} + (\tfrac{3}{\sqrt{2}}\lambda'_S - 4\lambda'_{HS}) s_\theta^2 c_\theta - (6\lambda_H - 4\lambda_{HS}) s_\theta c_\theta^2 + 2\lambda'_{HS} c_\theta^3 \\
\kappa_{hSS} &= 2 c_\theta^3 \lambda_{HS} + (\tfrac{3}{\sqrt{2}}\lambda'_S - 4\lambda'_{HS}) c_\theta^2 s_\theta + (6\lambda_H - 4\lambda_{HS}) c_\theta s_\theta^2 + 2\lambda'_{HS} s_\theta^3 \\
\kappa_{SSS} &= \tfrac{\lambda'_S}{\sqrt{2}} c_\theta^3 - 2\lambda_{HS} c_\theta^2 s_\theta - 2\lambda_H s_\theta^3 + \lambda'_{HS} s_\theta s_{2\theta},
\end{aligned} \tag{3.29}$$

where $c_\theta \equiv \cos\theta$, $s_\theta \equiv \sin\theta$ for brevity.

The mixing represents a special case, since it can be realized only with renormalizable interactions. Since those are not suppressed by the scale of the higher-dimensional operators, Λ, it is natural to assume that they will generically dominate over effects that arise at $D=5$. However, the LHC Higgs measurements severely constrain these kind of interactions [261, 262]. We will therefore treat mixing and effective operators on the same footing, and include both in our analysis.

3.3.2 Pseudoscalar Mediator

After introducing and discussing the scalar mediator case, we will now turn to the case where the SM is connected to the dark sector via a pseudoscalar mediator. While sharing basic features with the scalar model, the changed $\mathcal{CP}$-properties of the mediator leads to striking phenomenological differences in a number of observables. The eDMEFT Lagrangian for fermionic DM χ and a pseudoscalar mediator $\tilde{\mathcal{S}}$ reads [245]

$$\begin{aligned}
\mathcal{L}_{\text{eff}}^{\tilde{\mathcal{S}}\chi} =& \mathcal{L}_{\text{SM}} + \tfrac{1}{2}\partial_\mu \tilde{\mathcal{S}} \partial^\mu \tilde{\mathcal{S}} - \tfrac{1}{2}\mu_{\tilde{\mathcal{S}}}^2 \tilde{\mathcal{S}}^2 + \bar{\chi} i \partial\!\!\!/ \chi - m_\chi \bar{\chi}\chi \\
& - \tfrac{1}{4}\lambda_{\tilde{\mathcal{S}}} \tilde{\mathcal{S}}^4 - \lambda_{H\tilde{\mathcal{S}}} |H|^2 \tilde{\mathcal{S}}^2 \\
& - i y_{\tilde{\mathcal{S}}} \tilde{\mathcal{S}}\, \bar{\chi}_L \chi_R - \frac{y_\chi^{\tilde{\mathcal{S}}} \tilde{\mathcal{S}}^2 + y_\chi^H |H|^2}{\Lambda}\, \bar{\chi}_L \chi_R + \text{h.c.} \\
& - \frac{\tilde{\mathcal{S}}}{\Lambda}\left[i\big(Y_d^{\tilde{\mathcal{S}}}\big)^{ij} \bar{Q}_L^i H d_R^j + i\big(Y_u^{\tilde{\mathcal{S}}}\big)^{ij} \bar{Q}_L^i \tilde{H} u_R^j + i\big(Y_\ell^{\tilde{\mathcal{S}}}\big)^{ij} \bar{L}_L^i H \ell_R^j + \text{h.c.}\right] \\
& - \frac{\tilde{\mathcal{S}}}{\Lambda}\left[C_{BB}^{\tilde{\mathcal{S}}}\, \tilde{B}_{\mu\nu} B^{\mu\nu} + C_{WW}^{\tilde{\mathcal{S}}}\, \tilde{W}^{I\mu\nu} W_{\mu\nu}^I + C_{GG}^{\tilde{\mathcal{S}}}\, \tilde{G}^{a\mu\nu} G_{\mu\nu}^a \right].
\end{aligned} \tag{3.30}$$

The notation follows the conventions detailed in the previous section, and we adopt a similar rescaling as in Eq. (3.22) between $C_{VV}^{\tilde{\mathcal{S}}}$ and $c_V^{\tilde{\mathcal{S}}}$. Due to the assumption of $\mathcal{CP}$-conservation, the operator $|H|^2\tilde{\mathcal{S}}$ is forbidden. We assume again that $\tilde{\mathcal{S}}$ does not develop a vev. Therefore, the SM Higgs φ and the mediator $\tilde{\mathcal{S}}$ do not mix, and they are equal to their mass eigenstates h and $\tilde{S}$. As another consequence, Higgs precision measurements are less sensitive to this model.

The effective Higgs portal operator $|H|^2\bar{\chi}_L\chi_R$ does not depend on $\tilde{\mathcal{S}}$ (or $\mathcal{S}$) and thus can also be included in the pseudoscalar model. In order to work out the differences between the scalar and the pseudoscalar eDMEFT, and since the strength of y_χ^H is rather constrained, we restrict our analysis to $y_\chi^H = 0$ in the pseudoscalar case. The results are similar to the ones

obtained in the scalar model. For analogous reasons we will neglect the $y_\chi^{\tilde{S}}$ coupling, since the corresponding operator does not distinguish the $\mathcal{CP}$-even versus $\mathcal{CP}$-odd nature of the mediator.

Matching the 2HDM+PS The eDMEFT with a pseudoscalar mediator can be connected to the 2HDM+PS discussed in Chapter 2. To show this, and the operator subset of the Lagrangian in Eq. (3.30) generated by a UV-complete model, we exemplarily perform the tree-level matching of the 2HDM+PS to the eDMEFT.

To separate the SM Higgs doublet from the second doublet, we work in the Higgs basis with the $\mathbb{Z}_2$ symmetric potential defined in Eq. (2.12). Using the technique laid out in Sec. 3.1.3, the second Higgs doublet Φ_H is integrated out by employing its equation of motion at zero momentum. For this approximation to be valid, we assume its mass scale to be far above the EW scale, $\hat{M}_{HH} \gg v$. The equation of motion for Φ_H for the interaction potential in Eqs. (2.16) and (2.29), taking only operators linear in Φ_H into account, reads

$$\begin{aligned}\hat{M}_{HH}^2\,\Phi_H =& \mu_{P12}\, i\, P\, \Phi_h - \hat{\lambda}_{hHP}\, P^2\, \Phi_h \\ &- \left((Y_H^u)_{ij}^*\, \bar{u}_R^i \epsilon Q_L^j + (Y_H^d)_{ij}^*\, \bar{d}_R^i Q_L^j + (Y_H^\ell)_{ij}^*\, \bar{\ell}_R^i L_L^j \right).\end{aligned} \tag{3.31}$$

We note that this approach is appropriate only if the mixing angle $\sin\theta \sim \mu_{P12}$ between the $\mathcal{CP}$-odd states A and P is not too large in the 2HDM+PS after EWSB. We thus write $\mu_{P12} = \lambda_{P12} M$, requiring $M/\Lambda \equiv \varepsilon_M < 1$, as also suggested by perturbative unitarity. In the eDMEFT, P is identified with $\tilde{\mathcal{S}}$. Moreover, the mass scale of the heavy doublet is identified with the cutoff, $\hat{M}_{HH} = \Lambda \gg v$ [197, 263]. Solving Eq. (3.31) for Φ_H, and inserting it back into the original Lagrangian in Eq. (2.26) gives rise to the effective Lagrangian. At $D=4$ it contains higher order corrections to the Higgs-portal, and at $D=5$ it contains the effective Yukawa operators

$$\begin{aligned}\mathcal{L}_{\text{P2HD}}^{(4)} &= \left(-\hat{\lambda}_{hhP} + \lambda_{P12}^2 \varepsilon_M^2 \right) P^2\, \Phi_h^\dagger \Phi_h \\ \mathcal{L}_{\text{P2HD}}^{(5)} &= \frac{i \lambda_{P12} \varepsilon_M}{\Lambda}\, P \left((Y_H^u)_{ij}\, \bar{Q}_L^i u_R^j \widetilde{\Phi}_h + (Y_H^d)_{ij}\, \bar{Q}_L^i d_R^j \Phi_h + (Y_H^\ell)_{ij}\, \bar{L}_L^i \ell_R^j \Phi_h + \text{h.c.} \right).\end{aligned} \tag{3.32}$$

To translate the coefficients from the Higgs basis to the interaction basis, we employ Eqs. (2.17) and (2.18) for $\hat{\lambda}_{hhP}$ and $\sin\theta$. With them, we obtain the matching results for a 2HDM+PS of type II (for other types t_β is replaced according to Table 2.1)

$$\begin{aligned} y_t^{\tilde{\mathcal{S}}} &= \frac{\mu_{P12}}{\Lambda}\, Y_{H,33}^u = \lambda_{P12} \epsilon_M Y_{H,33}^u = \frac{m_A^2 - m_{\tilde{\mathcal{S}}/a}^2}{2vM}\, \frac{y_t^{\text{SM}}}{t_\beta}\, \epsilon_M \sin(2\theta), \\ \lambda_{H\tilde{\mathcal{S}}} &= c_\beta^2 \lambda_{P1} + s_\beta^2 \lambda_{P2} - \lambda_{P12}^2\, \varepsilon_M^2. \end{aligned} \tag{3.33}$$

We used the covariant derivative expansion [197] for matching at one-loop-level. We found no new operators which are phenomenology important and corrections to already existing ones can be safely neglected due to the stronger suppression.

While first numerical results in the mono-h channel confirm the EFT validity for $\Lambda \gtrsim 1.5\,\text{TeV}$, the corresponding cross sections are far below the current exclusion limits. Therefore, we leave detailed numerical tests of the matching validity for future work. As a consequence, it would be interesting to consider more complex dark sectors containing for instance additional vector-like quarks. Those could enhance the desired cross sections, and give rise to some of the effects discussed in the next chapter.

Chapter 4

Phenomenology of the eDMEFT

After introducing the eDMEFT as a potential next step in the evolution of effective models for DM searches, we extensively explore its phenomenological aspects in this chapter.

In the first half, constraints on the general eDMEFT parameter space considering the predicted relic abundance, present and future DD and ID experiments, as well as collider searches are discussed. Besides mono-jet searches for DM, we take Higgs precision measurements and resonance searches for the mediator into account, including vector-boson, di-jet, and di-Higgs final states. We determine viable areas in the parameter space for the scalar and pseudoscalar mediator and identify regions where cancellations in the DD cross section appear. These cancellations can lead to allowed regions for the scalar mediator that could be missed in a simplified-model approach. Those regions are present in the eDMEFT and could result in LHC discoveries.

To further demonstrate the flexibility of the eDMEFT, we investigate two slightly modified scenarios in the second half of the chapter. In the first scenario, the mediator together with the first fermion generation are charged under an additional $\mathbb{Z}_2$-symmetry. This symmetry gets spontaneously broken by the vev of the mediator. Thereby, this symmetry assignment could provide a mechanism to generate small masses for the first fermion generation, and would strongly suppress the usual $\mathcal{S}\bar{\chi}\chi$ interaction. The bi-quadratic term $\mathcal{S}^2\bar{\chi}\chi$ would be allowed, and could lead to interesting di-fermion plus $\not{E}_T$ signatures at current and future colliders. For the second scenario, we further extend the setup with a second $\mathbb{Z}_2$ symmetry and an associated mediator motivated by generating neutrino masses. In this setup, it is possible to characterize the excess in low energy electron recoil events recently announced by the XENON1T collaboration. We consider the scattering of DM and neutrinos on electrons, and find that the neutrino option leads to a significantly better fit. The preferred parameter region is then confronted with several constraints, which can be circumvented by appropriate choices of parameters, and a non-trivial thermal history of the universe.

In detail, this chapter is organized as follows. Starting with the scalar eDMEFT, we survey its astrophysical DM phenomenology in Sec. 4.1.1, and provide expressions for relevant cross sections. In Sec. 4.1.2, the collider observables listed above are discussed and exclusions from the mono-jet final state are given. Consequently, we systematically explore the eDMEFT parameter space in an increasing level of complexity in Sec. 4.1.3, taking into account all relevant constraints discussed so far. We start with simple, portal-like subsets of the higher-dimensional operators, which then are extended by additional effective interactions. Finally, the full eDMEFT parameter space is approached with generic scans. The analysis is repeated for a pseudoscalar mediator in Sec. 4.2 with a similar structure. Sections 4.1 and 4.2 closely follow Ref. [264]. In Sec. 4.3, we investigate the scenario of the mediator being charged under a $\mathbb{Z}_2$-symmetry; following Ref. [265]. Limits from the di-fermion+$\not{E}_T$ final state are derived for the (HL-)LHC in Sec. 4.3.1 and for CLIC in Sec. 4.3.2. The reported XENON1T excess is

addressed in Sec. 4.4; following Ref. [266]. After laying out the setup in Sec. 4.4.1, we present fits to the excess in Sec. 4.4.2 and the considered constraints in Sec. 4.4.3, and summarize our findings in Sec. 4.5.

4.1 Scalar Mediator

We start exploring the phenomenological variety of the eDMEFT with the case of a scalar mediator. With the expressions from Sec. 3.3.1 and the Lagrangian in Eq. (3.20) at hand, we will scrutinize the spanned parameter space in an increasing order of complexity. To this end, we will first briefly review astrophysical and collider bounds on the DM properties and how they manifest themselves in the eDMEFT. For first insights into the framework under consideration we identify simple portals to the dark sector and complete them with additional effective operators. This can lead to viable regions in parameter space through cancellations in DD, which would be missed in simplified models. We then combine all experimental constraints in general parameter scans to unfold the full strength of the eDMEFT.

4.1.1 Dark Matter Phenomenology

Besides parameterizing DM searches, the aim of the eDMEFT is to provide guidelines towards consistent models of DM. Therefore, it is essential to consider general DM properties, and to investigate how they can be realized in this framework. To this end, and to help interpreting later results, this section revisits the annihilation cross sections for the relic density and ID, as well as constraints from DD. Here, first crucial differences to simplified models will appear.

Relic Density Throughout this work, we assume that the DM was produced by thermal freeze-out. An approximate condition to generate the correct relic density is a thermally averaged annihilation cross section $\langle\sigma v\rangle \approx 2\times10^{-26}\text{cm}^3\text{s}^{-1} \equiv \sigma_v^0$ [267]. A number of channels can contribute to the total annihilation rate, the dominant ones are briefly discussed hereafter. In addition, approximate results for the cross sections are given in the velocity expansion $\langle\sigma v\rangle \approx a + b\, v_\chi^2$, in order to build up some intuition for the most relevant contributions. The velocity expansion is not a reliable approximation in some phenomenologically relevant regimes, e.g. around the pole $m_\chi \simeq m_S/2$ [268]. For the actual analyses, the freeze-out equations are solved numerically with micrOmegas [269, 270], and we do not rely on analytic estimates.

The DM can annihilate into SM fermions, f, through s-channel exchange of the mediator S or the SM Higgs h. The effective operator induced cross sections scale as $(y_S\, y_f^S\, v/\Lambda)^2$ or $(y_\chi^H\, y_f\, v/\Lambda)^2$, where y_f is the corresponding SM Yukawa coupling. Neglecting the Higgs portal interaction and scalar mixing via λ'_{HS}, the leading contribution in the velocity expansion is

$$\begin{aligned}\langle\sigma v\rangle_{ff} &\approx \frac{N_c}{8\pi}\frac{v^2}{\Lambda^2}\frac{y_S^2\left(y_f^S\right)^2 m_\chi^2}{\left(m_S^2-4m_\chi^2\right)^2}\, v_\chi^2 \qquad (4.1)\\ &\approx \begin{cases} 2.5\times10^{-3}\,\sigma_v^0 N_c\left(\frac{3\,\text{TeV}}{\Lambda}\right)^2\left(\frac{m_\chi}{100\,\text{GeV}}\right)^2\left(\frac{500\,\text{GeV}}{m_S}\right)^4\left(y_S\, y_f^S\right)^2, & m_\chi \ll \frac{m_S}{2}\\ 0.1\,\sigma_v^0 N_c\left(\frac{3\,\text{TeV}}{\Lambda}\right)^2\left(\frac{100\,\text{GeV}}{m_\chi}\right)^2\left(y_S\, y_f^S\right)^2, & m_\chi \gg \frac{m_S}{2}, \end{cases}\end{aligned}$$

where $v_\chi^2 \approx 0.1$ is used for the numerical estimates throughout this section.

If the coefficients C_{VV}^S, with $V = G$, B, W, or y_χ^H are sizable, the DM can also annihilate into gauge bosons, through s-channel exchange of S or h. Taking the annihilation into gluons as an example, the cross section for that case can be estimated as

$$\begin{aligned}\langle\sigma v\rangle_{gg} &\approx \frac{1}{\pi\Lambda^2}\frac{\left(C_{GG}^S\right)^2 y_S^2\, m_\chi^4}{\left(m_S^2-4m_\chi^2\right)^2}\, v_\chi^2 \\ &\approx \begin{cases} 3.2\times10^{-3}\,\sigma_v^0\left(\frac{3\,\text{TeV}}{\Lambda}\right)^2\left(\frac{m_\chi}{100\,\text{GeV}}\right)^4\left(\frac{500\,\text{GeV}}{m_S}\right)^4\left(\frac{\alpha_S c_G^S}{4\pi}\right)^2 y_S^2, & m_\chi \ll \frac{m_S}{2} \\ 0.1\,\sigma_v^0\left(\frac{3\,\text{TeV}}{\Lambda}\right)^2\left(\frac{\alpha_S c_G^S}{4\pi}\right)^2 y_S^2, & m_\chi \gg \frac{m_S}{2}. \end{cases}\end{aligned} \tag{4.2}$$

From the equations above, we see that the annihilation cross section into gluons remains in general below the thermally favored value, unless a rather low scale and sizable couplings enhance the annihilation rate considerably.

For DM heavier than the scalars, the hh, hS and SS annihilation channels become kinematically allowed. These are particularly interesting since they can be realized at $D=4$, and the cross sections are therefore not suppressed by $1/\Lambda^2$. For example, the minimal contribution to the annihilation into the SS final state is given by

$$\langle\sigma v\rangle_{SS} \approx \frac{3}{64\pi}\frac{y_S^4}{m_\chi^2}\, v_\chi^2 \approx 87.5\,\sigma_v^0\left(\frac{100\,\text{GeV}}{m_\chi}\right)^2 y_S^4 \quad \text{for } m_S \ll m_\chi. \tag{4.3}$$

The annihilation into the other scalar states can also be realized without higher-dimensional operators. However, the cross sections are proportional to powers of s_θ, which is small due to the constraints from Higgs physics.

Finally, an intriguing new option arises due to the presence of y_χ^S, which enables the annihilation into mediator pairs without inducing s-channel interactions of DM with SM particles. Thus, DD bounds can be avoided even in the presence of sizable values for C_{VV}^S, y_f^S or λ'_{HS}. For $m_S \ll m_\chi$, the corresponding annihilation cross section is approximately given by

$$\langle\sigma v\rangle_{SS} \approx \frac{1}{64\pi}\left(\frac{y_\chi^S}{\Lambda}\right)^2 v_\chi^2 \simeq 3.2\times10^{-2}\,\sigma_v^0\left(\frac{3\,\text{TeV}}{\Lambda}\right)^2\left(y_\chi^S\right)^2. \tag{4.4}$$

Even though this contribution is naturally suppressed by m_χ^2/Λ^2 relative to the one from $\mathcal{S}\bar\chi\chi$, it can dominate the annihilation channels for $y_S < 1$, $\Lambda = \mathcal{O}(1\,\text{TeV})$, and $y_\chi^S = \mathcal{O}(1)$.

For all annihilation channels, the first non-zero term in the velocity expansion of the thermally averaged cross section is p-wave, meaning $\langle\sigma v\rangle \sim v_\chi^2$. This leads to a generic suppression of the DM annihilation cross section, since $v_\chi^2 \approx 0.1$ at freeze-out. Hence, obtaining the observed relic density requires larger couplings than in the s-wave case.

Another important aspect is the overall scaling of the annihilation cross sections with $1/\Lambda^2$, with the notable exception of the SS final state. The cutoff suppression originates from the coupling of DM with the Higgs boson, or of S with SM fermions or gauge bosons. This represents a relevant difference between the eDMEFT and simplified models [56–59]. In the former case, a gauge-invariant construction imposes a Higgs insertion, or mixing between the scalar mediator and the Higgs. Both variants imply a suppression factor for the couplings of S with SM fermions, proportional to v/Λ or the mixing angle s_θ. In contrast, simplified models frequently consider arbitrary couplings between the mediator and SM fermions limited

only by perturbativity. This has relevant phenomenological implications since it implies that the simplified models allow for artificially larger annihilation cross sections of DM into SM fermions, than an appropriately applied EFT.

Direct Detection As mentioned in Sec. 2.2.2 severe constraints on scalar mediated DM arise from DD experiments, which are mostly sensitive to SI scattering of DM on nucleons. Those interactions are induced by diagrams with a t-channel exchange of h or S between DM and the constituents of the nucleons, namely quarks and gluons. The SI cross section for DM-proton scattering can be written as

$$\sigma_{\chi p}^{\mathrm{SI}} = \frac{\mu_{\chi p}^2}{\pi} \frac{m_p^2}{\Lambda^2} \left[\sum_{q=u,d,s,c,b,t} f_q^p \left(\frac{g_{H\chi\chi} g_{Hqq}}{m_h^2} + \frac{g_{S\chi\chi} g_{Sqq}}{m_S^2} \right) - \frac{2\, g_{S\chi\chi} c_G^S}{9 m_S^2}\, f_{TG} \right]^2 , \tag{4.5}$$

where $\mu_{\chi p}$ is the reduced mass of the DM-proton system and m_p the proton mass. Here, generic expressions are used for the couplings of h and S with pairs of DM and SM quarks. In the absence of mixing between the scalars, they simply read $g_{H\chi\chi} = y_\chi^H$, $g_{S\chi\chi} = y_S$, $g_{Hqq} = 1$ and $g_{Sqq} = y_q^S v/(\sqrt{2} m_q)$, while becoming more complicated in the presence of mixing. The parameters f_q^p are the structure functions of the proton with $f_c^p = f_b^p = f_t^p = \frac{2}{27} f_{TG}$ and $f_{TG} = 1 - \sum_{q=u,d,s} f_q^p$ with adopted default assignations of micrOmegas [269, 270]. The cross section for scattering on neutrons can be obtained by replacing m_p with the neutron mass, and substituting the appropriate values for the structure functions f^n, instead of f^p in Eq. (4.5).

The terms in the SI cross section in Eq. (4.5) feature a relative minus sign. Therefore, destructive interference between the different contributions is possible. A perfect cancellation leads to a so-called blind spot in which DD experiments are unable to probe the dark sector. While blind spots are known in the DM literature, so far they have been found when combining different types of mediators [271–274]. Also in the eDMEFT in the case of pure mixing, a natural blind spot arises at $m_S = m_h$. In the eDMEFT a new type of blind spots are present, caused by different operators featuring only one mediator. It is instructive to consider the conditions for the occurrence of such blind spots for simple cases. If the mediator couples only with gluons and top quarks via their effective operators to the SM, a blind spot arises for

$$c_G^S = \frac{y_t^S\, v}{3\sqrt{2}\, m_t}. \tag{4.6}$$

In the case in which the couplings of S with the SM quarks are exclusively induced by mixing with the Higgs, the blind spot condition is slightly more complicated, and given by

$$c_G^S = \sqrt{2}\, \frac{f_u^p + f_d^p + f_s^p + \frac{2}{27} f_{TG}}{f_{TG}}\, \frac{\Lambda}{v}\, \frac{\left(m_h^2 - m_S^2\right) c_\theta s_\theta}{m_h^2 c_\theta^2 - m_S^2 s_\theta^2}. \tag{4.7}$$

Blind spots can also be realized in more general scenarios but the analytic conditions become complicated and do not add significantly to the understanding. Therefore, we do not report them explicitly but note that they are considered in the numerical analysis.

Indirect Detection In order to assess potential implications of ID for the DM properties of the eDMEFT, the velocity expansion of the annihilation cross section is of great interest. The typical velocity of DM in astrophysical structures today is $\mathcal{O}(10^{-3})$ whereas the typical

velocity at freeze-out is ~ 0.3. Consequently, higher-order terms in the velocity expansion are strongly suppressed nowadays, and only s-wave annihilations lead to a rate in the ballpark of the canonical cross section for a thermal relic of $\langle\sigma v\rangle \approx 2 \times 10^{-26}\,\mathrm{cm}^3/\mathrm{s}$. As explained above, the relevant DM annihilation channels in the scalar eDMEFT have velocity-dependent annihilation cross sections. Therefore, the impact of ID constraints for a scalar mediator is expected to be marginal, and will not be considered in the following.

4.1.2 Collider Signals

Now that we have reviewed bounds related to astrophysics and cosmology, we summarize collider searches with potential impact on the extended particle content. Obtaining a valid collider phenomenology has been among the main motivations for the development of the eDMEFT.

The framework is characterized by different collider signatures, whose relative relevance depends on the values of the effective couplings and the mass hierarchy. Most of these signatures are associated to the resonant production and subsequent decay of the mediator, S. Taking the MFV-inspired ansatz detailed above for the $D=5$ couplings of S with the SM quarks, the main production channels of the new mediator are via Higgs-mixing, or via gluon fusion with the effective coupling c_G^S, or via y_t^S induced top-loops. The case of gluon fusion can be approximated by Eq. (2.40) with $i = gg$. The decay width of S to gluons via the effective contact interaction is given by

$$\Gamma(S \to gg) = \frac{2\, m_S^3}{\pi \Lambda^2} \left(\frac{\alpha_s c_G^S}{4\pi} \right)^2 , \tag{4.8}$$

while the contribution from quark loops (dominated by the top) is given by

$$\Gamma(S \to gg) = \frac{\alpha_s^2}{16\pi^3} \frac{v^2}{\Lambda^2}\, m_S \sum_q \left(y_q^S\right)^2 F_S(\tau_{q,S}) , \tag{4.9}$$

where $\tau_{q,S} = 4m_q^2/m_S^2$, and the loop function F_S is given in Eq. (A.9) [139, 275]. The Higgs-mixing case is obtained by the replacement $y_q^S v/\Lambda \to y_q^{\mathrm{SM}} \sin\theta$. In the presence of sizable c_B^S and c_W^S couplings, vector-boson fusion (VBF) production would also be possible but is not explicitly explored here.

After production, the particle S can decay into four classes of final states: (i) DM pairs $\chi\bar{\chi}$; (ii) SM fermion pairs $f\bar{f}$; (iii) gauge boson pairs VV; (iv) di-Higgs hh. The DM pair production processes can be tagged only if accompanied by additional radiation. In our study we will mainly focus on mono-jet events, as the emission of gluons or quarks from the initial state provide the strongest constraints [61, 75]. Interesting correlations might be probed by exploring mono-Higgs signals [245]. In addition the bi-quadratic portal y_χ^S can give rise to interesting di-jet+$\not{E}_T$ signatures and is discussed in more detail in Sec. 4.3. While being out of reach of current LHC runs, they can potentially be probed in upcoming collider experiments. Besides from ISR, mono-Z events could originate from dimension six operators with an additional momentum dependence and cutoff suppression, which are beyond the truncation of the eDMEFT.

In order to obtain bounds for the eDMEFT, simulations for the mono-jet final state are needed to rederive the limits obtained Ref. [77]. To this end, we implemented the eDMEFT

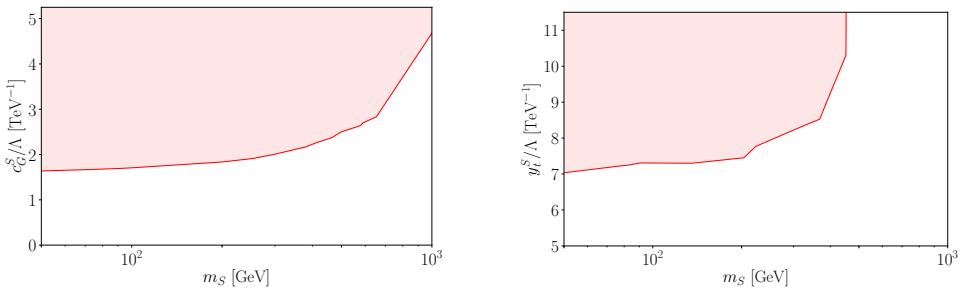

Figure 4.1: Exclusion limits from the ATLAS mono-jet search [77] in the m_S–c_G^S (left) and m_S–y_t^S plane (right), normalized to Λ. In both cases $y_S = 1$, $m_\chi = 10\,\text{GeV}$, and all other couplings are equal to zero.

setup in the event generator MadGraph5_aMC@NLO 2.6.3 [140].[1] The simulated events have been processed through CheckMATE 2.0.26 [135, 228, 229, 276, 277], linked with PYTHIA 8.1 [278, 279] for the parton showering, and Delphes 3 [148] for a fast detector simulation employing the mono-jet search performed by ATLAS in 2017 [77]. A k-faktor $\mathcal{K}_{gg} = 1.5$ is taken into account which is known from Higgs production to describe the NLO QCD corrections for scalar masses in the range of $100 - 1000\,\text{GeV}$ in good approximation [280]. In this search, twenty signal regions binned in terms of the missing transverse energy $\not{E}_T$ are defined. To ensure the EFT validity only "exclusive signal regions" (EM) with $\not{E}_T < 500\,\text{GeV}$ are considered. We find that for most values of m_S EM4, with $\not{E}_T = (400 - 500)\,\text{GeV}$, gives the strongest constraints of all bins, while ensuring the validity of the eDMEFT for $\Lambda \gtrsim 1\,\text{TeV}$. Therefore, we stick to it, which also avoids additional fluctuation due to changes of the signal region.

For illustration, Fig. 4.1 shows the exclusion limits from mono-jet searches as function of the mediator mass for a fixed value of $m_\chi = 10\,\text{GeV}$, assuming that the mediator exclusively couples to top quarks via the y_t^S Yukawa portal (right panel) or to gluons through the effective c_G^S portal (left panel). The choice of DM mass does not harm the generality of the results, since we have verified that the experimental sensitivity is basically independent of m_χ as long as it is below the threshold at $m_S \sim 2\,m_\chi$. For heavier DM, no robust constraints can be derived since the required couplings would violate perturbativity. The exclusion limits can be expressed in terms of the dimensional ratios c_G^S/Λ and y_t^S/Λ. We find that, even for $m_\chi < m_S/2$ the region of parameter space which can be probed through current mono-jet searches is rather limited — typically allowing only $\mathcal{O}(1)$ couplings to be tested. In addition, the sensitivity for y_t^S/Λ decreases significantly for $m_S \geq 2\,m_t$ due to the growing partial width of S to tops, suppressing the $\text{BR}(S \to \chi\bar{\chi})$, as shown in the right panel of Fig. 4.1.

If the coupling y_χ^H is non-zero, or the mass mixing between S and h is sizable, DM pairs can also be produced from Higgs decays. Limits have been determined through Higgs-to-invisible searches; for recent reviews see e.g. Refs [110, 132, 281]. Hence they are effective only for $m_\chi \leq m_h/2$; see Ref. [110] for a discussion of possible prospects for $m_\chi > m_h/2$, and Sec. 2.1.3 for the case of light mediators. In the following we use the analysis [130] performed by ATLAS, combining the 7–8 TeV and 13 TeV data sets and different signal topologies leading to the limit of $\text{BR}(h \to \chi\bar{\chi}) < 0.26$. We note that the new limit of $\text{Br}(h \to \chi\bar{\chi}) < 0.11$ presented in [132] does not change our findings significantly. Here the improvement is mainly driven by a new search in VBF production [131].

[1] We only simulated events with the emission of one hard jet.

Concerning category (ii), under the assumption of a MFV like structure for the dimension-five couplings of S with the SM fermions, we do not expect sizable signals at colliders from decays induced by this couplings. In particular, the current limits from $t\bar{t}$ resonance searches [151,282] are too weak to constrain the range of couplings considered here. Once compatibility with measurements of the Higgs signal strengths is required, the prospects for direct searches of this category are similarly poor in the case of mixing between h and S.

Moving to category (iii), the most promising searches are those for EW gauge boson pairs. For our study we have applied the latest results from searches for W^+W^-, ZZ [283–285] and diphoton [286,287] resonances[2]. We remark that while a sizable diphoton signal relies basically on the presence of $D=5$ couplings of the scalar mediator with gauge bosons, a detectable WW/ZZ signal can also be generated in presence of non-negligible h–S mixing. As pointed out in e.g. [262], WW/ZZ searches provide the strongest constraints on the mixing angle, θ, for $m_S > m_h$. In addition to EW gauge boson pair signatures we also consider limits from dijet searches [290] possibly originating from the decay of the resonance into gluon pairs. All these constraints will be implemented when exploring the eDMEFT parameter space in the next section.

Finally, the last category of signals from S decays, the hh final states, arises for sizable values of λ_{HS}, and thus in the presence of significant h–S mixing. We consequently include in our analysis limits on di-Higgs production considering the final states: $4b$ [291,292], $bbWW$ [293], $bb\tau\tau$ [294], $\gamma\gamma WW$ [295] and $\gamma\gamma bb$ [296]. A combination of the individual constraints has been given in [297,298].

The collider searches just illustrated are sensitive mostly to heavy masses of the mediator, namely above the mass of the SM Higgs. Since we also consider the case of a light mediator, we include bounds from searches for a low mass Higgs at LEP [299,300] as well as constraints from b-physics [301,302]. Furthermore, we have imposed that the sum of $\mathrm{BR}(h \to SS)$ and $\mathrm{BR}(h \to \chi\bar{\chi})$ does not exceed the constraint on the Higgs-to-invisible width.

4.1.3 Combined Results

After discussing several sources of constraints we will apply them systematically to the parameter space of the eDMEFT. The general Lagrangian in Eq. (3.20) includes three new mass scales m_χ, m_S, and Λ and several new couplings. In order to avoid an excessively high dimensionality of the parameter space, the following simplifying assumptions have been adopted, unless differently stated.

First, the scalar couplings λ_S, λ'_S, λ_{HS} and the $D=5$ terms of the potential $c_{\lambda S}$, c_{HS}, $c_{\lambda H}$ are set to zero, since they are expected to have a negligible impact on the analysis. As already pointed out, we will adopt a flavor-diagonal ansatz for the $D=5$ couplings of S to SM fermions, following $y_f^S = c_S\, y_f$. Similarly, a single free parameter $c_G^S = c_B^S = c_W^S = c_V^S$ describing the $D=5$ couplings of the mediator with gauge bosons is typically assumed. Further, we will neglect the effective Higgs–DM interaction $\sim y_\chi^H$ for most of the analysis, since it is independent of S, well studied, and strongly constrained by DD. In summary the considered parameter space of the eDMEFT is spanned by $(m_\chi,\, m_S,\, y_S,\, \lambda'_{HS},\, c_S,\, c_V^S,\, y_\chi^S)$.

The following analysis will go through three steps with increasing degree of complexity. At the beginning, we will consider four basic portals which can be obtained from the eDMEFT by setting most of the couplings to zero. Since a lot of results for these portals are already

[2] In principle searches for $Z\gamma$ resonances should also be considered. However, most recent analyses [288,289] only consider scalar resonance with masses above 1 TeV and these high values are not part of our analysis.

present in the literature, the following paragraph should be seen as a brief review. The next step will consist of studying in more detail some benchmarks for a Higgs-mixing portal scenario augmented with the presence of $D=5$ couplings of S with gauge bosons. This will represent a first illustration of the strength of the eDMEFT and will provide some insights into the interplay of the different operators. Finally, a systematic analysis of the full parameter space of the model will be presented. In order to assess the robustness of the main results we will relax some of the assumptions mentioned above, and comment on their impact.

Four Basic Portals in Isolation The eDMEFT implies four basic portals between DM and the SM, each corresponding to subsets of operators of the Lagrangian in Eq. (3.20). These portals emergie via:

1. S–Higgs mixing: $\mathcal{L} \subset -y_S S\,\bar{\chi}\chi - \lambda'_{HS} v |H|^2 S$
2. the effective Yukawa operator: $\mathcal{L} \subset -y_S S\,\bar{\chi}\chi - c_S\, y_f \frac{v}{\Lambda}\, S\,\bar{f} f$
3. the effective gauge operator: $\mathcal{L} \subset -y_S S\,\bar{\chi}\chi - \frac{C^S_{VV}}{\Lambda}\, S\, V^{\mu\nu} V_{\mu\nu}, \quad V = G,\, W,\, B$
4. the effective Higgs–DM operator: $\mathcal{L} \subset -\frac{y^H_\chi}{\Lambda}\, |H|^2\, \bar{\chi}\chi,$

where the Higgs field is set to its vev for the effective Yukawa portal. These portals in isolation have been considered in the literature and received substantial attention in recent years. Before summarizing their main properties, we remind that the eDMEFT uplifts these portals to a complete $D=5$ field theory, besides being agnostic about the origin of operators. This includes for example the bi-quadratic $S^2\bar{\chi}\chi$ term discussed in Sec. 4.3. It thereby allows to capture a large class of DM scenarios as well as new cancellation patterns in DD emerging non-trivially in the full EFT.

Some of the generic features of the mixing portal have been discussed in Sec. 3.3.1, more details can be found in e.g. [110, 303]. In this setup the dark Yukawa operator $S\bar{\chi}\chi$ is combined with the mixing between S and h induced by the scalar potential. It is noteworthy that this connection between the DM and the SM is realized by renormalizable interactions. Therefore, the strength of this potential is not controlled by the scale of the higher-dimensional operators and could potentially be rather large. However, the mixing is limited by Higgs measurement as discussed in the previous section. Very roughly the bound can be approximated as $s_\theta \leq 0.2$ in substantial parts of the parameter space. This is comparable with the generic suppression of higher-dimensional operators that feature a Higgs field, $v/\Lambda \sim 0.25$, for $\Lambda \sim 1\,\text{TeV}$. We refrain from linearizing the effects of mixing, and always take the full diagonalization of the fields into account.

The effective Yukawa portal combines the renormalizable $S\bar{\chi}\chi$ interaction with a $D=5$ coupling of the scalar mediator to a pair of SM quarks. It corresponds to a realization of the not gauge invariant, simplified models for a scalar mediator coupled to fermionic DM [56, 57, 241, 242, 304].

Analogous the effective gauge portal connects $S\bar{\chi}\chi$ to the SM via an effective interaction of S with the gauge field strength tensors. This kind of interaction is actually present in the simplified Yukawa portal, where it arises at the one-loop level from couplings of the scalar mediator with (mostly) two top quarks and plays a relevant role in its collider phenomenology [241, 242]. Alternatively, the $SG_{\mu\nu}G^{\mu\nu}$ vertex can for example be generated in models with heavy vector-like fermions, e.g. studied in [138, 305–308]. We remain agnostic about its origin here.

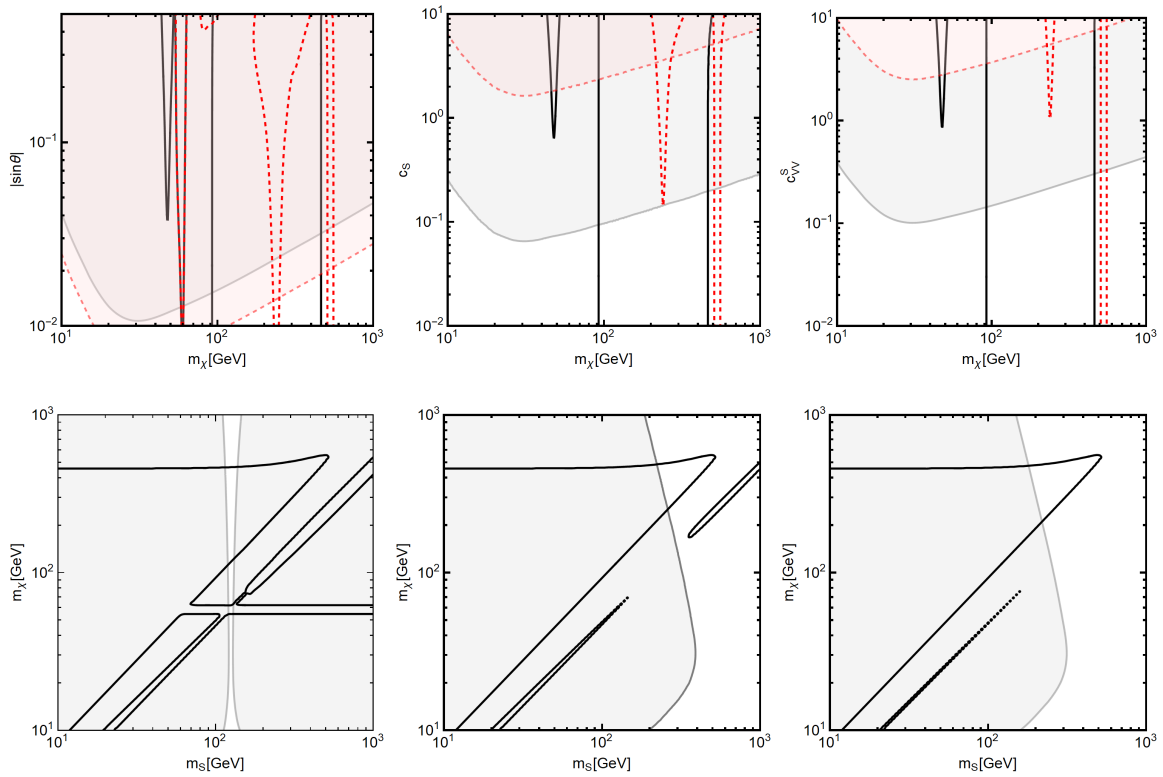

Figure 4.2: Isocontours of the correct relic abundance for the mixing (left), Yukawa (center), and gauge (right) portal for $y_S = 1$. The upper panels display the m_χ–coupling plane for $m_S = 100\,\text{GeV}$ (black, solid) and $m_S = 500\,\text{GeV}$ (red, dashed). In the case of the mixing portal, the y-axis is $|\sin\theta|$ instead. The lower row shows the m_S–m_χ plane for $\sin\theta = 0.1$, $c_S = 1$ and $c_V^S = 1$, respectively. Limits from XENON1T are given as light red (gray) shaded regions for a light (heavy) mediator. In all cases we have set $\Lambda = 3\,\text{TeV}$.

Finally, the effective Higgs portal is distinct since it does not involve the new scalar mediator and has only two free parameters, namely y_χ^H/Λ and m_χ. Since there is only one coupling, the relic density is tightly connected with the DD rate. Values of y_χ^H leading a successful thermal freeze out are excluded by the strong constraints from DD; see Refs. [110, 303, 309] for an in-depth discussion. Therefore, we will not consider it further.

We will review the DM phenomenology of the portals in the following. The well-known features of the first three portals are visualized in Fig. 4.2, which displays isocontours corresponding to the observed relic density as well as DD constraints in the coupling–m_χ plane (upper row) for fixed $m_S = 100\,\text{GeV}$ (black) and $m_S = 500\,\text{GeV}$ (red), as well as in the m_S–m_χ plane (lower row) for fixed values of $\sin\theta = 0.1$, $c_S = 1$, and $c_V^S = 1$, for the mixing, Yukawa and gauge portal respectively.

As can be seen the correct relic density is typically achieved only for special kinematic configurations. A noticeable region is represented by the resonance at $m_\chi \approx m_S/2$, corresponding to a strong dip in the relic density curves in the upper panels of Fig. 4.2 and the rightmost diagonal lines in the lower panels. Then, the correct relic density can be achieved at the opening of the annihilation channel $\chi\bar{\chi} \to S^2$ at $m_\chi \approx m_S$, the so-called secluded regime [310, 311]. In

the secluded regime, the relic density depends only weakly on the couplings between S and the SM and is therefore characterized by the almost vertical lines close to the threshold in the upper panels of Fig. 4.2 and the left diagonal in the lower panels. The annihilation into S^2 can also account for the correct relic density when m_χ is considerably higher than m_S, see Eq. (4.3) Hence, a second vertical line is present in the upper row of Fig. 4.2 corresponding to the nearly horizontal lines in the lower one. In addition, the annihilation cross sections receive an enhancement at $m_\chi \approx m_h/2$ in portals which lead to a direct coupling of DM and h, such as the Higgs-mixing portal, shown in left column of Fig. 4.2.

Limits from DD play the most important role in determining whether a model with a real scalar mediator is viable or not. The scattering of the DM with nuclei is induced by three different types of interactions with the SM in the various portals. It is then worth considering the interplay of the individual interactions with the relic density. As can be seen in the lower row of Fig. 4.2, the DD constraints resulting from XENON1T, depicted by the shaded regions, are most constraining for low mediator masses and relax somewhat for $m_S \geq 200\,\text{GeV}$ in the effective Yukawa and gauge portals. In case of the Higgs mixing the softening of the constraints for large scalar masses is less pronounced since the pure Higgs contribution is not directly sensitive to m_S and then dominates the DD cross section. However, fixing a value for $\sin\theta$ while varying m_S as shown in the lower left plot corresponds to changing parameters in the scalar potential. In general, the contributions from Higgs and S exchange interfere destructively such that an unconstrained region at $m_h \approx m_S$ shows up. In all considered models the DM abundance relies on annihilation with velocity suppressed cross sections such that ID searches are not relevant.

Completing Simplified Models with EFT After reviewing the simple DM–SM portals in isolation, we move to more complex scenarios unfolding the strength of the eDMEFT. To this end, we will start with the case of the Higgs mixing portal completed with the effective couplings of S with the SM gauge bosons. As already discussed, this setup may allow for the presence of blind spots in DD and, consequently, potentially relax the strong bounds found in the simple portal case. To the end of this paragraph we will also show results for the combination of the effective gauge and Yukawa couplings.

In the discussion of the two scenarios we will focus on three selected benchmarks, which are identified by specific assignments of the $(m_\chi,\, m_S)$ pair, namely $(80,\, 200)\,\text{GeV}$, $(225,\, 500)\,\text{GeV}$ and $(500,\, 300)\,\text{GeV}$. For each of the considered benchmarks we will compare the different DM and, where relevant, collider constraints in the λ'_{HS}–y_S, or c_S–y_S plane, respectively, for three values of $c_V^S = 0,\, 1,\, 5$ and fixed $\Lambda = 3\,\text{TeV}$.

The first benchmark is characterized by relatively low values of $m_\chi = 80\,\text{GeV}$ and $m_S = 200\,\text{GeV}$, and is displayed in the upper row of Fig. 4.3. With $m_\chi > m_h/2$ Higgs-to-invisible searches have no impact on this benchmark. Nevertheless, due to the small value of m_S, values of $\lambda'_{HS} \gtrsim 0.2$ are excluded by constraints on Higgs mixing. Furthermore, current LHC searches of resonances decaying into visible products are not effective for this low value of m_S. On the contrary, for $c_V^S = 5$ a part of the viable region for the relic density is excluded by the mono-jet search [77]. Another notable feature is that the presence of the effective coupling c_V^S has only a modest impact on the relic density since $m_\chi < m_W$. Thus, the corresponding isocontours are similar for the three considered assignments of c_V^S. The relic density is driven by annihilation into SM fermions, mostly $b\bar{b}$, with a modest s-channel enhancement since the DM mass is not too close to the pole at $m_S/2$. This requires rather high values of y_S to comply with the

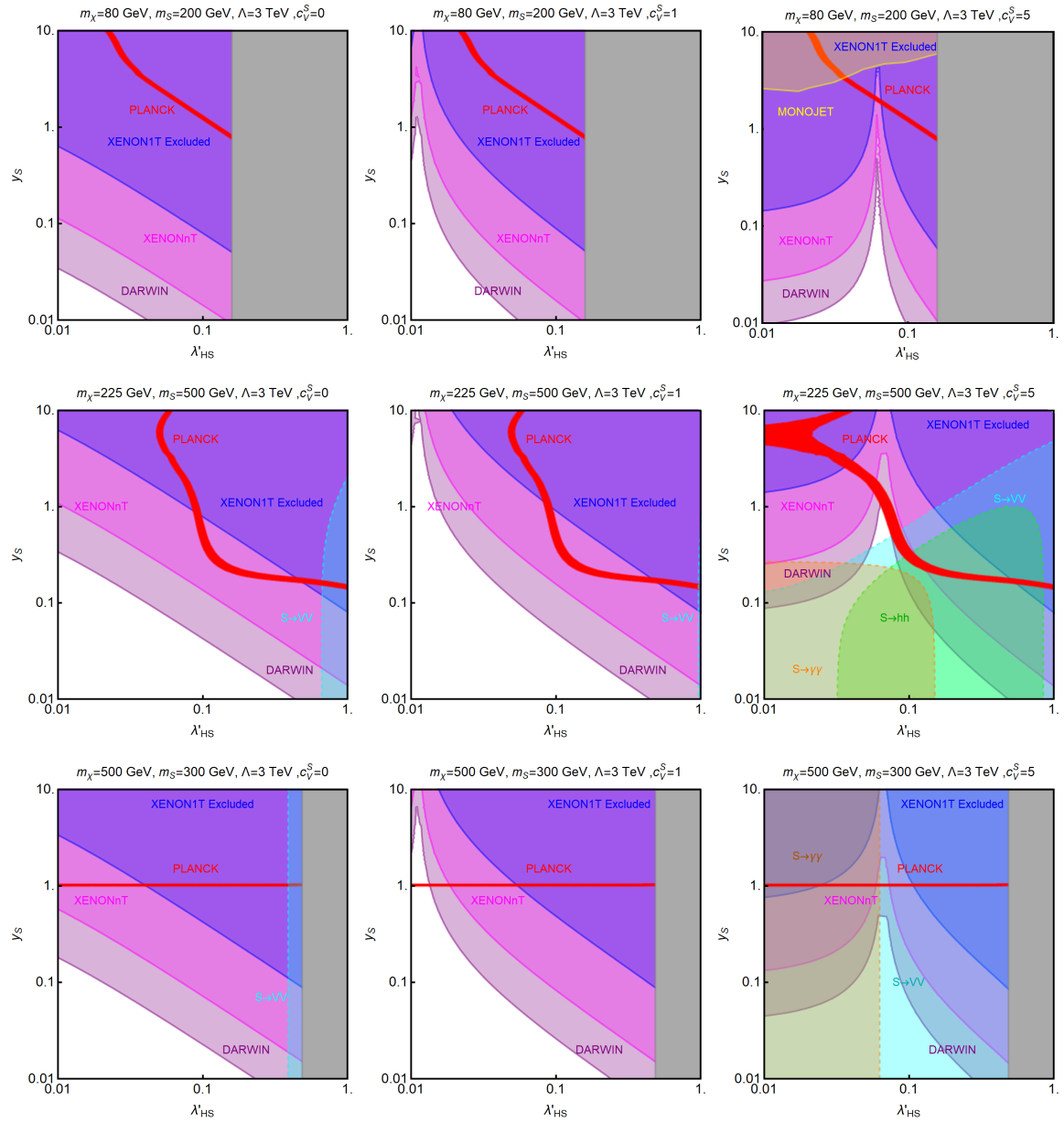

Figure 4.3: Summary of constraints for the mixing portal completed with effective mediator-gauge boson interactions. The results are shown in the λ'_{HS}–y_S plane for $c_V^S = 0, 1, 5$ and three (m_χ, m_S) assignations as indicated in the individual panels. The red contours correspond to the correct relic density while the blue regions are excluded by DD, as given by XENON1T, and the magenta (purple) regions represent the projected sensitivities of XENONnT (DARWIN). The regions excluded by Higgs signal strengths are depicted in gray. Green, cyan, and orange regions are excluded by collider searches for resonances decaying into SM Higgs pairs, massive gauge bosons, and photons, respectively. The latter bounds rely on the assumption of a common parameter c_V^S for the couplings with gauge bosons, and could be lifted by setting c_B^S, $c_W^S \ll c_G^S$. The yellow region in the top right plot is excluded by mono-jet searches.

correct relic density. While for c_V^S equal to zero or one this benchmark is ruled out by current bounds from XENON1T, for $c_V^S = 5$ a small window remains open where a DD blind spot can occur along the relic density isocontour. This already rather small stripe will soon be reduced substantially if DM signals at the next generation of DD experiments remain absent — or might allow for a potential discovery.

Our next benchmark with $m_\chi = 225\,\text{GeV}$ and $m_S = 500\,\text{GeV}$ is explored in the second row of Fig. 4.3 and represents a scenario with m_χ close to the pole at $m_S/2$. Contrary to the previous benchmark, large values of c_V^S do have a significant impact on the relic density since it is very sensitive to the total width of the scalar mediator. Given also the occurrence of the blind spot, we notice that the viable region of parameter space for $c_V^S = 5$ is wider with respect to the two other assignments. A small portion of parameters evade even the projected constraints from the future DARWIN experiment. On the other hand our choice of m_S renders this benchmark sensitive to collider experiments. The colored regions represent the exclusions from the various searches mentioned in the previous section. As evident, searches for diboson final states are most effective, and their exclusions are indicated by the cyan regions in the plots. This is because the cross section $\sigma(pp \to S \to WW/ZZ)$ can be substantial both for sizable values of $\sin\theta$, induced by $\lambda_{HS}^{'}$, and for large values of $c_{B,W}^S$. The high value of m_S makes mono-jet searches inefficient, compare Fig. 4.1.

The last studied benchmark corresponds to $m_\chi = 500\,\text{GeV}$ and $m_S = 300\,\text{GeV}$, and is summarized in the bottom row of Fig. 4.3. In all three panels the correct relic density is determined by a basically constant $\mathcal{O}(1)$ value of y_S. This reflects the fact that it is obtained in the secluded regime [310, 311], hence fixed via the $\chi\bar{\chi} \to S^2$ annihilation process. In consequence, the relic density is entirely set by parameters of the dark sector, m_χ, m_S, and y_S. The coupling c_V^S affects the DM phenomenology by changing the position of the blind spot, therefore determining the range of $\lambda_{HS}^{'}$ for which even future DD constraints can be evaded. On the other hand, for large values of $c_V^S \sim 5$ this benchmark is ruled out by collider bounds, and those from diboson searches are dominant again.

Indeed the collider constraints strongly rely on the assumption of a universal coefficient c_V^S for all gauge boson couplings, and lifting this assumption would allow to evade them. Considering for example c_B^S, $c_W^S \ll c_G^S$ would remove the bounds from diboson searches but keep those from DD which are sensitive to c_G^S. In the secluded regime this would further open an interesting window at moderate values of $\lambda_{HS}^{'}$, which could evade projected XENONnT exclusions via destructive interference between different operators, but would become testable at DARWIN, as shown in the bottom right panel of Fig. 4.3.

To facilitate the understanding of the more general results discussed in the next paragraph, in particular the cancellations in DD, we express the results concerning the combined DM and collider constraints in the $\lambda_{HS}^{'}$–c_V^S plane for $y_S = 1$ in Fig. 4.4. The two benchmarks $(m_\chi, m_S) = (225, 500)\,\text{GeV}$ (left panel) and $(500, 300)\,\text{GeV}$ (right panel) show a clear blind spot in DD due to the interplay of c_V^S and S-Higgs-mixing via $\lambda_{HS}^{'}$, as given in Eq. (4.7). The case $m_\chi = 80\,\text{GeV}$, $m_S = 200\,\text{GeV}$ is not shown, since it does not allow for the correct relic density. The right panel of Fig. 4.4 does not show a relic density isocontour since the DM abundance is determined entirely by the annihilation process $\chi\bar{\chi} \to S^2$, which depends on y_S. We also notice a non-trivial interplay between $\lambda_{HS}^{'}$ and c_V^S regarding the shape of the excluded regions from diboson searches emerging for c_V^S larger than one. In particular for both c_V^S, $\lambda_{HS}^{'} \sim O(1)$ a destructive interference can be present between the different contributions to the production process of the resonance.

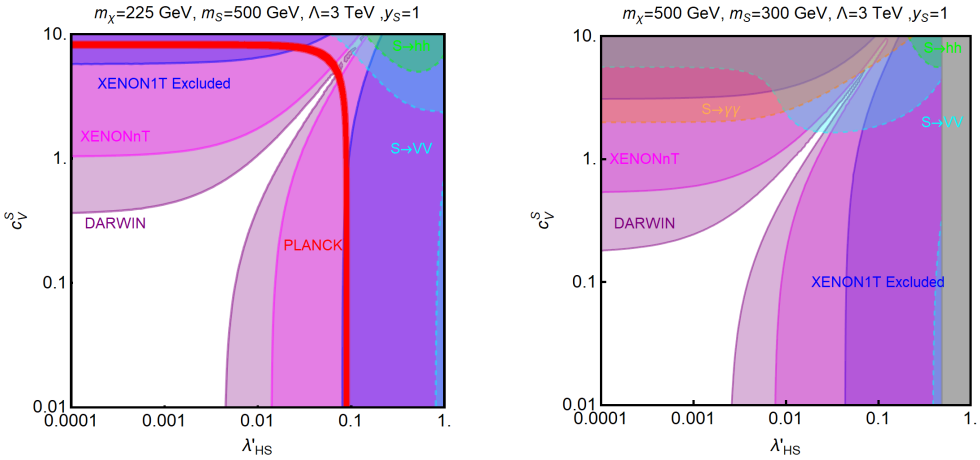

Figure 4.4: Summary of constraints in the λ'_{HS}–c_V^S plane for the benchmarks in the second and third row of Fig. 4.3, employing the same color code. In the right panel the relic density can be obtained in the whole region with a suitable choice of y_S. The case $m_\chi = 80\,\text{GeV}$, $m_S = 200\,\text{GeV}$ is not shown, since it does not allow for the correct relic density.

Before moving to the systematic survey of the parameter space, we consider a different combination of portals in Fig. 4.5, turning on the $D = 5$ Yukawa and gauge portals with non-vanishing couplings c_S and c_V^S, while setting the h–S mixing to zero. We stick to the same benchmark masses as in Fig. 4.3, excluding the case of $(m_\chi, m_S) = (80, 200)\,\text{GeV}$, since here the correct relic density cannot be achieved. We notice again the occurrence of blind spots, and a globally weaker impact from DD constraints, because the SM Higgs does no longer act as a mediator. Conversely, the lower branching ratio of S into massive gauge bosons makes the bounds from diphoton resonance searches stronger. They cover the region of small y_S, where also the decay width to DM is small, and therefore act complementarily to DD.

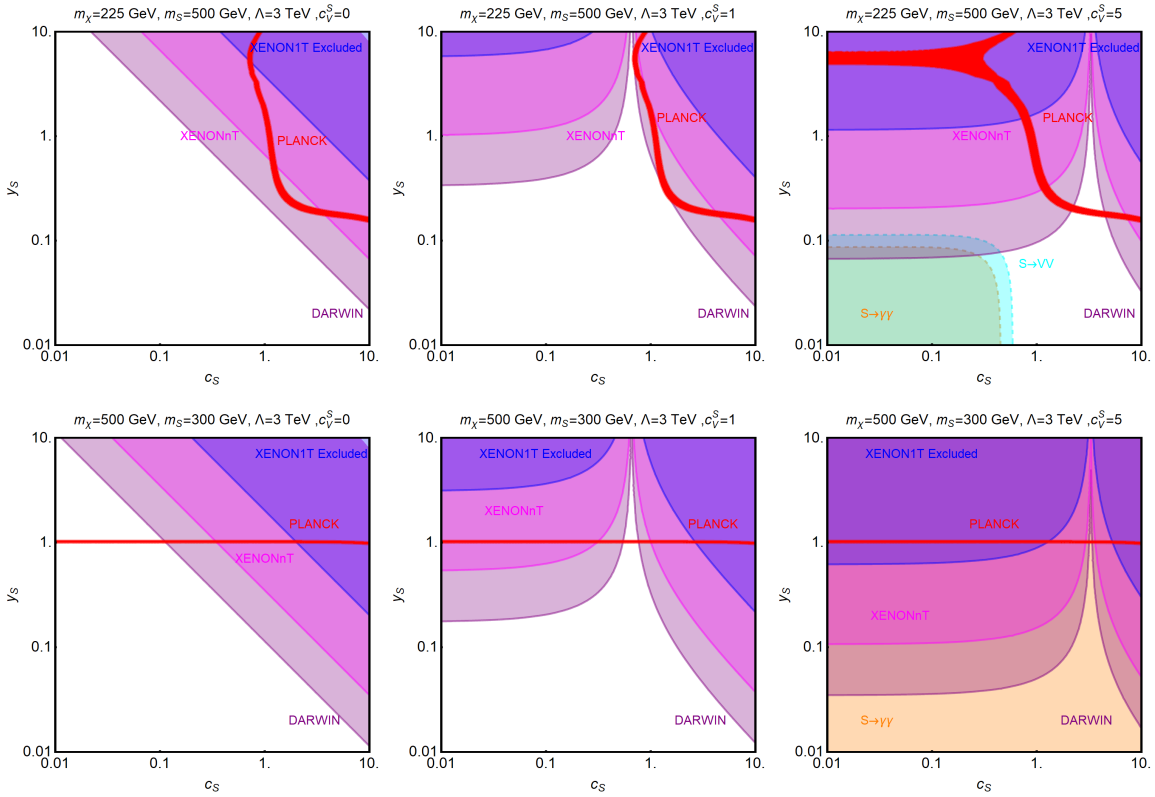

Figure 4.5: Summary of constraints in the c_S–y_S plane and setting the h–S mixing to zero for the benchmark masses from the second and third row of Fig. 4.3 with the same color code. The case $m_\chi = 80\,\text{GeV}$, $m_S = 200\,\text{GeV}$ is not shown, since it does not allow for the correct relic density.

Generic Parameter Scan We finally survey the full eDMEFT. As discussed in detail in this paragraph, important quantitative differences will emerge between the full eDMEFT and the simplified model cases discussed above. Especially new allowed regions in parameter space will open up, even surviving the projected XENONnT constraints. To this end, we perform a scan considering the simultaneous presence of all parameters identified at the beginning of this section. With the mentioned restrictions and for fixed $\Lambda = 3\,\text{TeV}$ the considered ranges are:

$$\begin{aligned} m_\chi &\in [10, 1000]\,\text{GeV} \\ m_S &\in [10, 1000]\,\text{GeV} \\ \lambda'_{HS} &\in [10^{-4}, 1] \\ y_S &\in [10^{-2}, 10] \\ c_S &\in [10^{-2}, 10] \\ c_V^S &\in [10^{-2}, 10] \\ y_\chi^S &\in [10^{-2}, 10]. \end{aligned} \tag{4.10}$$

For each obtained configuration, we compute a comprehensive set of observables. We consider the relic density, the SI scattering cross section for DD, the Higgs-to-invisible width, the LHC mono-jet rate, and the production cross sections of the diboson resonances listed above. In addition, we apply the general bound on the mixing between the SM Higgs and a real scalar singlet as determined e.g. in Refs. [262, 312].

In Fig. 4.6 the results of the analysis are shown, where the points found in the scan are projected into the m_S–m_χ (upper left), m_S–c_V^S (upper right), m_S–$|\sin\theta|$ (bottom left), and m_S–c_S planes (bottom right). The color code identifies three sets of parameters

- green: account for the correct relic density but excluded otherwise;
- orange: allowed by the relic density and DD but excluded by collider constraints;
- blue: satisfy all constraints.

The m_S–m_χ plane is particular illustrative, and shown in the upper left panel of Fig. 4.6. Here, the areas with the highest density of viable (blue) points, are the special kinematic regions identified above: the secluded regime with $m_\chi > m_S$, in particular for $m_S > 100\,\text{GeV}$ to avoid DD constraints, and the poles at $m_\chi \sim m_{S,h}/2$. Another notable feature of the first plot in Fig. 4.6 is the rather small number of orange points compared to the green and blue ones. This suggest that, currently bounds from DD are the most severe.

Collider bounds mostly depend on the value of c_V^S, and only become relevant for $c_V^S > 1$ and $m_S \gtrsim 200\,\text{GeV}$, as shown in the upper right plot of Fig. 4.6. We note again that the impact of collider constraints depends on the assumption $c_G^S = c_B^S = c_W^S = c_V^S$, and results might change in case the latter is lifted. The lower panel of Fig. 4.6 shows the impact of the applied bounds on $\sin\theta$ and c_S. The latter parameter appears to be constrained only by DD and mostly for $m_S \lesssim 100\,\text{GeV}$. In the case of $\sin\theta$, instead, the combination of searches forms a useful complement, especially for $50\,\text{GeV} \lesssim m_S \lesssim 300\,\text{GeV}$. Finally, one can observe overall how larger mediator masses allow for bigger couplings to SM states due to weaker DD constraints.

In Fig. 4.7 we continue to explore the parameter space focusing now on the possible size of y_S in dependence on m_S (upper row) and m_χ (lower row). In addition we confront the full eDMEFT parameter set (right column), as defined in Eq. (4.10), with a scenario in which

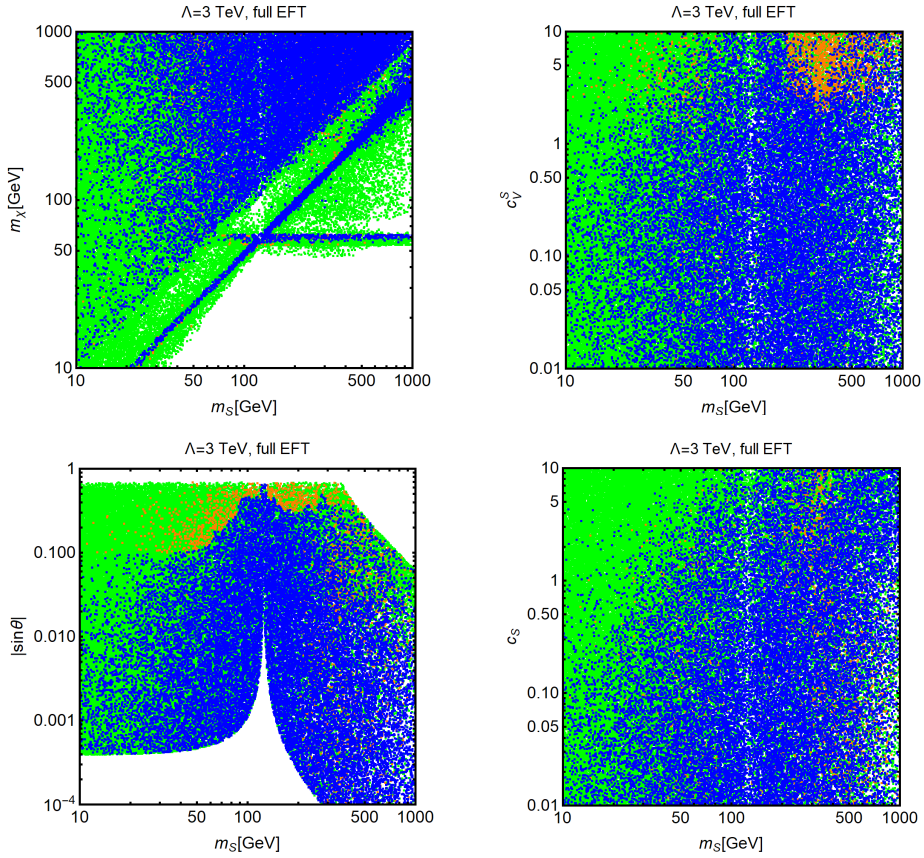

Figure 4.6: Results of the parameter scan for the scalar eDMEFT setup in the m_S–m_χ, m_S–c_V^S, m_S–$|\sin\theta|$, and m_S–c_S planes. The green points provide the correct relic density according to the WIMP paradigm, while the orange points are, in addition, compatible with constraints from DD. The blue points are, finally, also compatible with collider constraints. See main text for details on the scan and the constraints accounted for.

the bi-quadratic $S^2\bar{\chi}\chi$ interaction (left column) vanishes. In the upper left plot one can clearly identify the secluded region around $y_S \lesssim 1$ opening up for smaller m_S. Including the couplings y_χ^S in the full eDMEFT, as done in the upper right plot, shifts the valid points significantly towards smaller y_S, since now the bi-quadratic mediator-DM portal allows for efficient annihilation of the DM, and thus relaxes the DD constraints. A similar trend is visible in the m_χ–y_S plane, shown in the lower panel. Furthermore, the latter plane evidences a narrow strip of viable model points for $m_\chi \sim 60\,\text{GeV}$ corresponding to the $m_\chi \sim m_h/2$ resonance.

To improve the understanding of the obtained results, and to localize the viable parameter regions that conventional simplified models might miss, we disentangle the portals identified above. We skip the effective Higgs portal via $|H|^2\chi\bar{\chi}$ as it is independent of S. Thus, in addition to the scan over the full set (m_χ, m_S, y_S, λ'_{HS}, c_S, c_V^S, y_χ^S), we performed dedicated scans of restricted parameter sets corresponding to the different portals taken individually, while the corresponding intervals remain as given in Eq. (4.10). In Fig. 4.8 we compare the viable regions in the m_S–m_χ plane of those portals with the results of the full eDMEFT

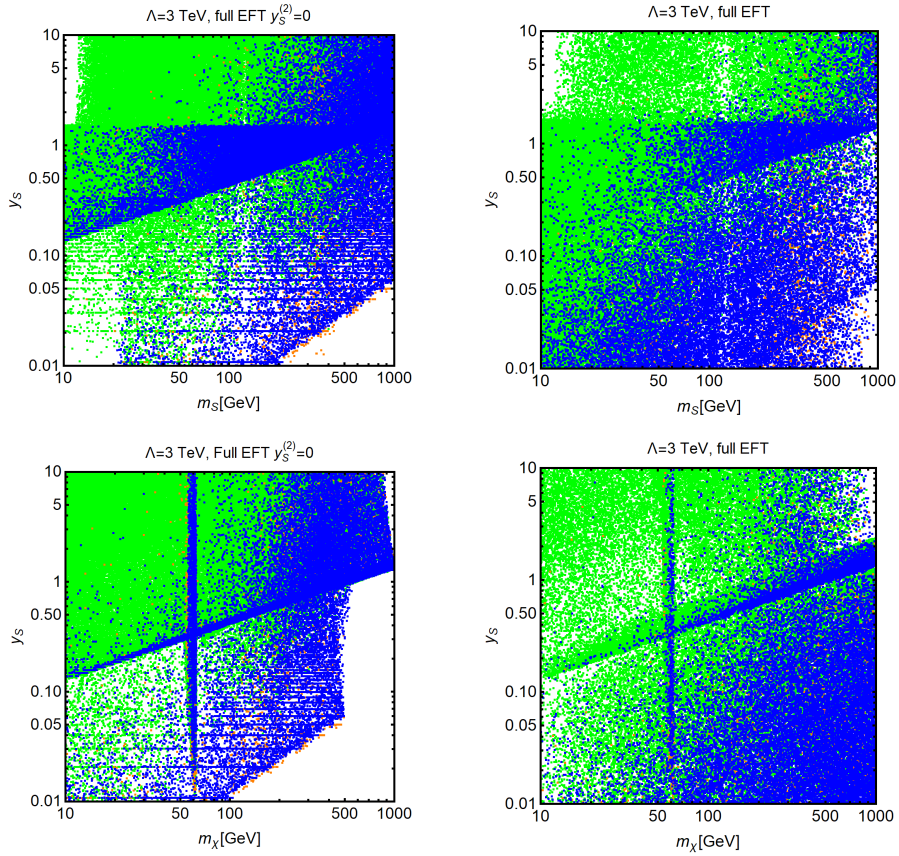

Figure 4.7: Results of the parameter scan for the scalar eDMEFT setup in the m_S–y_S and m_χ–y_S planes, following the same color code as in Fig. 4.6. The right column corresponds to the full eDMEFT parameter set, while in the left $y_\chi^S = 0$.

and the $y_\chi^S = 0$ case.[3] For simplicity, we only show two kind of points: in blue, those that simultaneously satisfy all constraints entertained before, and in red, those which also pass the projected XENONnT bounds. This makes particularly transparent which scenarios can remain valid while constraints from DD get stronger. In the upper left and middle panels, one can see that regarding current bounds the $D=5$ Yukawa and gauge portals tend to occupy rather similar regions of the parameter space mostly restricted to the secluded regimes and the poles $m_\chi \sim m_S/2$. However, the former portal features a larger viable region around $m_\chi \sim m_S/2$ for $m_S \geq 2\,m_t$. In this regime the decay $S \to t\bar{t}$ is allowed increasing the total decay width of S. Since a wider resonance boosts the annihilation cross section further away from the exact resonance condition, the allowed region also broadens. For this case, it could be interesting to also consider correlated limits from mono-Higgs final states that necessarily emerge, but are not captured in the simple Yukawa portal. As shown in the upper right panel, the mixing portal features a significantly smaller population in the secluded regime, especially for $m_h < m_S \lesssim 500\,\text{GeV}$. In this region even the smallest scalar couplings considered in our scan are under pressure from DD. However, it adds a pronounced $m_\chi \approx m_h/2$ resonance region, which will be mostly tested by XENONnT.

[3]Further potential effects of y_χ^S are investigated in more detail in Sec. 4.3.

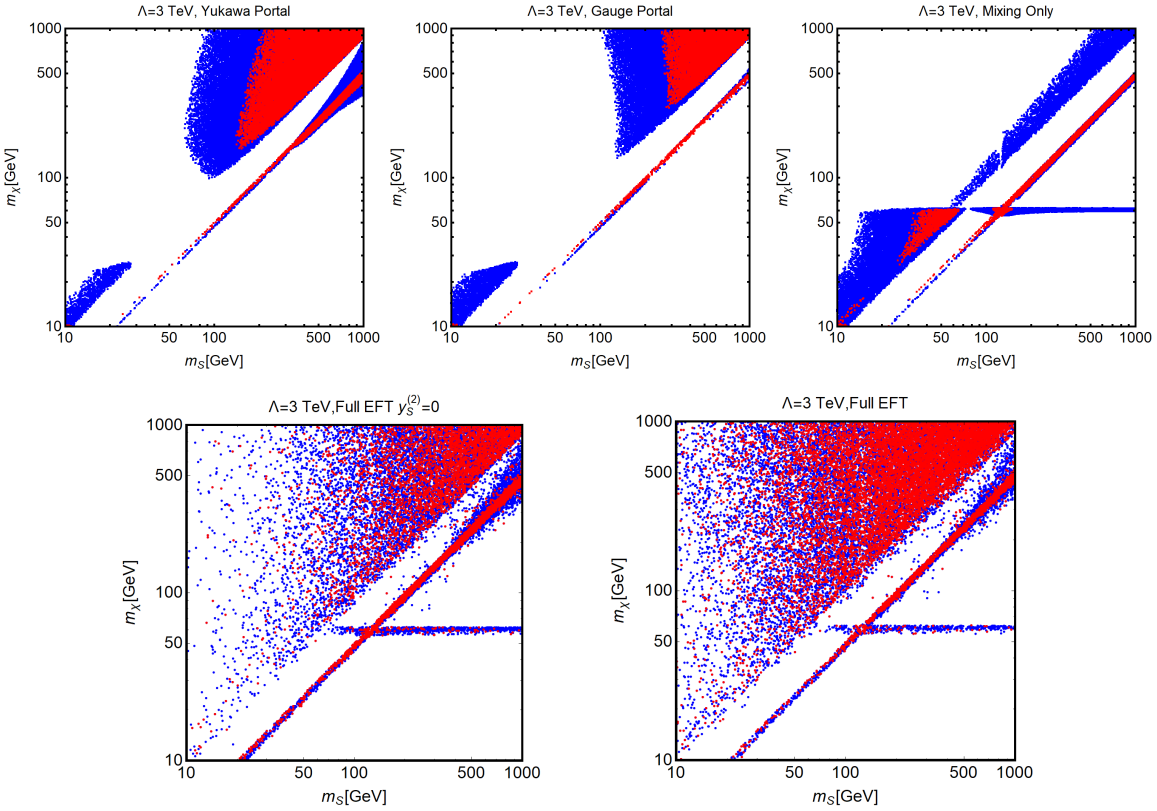

Figure 4.8: Viable model points for the $D = 5$ flavor-diagonal Yukawa portal (upper left), $D = 5$ scalar gauge portal (upper middle), Higgs mixing portal (upper right), and full eDMEFT with (lower right) and without (lower left) considering y_χ^S, in the m_S–m_χ plane. While the blue points satisfy all DM and collider bounds entertained before, the red points represent configurations evading also a projected XENONnT exclusion.

Once the full parameter space of eDMEFT is considered a significant extension of the allowed parameter space is present, as done in the lower right panel of Fig. 4.8. This can be traced back to basically two effects: non-trivial interplay between the different operators causing for example blind spots in DD, and possible new DM annihilations via the $S^2\bar{\chi}\chi$ operator, as explained before. To disentangle these effects, also the scenario with $y_\chi^S = 0$ is shown in the lower left panel. We see that even there the parameter space increases notably due to the operator interplay leading to a broader region of points around the $m_\chi \sim m_S/2$ resonance and the opening of the region towards lighter mediators of $m_S \lesssim 100\,\text{GeV}$ for moderate and larger DM masses. Including finally the coupling y_χ^S fully opens the light-S−heavy-DM quadrant. This includes even smaller m_S due to possible annihilations via the $S^2\bar{\chi}\chi$ operator which allows for more modest values of y_S and thereby evades DD limits.

The differences between the portals and the eDMEFT get even more pronounced once we look at the red points in Fig. 4.8, which also pass the projected XENONnT constraints. The further strengthened DD constraints would reduce the viable region of the Higgs-mixing portal mostly to a rather tuned, narrow band around the resonance $m_S \approx 2m_\chi$, and exclude the region around the Higgs pole. While the Yukawa and gauge portals would be constrained to

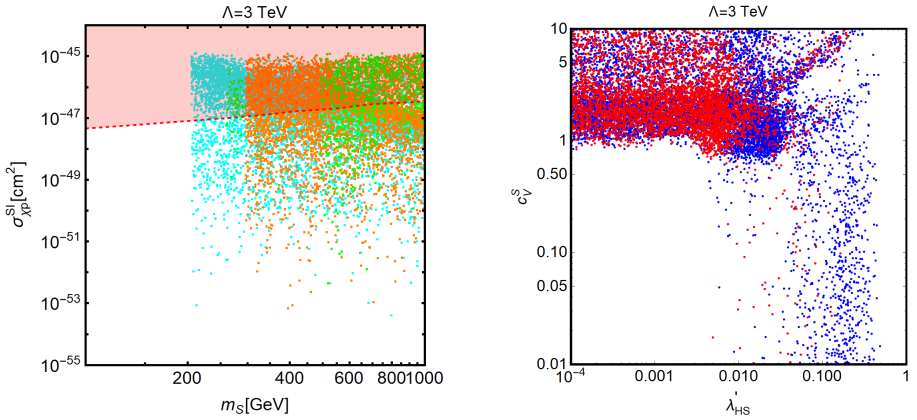

Figure 4.9: Left Panel: Model points in the m_S–$\sigma_{\chi p}^{\rm SI}$ plane for the full eDMEFT, complying with all current experimental constraints but being potentially testable at colliders in the near future according to the criteria given in the main text. The different colors indicate the processes which can be used to probe the corresponding points, namely $pp \to S \to VV$ (cyan), $pp \to S \to hh$ (green) and $pp \to S \to \gamma\gamma$ (orange). The regions marked in red will be excluded in the case of no signal at XENONnT. Right Panel: Same model points in the λ'_{HS}–c_V^S plane, where blue points feature DM scattering cross sections above the projected limit from XENONnT while red ones will also pass this upcoming constraint.

that band and small regions in the secluded regime, the full eDMEFT stays vital in large areas of parameter space. This includes in particular the Higgs resonance, which in the presence of the new operators remains viable due to cancellations in DD.

One remark about the secluded region, there the correct relic density depends basically on the parameters y_S and y_χ^S. Consequently, viable model points evading even future DD prospects could be obtained by considering extremely small values for the coupling of S with the SM sector, namely c_V^S, λ'_{HS}, and c_S. The restriction of the viable parameter regions for $m_\chi > m_S$ of the individual portals shown in Fig. 4.8 is basically due to our choice of the lower limits for c_V^S, λ'_{HS}, c_S as given in Eq. (4.10). This choice is motivated by the "bottom-up" approach of considering non-vanishing values for each operator not forbidden by a symmetry. Moreover, we cannot just set all these couplings to zero, since a small but non-zero coupling with SM states is needed to ensure that the DM was in thermal equilibrium in the early Universe, such that the standard thermal freeze-out computations are valid. Beyond this, in the full eDMEFT (or its variant with $y_\chi^S = 0$) the enlarged amount of viable parameter points in the secluded region compared to the simple portals is partially achieved with moderate values of c_V^S, λ'_{HS}, and c_S. Those values could already be excluded in the corresponding isolated portals, and could be large enough to be probed by future experimental upgrades, especially at the HL-LHC. We will estimate the reach of upcoming experiments in the next paragraph.

In summary, the eDMEFT scenario for fermionic DM with a scalar mediator appears currently to be most constrained by DD experiments, while LHC searches can exclude limited regions of the parameter space characterized by high values of the mixing angle θ or of the $D=5$ couplings c_V^S. We now explore whether this situation might change in the near future. Therefore, if updated LHC results could be more competitive than future DD constraints, at least in some

regions of the eDMEFT parameter space. Thus allow for a potential "discovery" of DM at the LHC within our extended framework.

A naive estimate of rescaling the luminosity puts the potential improvement of the collider limits at $\sqrt{L_{\text{HL-LHC}}/L_{\text{curent}}} \approx 10$. Therefore, we select from our general parameter scan all viable points that have a cross section less than one order of magnitude below the present bound in at least one of the considered collider processes, namely $pp \to S \to VV$ (cyan), $pp \to S \to hh$ (green) and $pp \to S \to \gamma\gamma$ (orange). Points selected in this way are displayed in the left panel of Fig. 4.9 in the m_S–$\sigma^{\text{SI}}_{\chi p}$ plane, and compared to the expected exclusion from XENONnT (red region). As can be seen, a sizable fraction of points is characterized by strongly suppressed DD cross sections far below the future experimental reach. To better characterize these parameter points we finally display them in the λ'_{HS}–c_V^S plane in the right panel of Fig. 4.9. In this plot the parameter points with scattering cross sections above the projected XENONnT bound are marked in blue, while those evading it are shown in red. The distribution resembles the shape of Fig. 4.4. We notice in particular a stripe at high values of c_V^S and substantial h–S mixing which corresponds to the blind spot highlighted in Fig. 4.4.

It is interesting to note, that the eDMEFT framework allows for detectable collider signatures, while simultaneously obtaining the correct relic density, and avoiding DD constraints. This combination is non-trivial. While the next-generation simplified models discussed in Chapter 2 provide strong BMs for mono-X searches, they usually struggle to set the relic density without the presence of further states.

4.2 Pseudoscalar Mediator

Similar to the next-generation simplified models discussed in Chapter 2, we will also investigate the important benchmark of a pseudoscalar mediator. The eDMEFT Lagrangian for this case is given in Eq. (3.30). While sharing basic features with the scalar model discussed in the previous section, the change in $\mathcal{CP}$ property leads to important phenomenological differences in a number of observables. In the following we revisit various observables for the pseudoscalar mediator, and work out differences and similarities to the scalar case. We again conclude with analyzing the full parameter space of the pseudoscalar eDMEFT.

4.2.1 Dark Matter Phenomenology

Since the eDMEFT should provide a valid description of DM, we revisit important quantities to obtain this, and to get an insight in the results obtained later on. Here, first crucial differences to the scalar case will appear regarding the velocity dependence of the cross sections.

Relic Density In analogy to the case of the scalar mediator, we present the DM annihilation cross sections for the relevant channels retaining just the leading part. The thermally averaged cross section into fermions can be approximated by

$$\begin{aligned}\langle\sigma v\rangle_{ff} &\approx \frac{N_c}{4\pi}\frac{v^2}{\Lambda^2}\frac{(y_{\tilde{S}}\, y_f^{\tilde{S}})^2\, m_\chi^2}{(m_{\tilde{S}}^2 - 4m_\chi^2)^2} \qquad (4.11)\\ &\approx \begin{cases} 5\times 10^{-2}\sigma_v^0 N_c \left(\frac{3\,\text{TeV}}{\Lambda}\right)^2\left(\frac{m_\chi}{100\,\text{GeV}}\right)^2\left(\frac{500\,\text{GeV}}{m_{\tilde{S}}}\right)^4 (y_{\tilde{S}}\, y_f^{\tilde{S}})^2, & m_\chi \ll \frac{m_{\tilde{S}}}{2} \\ 1.95\,\sigma_v^0 N_c \left(\frac{3\,\text{TeV}}{\Lambda}\right)^2\left(\frac{100\,\text{GeV}}{m_\chi}\right)^2 (y_{\tilde{S}}\, y_f^{\tilde{S}})^2, & m_\chi \gg \frac{m_{\tilde{S}}}{2}. \end{cases}\end{aligned}$$

In contrast to the case of the scalar mediator, the annihilation is s-wave instead of p-wave and therefore of order v_χ^0. Consequently, the annihilation cross section at freeze-out is typically enhanced by a factor of $1/v_\chi^2 \sim 10$, and the cosmologically preferred values of the couplings are smaller than the ones found in Sec. 4.1.1.

The same effect can be observed for annihilations into gauge bosons. Taking gluons as a representative choice for the VV final state, the cross section can be estimated as

$$\begin{aligned}\langle\sigma v\rangle_{GG} &\approx \frac{2}{\pi\Lambda^2}\frac{(C_{GG}^{\tilde{S}})^2\, y_{\tilde{S}}^2\, m_\chi^4}{(m_{\tilde{S}}^2 - 4m_\chi^2)^2} \qquad (4.12)\\ &\approx \begin{cases} 6.6\times 10^{-2}\sigma_v^0 \left(\frac{3\,\mathrm{TeV}}{\Lambda}\right)^2 \left(\frac{m_\chi}{100\,\mathrm{GeV}}\right)^4 \left(\frac{500\,\mathrm{GeV}}{m_{\tilde{S}}}\right)^4 \left(\frac{\alpha_s c_G^{\tilde{S}}}{4\pi}\right)^2 y_{\tilde{S}}^2, & m_\chi \ll \frac{m_{\tilde{S}}}{2} \\ 2.58\,\sigma_v^0 \left(\frac{3\,\mathrm{TeV}}{\Lambda}\right)^2 \left(\frac{\alpha_s c_G^{\tilde{S}}}{4\pi}\right)^2 y_{\tilde{S}}^2, & m_\chi \gg \frac{m_{\tilde{S}}}{2}. \end{cases}\end{aligned}$$

The situation is different for the $\tilde{S}\tilde{S}$ final state. In the limit $m_\chi \gg m_{\tilde{S}}$ the thermal averaged cross section can be approximated as

$$\langle\sigma v\rangle_{\tilde{S}\tilde{S}} \approx \frac{y_{\tilde{S}}^4\, v_\chi^2}{192\pi\, m_\chi^2} \approx 10\,\sigma_v^0 \left(\frac{100\,\mathrm{GeV}}{m_\chi}\right)^2 y_{\tilde{S}}^4\,. \qquad (4.13)$$

In this case the p-wave suppression is not lifted by switching the $\mathcal{CP}$ property of the mediator, and the leading contribution arises at $\mathcal{O}(v_\chi^2)$. However, this annihilation channel can be realized without higher dimensional operators. Therefore, it comes without the $1/\Lambda^2$ suppression of the previously discussed channels. Unless the masses of the new states are rather close to the cutoff scale, this can compensate for the velocity suppression. It makes annihilations to $\tilde{S}\tilde{S}$ one of the most important channels for setting the relic density in the secluded regime. While the $\tilde{S}^2\bar{\chi}\chi$ operator can also contribute to $\tilde{S}\tilde{S}$ final state, its cross section is identical to the scalar case in Eq. (4.4), which can be used to estimate its importance.

Interestingly, the mixed annihilation channel into the $h\tilde{S}$ final state is both s-wave and can be realized with $D=4$ operators. Taking for simplicity the limit $m_\chi \gg (m_{\tilde{S}} + m_h)/2$, the leading contribution is given by

$$\langle\sigma v\rangle_{h\tilde{S}} \approx \frac{y_{\tilde{S}}^2\, \lambda_{\tilde{S}H}^2\, v^2}{256\pi\, m_\chi^4} \approx 4.4\times 10^2 \sigma_v^0 \left(\frac{100\,\mathrm{GeV}}{m_\chi}\right)^4 \lambda_{\tilde{S}H}^2\, y_{\tilde{S}}^2. \qquad (4.14)$$

In particular for m_χ around the electroweak scale this annihilation rate can naturally become large and should be expected to contribute significantly to the relic density.

Besides shifting the parameter space for a successful thermal freeze-out towards lower couplings, the presence of s-wave cross sections turns ID in an effective search channel as discussed in the next paragraph.

Indirect Detection In the case of a pseudoscalar mediator the DM annihilation cross sections into pairs of SM fermions or gauge boson as well as into $h\tilde{S}$ are s-wave dominated. Hence their values at thermal freeze-out and at present times are comparable, and ID experiments have the potential to test thermally produced DM. There are various signatures that can be used to search for DM annihilations in our local galactic environment. In our analysis we will include two of the cleanest bounds on a DM annihilation signal: i) limits on continuum γ-ray flux

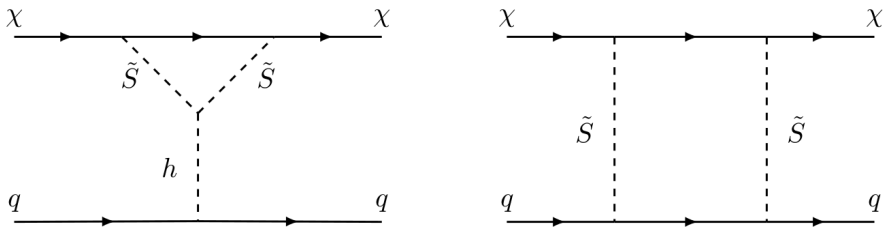

Figure 4.10: Representative one-loop diagrams for the dominant contribution to the DM-nucleons scattering cross section in the case of a pseudoscalar mediator.

produced by DM annihilations in dwarf galaxies from Fermi-LAT data in [37], and ii) limits on gamma-ray lines from $\gamma\gamma$ and $Z\gamma$ final states derived by the Fermi collaboration in [38].

Concerning the $h\tilde{S}$ final state, it will mostly lead to a $4b$ signature which could again be probed through γ-ray signatures. However, to our knowledge there are no dedicated studies for this kind of signature.

Direct Detection The DD phenomenology is crucially different from the scalar mediator case, as long as the direct coupling of DM to the Higgs boson via y_χ^H is absent or suppressed. The interaction of DM with quarks via a pseudoscalar leads to SD scattering cross sections, which are in addition suppressed by $q^4/(m_\chi^2 m_p^2)$, with q being the (small) momentum transfer. The scattering rate induced by this interaction is far below the experimental sensitivity for the considered mediator masses [113]. Similarly the effective coupling of $\tilde{S}$ with gluons leads to a tiny momentum-suppressed cross section [111].

Therefore, the most relevant interactions with nuclei occur at one-loop level as shown in [121, 124–126]. For illustration we report two representative diagrams in Fig. 4.10 leading to SI scattering cross sections. From them it is straightforward to notice that the contribution to the amplitude from box-shaped diagrams is suppressed by a factor $1/\Lambda^2$, while the triangle shaped diagrams contain no coupling depending on Λ. To good approximation we can then compute the DM scattering cross section retaining only the latter ones, and write it as

$$\sigma_{\chi p}^{\text{SI loop}} = \frac{\mu_{\chi p}^2}{\pi} \left| \sum_{q=u,d,s} \frac{\lambda_{H\tilde{S}}}{m_h^2}\, m_p f_q^p\, C_{\tilde{S}}^{\text{triangle}} + \frac{6}{27}\, \frac{\lambda_{H\tilde{S}}}{m_h^2}\, m_p f_{TG}\, C_{\tilde{S}}^{\text{triangle}} \right|^2 , \tag{4.15}$$

where f_q^p, f_{TG} are introduced below Eq. (4.5), and

$$C_{\tilde{S}}^{\text{triangle}} = \frac{y_{\tilde{S}}^2}{(4\pi)^2}\, m_\chi\, C_2(m_\chi^2, m_{\tilde{S}}^2, m_\chi^2) \tag{4.16}$$

with

$$\begin{aligned} C_2(m_\chi^2, m_{\tilde{S}}^2, m_\chi^2) = &- \frac{1}{m_\chi^2} - \frac{m_{\tilde{S}}^3 - 3 m_{\tilde{S}}\, m_\chi^2}{m_\chi^4 \sqrt{m_{\tilde{S}}^2 - 4 m_\chi^2}}\, \log\left[\frac{m_{\tilde{S}} + \sqrt{m_{\tilde{S}}^2 - 4 m_\chi^2}}{2 m_\chi}\right] \\ &+ \frac{m_{\tilde{S}}^2 - m_\chi^2}{2 m_\chi^4}\, \log\left[\frac{m_{\tilde{S}}^2}{m_\chi^2}\right] . \end{aligned} \tag{4.17}$$

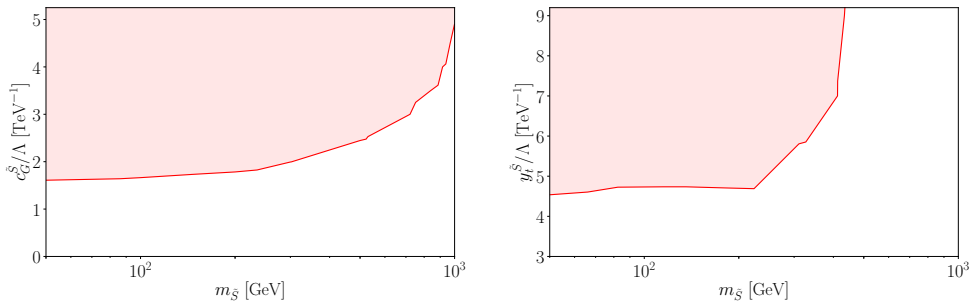

Figure 4.11: Exclusion limits from the ATLAS mono-jet search in [77] in the $m_{\tilde{S}}$–$c_G^{\tilde{S}}$ (left) and $m_{\tilde{S}}$–$y_t^{\tilde{S}}$ plane (right) for the pseudoscalar mediator. In both cases $y_{\tilde{S}} = 1$, $m_\chi = 10\,\text{GeV}$ and all other couplings are equal to zero.

Even though the bounds will turn out to be less strong than in the case of a scalar mediator, those from xenon-based experiments are not negligible in certain limits, which will be illustrate in more detail in Sec. 4.2.3.

4.2.2 Collider Signals

The collider phenomenology of the pseudoscalar model is very similar to the scalar case. As before, the cross section for resonant production can be estimated by using Eq. (2.40), and only the widths need to be re-evaluated. For the gauge-portal the square matrix elements of the $\tilde{S} \to gg$ and the $\tilde{S} \to \gamma\gamma$ processes are identical to the scalar mediator case, while the width into the massive gauge bosons tends to the same value for $m_{\tilde{S}} \gg m_{W/Z}$. Therefore, the bounds from searches for the visible decays of the pseudoscalar mediator are essentially the same as in the scalar model.

For the loop-induced production from gluons due to the effective Yukawa operator a minor modification of the decay width in Eq. (4.9) is necessary as the scalar loop function, $F_S(x)$, has to be replaced by the pseudoscalar one, $F_P(x)$, given in Eq. (A.21). Since $F_P(x) \geq F_S(x)$ for all x, the production rate of pseudoscalars is always bigger than the one of scalars with the same mass, and the bounds are stronger by an $\mathcal{O}(1)$ factor.

Our practical implementation of the limits on $\tilde{S}$ from decays to visible states is analogous to the one in the previous section. These signatures can be complemented by mono-jet signals associated to the invisible decay of $\tilde{S}$ for $m_{\tilde{S}} \geq 2m_\chi$. Again, similarly to the case of the scalar mediator, we have applied the results from the ATLAS search in [77] employing Madgraph and the CheckMATE package, for details see Sec. 4.1.2. For illustration we show in Fig. 4.11 the excluded regions in the $m_{\tilde{S}}$–$c_G^{\tilde{S}}$ and $m_{\tilde{S}}$–$y_t^{\tilde{S}}$ planes, assuming $m_\chi = 10\,\text{GeV}$. As expected, we find that the limits on the gluon-portal are indistinguishable from the scalar case, while the bounds on the Yukawa-portal improve by a factor ~ 1.5 for low values of $m_{\tilde{S}}$.

The decay of h to $\tilde{S}\tilde{S}$ is an important contribution to the Higgs-to-invisible width for $m_h \geq 2\,m_{\tilde{S}}$ and non-vanishing $\lambda_{H\tilde{S}}$; see also Sec. 2.1.3. Using the limit from [130] we find stringent constraints on $\lambda_{H\tilde{S}}$, see also e.g. [61, 313, 314].

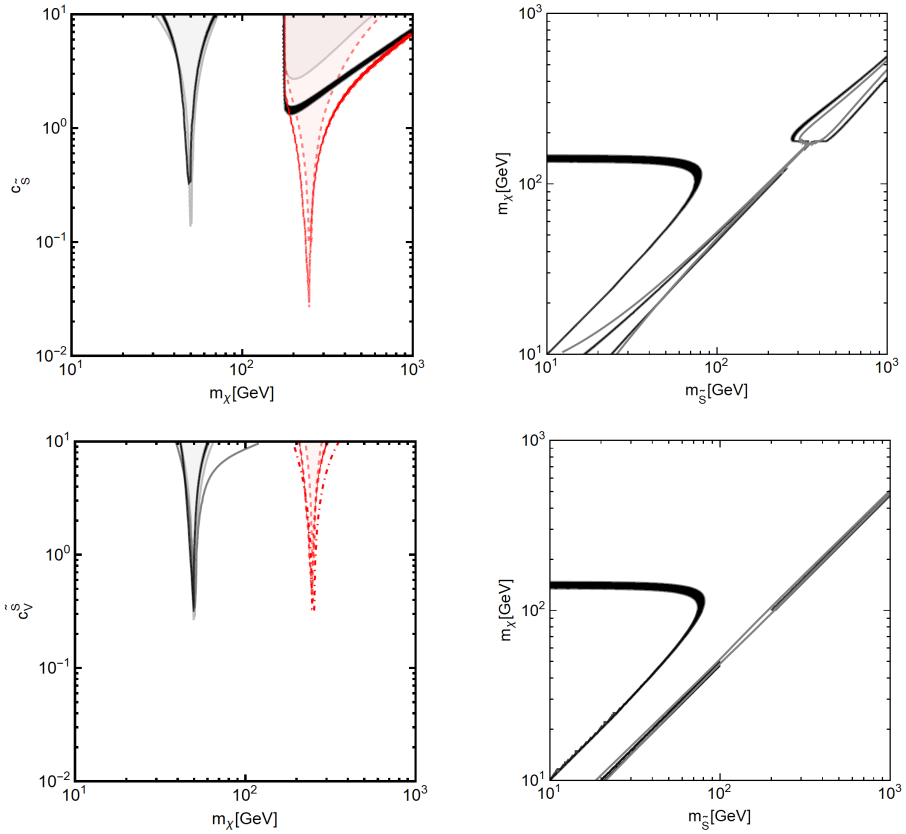

Figure 4.12: Isocontours of the correct relic density for the Yukawa (top), and gauge (bottom) portals. The left column display the m_χ–coupling plane for $m_{\tilde{S}} = 100\,\text{GeV}$ (black) and $m_{\tilde{S}} = 500\,\text{GeV}$ (red). The shaded regions, and the regions inside the dashed lines represent bounds from ID for the corresponding BMs.
The right column shows the $m_{\tilde{S}}$–m_χ plane for $y_\S = 1$ and $c_{\tilde{S}} = 1$ (top) and $c_V^{\tilde{S}} = 1$ (bottom). The regions inside the gray contours are excluded by ID. For all plots we set $\Lambda = 3\,\text{TeV}$.

4.2.3 Combined Results

To obtain a global picture, we will follow the strategy laid out in Sec. 4.1.3. We perform an analysis of the eDMEFT parameter space with a pseudoscalar mediator by considering increasingly refined sets of operators.

Basic Portals in Isolation In order to illustrate the effects of individual interactions we start again with considering basic portals that form a subset of the Lagrangian in Eq. (3.30). In the pseudoscalar case only two portals are relevant: the gauge one with the coupling $c_V^{\tilde{S}}$ and the Yukawa one with $c_{\tilde{S}}$. The mixing portal is forbidden by the assumption of $\mathcal{CP}$ conservation, and the effective Higgs portal is in principle present but its phenomenology is identical to the scalar case, so we will not recapitulate it.

A visualization of the cosmologically preferred parameter space for these two scenarios is presented in Fig. 4.12. We display isocontours corresponding to the observed relic density for

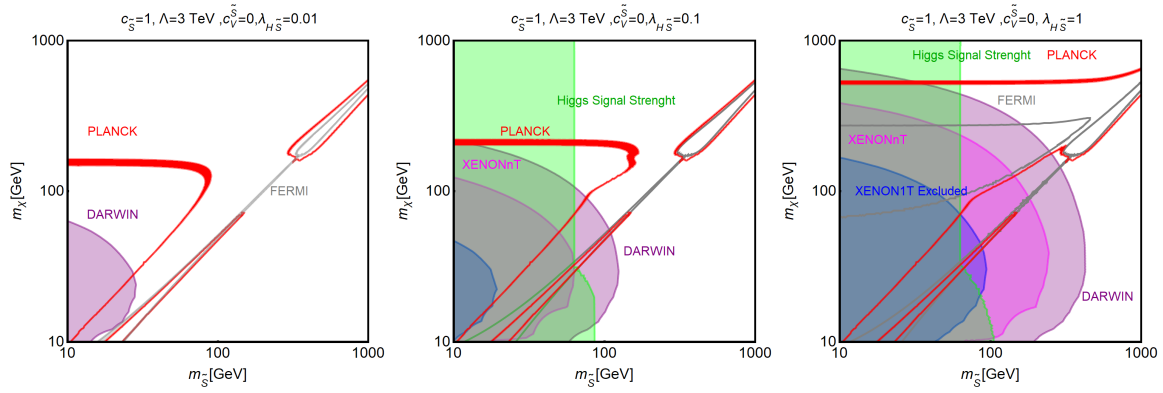

Figure 4.13: Constraints in the $m_{\tilde{S}}$–m_χ plane for the Yukawa portal with $c_{\tilde{S}} = 1$, $y_{\tilde{S}} = 1$ and three different values of $\lambda_{H\tilde{S}} = 0.01, 0.1, 1$ (from left to right). Isocontours of the correct relic density are shown in red, and current (projected) limits from XENON1T (XENONnT/DARWIN) in blue (magneta/purple). The gray isocontours indicate ID limits, where viable regions are outside of these contours. Bounds from Higgs-to-invisible searches on the $h \to \tilde{S}\tilde{S}$ decay are shown in green.

$m_{\tilde{S}} = 100\,\text{GeV}$ (black) and $m_{\tilde{S}} = 500\,\text{GeV}$ (red) in the m_χ–coupling plane (left column), as well as in the $m_{\tilde{S}}$–m_χ plane (right column) for $c_{\tilde{S}} = 1$ (top) and $c_V^{\tilde{S}} = 1$ (bottom), respectively. In all cases $\lambda_{H\tilde{S}} = 0$, $y_{\tilde{S}} = 1$ and $\Lambda = 3\,\text{TeV}$ are fixed. The plots show that the preferred regions for the relic density are again the resonance, i.e. $m_\chi \simeq m_{\tilde{S}}/2$, and the secluded regime. By comparing Fig. 4.12 with the analogous plots for the scalar mediator in Fig. 4.2, we notice that those regions are wider. This is a consequence of the s-wave enhanced cross section into SM fermions and gauge bosons. By setting $\lambda_{H\tilde{S}} = 0$ the impact from DD is negligible, so no related contours appear in Fig. 4.12. In contrast, ID bounds both from γ-ray continuum and lines are relevant, and indicated by the shaded and dashed regions in Fig. 4.12. As mentioned above, those searches test regions close to ones preferred by the relic density, due to the s-wave nature of the annihilation cross sections.

In order to illustrate the impact of the loop-induced DM-nucleon scattering discussed above, we reconsider the Yukawa portal in Fig. 4.13 for $c_{\tilde{S}} = y_{\tilde{S}} = 1$ and three values of $\lambda_{H\tilde{S}} = 0.01$, 0.1, and 1. The value of $\lambda_{H\tilde{S}}$ has a strong impact, since it controls the strength of the triangle contribution to the SI scattering cross section. For $\lambda_{H\tilde{S}} = 0.01$ even a highly sensitive future experiment like DARWIN can only probe a quite limited region of the $m_{\tilde{S}}$–m_χ plane. The testable region becomes significant bigger for higher values of $\lambda_{H\tilde{S}}$. Current constraints from XENON1T are only sensitive to masses of the mediator $m_{\tilde{S}} \lesssim 100\,\text{GeV}$ even for $\lambda_{H\tilde{S}} = 1$. Most of this region is already excluded by collider bounds on $\text{BR}(h \to \tilde{S}\tilde{S})$ marked in green in Fig. 4.13. Concerning the latter region, we see that those extend to values of $m_{\tilde{S}} > m_h/2$ up to around 100 GeV for small DM masses, because the decay $h \to \tilde{S}\tilde{S}^\star \to \tilde{S}\chi\bar{\chi}$ is significant, with $\tilde{S}^\star$ denoting an off-shell mediator, as shown in Fig. 2.1 and in [45]. However, future generations of DD experiments are expected to change this picture. Pseudoscalar masses up to several hundreds of GeV will be in reach for sizable $\lambda_{H\tilde{S}}$.

Combining Portals In the next step, the two aforementioned portals are taken to be simultaneously present. More specifically both couplings $c_V^{\tilde{S}}$ and $c_{\tilde{S}}$ are assumed to be different from

zero while $\lambda_{H\tilde{S}}$ is set to zero. We consider the same values for the DM and mediator masses as in the benchmarks for the scalar mediator, i.e. $(m_\chi, m_{\tilde{S}}) = (80, 200)\,\text{GeV}$, $(225, 500)\,\text{GeV}$ and $(500, 300)\,\text{GeV}$. The combined constraints from DM and collider phenomenology are shown in Fig. 4.14 considering the $c_{\tilde{S}}$–$y_{\tilde{S}}$ plane for $c_V^{\tilde{S}} = 0$, 1 and 5.

In each panel, the red isocontours represent the correct relic density, while the orange regions are excluded by searches for diphoton resonances and the green one by mono-jet searches. The absence of mixing between the Higgs and the mediator reduces the branching ratio of the latter into massive gauge bosons. Therefore, we found no notable constraints from searches for diboson resonances for the considered benchmarks. For $m_{\tilde{S}} = 200\,\text{GeV}$ mono-jet searches (green) exclude large values of the couplings.

The exclusions from ID display two distinct regions corresponding to bounds from γ-ray continuum (dark grey) and γ-ray line (light grey) searches, respectively. Possible line signals depend only on $c_V^{\tilde{S}}$ and $y_{\tilde{S}}$, hence appear as horizontal bands in the plots. As expected from the discussion above, DD has no impact on the benchmarks with $\lambda_{H\tilde{S}} = 0$.

The interplay of the different operators is most evident in the relic density contours. The two BMs with $m_\chi \leq m_{\tilde{S}}$ show a substantial change of the relic density isocontours for $c_V^{\tilde{S}} \neq 0$. For the third benchmark, in the secluded mass regime, the relic density is mostly determined by $y_{\tilde{S}}$ indicating that it is primarily fixed by $\chi\bar{\chi} \to \tilde{S}\tilde{S}$ processes. Contrary to the scalar mediator case, we see a change for $c_{\tilde{S}} > 1$, where annihilations into fermion pairs contribute significantly to the relic density since this channel is not velocity suppressed for a pseudoscalar mediator.

Generic Parameter Scan The survey concludes with a scan of the general parameter space. Following the analysis and conventions of the scalar case, the six free parameters under consideration are $(m_\chi, m_{\tilde{S}}, y_{\tilde{S}}, \lambda_{H\tilde{S}}, c_{\tilde{S}}, c_V^{\tilde{S}})$. For fixed $\Lambda = 3\,\text{TeV}$ they get varied within the ranges:

$$\begin{aligned} m_\chi &\in [10, 1000]\ \text{GeV} \\ m_{\tilde{S}} &\in [10, 1000]\ \text{GeV} \\ \lambda_{H\tilde{S}} &\in \left[10^{-2}, 1\right] \\ y_{\tilde{S}} &\in \left[10^{-2}, 10\right] \\ c_{\tilde{S}} &\in \left[10^{-2}, 10\right] \\ c_V^{\tilde{S}} &\in \left[10^{-2}, 10\right]. \end{aligned} \tag{4.18}$$

The corresponding model points are shown in Fig. 4.15 and 4.16 and distinguished through a color code, namely

- green: account for the observed relic density but otherwise excluded;
- orange: comply with DD and ID but excluded by collider searches;
- blue: pass all applied constraints.

Various slices through the considered higher-dimensional parameter space projected on the $m_{\tilde{S}}$–m_χ and $m_{\tilde{S}}$–coupling planes are shown in Fig. 4.15. Focusing on the upper left plot displaying the $m_{\tilde{S}}$–m_χ plane, we notice a broader viable parameter space with respect to the scalar mediator case. While for $m_\chi \lesssim 150\,\text{GeV}$, only the pole $m_\chi \sim m_{\tilde{S}}/2$ and the secluded regime are viable regions, points compatible with all considered constraints are present also for $m_\chi < m_{\tilde{S}}/2$ for higher values of m_χ. This feature is due to the much weaker DD limits, and

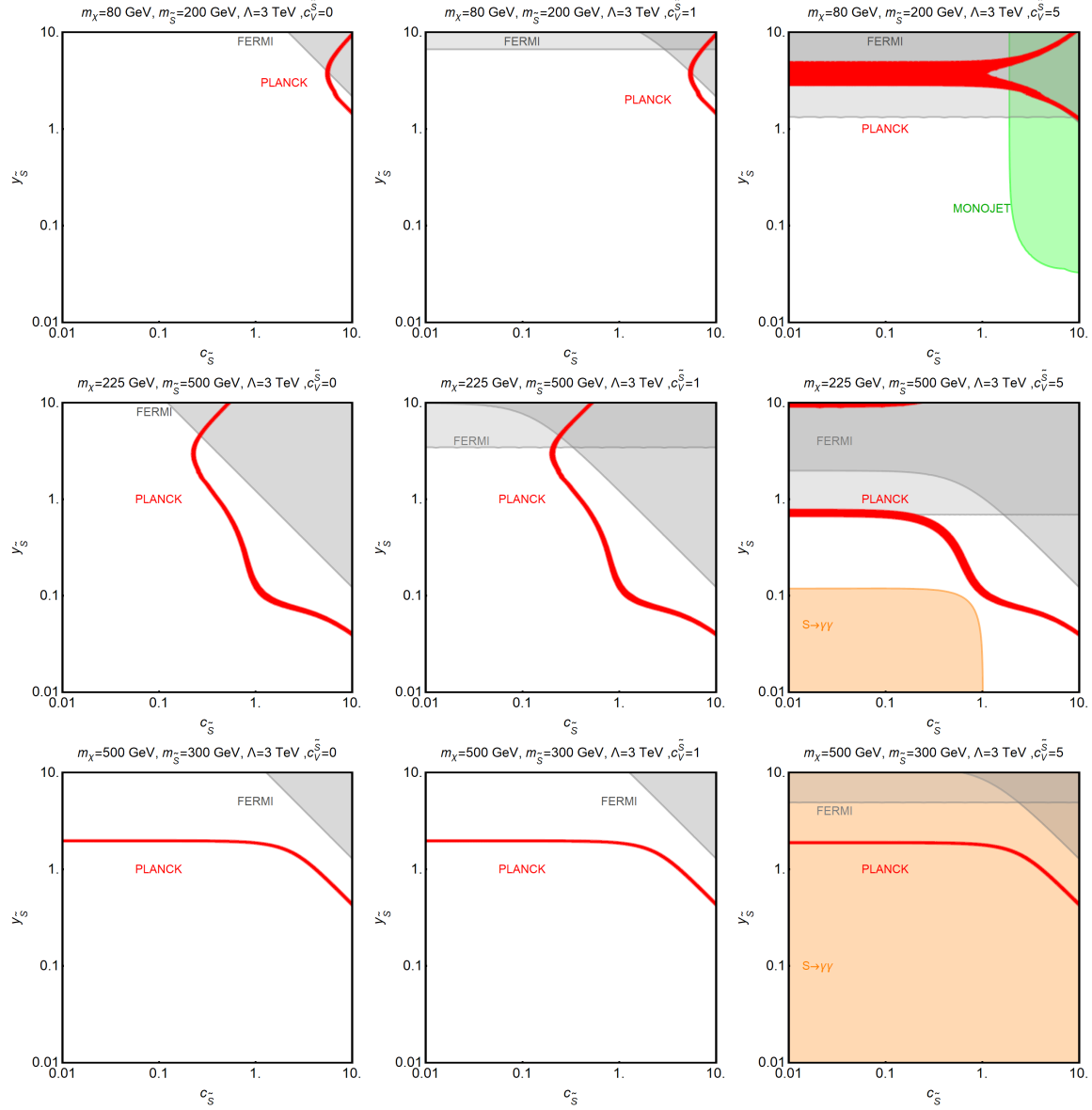

Figure 4.14: Summary of constraints in the $c_{\tilde{S}}$–$y_{\tilde{S}}$ plane for $c_V^{\tilde{S}} = 0$ (left column), $c_V^{\tilde{S}} = 1$ (center column), and $c_V^{\tilde{S}} = 5$ (right column) and three different mass assignations as indicated in the individual panels. The red contours correspond to the correct relic density while regions excluded by ID are depicted in dark grey for γ-ray continuum and in light grey for γ-ray line searches. Orange regions are excluded by collider searches for resonances decaying into photons and the green region by mono-jet searches.

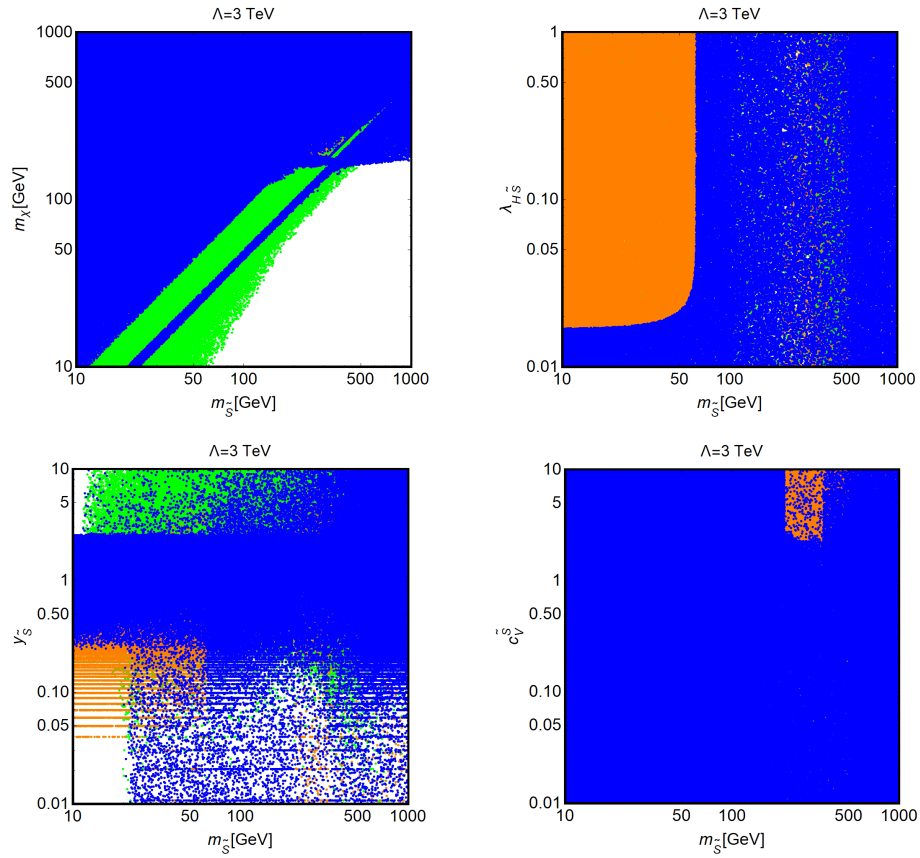

Figure 4.15: Results of the parameter scan for the pseudoscalar eDMEFT projected in the $m_{\tilde{S}}$–m_χ and $m_{\tilde{S}}$–coupling planes, analogous to the scalar mediator case presented in Fig. 4.6 and 4.7 without the $m_{\tilde{S}}$–$c_{\tilde{S}}$ plane, since the latter is not impacted by the considered constraints. Green points account only for the correct relic density, orange points are excluded by collider searches, while blue points pass all applied constraints, see text for more details.

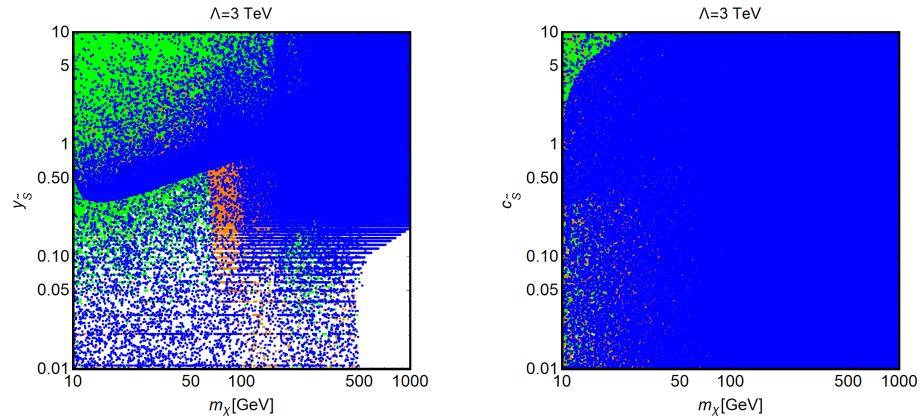

Figure 4.16: Results of the parameter scan for the pseudoscalar eDMEFT projected in the m_χ–$c_{\tilde{S}}$ (left) and m_χ–$y_{\tilde{S}}$ planes (right), analogous to the scalar mediator case presented in Fig. 4.7, see text for details.

therefore is absent in the scalar mediator case. Relevant constraints on the parameter space arise from ID. Its impact is localized at small DM masses since current experimental sensitivity to test cross section preferred by the relic density reaches at most up to $m_\chi \sim 150\,\text{GeV}$.

The right column of Fig. 4.15 shows that collider searches impact a limited region of parameter space, in particular for $c_V^{\tilde{S}} > 1$ and $m_{\tilde{S}} \gtrsim 100\,\text{GeV}$, as well as for $m_{\tilde{S}} \leq m_h/2$ and $\lambda_{H\tilde{S}} \gtrsim 0.02$. In this last region the exclusion bound originates from Higgs-to-invisible searches which are sensitive to the decay $h \to \tilde{S}\tilde{S}$. Besides that, the couplings $c_V^{\tilde{S}}$ and $\lambda_{H\tilde{S}}$ are currently only weakly constrained. According to Fig. 4.13 the next-generation of DD experiments might change this.

In the (lower) left panel of Fig. 4.15 and Fig. 4.16, we investigate $y_{\tilde{S}}$ in dependence of $m_{\tilde{S}}$ and m_χ respectively. For $m_{\tilde{S}}, m_\chi \lesssim 100\,\text{GeV}$, an interesting interplay of constraints occurs from collider searches for small couplings and from ID for high values of the coupling. Higher masses are basically unconstrained. With the $y_\chi^{\tilde{S}}$ and y_χ^H couplings set to zero, the only way to achieve a viable DM phenomenology at small $y_{\tilde{S}}$ is via the $m_\chi \sim m_{\tilde{S}}/2$ pole. As the considered parameter space is limited to $m_{\tilde{S}} \leq 1\,\text{TeV}$, the resonant regime is not included in our analysis for $m_\chi \gtrsim 500\,\text{GeV}$. Therefore, valid model points are absent for $y_{\tilde{S}} \lesssim 0.1$ and $m_\chi \geq 500\,\text{GeV}$ in the left panel of Fig. 4.16.

Finally moving to the $c_{\tilde{S}}$ parameter, we depict the m_χ–$c_{\tilde{S}}$ plane in the right panel of Fig. 4.16 instead of the $m_{\tilde{S}}$–$c_{\tilde{S}}$ plane as in the scalar mediator case, since the latter is not impacted by the considered constraints for a pseudoscalar mediator. Still $c_{\tilde{S}}$ is weakly constrained, with current exclusions dominated by ID for $c_{\tilde{S}} \gtrsim 1$ and $m_\chi \lesssim 50\,\text{GeV}$.

4.3 Di-Fermions plus $\not{E}_T$

The previous parts of this chapter investigated the eDMEFT phenomenology in a general setting. This enabled us to identify relevant portals to the dark sector similar to simplified models, and to extend them in a theoretically consistent way to open up new valid regions in parameter space.

This section explores a slightly more specific scenario, where the scalar mediator $\mathcal{S}$ is odd under a new $\mathbb{Z}_2$ symmetry. In this case, linear interactions of the mediator are absent, and the DM related phenomenology is mainly characterized by the $D=5$ operator $\mathcal{S}^2\bar{\chi}\chi$. While this operator has been briefly discussed in Sec.4.1.3, in this section we focus on it to further investigate its effects. If this operator is the main portal to the dark sector, it could lead to interesting signatures for DM searches at colliders, such as $\not{E}_T$ in association with two correlated jets or electrons. Points in Figs. 4.7 and 4.8 passing the constraints due to the presence of y_χ^S might be testable through the specific collider discussion.

To investigate this, we first discuss the aforementioned eDMEFT setup that also allows the smallness of first-generation fermion masses to be addressed via suppressed $\mathbb{Z}_2$-breaking effects. Then, we turn to an analysis of di-jet plus $\not{E}_T$ at the LHC, where rather loose bounds on the effective $\mathcal{S}^2\bar{\chi}\chi$ interactions can be obtained unless the mediator couples very strongly to SM fermions. Therefore, we investigate a similar process at a potential future e^+e^- collider, such as CLIC, which could deliver tighter constraints on the corresponding model parameters, given that the mediator is leptophilic. We finally highlight the parameter space that allows to produce the observed DM density and include constraints from DD. The results in this section were first derived in [265].

Setup We start from the eDMEFT setup laid out in Sec. 3.3.1, with the additional assumption of a symmetry forbidding the $D=4$ interaction of $\mathcal{S}$ with DM.[4] A simple realization is given by $\mathcal{S}$ being odd under a $\mathbb{Z}_2$ parity, $\mathcal{S}\xrightarrow{\mathbb{Z}_2}-\mathcal{S}$, under which all SM and DM fields are even except for the right-handed first generation fermions, which are odd. With this assumption, many terms of the eDMEFT Lagrangian in Eq. (3.20) vanish including those with an odd power of the mediator, unless they feature the right-handed electron, or the up or down quark. The corresponding Lagrangian, following the notation of Eq. (3.20), reads

$$\begin{aligned}\mathcal{L}_{\text{eff}}^{\mathcal{S}\chi} =& \mathcal{L}_{\text{SM}'} + \tfrac{1}{2}\partial_\mu\mathcal{S}\,\partial^\mu\mathcal{S} - \tfrac{1}{2}\mu_{\mathcal{S}}^2\,\mathcal{S}^2 + \bar{\chi}i\partial\!\!\!/\chi - m_\chi\,\bar{\chi}\chi \\ & - \tfrac{1}{4}\lambda_{\mathcal{S}}\mathcal{S}^4 - \lambda_{H\mathcal{S}}|H|^2\mathcal{S}^2 \\ & - \frac{\mathcal{S}}{\Lambda}\left[\left(Y_d^{\mathcal{S}}\right)_i\bar{Q}_L^i H d_R + \left(Y_u^{\mathcal{S}}\right)_i\bar{Q}_L^i\tilde{H}u_R + \left(Y_e^{\mathcal{S}}\right)_i\bar{L}_L^i H e_R + \text{h.c.}\right] \\ & - \frac{y_\chi^{\mathcal{S}}\,\mathcal{S}^2 + y_\chi^H\,|H|^2}{\Lambda}\,\bar{\chi}_L\chi_R + \text{h.c.},\end{aligned} \tag{4.19}$$

where $\mathcal{L}_{\text{SM}'}$ denotes the SM Lagrangian without the Yukawa couplings of the first generation.

Beyond representing a new portal to the dark sector which is testable at (future) particle colliders, yet in agreement with null-results in DD, this scenario can also motivate the small masses of the first-generation fermions. Although it would be interesting to address all flavor hierarchies with a more extended scalar sector, this is beyond the scope of this discussion. As the SM Yukawa couplings of the first generation are now forbidden at the renormalizable level, their masses will only be generated via small $\mathbb{Z}_2$-breaking effects equipped with additional cutoff suppression. To achieve that, and in contrast to the setup discussed in the previous sections, we assume that the mediator develops a small vev $|\langle\mathcal{S}\rangle| \equiv v_{\mathcal{S}} \sim \mathcal{O}(1-10)\,\text{MeV}$, which finally generates masses for the first fermion generation. In the following analysis, we will consider the mediator to be much heavier than its vev, which requires an additional contribution to the Lagrangian (4.19). While an additional cubic term needs a very large (non-perturbative) coefficient, a straightforward possibility is to add another singlet $\mathcal{S}_2$, as already envisaged above. The desired splitting can be achieved with either a $\mathcal{O}(\text{TeV}^2)$ quadratic term and a mass mixing term $\mathcal{S}\mathcal{S}_2$ with a $\mathcal{O}(1\,\text{GeV}^2)$ coefficient, or a $\mathcal{S}\mathcal{S}_2^3$ portal with a $\mathcal{O}(10^{-6})$ coefficient. We checked that other effects of the new scalar can be effectively decoupled.

The mass mixing of $\mathcal{S}$ with the SM Higgs via the $|H|^2\mathcal{S}^2$ operator is $\sim v_{\mathcal{S}}$ and hence suppressed, thus it will not be considered in the following, in this context see the discussion in Sec. 4.1.3, and e.g. Ref. [28]. The conventional DM operator, $\mathcal{S}\bar{\chi}\chi$, is generated by spontaneous breaking of the $\mathbb{Z}_2$ symmetry, with its coefficient $\sim 2y_\chi^{\mathcal{S}}v_{\mathcal{S}}/\Lambda$. As this operator is strongly suppressed, it only plays a role in DD which is discussed during the end of this section. Finally, the coefficient of the second $D=5$ portal to the dark sector allowed by the symmetry, $|H|^2\bar{\chi}\chi$, is taken to be small from the start. This assumption is motivated to evade DD constraints, since the contribution of $|H|^2\bar{\chi}\chi$ is enhanced by $v/v_{\mathcal{S}} \sim \mathcal{O}(10^4)$. Therefore, limits from Higgs-to-invisible decays for light DM [315] play no role in the collider discussion.

Fermion masses Neglecting leptons for simplicity, because they can be treated analogously, the resulting mass terms after spontaneous symmetry breaking read

$$\mathcal{L}_{\text{mass}} \supset -\sum_{q=u,d}\bar{q}_L\frac{v}{\sqrt{2}}\left(Y_q^H + \frac{v_{\mathcal{S}}}{\Lambda}Y_q^{\mathcal{S}}\right)q_R \equiv -\sum_{q=u,d}\bar{q}_L M^q q_R, \tag{4.20}$$

[4] We note, that if both the $D=4$ and $D=5$ terms would enter, they could be disentangled by their kinematic distributions.

where $q = u,\, d$ are three-vectors in flavor space, and the Yukawa matrices

$$Y_q^{\mathcal{S}} = \begin{pmatrix} (y_q^{\mathcal{S}})_1 & 0 & 0 \\ (y_q^{\mathcal{S}})_2 & 0 & 0 \\ (y_q^{\mathcal{S}})_3 & 0 & 0 \end{pmatrix}, \qquad Y_q^H = \begin{pmatrix} 0 & y_{12}^q & y_{13}^q \\ 0 & y_{22}^q & y_{23}^q \\ 0 & y_{32}^q & y_{33}^q \end{pmatrix} \tag{4.21}$$

reflect the $\mathbb{Z}_2$ assignments. Without breaking of the latter symmetry via $v_{\mathcal{S}} > 0$, one quark family would remain massless corresponding to the vanishing eigenvalue of Y_q^H. On the other hand, a small value of $v_{\mathcal{S}} \sim \mathcal{O}(10)\,\text{MeV}$ is enough to generate $m_u \sim m_d \sim \mathcal{O}(5\,\text{MeV})$ with $\mathcal{O}(1)$ Yukawa couplings and $\Lambda \gtrsim 1\,\text{TeV}$. After performing a rotation to the mass basis via

$$\begin{aligned} M^u &= U_L^u\, M_{\text{diag}}^u U_R^{u\,\dagger} \qquad \text{with} \qquad M_{\text{diag}}^u = \text{diag}(m_u,\, m_c,\, m_t), \\ M^d &= U_L^d\, M_{\text{diag}}^d U_R^{d\,\dagger} \qquad \text{with} \qquad M_{\text{diag}}^d = \text{diag}(m_d,\, m_s,\, m_b), \end{aligned} \tag{4.22}$$

and $U_L^d = U_L^u\, V_{\text{CKM}}$, we obtain the couplings of the physical quarks with the Higgs boson and the scalar mediator $\hat{Y}_q^{H,\mathcal{S}} = U_L^{q\,\dagger} Y_q^{H,\mathcal{S}} U_R^q$ with $q = u,\, d$. Those enter the interaction Lagrangian

$$\mathcal{L}_{\text{inter}} \supset -\sum_{q=u,d} \bar{q}_L \left(\frac{\hat{Y}_q^H + v_{\mathcal{S}}/\Lambda\; \hat{Y}_q^{\mathcal{S}}}{\sqrt{2}}\; h + \frac{v\, \hat{Y}_q^{\mathcal{S}}}{\sqrt{2}\Lambda}\, \mathcal{S} \right) q_R, \tag{4.23}$$

where the $\mathcal{S} q_L q_R$ terms are crucial, as they provide a coupling of $\mathcal{S}$ to the SM.

Flavor Structure To fully define the model, we need to fix a flavor structure, that avoids excessive FCNCs which are generically generated, since the fermion mass matrices M^q receive contributions from different sources; see Eq. (4.20). Those are in general not aligned with the individual scalar-fermion couplings $\sim Y_q^{H,\mathcal{S}}$, and thus $\hat{Y}_q^{H,\mathcal{S}}$ will not be diagonal. To this end, we first note that the Yukawa matrices can be expressed in the interaction basis in terms of the mass matrices as

$$\begin{aligned} Y_q^{\mathcal{S}} &= \frac{\sqrt{2}\Lambda}{v v_{\mathcal{S}}}\, M^q\, \text{diag}(1,0,0) & Y_q^H &= \frac{\sqrt{2}}{v}\, M^q\, \text{diag}(0,1,1) \\ &= \frac{\sqrt{2}\Lambda}{v v_{\mathcal{S}}}\, U_L^q\, M_{\text{diag}}^q U_R^{q\,\dagger}\, \text{diag}(1,0,0), & &= \frac{\sqrt{2}}{v}\, U_L^q\, M_{\text{diag}}^q U_R^{q\,\dagger}\, \text{diag}(0,1,1). \end{aligned} \tag{4.24}$$

In the mass basis they become

$$\hat{Y}_q^{\mathcal{S}} = \frac{\sqrt{2}\Lambda}{v v_{\mathcal{S}}}\, M_{\text{diag}}^q U_R^{q\,\dagger} \text{diag}(1,0,0)\, U_R^q, \qquad \hat{Y}_q^H = \frac{\sqrt{2}}{v}\, M_{\text{diag}}^q U_R^{q\,\dagger}\, \text{diag}(0,1,1)\, U_R^q, \tag{4.25}$$

where the unitary rotations of the left-handed fermions drop out since they share the same $\mathbb{Z}_2$ charges and their couplings with a fixed right-handed fermion are thus aligned with the corresponding mass terms. This is not true for the right-handed fermions, where the corresponding rotation matrices induce a misalignment and thus FCNCs. While it is not possible to set $U_L^u = U_L^d = \mathbb{I}$, since then $V_{\text{CKM}} = \mathbb{I}$, which is in conflict with observation, the Yukawas matrices in Eq. (4.24) can in fact be chosen, such that $U_R^u = U_R^d = \mathbb{I}$ starting from M_{diag}^q. This choice avoids FCNCs, whereas the left-handed rotations can be arbitrary with the only constraint $U_L^{u\,\dagger} U_L^d = V_{\text{CKM}}$.[5] Although a more systematic analysis of FCNCs in such

[5] This approach is somewhat similar to the recently discussed pattern of "singular alignment" [96, 316].

a scenario would be interesting, we will stick to the latter choice for the rest of this section, ending up with diagonal couplings

$$\begin{aligned} \hat{Y}_u^{\mathcal{S}} &= \frac{\sqrt{2}\Lambda}{v v_{\mathcal{S}}}\,\mathrm{diag}(m_u,\,0,\,0), \qquad \hat{Y}_u^{H} &= \frac{\sqrt{2}}{v}\,\mathrm{diag}(0,\,m_c,\,m_t), \\ \hat{Y}_d^{\mathcal{S}} &= \frac{\sqrt{2}\Lambda}{v v_{\mathcal{S}}}\,\mathrm{diag}(m_d,\,0,\,0), \qquad \hat{Y}_d^{H} &= \frac{\sqrt{2}}{v}\,\mathrm{diag}(0,\,m_s,\,m_b). \end{aligned} \tag{4.26}$$

So far, we did not include the lepton sector, however a similar setup is possible and leads directly to

$$\hat{Y}_e^{\mathcal{S}} = \frac{\sqrt{2}\Lambda}{v v_{\mathcal{S}}}\,\mathrm{diag}(m_e,\,0,\,0), \qquad \hat{Y}_e^{H} = \frac{\sqrt{2}}{v}\,\mathrm{diag}(0,\,m_\mu,\,m_\tau). \tag{4.27}$$

This means that the second and third generation fermions couple to the Higgs boson as in the SM, while the ones of the first generation couple to $\mathcal{S}$ instead with strength determined by the free parameter $v_{\mathcal{S}}$. We will trade it for $y_u^{\mathcal{S}}/\Lambda \equiv (\hat{Y}_u^{\mathcal{S}})_{11}/\Lambda$ in the following. While the latter should not be too small, since then a very large $\mathbb{Z}_2$-breaking vev $v_{\mathcal{S}}$ will be required to reproduce the quark masses, values of $y_u^{\mathcal{S}} v/\Lambda = \mathcal{O}(1)$ are in perfect agreement with a modest vev and a reasonable cutoff. Thus, we can express all $\mathcal{S}$-Yukawas in terms of $y_u^{\mathcal{S}}$. We obtain the approximate relations

$$y_e^{\mathcal{S}} = y_d^{\mathcal{S}}/10 = y_u^{\mathcal{S}}/5 \tag{4.28}$$

for the couplings of the mediator to SM fermions using $m_u \simeq 2.5\,\mathrm{MeV}$, $m_d \simeq 5\,\mathrm{MeV}$ and $m_e \simeq 0.5\,\mathrm{MeV}$. As mentioned, the value of $y_u^{\mathcal{S}}/\Lambda$ can be chosen freely, however it should not violate perturbativity of the EFT and potential UV completions. This induces the constrains $y_f^{\mathcal{S}} v/(\sqrt{2}\Lambda) < 4\pi$, and $y_f^{\mathcal{S}} < 16\pi^2$ respectively, with $f = u,\, d,\, e$, where we made use of the fact that $y_f^{\mathcal{S}} \sim g_{\mathrm{UV}}^2$.

Relevant Parameters In the nest sections, we will derive the prospects to constrain the $\mathbb{Z}_2$-symmetric bi-quadratic portal $\mathcal{S}^2\bar{\chi}\chi$, and the $\mathcal{S}$-Yukawa couplings from LHC and future (e^+e^-) collider data. Those results will be combined with constraints from DD and the observed relic density. For an overview we summarize the relevant physical parameters for the model at hand:

- the mediator mass $m_{\mathcal{S}} = \sqrt{\mu_{\mathcal{S}}^2 + 3\lambda_{\mathcal{S}}\, v_{\mathcal{S}}^2}$
- the DM mass m_χ
- the bi-quadratic portal coupling $y_\chi^{\mathcal{S}}/\Lambda$
- the $\mathcal{S}-$Yukawa coupling $y_u^{\mathcal{S}}/\Lambda$.

We neglected the potential scalar mixing from $\lambda_{H\mathcal{S}}$. While this defines the main model being studied in the following sections, there are also two interesting variants obtained by either assigning positive $\mathbb{Z}_2$ parity to all leptons or to all quarks. This will lead to a *leptophobic* or *hadrophobic* mediator, respectively, with $y_e^{\mathcal{S}} = 0$ and finite $y_d^{\mathcal{S}} = 2y_u^{\mathcal{S}}$ or vice versa.

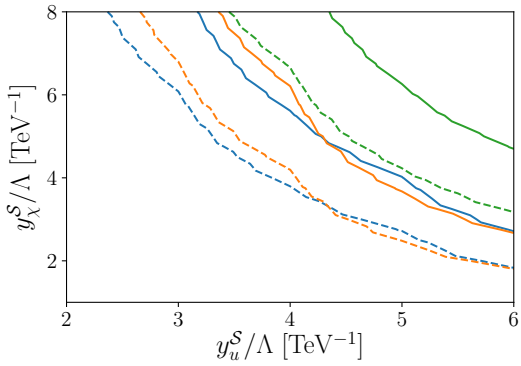

Figure 4.17: Exclusion reach of the current LHC run (solid) and projections for the future HL-LHC (dashed) both for $m_{\mathcal{S}} = 200\,\text{GeV}$ and DM masses of 5 GeV (blue), 100 GeV (yellow) and 300 GeV (green) derived from [77].

4.3.1 (HL-)LHC searches

A unique signature to constrain $y_\chi^{\mathcal{S}}$, is di-jet plus $\not{E}_T$ with the Feynman-diagrams shown in Fig. 4.18 by replacing the electrons with up or down quarks. To derive bounds from current and projected LHC runs on the new DM portal, we employ CheckMate [135, 277] implementations of ATLAS analyses. In particular we considered the mono-jet search in Ref. [77] using 36.1 fb^{-1} of data and a SUSY motivated search for multiple jets plus $\not{E}_T$ in Ref. [317].

Although a dedicated analysis of the particular di-jet topology is expected to improve the sensitivity, we refrain from setting up a custom analysis, and leave a detailed study for future work. We rather focus on a specific analysis for future lepton colliders, where in particular the large QCD backgrounds faced at the LHC are absent. In addition the limits can be obtained more reliably and are expected to be stronger. The final state appears similar to that of Higgs-to-invisible searches in VBF production. However, we find that the signal and background distributions in the important kinematic variables are very similar. Therefore, via this analysis no efficient separation is possible.

Regarding the two aforementioned ATLAS analyses, the latter one naively delivers stronger constraints. However, this analysis uses events with energies above the envisaged cutoff $\Lambda = \mathcal{O}(1)$ TeV, such that the EFT validity becomes questionable [50, 247, 318]. The scalar sum of the transverse momenta of the leading jets and $\not{E}_T$ is required to be at least 1.6 TeV. Therefore, a reasonable value for the cut-off would be $\Lambda \gtrsim 3\,\text{TeV}$, thus strongly suppressing the signal. In addition, all signal-regions are inclusive, which means they include events with arbitrary high energies. Therefore, the resulting constraints would only be valid for borderline large values of $y_u^{\mathcal{S}}$. In contrast, exclusive signal regions (EM) provided in the mono-jet analysis [77] allow for a better estimate of the momentum flow of an event. To obtain robust limits we constrain our analysis to signal regions up to EM6 of Ref. [77], containing events with $\not{E}_T = (600 - 700)\,\text{GeV}$.

The signal events are simulated with MadGraph5_aMC@NLO 2.6.5 [140], employing a UFO [319] file of the eDMEFT, generated with FeynRules [320, 321]. The parton-showering is done with Pythia 8.1 [278, 279] and the detector simulation with Delphes 3.4.1 [148], with the latter two run internally in CheckMATE 2.0.26 [135, 277].

The actual bounds on the couplings and the prospects for the HL-LHC with a luminosity of 3 ab^{-1} are shown in Fig. 4.17 as solid and dashed lines, respectively, for $m_{\mathcal{S}} = 200\,\text{GeV}$

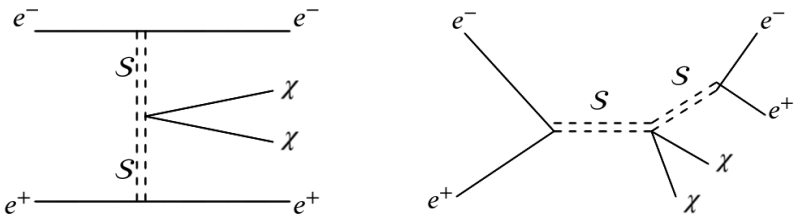

Figure 4.18: Feynman diagrams for $\chi\bar{\chi} + e^+e^-$ production at CLIC — for the LHC case, the electrons can be replaced with up or down quarks.

and three different DM masses, $m_\chi = (5,\, 100,\, 300)\,\text{GeV}$.[6] To obtain the projections, we used the r-value defined in CheckMate with upscaled event numbers, thus assuming a similar background-only like event distribution. Following Ref. [323], we further assume that the systematic uncertainty on the SM background can be lowered by a factor of four. Interestingly, due to the nature of the process, an internal mediator radiating off two DM particles, the limits do not vanish for $m_\chi > m_\mathcal{S}/2$, allowing this mass hierarchy to be tested, typically unaccessible for collides, as laid out in Sec. 4.1.2.

We carefully estimated the effects of gauge boson couplings induced by light quark loops. Even featuring $y_u^\mathcal{S}/\Lambda = \mathcal{O}(1)/v$, those loops are suppressed by a quark mass insertion, due to the required chirality flip. As a consequence, the partial width of $\mathcal{S}$ to photons (gluons) is smaller than the corresponding Higgs width by a factor of $\mathcal{O}(10^5)$ ($\mathcal{O}(10^3)$). Therefore, the contribution of gluon-fusion to the production cross section can be neglected. The width to photons is more strongly suppressed, since the W-loop dominating partial width of the SM Higgs [275], is absent. In addition, the $\text{BR}(\mathcal{S} \to \gamma\gamma)$ is suppressed by the large decay width of $\mathcal{S}$ to quarks leading to no relevant constraints from present di-photon searches, see e.g. [286].

4.3.2 CLIC Prospects

An interesting proposal for a next high-energy e^+e^- collider facility is the Compact Linear Collider (CLIC) at CERN. It would be the first mature realization of a collider with these characteristics and could start running in 2035. In this section, we will analyze the prospects of probing $y_\chi^\mathcal{S}$ at the three foreseen stages of CLIC. Stage I features $\sqrt{s} = 380\,\text{GeV}$ with an envisaged luminosity of $1\,\text{ab}^{-1}$, stage II $\sqrt{s} = 1.5\,\text{TeV}$ with $2.5\,\text{ab}^{-1}$ and stage III $\sqrt{s} = 3\,\text{TeV}$ with $5\,\text{ab}^{-1}$, respectively [324, 325].

To test the $\mathbb{Z}_2$ symmetric portal, we propose a search in the $e^+e^- + \not{E}_T$ final state with the signal processes depicted in Fig. 4.18, where the right one dominates the cross section for large parts of the parameter space. The background is mainly given by the irreducible process $e^+e^- \to e^+e^-\,\bar{\nu}\nu$, with the most important contribution from ZZ intermediate states, while further backgrounds are found to be negligible [326]. To obtain signal and background samples, we employ again MadGraph5_aMC@NLO 2.6.5 [140] at leading order for generating parton level events, Pythia 8.1 for hadronization and Delphes 3 for a fast detector simulation using the CLIC card [148]. The cuts for the final analysis are implemented within MadAnalysis5 [149,150].

When $\mathcal{S}$ couples to electrons and quarks with the couplings related as in Eq. (4.28), the

[6] While with this choice the considered flavor model is viable, note that for $m_\mathcal{S} \gtrsim 225\,\text{GeV}$ strong bounds on $y_u^\mathcal{S}/\Lambda$ arise from the ATLAS search for di-lepton resonances [322]. Those bounds would exceed the projected limits in Fig. 4.17. Clearly, this can be avoided by moving either to the leptophobic or the hadrophobic scenario.

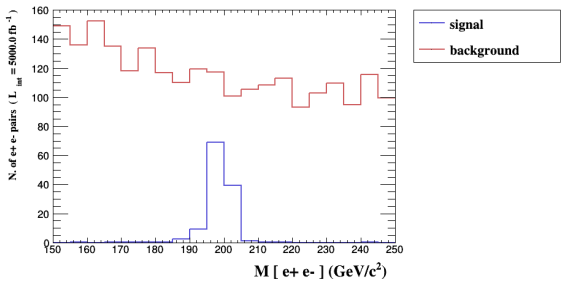

Figure 4.19: Comparison of signal and background shape in m_{ee} for CLIC stage III. The signal corresponds to $y_e^{\mathcal{S}}/\Lambda = 1.5/\text{TeV}$ and $y_\chi^{\mathcal{S}}/\Lambda = 0.25/\text{TeV}$, close to the later derived exclusion limit.

$\not{E}_T$	m_{ee}	$p_T(e)$	$\Delta R(e^+e^-)$	$\theta(e^+)$	$\theta(e^-)$
$> 80\,\text{GeV}$	$> 150\,\text{GeV}$	$> 25\,\text{GeV}$	< 3.25	> 0.6	< 2.4

Table 4.1: Cuts for the signal region for all CLIC stages applied throughout our analysis.

signal process is suppressed as $\mathcal{S}$ dominantly decays to quarks, which significantly increases the total width. Therefore we focus on the hadrophobic case, with $y_d^{\mathcal{S}} = y_u^{\mathcal{S}} = 0$. While it would be interesting to consider the di-jet final state also at CLIC or to constrain the bi-quadratic portal at an *ep* collider for example, these analyses face their own challenges and will be left for future work. Still, a small signal is hidden within a sizable background, leading to weak constraints from a pure cut-and-count analysis, in particular when a systematic uncertainty in the background normalization is taken into account. To improve this, we make use of the fact that the signal features a peak in the spectrum of the invariant electron mass, m_{ee}, while the background is smoothly falling, see Fig. 4.19. To do this we perform a shape analysis with a binned likelihood function. This also reduces the impact of the uncertainty of the background normalization. Details to this procedure are laid out in App. B. The peak is caused by on-shell $\mathcal{S}$ decays to an electron pair, as the resonant diagram in the right panel of Fig. 4.18 dominates the cross section. To achieve a preliminary separation of signal and background events, we apply the cuts given in Tab. 4.1, where the cut on m_{ee} is applied to lower the impact of Z decays. In Fig. 4.19 the shapes of the signal and background after cuts, and before fitting are shown for stage III and $y_e^{\mathcal{S}}/\Lambda = 1.5/\text{TeV}$, and $y_\chi^{\mathcal{S}}/\Lambda = 0.25/\text{TeV}$ chosen to be close to the exclusion limit derived below.

Fitting Signal and Background In order to use the m_{ee} spectrum to discriminate signal and background, we generate sizable Monte-Carlo samples of both processes with 50.000 and 10^6 events, respectively. Since the signal shape depends on the width of $\mathcal{S}$, it is simulated for various values of the latter depending non-trivially on the input parameters given at the end of Sec. 4.3, where $m_{\mathcal{S}}$ and $y_e^{\mathcal{S}}$ have the greatest impact. The background spectrum is fitted to a fourth order polynomial, and the signal spectrum to a Breit-Wigner distribution. The signal is characterized by the total number of events and the width of the Breit-Wigner distribution allowing several coupling values to be easily tested.

Limits To establish constraints on the model parameters, we translate limits on the signal-strength modifier, μ, into limits for the former. Details are given in App. B. For fixed $y_e^{\mathcal{S}}$ and

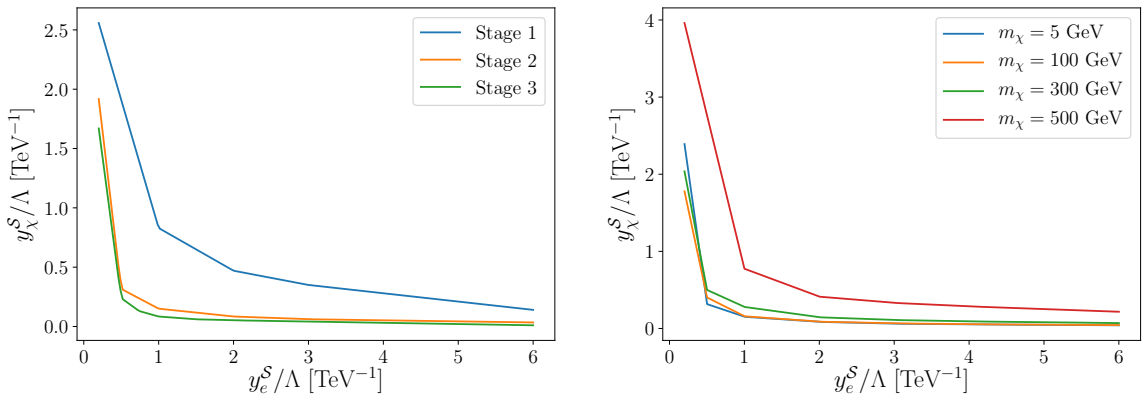

Figure 4.20: Left panel: Comparison of the expected limits on the couplings obtained at the three stages of CLIC, assuming $m_{\mathcal{S}} = 200\,\text{GeV}$ and $m_\chi = 5\,\text{GeV}$.
Right panel: Expected limits on the couplings obtained at the second stage of CLIC, with $\sqrt{s} = 1.5\,\text{TeV}$, for $m_{\mathcal{S}} = 200\,\text{GeV}$ and several dark matter masses.

thereby fixed width and shape of the m_{ee} distribution, we have $\mu = (y_\chi^{\mathcal{S}}/\Lambda)^2$. For all limits we take a 5 % uncertainty on the background normalization into account, i.e. $\sigma_B = 0.05$, while the signal uncertainty σ_S is taken to be negligible.

In the left panel of Fig. 4.20, we compare the reach of the three CLIC stages on the couplings, assuming $m_{\mathcal{S}} = 200\,\text{GeV}$ and $m_\chi = 5\,\text{GeV}$. Already the first stage would be sensitive to $\mathcal{O}(1/\text{TeV})$ couplings, while at the later stages the reach extends well beyond a TeV^{-1}. In the right panel of Fig. 4.20 we show the expected limits obtained with stage II for fixed $m_{\mathcal{S}} = 200\,\text{GeV}$ and four values for m_χ. Similar to the LHC analysis this plot demonstrates that the sensitivity does not vanish for $m_\chi > m_{\mathcal{S}}/2$. Thus, the operator under consideration allows the testing of a mass hierarchy typically inaccessible for collider studies, see Sec. 4.1.2.

We further note that direct searches for the mediator, e.g. in the e^+e^- final state, could break the degeneracy between the two couplings. It may happen that the mediator would first be found via such a resonance search. However, in this case the present analysis would be crucial to further investigate the structure of the dark sector.

4.3.3 Dark Matter Phenomenology

As discussed in Sec. 4.1.1, the relic density can be set via the annihilation process $\bar{\chi}\chi \to \mathcal{S}^2$ for $m_{\mathcal{S}} \lesssim m_\chi$. Since annihilations to SM fermions via $\mathcal{S}$ induced by $v_{\mathcal{S}} > 0$ are found to be negligible, even in the pole region, for $m_{\mathcal{S}} > m_\chi$ no efficient annihilation channel to set the relic density is accessible. This is illustrated in the left panel of Fig. 4.21, where the viable parameter region with $0.11 < h^2\Omega_{\text{DM}} < 0.13$ is shown in blue in the $m_{\mathcal{S}}$–m_χ plane for $y_\chi^{\mathcal{S}} = 2.25$.

We also consider bounds from DD. Mediators with $m_{\mathcal{S}} \lesssim 200\,\text{GeV}$ (left of the green line) are already excluded by the XENON1T experiment [327], and heavier ones will be tested in future experiments as LZ [328] (red line) and DARWIN [329] (remaining region). The dominant contribution to DD rates arises from s-channel exchange of $\mathcal{S}$ at tree-level with up and down quarks, and therefore vanishes in the hadrophobic case. Since $v_{\mathcal{S}} \propto 1/y_f^{\mathcal{S}}$, the tree-level cross section is independent of the $\mathcal{S}$-Yukawa couplings.

Finally, the required values of $y_\chi^{\mathcal{S}}$ as a function of m_χ are shown in the right panel of Fig. 4.21

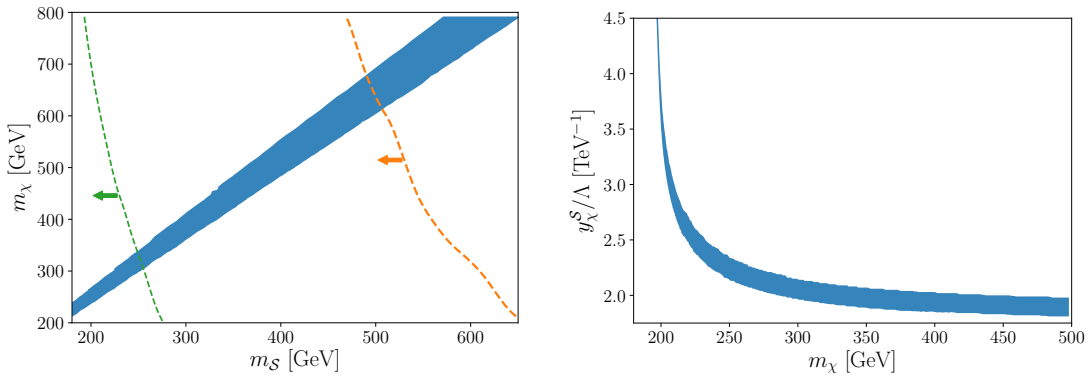

Figure 4.21: Left panel: Band of relic density $0.11 < h^2\Omega_{\rm DM} < 0.13$ (dark blue) for $y_\chi^\mathcal{S} = 2.25$, independent of $y_{u,d,e}^\mathcal{S}$. Exclusions from XENON1t (left of green line) and the LZ projection (left of orange line) are superimposed (which however are not present for the hadrophobic model). The remaining space can be tested with DARWIN. Right panel: Band of relic density $0.11 < h^2\Omega_{\rm DM} < 0.13$ for $m_\mathcal{S} = 200\,\text{GeV}$.

for $m_\mathcal{S} = 200\,\text{GeV}$. Note that also the relic density is independent of the values of $y_{u,e}^\mathcal{S}$, which do not enter the dominant annihilation amplitude. We find by comparing with the results in Fig. 4.20, that the viable parameter space could be tested at CLIC, besides very small values of $y_e^\mathcal{S}$. All numerical results in this section have been obtained with micrOmegas 5.0.8 [205, 270].

4.4 The Xenon1t Excess

In this section, we take a small detour to see if, and how, the excess in the low-energy electron recoil spectrum, recently announced by the XENON1T collaboration, could be explained in a slightly extended version of the eDMEFT.

The excess is observed in the energy range between $1 - 5\,\text{keV}$ and could point towards new physics [330]. An interpretation of the data in terms of a neutrino magnetic moment or solar axions, although being in tension with bounds from stellar physics, finds substantial statistical improvements over the background-only hypothesis with significances above 3σ. Nevertheless, it is clearly too early to celebrate the discovery of BSM physics, since a contamination with tritium, contributing to the recoil spectrum via its beta decays, cannot be excluded with the current understanding of the experiment. Still, it is of great interest to examine alternative explanations for this excess, and identify independent experimental probes that could confirm or refute this excess. As the excess is observed in a small number of bins above the threshold, only theories that predict a highly localized energy deposit, or an IR-dominated recoil spectrum can account for the observation. The announcement caused great interest, and several explanations have been proposed. They range from new neutrino properties [331–341], via non-standard DM scenarios [342–356] to more exotic explanations [357–362].

We attempt to characterize the XENON1T excess in a slightly expanded version of eDMEFT, introduced in Sec. 3.3.1. The setup is extended by a two spontaneously broken $\mathbb{Z}_2^{e,\nu}$ symmetry, under which neutrinos and electrons are charged. In this approach, the eDMEFT naturally includes the appropriate ingredients for explaining the excess, namely modified neutrino interactions with electrons, via a potentially light new scalar sector. The induced non-trivial

couplings of the new scalars allow the excess to be related to the observed electron and neutrino masses. As laid out in Sec. 4.3, the considered leptophilic variant is unconstrained from DD, via nucleon interactions, and thus invites searches employing electronic recoil.

In Sec. 4.4.1 details about the setup used in the analysis are discussed. Then in Sec. 4.4.2, fits to the XENONT1T electron recoil excess are presented, first assuming neutrino-electron scattering, and second DM-electron scattering as its origin. There, we also examine whether the correct DM relic abundance can be achieved consistently with our fits. Subsequently, in Sec. 4.4.3, the neutrino explanation is confronted with stringent limits on new electron and neutrino interactions from terrestrial and astrophysical observations. We identify benchmark points and non-trivial mechanisms to avoid the severe constraints. Also the case of free couplings is considered corresponding to a subset of eDMEFT operators, to characterize viable parameter regions. This section follows Ref. [266].

4.4.1 General Setup

We extend the scalar sector of the leptophilic eDMEFT from Eq. (4.19) by assuming a second $\mathbb{Z}_2$ symmetry. One of the symmetries is shared by the neutrinos and the other by the electron. Both are then broken by the small vevs of two distinct scalars $\mathcal{S}_{\nu,e}$, which allow the simultaneous generation of the tiny neutrino masses, and the small electron mass. The corresponding Lagrangian following the convention from Eq. (4.19) reads

$$\begin{aligned}\mathcal{L}_{\text{eff}}^{\mathcal{S}\chi} =& \mathcal{L}_{\text{SM}'} + \tfrac{1}{2}(\partial_\mu \mathcal{S}_\ell \partial^\mu \mathcal{S}_\ell - \mu_\ell^2 \mathcal{S}_\ell^2) + \bar{\chi} i\partial\!\!\!/ \chi - m_\chi \bar{\chi}\chi \\ & - \tfrac{1}{4}\lambda_\ell \mathcal{S}_\ell^4 - \lambda_{\nu e}\, \mathcal{S}_\nu^2 \mathcal{S}_e^2 - \lambda_{H\mathcal{S}_\ell} |H|^2 \mathcal{S}_\ell^2 \\ & - \frac{1}{\Lambda}\Big[\left(Y_\nu^{\mathcal{S}}\right)_{ij} \mathcal{S}_\nu\, \bar{L}_L^i H \nu_R^j + \left(Y_e^{\mathcal{S}}\right)_i \mathcal{S}_e\, \bar{L}_L^i H e_R + \text{h.c.}\Big] \\ & - \frac{y_\chi^{\mathcal{S}_\ell}\, \mathcal{S}_\ell^2 + y_\chi^H |H|^2}{\Lambda}\, \bar{\chi}_L \chi_R + \text{ h.c.},\end{aligned} \tag{4.29}$$

where a summation over $\ell = \nu, e$ is implied, and $\mathcal{L}_{\text{SM}'}$ denotes the SM Lagrangian without the Yukawa couplings of the electron.

Importantly, both mediators develop small vevs $|\langle \mathcal{S}_\ell \rangle| \equiv v_\ell \ll v$, which break the $\mathbb{Z}_2^\ell$ symmetries carried by all right-handed neutrinos and the right-handed electron, respectively, and thereby generate their masses. The mixings with the SM Higgs via the $|H|^2\mathcal{S}_\ell^2$ operators have to be small, and this effect will not be considered in this section. The conventional DM interaction $\mathcal{S}_\ell\, \bar{\chi}\chi$ is generated with a coefficient $\sim 2y_\chi^{\mathcal{S}_\ell} v_\ell/\Lambda$, which remains relevant for the analysis. Finally, the coefficient y_χ^H is again assumed to be negligibly small to evade DD constraints and limits from Higgs-to-invisible decays [110, 303, 309, 315].

Masses, Mixing, and Free Parameters To fully define our setup, we will study the fermion and scalar mass spectrum, and summarize the relevant free parameters.

The fermion mass terms after electroweak and $\mathbb{Z}_2^\ell$ symmetry breaking read

$$\mathcal{L} \supset -\sum_{\ell=e,\nu} \frac{v}{\sqrt{2}}\, \bar{\ell}_L \left(Y_\ell^H + \frac{v_\ell}{\Lambda} Y_\ell^{\mathcal{S}}\right) \ell_R \equiv -\sum_{\ell=e,\nu} \bar{\ell}_L M^\ell \ell_R\,, \tag{4.30}$$

where $\ell_{L,R} = e_{L,R}$, $\nu_{L,R}$ are three-vectors in flavor space and the Yukawa matrices

$$Y_\nu^{\mathcal{S}} = \begin{pmatrix} (y_\nu^{\mathcal{S}})_{11} & (y_\nu^{\mathcal{S}})_{12} & (y_\nu^{\mathcal{S}})_{31} \\ (y_\nu^{\mathcal{S}})_{21} & (y_\nu^{\mathcal{S}})_{22} & (y_\nu^{\mathcal{S}})_{32} \\ (y_\nu^{\mathcal{S}})_{31} & (y_\nu^{\mathcal{S}})_{32} & (y_\nu^{\mathcal{S}})_{33} \end{pmatrix}, \qquad Y_\nu^H = \mathbf{0}, \tag{4.31}$$

$$Y_e^{\mathcal{S}} = \begin{pmatrix} (y_e^{\mathcal{S}})_1 & 0 & 0 \\ (y_e^{\mathcal{S}})_2 & 0 & 0 \\ (y_e^{\mathcal{S}})_3 & 0 & 0 \end{pmatrix}, \qquad Y_e^H = \begin{pmatrix} 0 & y_{12}^e & y_{13}^e \\ 0 & y_{22}^e & y_{23}^e \\ 0 & y_{32}^e & y_{33}^e \end{pmatrix}, \tag{4.32}$$

reflect the $\mathbb{Z}_2^\ell$ assignments. Without breaking these symmetries via $v_\ell > 0$, the electron and neutrinos would remain massless, corresponding to vanishing eigenvalues of Y_ℓ^H, similar to the discussion in Sec. 4.3. On the other hand, a small breaking of $v_\nu \sim \mathcal{O}(\text{eV})$ and $v_e \sim \mathcal{O}(\text{MeV})$ is sufficient to generate $m_\nu \sim 0.1\,\text{eV}$ and $m_e \sim 0.5\,\text{MeV}$ with natural values of $y_\ell^{\mathcal{S}} \lesssim \mathcal{O}(1)$ and $\Lambda \gtrsim 1\,\text{TeV}$. To explain the XENONT1T excess in the light of various constraints, it will be necessary to deviate from these natural scales, remaining with a partial explanation of light-fermion masses.

After performing a rotation to the mass basis,

$$\begin{aligned} M^\nu &= U_L^\nu\, M_{\text{diag}}^\nu\, U_R^{\nu\,\dagger}, & M_{\text{diag}}^\nu &= \text{diag}(m_{\nu^1},\, m_{\nu^2},\, m_{\nu^3}), \\ M^e &= U_L^e\, M_{\text{diag}}^e\, U_R^{e\,\dagger}, & M_{\text{diag}}^e &= \text{diag}(m_e,\, m_\mu,\, m_\tau), \end{aligned} \tag{4.33}$$

with $U_L^e = U_L^\nu\, V_{\text{PMNS}}$, the couplings of the physical leptons to the SM Higgs and the scalar mediators are given by

$$\mathcal{L} \supset -\sum_{\ell=e,\nu} \bar{\ell}_L \left(\frac{\hat{Y}_\ell^H + v_\ell\, \hat{Y}_\ell^{\mathcal{S}}/\Lambda}{\sqrt{2}}\; h + \frac{v\, \hat{Y}_\ell^{\mathcal{S}}}{\sqrt{2}\Lambda}\; \mathcal{S}_\ell \right) \ell_R, \tag{4.34}$$

where $\hat{Y}_\ell^s = U_L^{\ell\,\dagger}\, Y_\ell^s\, U_R^\ell$ for $s = H$, $\mathcal{S}$, and (with some abuse of notation), we denote the mass eigenstates by the same spinors $\ell = e$, ν. The Yukawa matrices in the mass basis can be expressed as

$$\hat{Y}_\ell^{\mathcal{S}} = \frac{\sqrt{2}\Lambda}{v v_\ell}\, M_{\text{diag}}^\ell\, U_R^{\ell\,\dagger} C_\ell^S\, U_R^\ell, \qquad \hat{Y}_\ell^H = \frac{\sqrt{2}}{v}\, M_{\text{diag}}^\ell\, U_R^{\ell\,\dagger} C_\ell^H\, U_R^\ell, \tag{4.35}$$

where $C_e^S = \text{diag}(1,0,0)$, $C_\nu^S = \text{diag}(1,1,1)$, $C_e^H = \text{diag}(0,1,1)$ and $C_\nu^H = \mathbf{0}$. The unitary rotations of the left-handed leptons drop out, since they share the same $\mathbb{Z}_2^\ell$ charges. Their couplings with a fixed right-handed lepton are thus aligned with the corresponding mass terms. While this is not true for the right-handed leptons, here the Yukawa matrices starting from M_{diag}^ℓ can be chosen such that $U_R^e = \mathbb{I}$, thus avoiding possible FCNCs. We arrive at

$$\begin{aligned} \hat{Y}_\nu^{\mathcal{S}} &= \frac{\sqrt{2}\Lambda}{v v_\nu}\, \text{diag}(m_{\nu^1},\, m_{\nu^2},\, m_{\nu^3}), & \hat{Y}_\nu^H &= \mathbf{0}, \\ \hat{Y}_e^{\mathcal{S}} &= \frac{\sqrt{2}\Lambda}{v v_e}\, \text{diag}(m_e,\, 0,\, 0), & \hat{Y}_e^H &= \frac{\sqrt{2}}{v}\, \text{diag}(0,\, m_\mu,\, m_\tau). \end{aligned} \tag{4.36}$$

As a consequence, muons and taus interact with the Higgs as in the SM, while electrons and neutrinos couple only to $\mathcal{S}_e$, or $\mathcal{S}_\nu$ respectively. The strength of this interactions is determined

by inverse powers of the free parameters v_e, and v_ν, which can be traded for $\mathrm{y}_e^{\mathcal{S}}/\Lambda \equiv (\hat{Y}_e^{\mathcal{S}})_{11}/\Lambda$, and $\mathrm{y}_1^{\mathcal{S}}/\Lambda$ with $\mathrm{y}_i^{\mathcal{S}}/\Lambda \equiv (\hat{Y}_\nu^{\mathcal{S}})_{ii}/\Lambda$, respectively.

In addition to fermion mixing, the term $\sim\lambda_{\nu e}$ in the scalar potential leads to mixing between the scalar singlets after they obtain their vevs, v_ℓ. The rotation to the mass eigenstates s and S can be described with the mixing angle θ as

$$\begin{pmatrix} s \\ S \end{pmatrix} = \begin{pmatrix} \cos\theta & \sin\theta \\ -\sin\theta & \cos\theta \end{pmatrix} \begin{pmatrix} \mathcal{S}_\nu \\ \mathcal{S}_e \end{pmatrix} \qquad \text{with} \qquad \tan 2\theta = \frac{4\,\lambda_{\nu e} v_\nu v_e}{M_\nu^2 - M_e^2}, \tag{4.37}$$

where $M_\ell^2 = \mu_\ell^2 + 3\lambda_\ell v_\ell^2 + 2\lambda_{\nu e}\, v_\nu^2 v_e^2/v_\ell^2$. The resulting physical masses read

$$m_{s/S}^2 = \frac{M_\nu^2 + M_e^2}{2} \pm \frac{M_\nu^2 - M_e^2}{2\,\cos 2\theta}. \tag{4.38}$$

The lightness of the neutrinos compared to the charged lepton suggests to take $v_\nu \ll v_e$ and accordingly $M_\nu \ll M_e$. This leads to $m_s \approx M_\nu$, $m_S \approx M_e$ and $c_\theta \approx 1$, $s_\theta \ll 1$. The mixing induces suppressed couplings between the electron and the light s, as well as between the neutrinos and the heavy S, given by

$$\begin{aligned} \mathcal{L}_{\text{mix}} = &- \frac{v\,s}{\sqrt{2}\Lambda}\left(c_\theta\,\mathrm{y}_i^{\mathcal{S}}\,\bar{\nu}_L^i \nu_R^i + s_\theta\,\mathrm{y}_e^{\mathcal{S}}\,\bar{e}_L e_R\right) \\ &- \frac{v\,S}{\sqrt{2}\Lambda}\left(c_\theta\,\mathrm{y}_e^{\mathcal{S}}\,\bar{e}_L e_R - s_\theta\,\mathrm{y}_i^{\mathcal{S}}\,\bar{\nu}_L^i \nu_R^i\right). \end{aligned} \tag{4.39}$$

For brevity we denote the couplings of electrons and the first neutrino to the mediators by

$$\begin{aligned} y_e^s &\equiv \frac{v}{\sqrt{2}\Lambda}\,s_\theta\,\mathrm{y}_e^{\mathcal{S}}, \qquad & y_\nu^s &\equiv \frac{v}{\sqrt{2}\Lambda}\,c_\theta\,\mathrm{y}_1^{\mathcal{S}}, \\ y_e^S &\equiv \frac{v}{\sqrt{2}\Lambda}\,c_\theta\,\mathrm{y}_e^{\mathcal{S}}, \qquad & y_\nu^S &\equiv -\frac{v}{\sqrt{2}\Lambda}\,s_\theta\,\mathrm{y}_1^{\mathcal{S}}. \end{aligned} \tag{4.40}$$

Before moving to the fits and experimental constraints, we summarize the relevant, free parameters of the setup, which are

- the mediator masses $m_{s,S} \approx M_{\nu,e}$
- the $\mathcal{S}_{e,\nu}$ Yukawa couplings $\mathrm{y}_{e,i}^{\mathcal{S}}/\Lambda$
- the mixing portal $\lambda_{\nu e}$
- the DM mass m_χ
- the bi-quadratic DM portal $y_\chi^{\mathcal{S}_\ell}/\Lambda$,

and the remaining Yukawa couplings are given in Eq. (4.36).

4.4.2 Fitting the XENON1T Excess

In this part, the XENON1T excess is fitted by considering two possible explanations: first neutrino-electron and second DM-electron scattering. Furthermore, we examine if the DM relic abundance can be obtained simultaneously to these explanations.

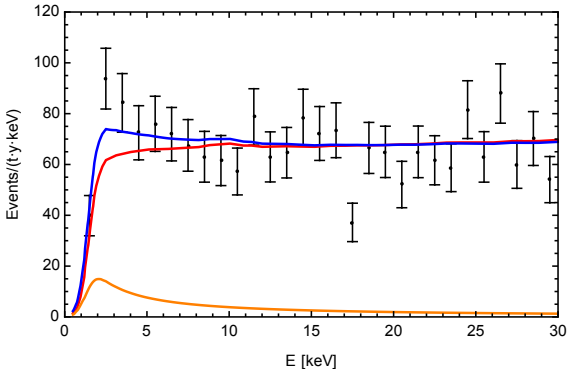

Figure 4.22: Comparison between an exemplary differential event rate for a scalar with $m_s = 60\,\text{eV}$ and $\sqrt{y_e^s\, y_\nu^s} = 7.9\times10^{-7}$, corresponding to the best fit point, and the observations in [330]. The full differential event rate is shown in blue, while the pure signal (background) contribution is depicted in orange (red).

Modified Neutrino Interactions We start by assuming that the excess is explained by neutrino-electron scatterings mediated by s and S. As we will see observational constraints prefer $m_s \ll m_S$, such that in good approximation the scattering can be described by s-exchange alone. The differential cross section for this new-physics signal reads [363]

$$\frac{d\sigma_{\nu e}}{dE_r} = \frac{(y_e^s\, y_\nu^s)^2}{4\pi(2m_e E_r + m_s^2)^2}\,\frac{m_e^2\, E_r}{E_\nu^2}, \tag{4.41}$$

where m_e is the electron mass, E_ν the incoming neutrino energy and E_r the electron recoil energy. The true differential event rate is given by convoluting the differential cross section and the incident neutrino flux, ϕ_ν, weighted by the number of electrons per unit mass N_e, as

$$\frac{dR}{dE_r} = N_e \int dE_\nu\, \frac{d\sigma_{\nu e}}{dE_r}\,\frac{d\phi_\nu}{dE_\nu}. \tag{4.42}$$

At the energy of the XENON1T excess, the neutrino flux is dominated by solar pp neutrinos. We use the observed pp-flux from [364], and employ the parameterization of the spectrum from [365].

Here we assume a universal interaction between s and the different neutrino flavors, such that oscillation effects do not affect the scattering rate. More details are given below. To connect our theoretical spectrum with the observed rate the detector efficiency reported in [330] is applied. In addition the limited detector resolution is taken into account via a gaussian smearing function with an energy dependent resolution. As suggested in [366] we take the ansatz

$$\frac{\sigma(E)}{E} = \frac{a}{\sqrt{E}} + b, \tag{4.43}$$

and assume that the resolution varies between $\sim$30% at $E_r = 1\,\text{keV}$ and $\sim$6% at 30 keV. The best fit background model from [330] is adopted allowing the normalization to vary within the 1σ range. In order to assess the impact of a light scalar on the electron neutrino scattering, a χ^2 analysis of the signal and background model is performed. We find that

$$\sqrt{y_e^s\, y_\nu^s} \approx 7.9\times10^{-7} \tag{4.44}$$

is preferred with very little dependence on m_s for $m_s \lesssim 20\,\text{keV}$. An exemplary comparison between data and the signal associated with the best fit point at $m_s = 60\,\text{eV}$, is shown in Fig. 4.22. This choice of parameters corresponds to $\chi^2_{\text{best}} = 38.9$ compared to $\chi^2_{\text{bg}} = 47.1$ for the background-only hypothesis. Our results are in good qualitative agreement with those in [331–333], which study a related setup. We will confront our results with a comprehensive set of complementary experimental constraints in Sec. 4.4.3.

DM Scattering and Relic Abundance Dark matter scattering on electrons in the detector could also account for the observed excess. Since the model contains a DM candidate, it is interesting to check whether the correct relic abundance can be achieved simultaneously, with an explanation of the XENON1T excess. These observables are correlated with each other, also in case of the neutrino explanation, via the mediator couplings to SM fermions.

A naive estimate of the maximum recoil energy in non-relativistic DM-electron collisions leads to

$$E_{r,\text{max}} = \frac{2\,\mu_{\chi e}^2\, v_{\text{max}}^2}{m_e} \approx 2\times 10^{-6}\, m_e, \tag{4.45}$$

where $\mu_{\chi e}$ is the reduced mass of the system and v_{max} is the maximum DM velocity. For $m_\chi \gg m_e$, and taking into account that the velocity is limited by the local escape velocity of our galaxy $v_{\text{max}} \sim v_{\text{esc}} \sim \mathcal{O}(10^{-3}\, c)$, this leads to an estimate of $E_{\text{r,max}} \approx 1\,\text{eV}$, and thus well below the energy scale required to account for the signal. However, it is important to consider that the electrons are part of a bound system, the xenon atom. Therefore, the electron momentum is not zero, and a typical value is expected to be $\mathcal{O}(\alpha_{em} m_e)$, which is small but allows for a larger energy transfer in the DM-electron scattering process [367]. Then the differential event rate is given by

$$\frac{dR}{dE_r} = \frac{n_{\text{Xe}}\,\rho_\chi}{m_\chi}\,\frac{d\langle\sigma_{\chi e}\rangle}{dE_r}, \tag{4.46}$$

where n_{Xe} is the number of xenon atoms per unit mass in the detector and $\rho_\chi \approx 0.3\,\text{GeV/cm}^3$ the local DM density. For the velocity-averaged differential cross section, we rely on the results of [368, 369]. In the limit where the mass of the mediator is much bigger than the t-channel momentum transfer, it can be parametrized as

$$\frac{d\langle\sigma_{\chi e}\rangle}{dE_r} = \frac{\sigma_{\chi e}}{2m_e}\int dv\,\frac{f(v)}{v}\int dq\, a_0^2\, q\, K(E_r, q), \tag{4.47}$$

where $\sigma_{\chi e}$ is the cross section for scattering on a free electron with a momentum transfer $a_0^{-1} = \alpha_{em} m_e$, while $f(v)$ denotes the DM velocity distribution on Earth. The atomic physics is encoded in the excitation factor K, originally computed in [368]. In order to estimate the implications of a DM signal, we consider the averaged cross sections reported in [369], and perform a fit to the signal using the same assumptions about the detector as in the neutrino case.

The best fit to the differential recoil rate that we found is shown in Fig. 4.23. It corresponds to $m_\chi = 10\,\text{GeV}$ and $\sigma_{\chi e} \approx 1.25\times 10^{-39}\,\text{cm}^2$, which could for instance be explained by an MeV scale mediator with an $\mathcal{O}(1)$ coupling to DM and $y_e^S \sim 10^{-5}$. The signal rises very steeply at low energies such that the peak occurs at $\sim 1.5\,\text{keV}$ instead of the $\sim 2.5\,\text{keV}$ needed to reproduce the data. While it is interesting that the fit shows some statistical improvement for

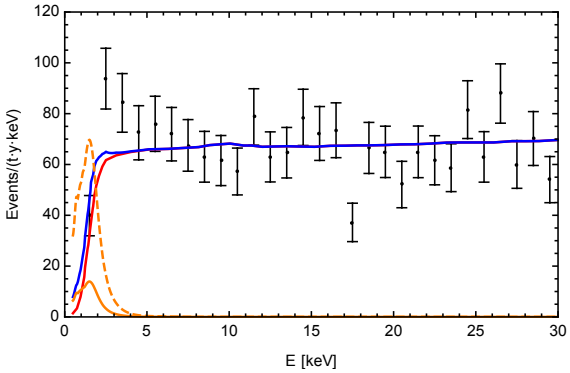

Figure 4.23: Comparison between the best fit differential event rate for a DM particle with $m_\chi = 10$ GeV and $\sigma_{e\chi} = 1.25 \times 10^{-39}\,\mathrm{cm}^2$ and the data. The style is similar to Fig. 4.22, and for better visualization we also show the signal rate enhanced by a factor of 5 as an orange dashed line.

a small DM signal, it amounts to marginally more than 1σ. Therefore, DM-electron-scattering does not provide a convincing explanation of the observation, and we do not entertain this possibility further. Similar conclusions were reached in [344]. Improving the fit requires a flatter recoil spectrum, which could for instance be achieved by a (semi-) relativistic DM sub-population [347, 348, 351] contributing to the signal, or an interaction with additional momentum dependence [344].

Nevertheless, it is interesting to ask whether the DM relic density can be obtained in our framework. To set it via freeze-out, the main DM annihilation channels are e^+e^- and S^2, similar to Sec. 4.3.3. Using the results and estimates derived for the general eDMEFT in Sec. 4.1.1, we find that annihilation into S^2 could give the correct relic density. However, only if Λ is lowered to the TeV scale, and values of $y_\chi^{\mathcal{S}_e} \gtrsim 1$ are chosen.

Therefore, we consider an alternative, namely the freeze-in mechanism [370], which is easier to realize within the setup at hand. In this case, the DM interactions are so weak ($y_\chi^{\mathcal{S}_\ell} \ll 1$) that DM has never been in thermal equilibrium with the SM bath the early universe. Then the relic density can be built up from a negligible initial value, by $SS(ss) \to \chi\bar{\chi}$ inverse annihilation and $S \to \chi\bar{\chi}$ decays for sufficiently light DM. Since it is realized via a $D = 5$ operator, the annihilation process leads to a UV dominated rate. Hence the relic density is sensitive to the largest temperature, and we need to specify our assumption for the reheating temperature T_R. In order not to exceed the validity of our EFT, we limit ourselves to T_R below the new physics scale Λ.

We compute the relic density with the freeze-in module of micrOMEGAs 5 [270], which takes the full momentum dependency of the annihilation and decay rates into account. In Fig. 4.24, we show isocontours of $\Omega_\chi h^2 = 0.12$ in the m_χ–$y_\chi^{\mathcal{S}_e}$ plane, assuming $y_\chi^{\mathcal{S}_\nu} = y_\chi^{\mathcal{S}_e}$ and adopting $T_R = 100\,\mathrm{GeV}$. Besides the plotted parameters, the relic density depends on m_S and v_e. Those were chosen accordingly to two benchmarks which are described in the next section. As the values $m_S \sim 5\,\mathrm{MeV}$, $v_e \sim 5\,\mathrm{GeV}$ are comparable in the two benchmarks, the contour lines in Fig. 4.24 are located close to each other and align in the high m_χ limit.

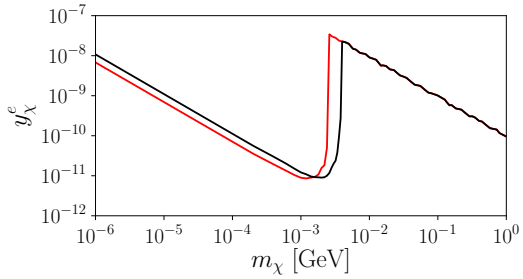

Figure 4.24: Isocontours of correct DM relic density assuming production through freeze-in and considering the assignations of model parameters for BM1 (red) and BM2 (black). The reheating temperature T_R has been set to 100 GeV.

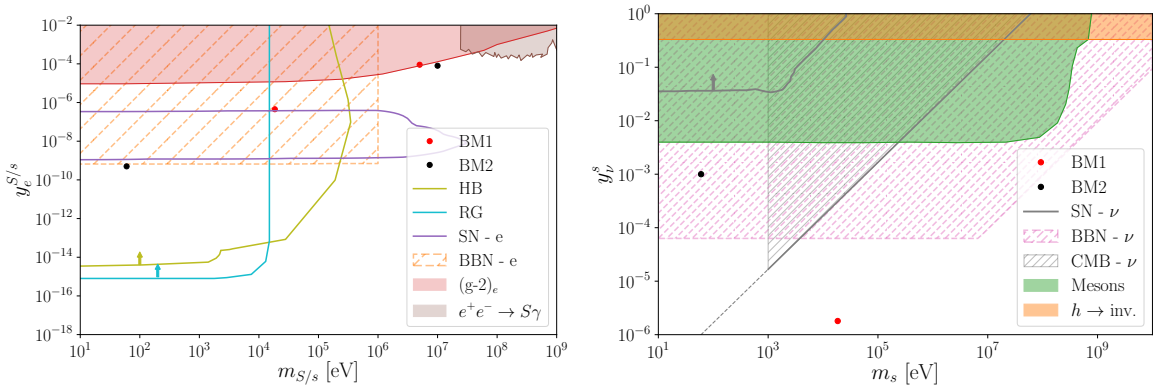

Figure 4.25: Left: Constraints in the $m_{S/s}$–$y_e^{S/s}$ plane from [371] and our own analysis, including the two BM points. For a discussion of the various limits and their shading see the main text.
Right: Constraints in the m_s–y_ν^s plane including our two BM points. The couplings of the heavier mediator are too small to appear.

4.4.3 Terrestrial and Astrophysical Constraints

Additional interactions of scalars with electrons and neutrinos, as used above to fit the XENON1T excess via neutrino-electron scattering, are targets of various experimental searches. The plots in Fig. 4.25 summarize important constraints for electron (left) and neutrino (right) couplings. In this section we comment on how they apply to our explanation of the XENON1T excess in the discussed $\mathbb{Z}_2^{e,\nu}$ symmetric setup, and in a more general subset of eDMEFT operators. In the final paragraph, we show how a late time phase transition can be realized in our setup helping to avoid constraints from BBN.

Bounds on electron-neutrino interaction Experiments aiming to observe solar and reactor neutrinos are well established. They probe very similar physics as XENON1T, and place an upper bound on the neutrino-electron scattering rate. Limits on NP scenarios leading to a recoil spectrum peaking at low energies are typically interpreted in terms of a neutrino magnetic moment μ_ν. Currently, Borexino and GEMMA provide the best limit of $\mu_\nu < 2.9\times10^{-11}\mu_B$ [372, 373]. This is exactly on the edge of the XENON1T excess preferred range of $\mu_\nu = 1.4\text{-}-2.9\times10^{-11}\mu_B$, found by the collaboration in [330], but cannot exclude the neutrino-magnetic-moment interpretation. This observation is highly relevant for the scenario under consideration featuring a light scalar mediator. As in the energy range of the XENON1T signal, the recoil energy distribution of events that are induced by solar neutrinos interacting via a light scalar ($m_s \lesssim E_r$), or a magnetic moment, are essentially indistinguishable.

Consequently, an interpretation of the Borexino data in our model will lead to a constraint that is just on the upper boundary of the preferred parameter region. With the signal and the expected exclusion so close to each other, the exact position will depend on details of the experimental data and the statistical procedure, and a naive phenomenological recast is unlikely to allow for a clear comparison. Thus, we refrain from quoting an explicit limit, and note that the bound is expected to be closely aligned with the upper edge of the preferred values of $\sqrt{y_e^s\, y_\nu^s}$.

Bounds on electron coupling New states coupling to electrons can be tested thoroughly with terrestrial precision experiments. In the relevant mass range, the most stringent constraints come from the anomalous magnetic moment of the electron a_e. This is because both the experimental measurement and the SM prediction are incredibly precise. At the 3σ level, a deviation of a_e from the SM expectation is limited to $\delta a_e \lesssim 1.4\times10^{-12}$ [374, 375]. The new scalars under consideration contribute [376]

$$\delta a_e^s = \frac{(y_e^s)^2}{4\pi^2}\,\frac{m_e^2}{m_s^2}\,I_S\Big(\tfrac{m_e^2}{m_s^2}\Big)\,, \tag{4.48}$$

where the loop function is given by

$$I_S(r) = \int_0^1 dz\;\frac{z^2\,(2-z)}{1-z+z^2 r}. \tag{4.49}$$

For $m_s \ll m_e$ this leads to $y_e^s \lesssim 10^{-5}$ while the limit relaxes for $m_s \geq m_e$. The exact behavior is shown as the red area in the left panel of Fig. 4.25. Softer terrestrial constraints can be derived from e^+e^- colliders through the process $e^+e^- \to \gamma s$, and dominate for $m_s \sim \mathcal{O}(1\,\text{GeV})$ [371].

In addition, there are a number of bounds on $y_e^{S,s}$ from astrophysical and cosmological observations. If the mass of the mediator is comparable or smaller than the core temperature

of a star, the emission of scalars can contribute to the energy loss and change the properties and dynamics of these astrophysical systems. Strong limits can be derived from red giants (RG) and horizontal branch stars (HB). We adopt the results of [371,377] where plasma mixing is considered to be the main production mechanism of the light scalars; for recent analysis on the stellar cooling impact on NP in other models see [378]. In principle, for $m_{s,S} \ll 10\,\text{keV}$, the RG bound excludes couplings $y_e^s \gtrsim 10^{-15}$ and therefore clearly excludes a solar neutrino interpretation of the XENON1T excess for all reasonable values of y_ν^s. The bounds from observations of HB stars are less severe at low masses, but take over for $m_{s,S} \gtrsim 10\,\text{keV}$. However, it is conceivable that these constraints can be circumvented in the presence of additional new physics such as an environment-dependent mass for the scalar similar to the chameleon mechanism considered in cosmology [379, 380]. First attempts to realize such a solution for theories that explain the XENON1T signal appear promising [381]. Following such a reasoning, we consider such astrophysical bounds less robust than the direct laboratory bounds discussed before, and in consequence draw them as lines removing the shading from the disfavored regions.

The observation of the supernova (SN) SN1987A sets another constraint for mediator masses up to $\mathcal{O}(10\,\text{MeV})$, as additional light degrees of freedom would cool the SN too rapidly [382]. Due to the very high density of the SN core for strong couplings, the scalar mediator can be trapped before leaving the core, thus the limits vanish for higher values of y_e^s, see left panel of Fig. 4.25. We consider the limits from [371], where only the resonant production via mixing with the longitudinal component of the photon is included, and direct production through Compton scattering or electron-ion recoil is neglected. This is possible for $m_s < w_p \sim 20\,\text{MeV}$, where w_p is the photon plasma frequency [383]. The trapping regime for resonant production is included by using the balance of production and absorption rate, with the requirement of the scalar to be re-absorbed in a range of $R \approx 10\,\text{km}$. In this trapping regime, the decay $s \to e^+e^-$ determines the bound for masses $1\,\text{MeV} \leq m_s \leq 30\,\text{MeV}$.

Finally, there are bounds from BBN for additional light degrees of freedom entering thermal equilibrium with e and γ. On top of an increase of the effective degrees of freedom N_{eff}, the entropy release from e^+e^- annihilation is diluted in that case. This leads to a lower photon temperature during BBN and therefore a higher baryon-to-photon ratio, which causes a decrease of the deuterium abundance [371]. For $m_s \lesssim 1\,\text{MeV}$ the robust BBN bound is largely flat and requires $y_e^s \lesssim 10^{-9}$, but can be circumvented in our setup. A late time phase transition in the new physics sector can prevent the mixing of s and S in the early universe, and thus remove the coupling between the lighter scalar and the electrons at the relevant temperatures. The mechanism is discussed in more detail below.

Bounds on neutrino couplings New scalar interactions with neutrinos are harder to test than in the case of electrons. Despite this, robust terrestrial constraints on such additional neutrino interactions arise from searches for meson decays such as $K^-/D^-/\pi^- \to s\nu e^-/\mu^-$ [384]. We show the strongest combination of those in the right panel of Fig. 4.25, assuming a flavor universal coupling. In case of flavor non-universality, the bounds for electron neutrinos are slightly stronger. Due to the $h \to s\nu\nu$ process, limits on the Higgs-to-invisible width give the strongest bound on y_ν^s for $m_h > m_s \gtrsim 1\,\text{GeV}$ [384]. We use the recent ATLAS result of $\text{BR}(h \to \text{inv.}) < 0.13$ [131].

The observation of MeV-scale neutrinos originating from SN1987A constrains the neutrino self-interaction [385]. This is because scattering of the SN-neutrinos with the CνB via the

new mediators would shift their energy to significantly lower values, and potentially below the detection threshold. In addition, the SN neutrinos get deflected, which delays their arrival on Earth. A first bound was derived in [386]. We show the bounds from [385] in Fig. 4.25, where recent limits on the neutrino masses were considered.

The model under consideration could also have an impact on the amount of radiation in the early Universe which can be tested via BBN. In particular, the right-handed neutrinos are dangerous, since fully thermalized each of them will contribute $\Delta N_{\text{eff}} = 1$ while the upper bound stands at ≈ 0.2 [387]. Therefore, the only parameters which are allowed by cosmology are those where the right-handed neutrinos do not reach thermal equilibrium before the left-handed ones decouple from the SM bath. Even if the initial population of ν_R is negligible they can be produced in neutrino-antineutrino scattering via t-channel s exchange. A good estimate for thermalization can be obtained by requiring that the production rate γ exceeds the Hubble rate H prior to neutrino decoupling which happens at about $2 - 3\,\text{MeV}$. In our model, the thermally averaged production rate reads

$$\gamma \approx \langle \sigma v \rangle \times n_\nu \approx \frac{(y_\nu^s)^4}{512\,\pi}\, T, \tag{4.50}$$

where n_ν is the equilibrium number density of neutrinos and $\langle \sigma v \rangle$ is the thermally averaged production cross section of ν_R. By requiring γ to be smaller than H we find $y_\nu^s \lesssim 6.3 \times 10^{-5}$ for $m_s \ll 2\,\text{MeV}$, while the bound weakens for larger masses, see right panel of Fig. 4.25 for details. The contribution of s is less pronounced than in the case of electrons since the absence of a ν_R bath prevents the direct production of s.

We note that this bound can be avoided if through additional mass terms the right-handed neutrinos become too heavy to contribute to N_{eff}. This can be realized in our setup by increasing v_ν, generating a more sizable Dirac-mass term that then leads to viable neutrino masses via see-saw suppression in the presence of large Majorana masses for the right-handed neutrinos. This would provide a hybrid explanation for the smallness of neutrino masses, which will however require a refined analysis going beyond the scope of this thesis.

Finally, if the interaction rate of neutrinos is high enough they cannot be treated as a free-streaming gas and the impact of their interactions has be to included in the Boltzmann equations governing the evolution of the primordial perturbations, leading to constraints from CMB. For a heavy mediator, they are $(y_\nu^s/m_s)^2 \leq (0.06\,\text{GeV})^{-2}$ [388]. In order for this estimate to be valid we need $m_s \gg 10\,\text{eV}$, and therefore the limit becomes unreliable towards the lower end of the mass range considered here.

Benchmark models In order to confront our model for the XENON1T excess with these astrophysical and laboratory constraints, we define two benchmarks (BMs) that both deliver a good fit to the excess as given in Eq. (4.44). While we require roughly natural scales for the model, we are mainly driven by the goal of avoiding the most severe experimental bounds. The BMs are defined by the independent input parameters:

	M_ν	M_e	$\mathrm{y}_\nu^{\mathcal{S}}$	$\mathrm{y}_e^{\mathcal{S}}$	Λ	$\lambda_{\nu e}$
BM1	18.5 keV	5 MeV	1×10^{-4}	0.005	10 TeV	3×10^{-4}
BM2	60 eV	10 MeV	0.06	0.005	10 TeV	0.001

These lead to the vevs and derived physical couplings:

	v_ν	v_e	y_ν^s	y_e^s	y_ν^S	y_e^S	s_θ
BM1	26.5 keV	5.3 GeV	1.8×10^{-6}	-4.5×10^{-7}	8.3×10^{-9}	9×10^{-5}	-5×10^{-3}
BM2	50 eV	5.9 GeV	0.001	-5×10^{-10}	6×10^{-9}	8×10^{-5}	-6×10^{-6}

They are displayed as red (BM1) and black (BM2) points in the landscape of collected bounds on $y_e^{s/S}$ and y_ν^s in Fig. 4.25. Both BMs arrive at a predicted strength for the anomaly of $\sqrt{y_e^s\, y_\nu^s} \approx -(7-9)\times10^{-7}$, in line with the best-fit value obtained before in Eq. (4.44). Moreover, they satisfy the positive-definiteness condition $M_\nu M_e > 2\lambda_{\nu e} v_\nu v_e$, ensuring a proper potential minimum.

In both BMs, the choice $v_e > M_e \gtrsim m_e$ leads to a coupling of electrons to the heavy mediator of $y_e^S \sim 10^{-4}$ that just evades the precision bounds for the corresponding mediator masses [371]. Second, the electron coupling to the potentially dangerously light s is suppressed by s_θ pushing it into the window above the SN1987a and below the $(g-2)_e$ exclusion region for BM1. While even the electron BBN constraints are evaded in BM2 without further treatment at the price of a higher neutrino coupling, for BM1, those can be avoided via a late phase transition generating $v_\nu > 0$ below $T \approx 150\,\text{keV}$, as we discuss below.

We note that two different assumptions regarding the neutrino masses can be made, both are consistent with the BM values and observations.

1) In the case of inverted neutrino-mass hierarchy with $m_{\nu^3} \ll m_{\nu^1} \sim m_{\nu^2} \sim 0.05\,\text{eV}$, both $\nu^{1,2}$ couple to s with similar strength y_ν^s, while the interaction of the lightest neutrino is negligible, see Eq. (4.36). Since $\nu^{1,2}$ contain almost all electron-flavor content and couple universally to s, basically no flux from the sun will be lost when considering neutrino-electron scattering in the detector, thus the analysis described above remains valid.

2) For normal hierarchy with $m_{\nu^1} \sim m_{\nu^2} \sim 0.05\,\text{eV} \ll m_{\nu^3}$, we assume that both chiralities of the heaviest state are even under the $\mathbb{Z}_2^\nu$ symmetry. Therefore, the heaviest state does not couple to s, while again the electron-neutrino content is almost entirely in the universally coupling eigenstates $\nu^{1,2}$.

Free EFT description We confront a subset of operators of the general eDMEFT discussed in Sec. 3.3.1 extended with scalar neutrino couplings to the XENONT1T anomaly, and to the constraints discussed above. Omitting kinetic and potential terms, the effective Lagrangian is given by

$$\mathcal{L}_{\text{eff}} = -\frac{\sqrt{2}\,s}{v}\left(y_\nu^s\, \bar{L}_L^1 H \nu_R^1 + y_e^s\, \bar{L}_L^1 H e_R + \text{h.c.}\right), \tag{4.51}$$

which can be obtained from Eq. (4.29) by neglecting the second scalar singlet, while coupling the remaining one to both electrons and neutrinos, and removing the Z_2 symmetries, as well as the vev of the mediator. In consequence, all fermion masses are solely induced by the Higgs and y_ν^s and y_e^s are now free couplings.

In the left and right panel of Fig. 4.26 the constraints and best fit region in the y_e^s–y_ν^s plane are shown for a mediator mass of 60 eV and 20 keV, corresponding to BM2, and BM1 respectively. For comparison, the coupling values of BM1 (BM2) are indicated by a red (black) point.

Two regions in the couplings preferred by the XENON1T fit remain potentially valid but both need extra mechanisms to avoid bounds derived from BBN. The one around $y_e^s \sim \mathcal{O}(10^{-9})$ is excluded by the neutrino BBN bound, which, as discussed before, could be avoided by additional mass terms for the right-handed neutrinos. The other region around $y_e^s \sim \mathcal{O}(10^{-6})$ is

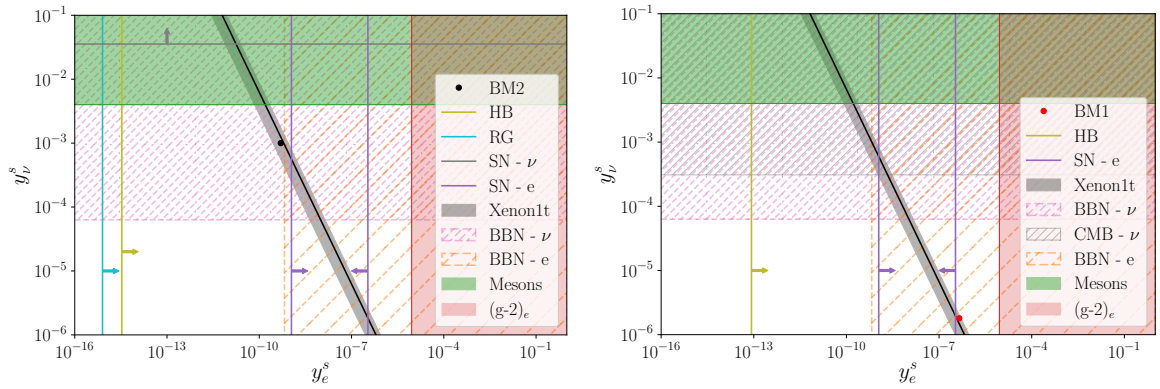

Figure 4.26: Constraints in the y_e^s–y_ν^s plane for a 60 eV (left, as in BM2) and a 20 keV mediator (right as in BM1) and the 1σ preferred region from the XENON1T fit (black line). For comparison the parameter values of the BMs are indicated by points. The BBN bound on the electron coupling, indicated by the hatched region, can be circumvent by a late time phase transition.

under pressure from the electron BBN bound. In this case, a late phase transition can remove the interaction of s and electrons during the relevant age of the universe, thus make this region potentially viable.

Avoiding BBN Bounds via a Late Phase Transition Here we demonstrate how our scenario naturally realizes a late $\mathbb{Z}_2$-breaking phase transition delaying the coupling of the electron to the light mediator until BBN has been completed. The scalar potential of our model can lead to a rich cosmological history in which the $\mathbb{Z}_2^\ell$ symmetries are broken in a stepwise fashion [389]. For simplicity we neglect mixing between the scalars S_ν, S_e and the SM Higgs by setting $\lambda_{HS_{e,\nu}} = 0$. The tree-level scalar potential is then given by

$$V_{\text{tree}} = \tfrac{1}{2}\mu_\nu^2 S_\nu^2 + \tfrac{1}{2}\mu_e^2 S_e^2 + \lambda_{\nu e} S_1^2 S_2^2 + \tfrac{1}{4}\lambda_\nu S_\nu^4 + \tfrac{1}{4}\lambda_e S_e^4. \tag{4.52}$$

To study the cosmological evolution of this potential we add the one-loop thermal corrections given by [390]

$$V_{\text{thermal}} = \frac{T^4}{2\pi^2}\left[J_B\left(\frac{m_s^2}{T^2}\right) + J_B\left(\frac{m_S^2}{T^2}\right)\right], \tag{4.53}$$

where $J_B(\alpha) = \int_0^\infty dx x^2 \ln(1 - e^{\sqrt{x^2+\alpha}})$ is the thermal correction for bosonic degrees of freedom. In the high-temperature limit, the thermal corrections have analytical forms $J_B(\alpha) = -\frac{\pi^4}{45} + \frac{\pi^2}{12}\alpha + O(\alpha^{3/2})$. Since mixing between S_ν and S_e is small, we can take $m_s \approx M_\nu$ and $m_S \approx M_e$. With these approximations, the critical temperature T_{c2} at which a second minimum $(\langle S_\nu\rangle, \langle S_e\rangle) = (0, v_e)$ degenerate with the $\mathbb{Z}_2^\nu \times \mathbb{Z}_2^e$ preserving vacuum $(\langle S_\nu\rangle, \langle S_e\rangle) = (0, 0)$ forms is given by

$$T_{c2} = \frac{\sqrt{-12\,\mu_e^2}}{2\lambda_{\nu e} + 3\lambda_e}. \tag{4.54}$$

A second phase transition appears once the temperature has dropped to T_{c1} at which a non zero vev of S_ν forms, with

$$T_{c1}^2 = \frac{12\left(2\lambda_{\nu e}\mu_e^2 - \lambda_e\mu_\nu^2\right)}{\lambda_e(2\lambda_{\nu e}+3\lambda_\nu) - 2\lambda_{\nu e}(2\lambda_{\nu e}+3\lambda_e)}. \tag{4.55}$$

For BM1 the first phase transition occurs at around 500 MeV, and the second one at 150 keV. At this temperature most of the photon heating is completed, and the electron density has dropped significantly. Therefore, the thermalization rates are starting to be exponentially suppressed.

4.5 Summary

The search for DM is one of the most important tasks in high energy physics today. This is reflected by the large number of experiments that probe various potential aspects of DM. Combining the results from the ongoing experimental efforts is challenging, and requires a versatile framework that allows for a consistent theoretical characterization of those. The eDMEFT, which combines DMEFTs with the simplified model approach provides such an analysis tool.

In the first half of this chapter, Secs. 4.1 and 4.2, we performed a comprehensive survey of the phenomenology of the eDMEFT with a scalar or pseudoscalar mediator. The measured DM abundance, constraints from DD and ID experiments, and relevant collider searches have been considered.

Presenting analytical and numerical results for various DM annihilation cross sections and the DM-nucleon scattering in the presence of $D=5$ operators allowed to identify first differences to simplified models. We turned to an analysis of mono-jet signatures at the LHC, and discussed searches for scalar resonances decaying to vector-boson, di-jet, and Higgs-pair final states. Afterwards we approached a survey of the full eDMEFT parameter space. First we explored four minimal portal scenarios that are realized within the eDMEFT, before turning to interference effects between various operators. Interestingly, these allow for cancellations in the DD cross section that lead to blind spots for scalar mediators. Those blind spots would be missed in the simplified models. Finally, we delivered comprehensive scans including the essential operators, that show which parameter space regions survive the constraints from DM phenomenology and collider searches, pointing out new viable regions emerging in the eDMEFT. In particular, we demonstrated how future XENONnT limits could corner conventional scalar portals to the dark sector, while in the eDMEFT larger parts in different regions of the m_S–m_χ plane remain open. We find that a significant part of this parameter space could be in reach of the HL-LHC. Thus, the complementarity between the different experimental search strategies is highlighted.

We repeated our analysis considering a $\mathcal{CP}$-odd mediator. While the collider phenomenology is largely similar to the one of scalar mediator there are striking differences regarding DD and ID constraints. In this case the DD cross section is loop or velocity suppressed and, therefore, the experimental limits provide a much looser constraint. In contrast, ID is much more sensitive to pseudoscalar mediators since the annihilation cross sections for a number of relevant final states is s-wave enhanced. Consequently, this scenario is most constrained for $m_\chi \lesssim 150\,\text{GeV}$ while the parameter space for heavier DM is largely open. Future experimental data will be crucial to test this kind of scenario, since the next generation DD experiments will be sensitive to the pseudoscalar mediated DM-nucleon cross section.

After considering the eDMEFT as general as possible we moved to two slightly extended setups, which address more specific questions. First, in Sec. 4.3, we considered the eDMEFT with an additional $\mathbb{Z}_2$ under which the scalar mediator and the right-handed first generation fermions are odd. This leads to a suppression of the usual $S\bar{\chi}\chi$ operator, while allowing for the effective $S^2\bar{\chi}\chi$ interaction. Besides enabling to address the smallness of light fermion masses without generating FCNCs, the changed interaction with the dark sector can give rise to interesting collider signatures, namely di-fermion+$\not{E}_T$. To test the related couplings we confronted those channels with current LHC data and projections for the HL-LHC and CLIC. To derive more strict limits we restricted ourselves to either a lepto- or hadrophilic mediator, remaining with a partial explanation of the smallness lepton masses. An interesting finding is, that in this portal colliders are sensitivity even to $m_\chi > m_S/2$, a case typically out of reach (due to resonant DM production). In addition we computed the relic density and DD rates in the favorite parameter space, and found that is possible to have collider signatures together with a valid DM phenomenology.

In the last part of this chapter, we investigated the excess in low energy electron recoil events recently reported by the XENON1T collaboration. To this end we added to the eDMEFT scenario from Sec. 4.3 a second $\mathbb{Z}_2$-symmetry assigned with an additional scalar, connected to neutrino mass generation. We found that the recoil energy spectrum for conventional DM-electron scattering peaks at lower values than needed to explain the excess. Even after taking the electron bound state and experimental conditions into account, the fit only marginally improves compared to the background-only hypothesis and conventional DM does not provide a convincing explanation. On the other hand, the new neutrino-electron coupling induced by the embedded light-lepton mass mechanism predicts a significant neutrino-electron scattering cross section. Including this, the fit prefers a light scalar with an averaged neutrino-electron coupling of $\sqrt{y_e^s\, y_\nu^s} \approx 7.9 \times 10^{-7}$ with more than $2\,\sigma$. In general, the parameter space that allows for a successful explanation of the XENON1T excess is constrained from various experiments. While bounds from terrestrial experiments can be avoided comparatively easily, the ones from cosmology and astrophysics are more constraining, in particular BBN bounds on a light scalar coupling to electrons. The rich scalar sector of the framework naturally allows for a late time phase-transition in the early universe which forbids the constrained scalar-electron coupling during BBN. In addition, contributions to the right-handed neutrino masses are required in order to avoid their thermalization prior to BBN. Once both are taken into account, there are solutions that comply with cosmological observations. The remaining strong tension with astrophysical bounds from stellar cooling can potentially be circumvented with a more complex new physics sector. A currently investigated approach with a environmental dependent value for the vev is promising [266]. While a explanation of the excess with new physics is a exciting possibility, in light of stringent constraints from other observations this potential sign of BSM physics should be taken with a grain of salt. Luckily, the upcoming run of the XENONnT will be able to weigh in on this question in the near future and either strengthen the excess or rule it out conclusively.

Chapter 5

Conclusion

The search for DM is one of the main topics of modern particle physics. It is tackled by a great variety of experiments and an ongoing progress in theory. On the experimental side it has initialized the development of new detector technologies and lead to an unthinkable gain in sensitivity. The prime example is DD, which might be able to detect the neutrino floor of coherent scattering in the near future. The theoretical purpose is to embed DM in a more fundamental theory of nature, since DM is among the observationally best-established evidence for BSM physics. To this end, new models have been developed and refined to characterize various DM candidates. The theory progress has helped to design new experimental approaches with observables from laboratory to cosmological scales.

From the particle-physics perspective, a special focus lies on collider-based DM searches, which have shaped the theory development significantly. In the last decades the discoveries of new particles at colliders have vastly improved our understanding of physics at the smallest scales. In the future such a discovery would be one of the most unambiguous ways to establish BSM physics. Although not fully designed for DM searches, colliders could play a crucial role in reliably investigating the connection between DM and the SM, as the physics and the experimental backgrounds there are well understood. On the other hand, the important cosmological properties of a DM candidate cannot be determined at colliders. In the case of a discovery of an invisible state at the LHC, the connection with DD and ID results could determine those properties. Therefore, the combination could establish whether such an invisible state could potentially be DM. The need to combine results from several experimental approaches to discover DM represents a strong reason for a consistent theoretical description of DM. Compared to DD and ID, the demand for concrete particle frameworks is even higher at the LHC to identify relevant kinematic regions. In the absence of direct hints for new particles at the LHC, the development has focused on more model-independent approaches with a less specified particle content than e.g. supersymmetric models. Frameworks to describe the dark sector are of course not unique, and they come with different advantages and drawbacks.

Especially for the interpretation of DD results, the DMEFT is commonly used. It only considers SM fields and a DM candidate. In the much higher-energetic LHC collisions the probed momentum transfers can be of the same order as the obtained limits on the cutoff scale. This leads to a breakdown of the underlying assumption of well-separated scales. These problems with the validity have lead to the development of simplified models. In those models a mediating state is explicitly taken into account, which significantly improves the kinematic behavior at the LHC. However, to keep those models rather generic and simple, they commonly do not respect the SM gauge group. It has been shown that in general the required UV contributions to the probed mono-X channels cannot be fully decoupled. In addition, the experimental collaborations are interested in theoretical frameworks which allow the investigation of more mono-X channels to use as much of the collected data as possible.

To overcome these problems, the next-generation simplified models have been developed and experimentally tested in the last years. Those models usually feature an extended scalar sector, which restores gauge invariance. The resonant enhancement of mono-X cross sections allows for the investigation of a broader variety of channels. Besides many advantages, they come with a non-negligible bias on the new particle content, and transferring obtained limits to more complex theories is not directly possible due to the specific production mechanism. The eDMEFT has been designed to provide a more versatile, and consistent gauge-invariant framework by combining the advantages of DMEFT and simplified models. To this end, a DM candidate and an explicit (pseudo)scalar mediator is added to the SM field content via effective interactions. The eDMEFT can combine several observational constraints, and opens up parameter space, which would be excluded by DD in simpler approaches. Those regions might be testable at the HL-LHC, even though mono-X cross sections tend to be smaller than in the next-generation simplified models, due to the absence of resonant production. Investigating these two different approaches to characterize DM was the main topic of this thesis.

In Chapter 2, we discussed the 2HDM+S and 2HDM+PS as examples for next-generation simplified models. The scalar and fermionic sector of both models consists of two Higgs doublets, an additional (pseudo)scalar singlet, and the DM candidate. The parameter space can be narrowed down via several assumptions motivated by experimental and theoretical requirements. These general constraints have also been established by the experimental collaborations. In addition, the aim for strong signals, and a comparable baseline for both models defines a rather small parameter set. These parameter are tested in dedicated collider searches. The analysis focuses on searches for $t\bar{t}$ resonances, mono-Z and mono-h signals. A detailed collider phenomenology of the 2HDM+S, and the model comparison was performed for the first time in Ref. [80], on which this discussion is based. While all three channels are relevant on their own to test BSM scenarios, they also feature an intriguing interplay to distinguish the two models under consideration.

The $t\bar{t}$ resonance search provides strong limits on the masses of the new heavy scalars. Those limits are basically independent on the additional mediator. Hence, they lead to similar constraints in both models, and exclude small values of $\tan\beta$. The strongest bounds on the mediator mass are obtained from mono-Z searches. Both models feature comparable cross sections in this channel. The conservative estimates for the mono-h exclusion are weaker than the ones from mono-Z. However, they differ significantly between the 2HDM+S and PS opening the possibility to distinguish them at the LHC. In case of a signal detection in one or both channels, disentangling the two models would be possible by comparing the ratio of signal strengths. In addition angular variables, and especially astrophysical tests would help to further separate the models. The mono-Z and mono-h channels are also of great interest due to their statistically dominated uncertainties. Therefore, significant improvements in sensitivity are expected by upcoming LHC runs. We exemplarily estimated this gain in the mono-Z channel for different future collider scenarios, and found significantly stronger bounds. The 2HDM+S/PS prove to be powerful benchmark models for the LHC, with a non-trivial interplay between a broad range of experimental signatures.

In Chapter 3, we briefly revisited some general EFT properties to set the theoretical background for the second approach to DM models discussed in this thesis. In addition, we discussed an example of a new physics search beyond DM. The Higgs sector is crucial for our understanding of the SM, and sensitive to a variety of BSM scenarios. Precision measurements

of this sector are capable to uncover new physics contributions too heavy to be produced directly. The Higgs decay to a Z boson and a photon is so far unmeasured and challenging. We proposed a search in the $t\bar{t}$-associated production channel, which features a bigger signal to background ratio than, for instance, gluon fusion production. Our analyses showed that this channel could potentially lead to a discovery of the decay already at the HL-LHC. A subset of SMEFT operators is used for a model-independent characterization of potential deviations from the SM prediction. The estimated sensitivity allows us to set limits on a so-far weakly constrained combination of SMEFT operators.

In Chapter 4, we investigated the phenomenology of the eDMEFT in various scenarios. The effective operators connecting the additional (pseudo)scalar mediator to the SM account for more complex BSM contributions. Interestingly, the leading effects arise at $D=5$, leading to a limited number of operators. We started with an in-depth study of the parameter space for a scalar mediator. To connect with previous results, we showed how simplified models are embedded in the eDMEFT as a subset of now gauge-invariant operators. Differences to the simplified models occur, for example in the scaling of annihilation cross sections for the relic density. An advantage of the eDMEFT is that those simple portals to the dark sector can be consistently enlarged by additional operators. This allows the presence of blind spots that open up parameter space previously excluded by DD. To fully unfold the potential of the eDMEFT, we performed generic parameter scans taking all relevant constraints and operators into account. While the exclusions are mainly driven by DD, current collider experiments, especially mono-jet searches, tend to constrain only limited regions of parameter space. Nevertheless, collider searches can be important to close blind spots, since those regions might also survive future DD experiments. We carried out a similar analysis for the pseudoscalar mediator. For this case DD and Higgs constraints are basically absent. In contrast, ID can play an important role for certain parts of the parameter space, and collider constraints tend to be slightly stronger.

While it is a drawback that the interplay and cross sections of mono-X signatures are smaller in the eDMEFT framework than in next-generation simplified models, it is not completely unexpected. As pointed out in the discussion of the next-generation simplified models, the collider signals there rely on the specific mass hierarchy in the extended scalar sector enabling the resonant enhancement. On the other hand, the eDMEFT naturally provides more annihilation channels for the DM to obtain the correct relic density. In the (next-generation) simplified models without further BSM contributions this is only possible in rather tuned kinematic regions often excluding the interesting collider phenomenology.

After these general considerations, we investigated two slightly more specific scenarios of the eDMEFT with particular phenomenological interest: di-fermion plus $\not{E}_T$ signatures, and the XENON1T excess. In both cases the required set of operators can be motivated by additional symmetries, which are potentially related to the lightest fermion masses. In the first scenario, only the mediator and the first right-handed fermion generation are odd under a new $\mathbb{Z}_2$ symmetry. The masses of those fermions are generated by spontaneously breaking this symmetry. Furthermore, the usual renormalazible DM interaction is strongly suppressed. Therefore, the DM phenomenology is dominated by the bi-quadratic interaction of the mediator with DM. It can lead to uncommon $\not{E}_T$ signatures at the (HL-)LHC and potential future electron colliders. A remarkable feature due to the kinematics of the bi-quadratic portal is that the sensitivity reaches beyond the threshold where the mediator can decay to DM. The combination of DD and those collider searches can probe large regions of the parameter space.

For the second scenario we extended the eDMEFT by two $\mathbb{Z}_2^{e,\nu}$ symmetries, which are

spontaneously broken by two companion scalars. In this way, the generation of electron and neutrino masses is possible. The setup facilitates a generic characterization of the excess in low-energy electron recoil events recently announced by the XENON1T collaboration. A DM recoil barely leads to an improvement of the fit, since the recoil energy of cold DM is too small. On the other hand, electron-neutrino scattering mediated by the lighter scalar can improve the fit significantly. New scalar interactions of electrons and neutrinos are severely constrained by several laboratory and astrophysical observations. We revisited the most important bounds, and showed that most of them can be circumvented by appropriate choices of parameters, and non-trivial mechanisms embedded in the framework. In case the signal gets confirmed to be of BSM origin, this analysis showed that a non-minimal new physics sector is needed to explain it, in agreement with other observations.

To further establish the connection between UV-complete models and the eDMEFT performing matching calculations in increasing complexity would be an interesting future task. The validity range of those calculations could be verified by comparing the reach in certain observables between the two models. A promising signature is mono-h, potentially combined with mono-jet searches. Matching of various complete models could give hints towards typically connected operators, and would allow constraints derived in the eDMEFT to be easier applied to those models. We also mentioned several assumptions throughout the work, for instance vanishing couplings, or the MFV ansatz for the Yukawa sector. In a future, more general analysis, those could be loosened. Together with taking more observables into account, this will lead to a significantly enlarged parameter space. In order to handle this, the use of more advanced techniques will become necessary, for instance machine learning in the context of EFTs [391–393]. While we already studied some collider signal in detail, more refined studies of existing analyses for a particular set of operators would be a tempting task. In the spirit of Sec. 4.3, designing new search channels could help to investigate the eDMEFT further, and to derive limits from new sources.

While DM is among the clearest hints towards BSM and a more fundamental theory of nature, the road to a discovery is long. Similar to the fact that different experiments are needed to approach this purpose, it seems that also having a variety of theoretical tools can be very useful. Therefore, the two approaches investigated here set different priorities. The 2HDM+S/PS allow for the exploration and combination of (new) mono-X channels at colliders. The eDMEFT enables the consistent analysis of a broad range of experimental searches and the connection to various UV theories. It will be exciting to see which direction will be preferred by upcoming observations.

Acknowledgments

The work leading to this PhD thesis was luckily not performed in the solitude of an ivory tower, even if the location of the MPIK and the pandemic caused isolation might suggest the opposite. I would therefore like to take this opportunity to thank those without whom preparing this thesis would have been impossible.

Firstly, I would like to deeply thank Dr. Florian Goertz for accepting me as a PhD student, and taking so much time to explain and discuss physics. Through the friendly, respectful, and supportive atmosphere you created in our research group, as well as through the travels you enabled me to do, I learnt a lot in our various projects. I really appreciate that you took my ideas seriously, and trusted me from the first day on.

Secondly, my immense gratitude goes to Dr. Tommi Alanne for many fruitful discussions, advice, some of which went well beyond physics, and many more. In particular I thank you for the extensive proof reading of early versions of this manuscript (which was probably quite though), while already being in Liverpool.

Special thanks go to Prof. Dr. Tilman Plehn, on the one hand for agreeing to be my second referee, and on the other hand, for my first insights in the fascinating field of dark matter. Your small but great lecture, together with Dr. Martin Bauer and Dr. Teresa Marrodan Undagoitia, sparked my interest, which I could deepen during my master thesis in your group. This thesis has significantly benefited from what I learnt there.

Furthermore, I am grateful to Prof. Dr. Monica Dunford and Prof. Dr. André Butz for taking the time to be part of my examination committee. I also thank Prof. Dr. Manfred Lindner for leading the division with great expertise, and being open for new research ideas. I thank Anja Berneiser and Britta Schwarz for helping with all kind of bureaucracy. I thank the IMPRS for Precision Tests of Fundamental Symmetries for its support.

I especially thank Dr. Simone Blasi for being not only a wonderful colleague and officemate (besides talking endlessly) but also a great friend. In the same vein, I would like to mention Tommi again, as I felt that I could always rely on you both. The uncountable amount of laughter, the holy coffee, the many funny nights in the Oldtown (together with Janet and others), and so many more things we did together, made my PhD time really special. I hope we stay in contact.

Also I thank Dr. Thomas Hugle for a lot of programming advice, a successful collaboration, and many interesting chats. Additionally I thank Dr. Ulisses Saldana-Salazar and Karla Tame-Narvaez, for many clarifying conversations, our finished and future projects, and your warm friendship. I also thank Dr. Stefan Vogl, Dr. Giorgio Arcadi, and Dr. Giorgio Busoni for friendly and fruitful collaborations in long standing projects. In addition to them (with no aim for completeness and in an alphabetic order), for many physics and non-physics related discussions, table-tennis, -soccer matches, which made office times really enjoyable, I thank: Andreas Bally, Cristina Benso (also for a great skiing lesson in Obergurgl), Ingolf Bischer, Vedran Brdar, Christian Döring, Lukáš Gráf, Carlos Jaramillo, Thomas Rink, Marc Schuh, and Andreas Trautner.

As work, and physics are not everything, I would like to take this chance to express my huge gratitude to my family and friends. First, as without them this all would not have been possible in so many ways, to my parents, Marion and Ulrich, for your endless, unconditional love and support in the last 29 years. To my brother, Kilian, you have grown into a man, who knows what the right things to do are and also does it, and whose opinion I highly value.

To my friends in Bottrop from school days, for knowing that I can always rely on you even (or especially) in difficult times. To my fellow students during the Bachelor in Duisburg, without you I probably would have quit physics after a month. You made the first three years incredibly joyful, and every meeting feels like coming home.

Last but not least, to Martine, your happiness, humor, and positivity made the last year so wonderful despite all adversities, also for your lovely and great support during the final preparation stage. I am eagerly awaiting to start new adventures with you.

Appendix A

Formulae for the Decay Widths

In this appendix we give analytic expressions for the dominant branching ratios of the spin-0 states in the 2HDM+S/PS as partially shown in Sec. 2.1.3.

We focus on the mass hierarchy M_A, M_{H/S_1}, $M_{H^\pm} > M_{a/S_2}$, M_h, the alignment limit, and $\tan\beta = \mathcal{O}(1)$. The values of ϵ_f, denoting the ratio between the Yukawa coupling of the fermion f in the different types of 2HDMs and the SM value $y_f = \sqrt{2}m_f/v$, are given in Table 2.1. In the following we use the abbreviation $\tau_{i,j} = 4M_i^2/M_j^2$.

Scalar Model

Higgs Boson h In the decoupling limit the couplings of h with the SM states substantially coincide with the ones for the SM Higgs boson. However its total width can deviate from the SM prediction, because of the eventual presence of additional decay channels. The most relevant is the one into a pair of S_2 states, if kinematically allowed. As the total Higgs width is small, also three-body decays can be relevant. The additional widths are given by

$$\Gamma(h \to S_2 S_2) = \frac{1}{32\pi}\, g_{hS_2S_2}^2\, M_h\, \sqrt{1-\tau_{S_2,h}}, \tag{A.1}$$

$$\Gamma\left(h \to S_2 \chi\bar{\chi}\right) = \frac{y_\chi^2}{32\pi^3}\, g_{hS_2S_2}^2\, M_h\, g(\tau_{S_2,h}) \cos^2\theta \left(1-\tau_{\chi,S_2}\right)^{3/2}, \tag{A.2}$$

$$\Gamma\left(h \to S_2 f\bar{f}\right) = \frac{N_c^f\, \epsilon_f^2\, y_f^2}{16\pi^3}\, g_{hS_2S_2}^2\, M_h\, g(\tau_{S_2,h}) \sin^2\theta \left(1-\tau_{f,S_2}\right)^{3/2}, \tag{A.3}$$

with [154]

$$g(\tau) = \frac{\tau-4}{8}\left[4 - \ln\left(\frac{\tau}{4}\right)\right] - \frac{5\tau-4}{4\sqrt{\tau-1}}\left[\arctan\left(\frac{\tau-2}{2\sqrt{\tau-1}}\right) - \arctan\left(\frac{1}{\sqrt{\tau-1}}\right)\right], \tag{A.4}$$

$$g_{hS_2S_2} = \frac{1}{M_h v}\, \left(M_h^2 - 2\left(M_{S_1}^2 - M_{S_2}^2\right)\cos^2\theta\right) \sin^2\theta. \tag{A.5}$$

Light Scalar S_2 The light scalar S_2 mostly decays into gg, $f\bar{f}$ and $\chi\bar{\chi}$ (direct couplings with gauge boson are forbidden in the alignment limit), depending on its mass. We quote the corresponding decay widths and the loop-induced one into gluons, which are useful for the

interpretation of the collider studies:

$$\Gamma(S_2 \to gg) = \frac{\alpha_s^2}{16\pi^3}\, M_{S_2}\, \sin^2\theta \sum_q \epsilon_q^2\, y_q^2\, F_S\left(\tau_{q,S_2}\right), \tag{A.6}$$

$$\Gamma(S_2 \to f\bar{f}) = \frac{N_c^f\, \epsilon_f^2\, y_v^2}{16\pi}\, M_{S_2}\, \sin^2\theta\, (1-\tau_{f,S_2})^{3/2}, \tag{A.7}$$

$$\Gamma\left(S_2 \to \chi\bar{\chi}\right) = \frac{y_\chi^2}{8\pi}\, M_{S_2}\, \cos^2\theta\, (1-\tau_{\chi,S_2})^{3/2}, \tag{A.8}$$

with the scalar loop function [139, 275]

$$F_S(x) = x\left|1 + (1-x)\arctan^2\frac{1}{\sqrt{x-1}}\right|^2. \tag{A.9}$$

Heavy Scalar S_1 Besides the $\cos^2\theta$ term due to mixing with the additional singlet the couplings of the heavy scalar to SM fields remain similar to the ones known from 2HDMs. Additional decay channels are $\chi\bar{\chi}$, S_2^2, which is very small for our parameter choice, and hS_2 important for the mono-h signal. The analytic expressions are given by

$$\Gamma(S_1 \to gg) = \frac{\alpha_s^2}{16\pi^3}\, M_{S_1}\, \cos^2\theta \sum_q \epsilon_q^2\, y_q^2\, F_S\left(\tau_{q,S_1}\right), \tag{A.10}$$

$$\Gamma\left(S_1 \to f\bar{f}\right) = \frac{N_c^f\, \epsilon_f^2\, y_f^2}{16\pi}\, M_{S_1}\, \cos^2\theta\, (1-\tau_{f,S_1})^{3/2}, \tag{A.11}$$

$$\Gamma\left(S_1 \to \chi\bar{\chi}\right) = \frac{y_\chi^2}{8\pi}\, M_{S_1}\, \sin^2\theta\, \left(1-\tau_{\chi,S_1}\right)^{3/2}, \tag{A.12}$$

$$\Gamma\left(S_1 \to S_2 S_2\right) = \frac{1}{32\pi}\, g_{S_1 S_2 S_2}^2\, M_{S_1}\, \sqrt{1-\tau_{S_2,S_1}}, \tag{A.13}$$

$$\Gamma\left(S_1 \to S_2 h\right) = \frac{1}{16\pi}\, \frac{\lambda^{1/2}(M_{S_1}, M_h, M_{S_2})}{M_{S_1}}\, g_{S_1 h S_2}^2, \tag{A.14}$$

with

$$g_{S_1 S_2 S_2} = \frac{1}{M_{S_1} v_S}\left(M_{S_1}^2 + 2M_{S_2}^2 - \frac{2-3\sin^2\theta}{\cos^2\theta}\, \hat{\lambda}_{HHS}\, v_S^2\right)\sin\theta\, \cos\theta, \tag{A.15}$$

$$g_{S_1 h S_2} = \frac{1}{M_{S_1} v}\left(M_h^2 + \left(M_{S_1}^2 - M_{S_2}^2\right)\cos 2\theta\right)\sin\theta\cos\theta. \tag{A.16}$$

Furthermore, we have introduced

$$\lambda(m_1, m_2, m_3) = \left(m_1^2 - m_2^2 - m_3^2\right)^2 - 4\, m_2^2\, m_3^2. \tag{A.17}$$

Pseudoscalar A Besides the partial widths known from 2HDMs, the heavy pseudoscalar features an additional decay channel to $S_2 Z$. The analytic expressions for its dominant decay

widths are given by

$$\Gamma(A \to gg) = \frac{\alpha_s^2}{16\pi^3}\, M_A \sum_q \epsilon_q^2\, y_q^2\, F_P\left(\tau_{q,A}\right), \tag{A.18}$$

$$\Gamma\left(A \to f\bar{f}\right) = \frac{N_c^f\, \epsilon_f^2\, y_f^2}{16\pi}\, M_A \left(1-\tau_{f,A}\right)^{1/2}, \tag{A.19}$$

$$\Gamma\left(A \to S_2 Z\right) = \frac{1}{16\pi}\, \frac{\lambda^{3/2}(M_A, M_{S_2}, M_Z)}{M_A^3\, v^2}, \tag{A.20}$$

with the pseudoscalar loop function [139, 275]

$$F_P(x) = x \left| \arctan^2 \frac{1}{\sqrt{x-1}} \right|^2. \tag{A.21}$$

Charged Scalar $H^\pm$ For completeness also the partial widths of $H^\pm$ to quarks and the new spin-0 state plus a $W^\pm$ are given

$$\Gamma\left(H^+ \to t\bar{b}\right) = \frac{1}{16\pi}\, N_c^t\, |V_{tb}|^2 \epsilon_t^2\, y_t^2\, M_{H^\pm} \left(1-\tau_{t,H^\pm}/4\right)^2, \tag{A.22}$$

$$\Gamma\left(H^\pm \to S_1 W^\pm\right) = \frac{1}{16\pi}\, \frac{\lambda^{3/2}(M_{H^\pm}, M_{S_1}, M_W)}{M_{H^\pm}^3 v^2}\, \cos^2\theta, \tag{A.23}$$

$$\Gamma\left(H^\pm \to A W^\pm\right) = \frac{1}{16\pi}\, \frac{\lambda^{3/2}(M_{H^\pm}, M_A, M_W)}{M_{H^\pm}^3 v^2}, \tag{A.24}$$

$$\Gamma\left(H^\pm \to S_2 W^\pm\right) = \frac{1}{16\pi}\, \frac{\lambda^{3/2}(M_{H^\pm}, M_{S_2}, M_W)}{M_{H^\pm}^3 v^2}\, \sin^2\theta, \tag{A.25}$$

where in $\Gamma\left(H^+ \to t\bar{b}\right)$ terms of $\mathcal{O}(m_b^2/M_{H^\pm}^2)$ are neglected, and $\Gamma(H^\pm \to hW^\pm)$ vanishes in the alignment limit.

Pseudoscalar Model

The results in this section are taken from [, 61] and transferred to our notation. The features are very similar to the ones in the previous section.

Higgs Boson h Again the couplings of h to quarks and gauge boson pairs are identical to their SM values. Its total width can be enlarged by additional two and three body decays given by [154]:

$$\Gamma\left(h \to aa\right) = \frac{1}{32\pi}\, g_{haa}^2\, M_h \left(1-\tau_{a,h}\right)^{1/2}, \tag{A.26}$$

$$\Gamma\left(h \to a\chi\bar{\chi}\right) = \frac{y_\chi^2}{32\pi^3}\, g_{haa}^2\, M_h\, g(\tau_{a,h}) \cos^2\theta \left(1-\tau_{\chi,a}\right)^{1/2}, \tag{A.27}$$

$$\Gamma\left(h \to af\bar{f}\right) = \frac{N_c^f\, \epsilon_f^2\, y_f^2}{16\pi^3}\, g_{haa}^2\, M_h\, g(\tau_{a,h}) \sin^2\theta \left(1-\tau_{f,a}\right)^{1/2}, \tag{A.28}$$

with $g(\tau)$ given in Eq. (A.4) and

$$g_{haa} = \frac{1}{M_h v}\Big[\left(M_h^2 - 2M_H^2 + 4M_{H^\pm}^2 - 2M_a^2 - 2\lambda_3 v^2\right)\sin^2\theta \\ - \left(\lambda_{11P}\cos^2\beta + \lambda_{22P}\sin^2\beta\right)v^2\cos^2\theta\Big]. \tag{A.29}$$

Light Pseudoscalar a The partial widths of a to gg, $f\bar{f}$ and $\chi\bar{\chi}$ are given by

$$\Gamma(a \to gg) = \frac{\alpha_s^2}{16\pi^3}\, M_a\, \sin^2\theta \sum_q \epsilon_q^2\, y_q^2\, F_P\left(\tau_{q,A}\right), \tag{A.30}$$

$$\Gamma\left(a \to f\bar{f}\right) = \frac{N_c^f\, \epsilon_f^2\, y_f^2}{16\pi}\, M_a \sin^2\theta\, (1-\tau_{f,a})^{1/2}, \tag{A.31}$$

$$\Gamma\left(a \to \chi\bar{\chi}\right) = \frac{y_\chi^2}{8\pi}\, M_a \cos^2\theta\, (1-\tau_{\chi,a})^{1/2}, \tag{A.32}$$

where F_P is given in Eq. (A.21).

Heavy Pseudoscalar A The dominant partial widths of the heavy pseudoscalar are given by

$$\Gamma(A \to gg) = \frac{\alpha_s^2}{16\pi^3}\, M_A\, \cos^2\theta \sum_q \epsilon_q^2\, y_q^2\, F_P\left(\tau_{q,A}\right), \tag{A.33}$$

$$\Gamma\left(A \to f\bar{f}\right) = \frac{N_c^f\, \epsilon_f^2\, y_f^2}{16\pi}\, M_A\, \cos^2\theta\, (1-\tau_{f,A})^{1/2}, \tag{A.34}$$

$$\Gamma\left(A \to \chi\bar{\chi}\right) = \frac{y_\chi^2}{8\pi}\, M_A\, \sin^2\theta\, (1-\tau_{\chi,A})^{1/2}, \tag{A.35}$$

$$\Gamma\left(A \to ah\right) = \frac{1}{16\pi}\, \frac{\lambda^{1/2}(M_A, M_a, M_h)}{M_A}\, g_{Aah}^2, \tag{A.36}$$

with

$$g_{Aah} = \frac{1}{M_A\, v}\Big[M_h^2 - 2M_H^2 - M_A^2 + 4M_{H^\pm}^2 - M_a^2 \\ + \left(\lambda_{11P}\cos^2\beta + \lambda_{22P}\sin^2\beta - 2\lambda_3\right)v^2\Big]\sin\theta\cos\theta. \tag{A.37}$$

Heavy Scalar H The partial widths to gg and $f\bar{f}$, aa and aZ are given by

$$\Gamma(H \to gg) = \frac{\alpha_s^2}{16\pi^3}\, M_H \sum_q \epsilon_q^2\, y_q^2\, F_S\left(\tau_{q,H}\right), \tag{A.38}$$

$$\Gamma\left(H \to f\bar{f}\right) = \frac{N_c^f\, \epsilon_f^2\, y_f^2}{16\pi}\, M_H\, (1-\tau_{f,H})^{3/2}, \tag{A.39}$$

$$\Gamma\left(H \to aa\right) = \frac{1}{32\pi}\, g_{Haa}^2\, M_H\, (1-\tau_{a,H})^{1/2}, \tag{A.40}$$

$$\Gamma\left(H \to aZ\right) = \frac{1}{16\pi}\, \frac{\lambda^{3/2}(M_H, M_a, M_Z)}{M_H^3 v^2}\, \sin^2\theta, \tag{A.41}$$

with

$$g_{Haa} = \frac{1}{M_H v}\Big[\cot(2\beta)\left(2M_h^2 - 4M_H^2 + 4M_{H^\pm}^2 - 2\lambda_3 v^2\right)\sin^2\theta + \sin(2\beta)\cos^2\theta\, v^2\,\left(\lambda_{11P} - \lambda_{22P}\right)/2\Big], \tag{A.42}$$

denoting the Haa coupling and λ is given in Eq. (A.17).

Charged Scalar $H^\pm$ Since in the alignment limit the H^+hW^+ vertex vanishes, the partial decay widths of the charged scalar $H^\pm$ relevant for small $\tan\beta$ are given by

$$\Gamma\left(H^+ \to t\bar{b}\right) = \frac{N_c^t\,|V_{tb}|^2\,\epsilon_t^2\,y_t^2}{16\pi}\; M_{H^\pm}\left(1 - \tau_{t,H^\pm}/4\right)^2, \tag{A.43}$$

$$\Gamma\left(H^\pm \to HW^\pm\right) = \frac{1}{16\pi}\,\frac{\lambda^{3/2}(M_{H^\pm}, M_H, M_W)}{M_{H^\pm}^3 v^2}, \tag{A.44}$$

$$\Gamma\left(H^\pm \to AW^\pm\right) = \frac{1}{16\pi}\,\frac{\lambda^{3/2}(M_{H^\pm}, M_A, M_W)}{M_{H^\pm}^3 v^2}\;\cos^2\theta, \tag{A.45}$$

$$\Gamma\left(H^\pm \to aW^\pm\right) = \frac{1}{16\pi}\,\frac{\lambda^{3/2}(M_{H^\pm}, M_a, M_W)}{M_{H^\pm}^3 v^2}\;\sin^2\theta, \tag{A.46}$$

where in the case of $H^+ \to t\bar{b}$ we have neglected terms of $\mathcal{O}(m_b^2/M_{H^\pm}^2)$ again.

Appendix B

Likelihood Analysis

This appendix we give details about the likelihood formalism used in Sec. 4.3.2.

Likelihood Function To derive exclusion regions, a binned likelihood function is used [231] similar to the one in CheckMate [135]. For the number of events n_i in the i-th bin

$$L(\mu,\, \theta_S,\, \theta_B) = \prod_i \frac{[\phi(\mu, \theta_S, \theta_B)]^{n_i}}{n_i!}\, e^{-\phi(\mu,\theta_S,\theta_B)}\, e^{-(\theta_S^2+\theta_B^S)/2}, \tag{B.1}$$

with

$$\phi(\mu, \theta_S, \theta_B) = \mu\, S e^{\sigma_S \theta_S} + B\, e^{\sigma_B \theta_B} \tag{B.2}$$

and

$$\sigma_S = \frac{\Delta S}{S}\,, \qquad \sigma_B = \frac{\Delta B}{B}. \tag{B.3}$$

Here, S and B are the predicted numbers of signal and background events, respectively, while $\theta_{S,B}$ are nuisance parameters incorporating the corresponding uncertainties ΔS and ΔB. Finally, the variation of the signal strength with the input parameters, given in Sec. 4.3, is parameterized by the signal-strength modifier μ, which is normalized for fixed $y_e^{\mathcal{S}}/\Lambda$ and masses such that $\mu = (y_\chi^{\mathcal{S}}/\Lambda)^2$.

To test the compatibility of different values for μ with data, we use the profile likelihood ratio [231]

$$\tilde{\lambda}(\mu) = \begin{cases} \frac{L(\mu,\hat{\hat{\theta}}_S(\mu),\hat{\hat{\theta}}_B(\mu))}{L(\hat{\mu},\hat{\theta}_S,\hat{\theta}_B)} & \text{for } \hat{\mu} \geq 0, \\ \frac{L(\mu,\hat{\hat{\theta}}_S(\mu),\hat{\hat{\theta}}_B(\mu))}{L(0,\hat{\hat{\theta}}_S(0),\hat{\hat{\theta}}_B(0))} & \text{for } \hat{\mu} < 0. \end{cases} \tag{B.4}$$

Here, $\hat{\hat{\theta}}_S(\mu)$, $\hat{\hat{\theta}}_B(\mu)$ maximize L for the given value of μ, while $\hat{\mu}$, $\hat{\theta}_S$, $\hat{\theta}_B$ correspond to the unconditional (global) maximum appearing in the denominator. The latter ones are called unconditional Maximum Likelihood (ML) estimators. The lower case in Eq. (B.4) accounts for the fact that we can only have a positive signal contribution. Finally, for the numerical analysis it is convenient to use the test statistics [231]

$$\tilde{q}_\mu = \begin{cases} -2 \ln \tilde{\lambda}(\mu) & \text{for } \hat{\mu} \leq \mu, \\ 0 & \text{for } \hat{\mu} > \mu, \end{cases} \tag{B.5}$$

to set upper limits (with higher values corresponding to less compatibility), for which we use the python package `iminuit` [394].

P-Value We assume that the true underlying theory features $\mu = 0$, i.e. we expect to see only background events and want to derive projected experimental exclusion regions on μ. In general, to quantify the agreement between a (potentially) observed measurement and a signal hypothesis $\mu > 0$ leading to a certain $\tilde{q}_{\mu,\text{obs}}$, the p-value

$$p_\mu = \int_{\tilde{q}_{\mu,\text{obs}}}^{\infty} f(\tilde{q}_\mu|\mu)\, d\tilde{q}_\mu \tag{B.6}$$

is calculated. Here, $f(\tilde{q}_\mu|\mu')$ is the probability density function of $\tilde{q}_\mu$ under the assumption that the data is distributed according to a true $\mu = \mu'$, while the subscript in the first argument denotes the hypothesis being tested. This quantifies the probability that, given the true signal strength is μ, we will observe a value of $\tilde{q}_\mu$ at least as large as $\tilde{q}_{\mu,\text{obs}}$. As we want to derive expected upper limits from future experiments assuming no signal to be present, we will use the median value of the corresponding distribution, $f(\tilde{q}_\mu|0)$, for $\tilde{q}_{\mu,obs}$. Finally, working at the 95% confidence level, we will solve for the value of μ that leads to $p_\mu = 0.05$.

To obtain the distributions $f(\tilde{q}_\mu|\mu')$ without performing large number of Monte Carlo simulations, we use the asymptotic formulas derived in Ref. [231]. Those are valid for a sufficiently high number of events in each bin, which is fulfilled in our case.[1] While in the case $\mu' = \mu$, $f(\tilde{q}_\mu|\mu)$ is given by a simple half-χ^2-distribution, for obtaining the median of $\tilde{q}_\mu$ according to $f(\tilde{q}_\mu|0)$ the so-called Asimov data set is used [231], where all estimators obtain their true values. This data set can be approximated via large MC simulations. We assume that our initial sets are large enough and use the fitted distributions as Asimov data. With this, the corresponding likelihood function and test statistics can be evaluated, which are denoted L_A and $q_{\mu,A}$. The variance needed to obtain $f(\tilde{q}_\mu|0)$, is then given by $\sigma_A^2 = \mu^2/q_{\mu,A}$ assuming background-only. In practice we can use the Asimov value $q_{\mu,A}$ for the median of $[\tilde{q}_\mu|0]$ according to [231]. Hence the expected p-value for a signal hypothesis becomes $p_\mu = 1 - \Phi\left(\sqrt{q_{\mu,A}}\right)$, with Φ being the cumulative Gaussian distribution. In the end, p_μ is evaluated for varying μ to find $p_\mu = 0.05$.

[1] We have checked the approximate agreement of the asymptotic formula with generated distributions for several values of μ.

References

[1] F. Zwicky, *Die Rotverschiebung von extragalaktischen Nebeln*, Helv. Phys. Acta 6 (1933) 110–127.

[2] J. C. Kapteyn, *First Attempt at a Theory of the Arrangement and Motion of the Sidereal System*, Astrophysical Journal 55 (May, 1922) 302.

[3] J. H. Oort, *The force exerted by the stellar system in the direction perpendicular to the galactic plane and some related problems*, Bulletin Astronomical Institute of the Netherlands 6 (Aug., 1932) 249.

[4] S. van den Bergh, *The Early history of dark matter*, Publ. Astron. Soc. Pac. 111 (1999) 657, [astro-ph/9904251].

[5] **CMS** Collaboration, S. Chatrchyan et al., *Observation of a new boson at a mass of 125 GeV with the CMS experiment at the LHC*, Phys. Lett. B716 (2012) 30–61, [arXiv:1207.7235].

[6] **ATLAS** Collaboration, G. Aad et al., *Observation of a new particle in the search for the Standard Model Higgs boson with the ATLAS detector at the LHC*, Phys. Lett. B716 (2012) 1–29, [arXiv:1207.7214].

[7] **ATLAS** Collaboration, G. Aad et al., *Combined measurements of Higgs boson production and decay using up to* 80 fb^{-1} *of proton-proton collision data at* $\sqrt{s} = 13$ *TeV collected with the ATLAS experiment*, Phys. Rev. D 101 (2020), no. 1 012002, [arXiv:1909.02845].

[8] **CMS** Collaboration, A. M. Sirunyan et al., *Combined measurements of Higgs boson couplings in proton–proton collisions at* $\sqrt{s} = 13$ *TeV*, Eur. Phys. J. C 79 (2019), no. 5 421, [arXiv:1809.10733].

[9] **WMAP** Collaboration, D. Spergel et al., *First year Wilkinson Microwave Anisotropy Probe (WMAP) observations: Determination of cosmological parameters*, Astrophys. J. Suppl. 148 (2003) 175–194, [astro-ph/0302209].

[10] **WMAP** Collaboration, E. Komatsu et al., *Seven-Year Wilkinson Microwave Anisotropy Probe (WMAP) Observations: Cosmological Interpretation*, Astrophys. J. Suppl. 192 (2011) 18, [arXiv:1001.4538].

[11] **Planck** Collaboration, P. Ade et al., *Planck 2013 results. I. Overview of products and scientific results*, Astron. Astrophys. 571 (2014) A1, [arXiv:1303.5062].

[12] **Planck** Collaboration, N. Aghanim et al., *Planck 2018 results. I. Overview and the cosmological legacy of Planck*, Astron. Astrophys. 641 (2020) A1, [arXiv:1807.06205].

[13] **Planck** Collaboration, N. Aghanim et al., *Planck 2018 results. VI. Cosmological parameters*, Astron. Astrophys. 641 (2020) A6, [arXiv:1807.06209].

[14] **Planck** Collaboration, Y. Akrami et al., *Planck 2018 results. X. Constraints on inflation*, Astron. Astrophys. 641 (2020) A10, [arXiv:1807.06211].

[15] V. C. Rubin, J. Ford, W. Kent, and N. Thonnard, *Extended rotation curves of high-luminosity spiral galaxies. IV. Systematic dynamical properties, Sa through Sc*, Astrophys. J. Lett. 225 (1978) L107–L111.

[16] D. Harvey, R. Massey, T. Kitching, A. Taylor, and E. Tittley, *The non-gravitational interactions of dark matter in colliding galaxy clusters*, Science 347 (2015) 1462–1465, [arXiv:1503.07675].

[17] D. Clowe, M. Bradac, A. H. Gonzalez, M. Markevitch, S. W. Randall, C. Jones, and D. Zaritsky, *A direct empirical proof of the existence of dark matter*, Astrophys. J. Lett. 648 (2006) L109–L113, [astro-ph/0608407].

[18] M. Vogelsberger, S. Genel, V. Springel, P. Torrey, D. Sijacki, D. Xu, G. F. Snyder, D. Nelson, and L. Hernquist, *Introducing the Illustris Project: Simulating the coevolution of dark and visible matter in the Universe*, Mon. Not. Roy. Astron. Soc. 444 (2014), no. 2 1518–1547, [arXiv:1405.2921].

[19] V. Springel, C. S. Frenk, and S. D. White, *The large-scale structure of the Universe*, Nature 440 (2006) 1137, [astro-ph/0604561].

[20] V. Springel et al., *First results from the IllustrisTNG simulations: matter and galaxy clustering*, Mon. Not. Roy. Astron. Soc. 475 (2018), no. 1 676–698, [arXiv:1707.03397].

[21] **BOSS** Collaboration, L. Anderson et al., *The clustering of galaxies in the SDSS-III Baryon Oscillation Spectroscopic Survey: baryon acoustic oscillations in the Data Releases 10 and 11 Galaxy samples*, Mon. Not. Roy. Astron. Soc. 441 (2014), no. 1 24–62, [arXiv:1312.4877].

[22] M. Colless et al., *The 2dF Galaxy Redshift Survey: Final data release*, [astro-ph/0306581].

[23] M. Taoso, G. Bertone, and A. Masiero, *Dark Matter Candidates: A Ten-Point Test*, JCAP 03 (2008) 022, [arXiv:0711.4996].

[24] S. Capozziello and M. Francaviglia, *Extended Theories of Gravity and their Cosmological and Astrophysical Applications*, Gen. Rel. Grav. 40 (2008) 357–420, [arXiv:0706.1146].

[25] M. Bauer and T. Plehn, *Yet Another Introduction to Dark Matter: The Particle Physics Approach*, vol. 959 of *Lecture Notes in Physics*. Springer, 2019.

[26] J. Einasto, *Dark Matter*, 1, 2009. [arXiv:0901.0632].

[27] L. Bergström, *Nonbaryonic dark matter: Observational evidence and detection methods*, Rept. Prog. Phys. 63 (2000) 793, [hep-ph/0002126].

[28] G. Arcadi, M. Dutra, P. Ghosh, M. Lindner, Y. Mambrini, M. Pierre, S. Profumo, and F. S. Queiroz, *The waning of the WIMP? A review of models, searches, and constraints*, Eur. Phys. J. C78 (2018), no. 3 203, [arXiv:1703.07364].

[29] J. L. Feng, *Dark Matter Candidates from Particle Physics and Methods of Detection*, Ann. Rev. Astron. Astrophys. 48 (2010) 495–545, [arXiv:1003.0904].

[30] **MACHO** Collaboration, C. Alcock et al., *The MACHO project: Microlensing results from 5.7 years of LMC observations*, Astrophys. J. 542 (2000) 281–307, [astro-ph/0001272].

[31] G. Bertone, D. Hooper, and J. Silk, *Particle dark matter: Evidence, candidates and constraints*, Phys. Rept. 405 (2005) 279–390, [hep-ph/0404175].

[32] T. Marrodan Undagoitia and L. Rauch, *Dark matter direct-detection experiments*, J. Phys. G43 (2016), no. 1 013001, [arXiv:1509.08767].

[33] **XENON** Collaboration, E. Aprile et al., *Dark Matter Search Results from a One Ton-Year Exposure of XENON1T*, Phys. Rev. Lett. 121 (2018), no. 11 111302, [arXiv:1805.12562].

[34] **PandaX-II** Collaboration, X. Cui et al., *Dark Matter Results From 54-Ton-Day Exposure of PandaX-II Experiment*, Phys. Rev. Lett. 119 (2017), no. 18 181302, [arXiv:1708.06917].

[35] D. S. Akerib et al., *Results from a search for dark matter in the complete LUX exposure*, [arXiv:1608.07648].

[36] **H.E.S.S.** Collaboration, H. Abdallah et al., *Search for dark matter annihilations towards the inner Galactic halo from 10 years of observations with H.E.S.S*, Phys. Rev. Lett. 117 (2016), no. 11 111301, [arXiv:1607.08142].

[37] **Fermi-LAT** Collaboration, M. Ackermann et al., *Searching for Dark Matter Annihilation from Milky Way Dwarf Spheroidal Galaxies with Six Years of Fermi Large Area Telescope Data*, Phys. Rev. Lett. 115 (2015), no. 23 231301, [arXiv:1503.02641].

[38] **Fermi-LAT** Collaboration, M. Ackermann et al., *Updated search for spectral lines from Galactic dark matter interactions with pass 8 data from the Fermi Large Area Telescope*, Phys. Rev. D91 (2015), no. 12 122002, [arXiv:1506.00013].

[39] **Fermi-LAT** Collaboration, M. Ackermann et al., *The Fermi Large Area Telescope On Orbit: Event Classification, Instrument Response Functions, and Calibration*, Astrophys. J. Suppl. 203 (2012) 4, [arXiv:1206.1896].

[40] L. E. Strigari, *Galactic Searches for Dark Matter*, Phys. Rept. 531 (2013) 1–88, [arXiv:1211.7090].

[41] J. M. Gaskins, *A review of indirect searches for particle dark matter*, Contemp. Phys. 57 (2016), no. 4 496–525, [arXiv:1604.00014].

[42] F. Kahlhoefer, *Review of LHC Dark Matter Searches*, Int. J. Mod. Phys. A 32 (2017), no. 13 1730006, [arXiv:1702.02430].

[43] **ATLAS** Collaboration, G. Aad et al., *The ATLAS Experiment at the CERN Large Hadron Collider*, JINST 3 (2008) S08003.

[44] **CMS** Collaboration, S. Chatrchyan et al., *The CMS Experiment at the CERN LHC*, JINST 3 (2008) S08004.

[45] T. Abe et al., *LHC Dark Matter Working Group: Next-generation spin-0 dark matter models*, Phys. Dark Univ. (2018) 100351, [arXiv:1810.09420].

[46] **ATLAS** Collaboration, M. Aaboud et al., *Constraints on mediator-based dark matter and scalar dark energy models using $\sqrt{s} = 13$ TeV pp collision data collected by the ATLAS detector*, JHEP 05 (2019) 142, [arXiv:1903.01400].

[47] Y. Bai, P. J. Fox, and R. Harnik, *The Tevatron at the Frontier of Dark Matter Direct Detection*, JHEP 12 (2010) 048, [arXiv:1005.3797].

[48] P. J. Fox, R. Harnik, J. Kopp, and Y. Tsai, *LEP Shines Light on Dark Matter*, Phys. Rev. D84 (2011) 014028, [arXiv:1103.0240].

[49] I. M. Shoemaker and L. Vecchi, *Unitarity and Monojet Bounds on Models for DAMA, CoGeNT, and CRESST-II*, Phys. Rev. D86 (2012) 015023, [arXiv:1112.5457].

[50] G. Busoni, A. De Simone, E. Morgante, and A. Riotto, *On the Validity of the Effective Field Theory for Dark Matter Searches at the LHC*, Phys. Lett. B728 (2014) 412–421, [arXiv:1307.2253].

[51] O. Buchmueller, M. J. Dolan, and C. McCabe, *Beyond Effective Field Theory for Dark Matter Searches at the LHC*, JHEP 01 (2014) 025, [arXiv:1308.6799].

[52] G. Busoni, A. De Simone, J. Gramling, E. Morgante, and A. Riotto, *On the Validity of the Effective Field Theory for Dark Matter Searches at the LHC, Part II: Complete Analysis for the s-channel*, JCAP 1406 (2014) 060, [arXiv:1402.1275].

[53] G. Busoni, A. De Simone, T. Jacques, E. Morgante, and A. Riotto, *On the Validity of the Effective Field Theory for Dark Matter Searches at the LHC Part III: Analysis for the t-channel*, JCAP 1409 (2014) 022, [arXiv:1405.3101].

[54] D. Racco, A. Wulzer, and F. Zwirner, *Robust collider limits on heavy-mediator Dark Matter*, JHEP 05 (2015) 009, [arXiv:1502.04701].

[55] M. Bauer, A. Butter, N. Desai, J. Gonzalez-Fraile, and T. Plehn, *Validity of dark matter effective theory*, Phys. Rev. D 95 (2017), no. 7 075036, [arXiv:1611.09908].

[56] J. Abdallah et al., *Simplified Models for Dark Matter and Missing Energy Searches at the LHC*, [arXiv:1409.2893].

[57] J. Abdallah et al., *Simplified Models for Dark Matter Searches at the LHC*, Phys. Dark Univ. 9-10 (2015) 8–23, [arXiv:1506.03116].

[58] D. Abercrombie et al., *Dark Matter Benchmark Models for Early LHC Run-2 Searches: Report of the ATLAS/CMS Dark Matter Forum*, Phys. Dark Univ. 27 (2020) 100371, [arXiv:1507.00966].

[59] A. Albert et al., *Recommendations of the LHC Dark Matter Working Group: Comparing LHC searches for heavy mediators of dark matter production in visible and invisible decay channels*, [arXiv:1703.05703].

[60] J. M. No, *Looking through the pseudoscalar portal into dark matter: Novel mono-Higgs and mono-Z signatures at the LHC*, Phys. Rev. D93 (2016), no. 3 031701, [arXiv:1509.01110].

[61] M. Bauer, U. Haisch, and F. Kahlhoefer, *Simplified dark matter models with two Higgs doublets: I. Pseudoscalar mediators*, JHEP 05 (2017) 138, [arXiv:1701.07427].

[62] M. Bauer et al., *Towards the next generation of simplified Dark Matter models*, [arXiv:1607.06680].

[63] M. Duerr, F. Kahlhoefer, K. Schmidt-Hoberg, T. Schwetz, and S. Vogl, *How to save the WIMP: global analysis of a dark matter model with two s-channel mediators*, JHEP 09 (2016) 042, [arXiv:1606.07609].

[64] N. F. Bell, G. Busoni, and I. W. Sanderson, *Two Higgs Doublet Dark Matter Portal*, JCAP 01 (2018) 015, [arXiv:1710.10764].

[65] S. von Buddenbrock, N. Chakrabarty, A. S. Cornell, D. Kar, M. Kumar, T. Mandal, B. Mellado, B. Mukhopadhyaya, R. G. Reed, and X. Ruan, *Phenomenological signatures of additional scalar bosons at the LHC*, Eur. Phys. J. C76 (2016), no. 10 580, [arXiv:1606.01674].

[66] S. von Buddenbrock, A. S. Cornell, E. D. R. Iarilala, M. Kumar, B. Mellado, X. Ruan, and E. M. Shrif, *Constraints on a 2HDM with a singlet scalar and implications in the*

search for heavy bosons at the LHC, J. Phys. G46 (2019), no. 11 115001, [arXiv:1809.06344].

[67] S. Baum, K. Freese, N. R. Shah, and B. Shakya, *NMSSM Higgs boson search strategies at the LHC and the mono-Higgs signature in particular*, Phys. Rev. D95 (2017), no. 11 115036, [arXiv:1703.07800].

[68] S. Baum and N. R. Shah, *Two Higgs Doublets and a Complex Singlet: Disentangling the Decay Topologies and Associated Phenomenology*, JHEP 12 (2018) 044, [arXiv:1808.02667].

[69] S. Baum and N. R. Shah, *Benchmark Suggestions for Resonant Double Higgs Production at the LHC for Extended Higgs Sectors*, [arXiv:1904.10810].

[70] F. Kahlhoefer, K. Schmidt-Hoberg, T. Schwetz, and S. Vogl, *Implications of unitarity and gauge invariance for simplified dark matter models*, JHEP 02 (2016) 016, [arXiv:1510.02110].

[71] N. F. Bell, Y. Cai, and R. K. Leane, *Impact of Mass Generation for Simplified Dark Matter Models*, [arXiv:1610.03063].

[72] N. F. Bell, G. Busoni, and I. W. Sanderson, *Self-consistent Dark Matter Simplified Models with an s-channel scalar mediator*, JCAP 1703 (2017), no. 03 015, [arXiv:1612.03475].

[73] C. Englert, M. McCullough, and M. Spannowsky, *S-Channel Dark Matter Simplified Models and Unitarity*, [arXiv:1604.07975].

[74] D. Goncalves, P. A. N. Machado, and J. M. No, *Simplified Models for Dark Matter Face their Consistent Completions*, Phys. Rev. D95 (2017), no. 5 055027, [arXiv:1611.04593].

[75] E. Bernreuther, J. Horak, T. Plehn, and A. Butter, *Actual Physics behind Mono-X*, SciPost Phys. 5 (2018), no. 4 034, [arXiv:1805.11637].

[76] M. Bauer, M. Klassen, and V. Tenorth, *Universal properties of pseudoscalar mediators in dark matter extensions of 2HDMs*, JHEP 07 (2018) 107, [arXiv:1712.06597].

[77] **ATLAS** Collaboration, M. Aaboud et al., *Search for dark matter and other new phenomena in events with an energetic jet and large missing transverse momentum using the ATLAS detector*, JHEP 01 (2018) 126, [arXiv:1711.03301].

[78] **CMS** Collaboration, A. M. Sirunyan et al., *Search for new physics in final states with an energetic jet or a hadronically decaying W or Z boson and transverse momentum imbalance at $\sqrt{s} = 13$ TeV*, Phys. Rev. D 97 (2018), no. 9 092005, [arXiv:1712.02345].

[79] **CMS** Collaboration, A. M. Sirunyan et al., *Search for dark matter prosuced in association with a Higgs boson decaying to a pair of bottom quarks in proton-proton collisions at $\sqrt{s}$=13 TeV*, Eur. Phys. J. C79 (2019), no. 3 280, [arXiv:1811.06562].

[80] G. Arcadi, G. Busoni, T. Hugle, and V. T. Tenorth, *Comparing 2HDM + Scalar and Pseudoscalar Simplified Models at LHC*, JHEP 06 (2020) 098, [arXiv:2001.10540].

[81] A. Djouadi, *The Anatomy of electro-weak symmetry breaking. II. The Higgs bosons in the minimal supersymmetric model*, Phys. Rept. 459 (2008) 1–241, [hep-ph/0503173].

[82] G. C. Branco, P. M. Ferreira, L. Lavoura, M. N. Rebelo, M. Sher, and J. P. Silva, *Theory and phenomenology of two-Higgs-doublet models*, Phys. Rept. 516 (2012) 1–102, [arXiv:1106.0034].

[83] J. F. Gunion and H. E. Haber, *The CP conserving two Higgs doublet model: The Approach to the decoupling limit*, Phys. Rev. D67 (2003) 075019, [hep-ph/0207010].

[84] S. Davidson and H. E. Haber, *Basis-independent methods for the two-Higgs-doublet model*, Phys. Rev. D72 (2005) 035004, [hep-ph/0504050]. [Erratum: Phys. Rev.D72,099902(2005)].

[85] H. E. Haber and D. O'Neil, *Basis-independent methods for the two-Higgs-doublet model. II. The Significance of tanβ*, Phys. Rev. D 74 (2006) 015018, [hep-ph/0602242]. [Erratum: Phys.Rev.D 74, 059905 (2006)].

[86] J. F. Gunion and H. E. Haber, *Conditions for CP-violation in the general two-Higgs-doublet model*, Phys. Rev. D 72 (2005) 095002, [hep-ph/0506227].

[87] H. E. Haber and O. Stål, *New LHC benchmarks for the $\mathcal{CP}$ -conserving two-Higgs-doublet model*, Eur. Phys. J. C 75 (2015), no. 10 491, [arXiv:1507.04281]. [Erratum: Eur.Phys.J.C 76, 312 (2016)].

[88] P. S. Bhupal Dev and A. Pilaftsis, *Maximally Symmetric Two Higgs Doublet Model with Natural Standard Model Alignment*, JHEP 12 (2014) 024, [arXiv:1408.3405]. [Erratum: JHEP11,147(2015)].

[89] S. L. Glashow and S. Weinberg, *Natural conservation laws for neutral currents*, Phys. Rev. D 15 (Apr, 1977) 1958–1965.

[90] E. A. Paschos, *Diagonal neutral currents*, Phys. Rev. D 15 (Apr, 1977) 1966–1972.

[91] A. Pich and P. Tuzon, *Yukawa Alignment in the Two-Higgs-Doublet Model*, Phys. Rev. D80 (2009) 091702, [arXiv:0908.1554].

[92] P. Tuzon and A. Pich, *The Aligned two-Higgs Doublet model*, Acta Phys. Polon. Supp. 3 (2010) 215–220, [arXiv:1001.0293].

[93] A. Pich, *Flavour constraints on multi-Higgs-doublet models: Yukawa alignment*, Nucl. Phys. Proc. Suppl. 209 (2010) 182–187, [arXiv:1010.5217].

[94] A. Peñuelas and A. Pich, *Flavour alignment in multi-Higgs-doublet models*, JHEP 12 (2017) 084, [arXiv:1710.02040].

[95] S. Gori, H. E. Haber, and E. Santos, *High scale flavor alignment in two-Higgs doublet models and its phenomenology*, JHEP 06 (2017) 110, [arXiv:1703.05873].

[96] W. Rodejohann and U. Saldaña-Salazar, *Multi-Higgs-Doublet Models and Singular Alignment*, JHEP 07 (2019) 036, [arXiv:1903.00983].

[97] S. Centelles Chuliá, W. Rodejohann, and U. Saldaña-Salazar, *Two-Higgs-doublet models with a flavored $\mathbb{Z}_2$ symmetry*, Phys. Rev. D 101 (2020), no. 3 035013, [arXiv:1911.06824].

[98] S. Kanemura and K. Yagyu, *Unitarity bound in the most general two Higgs doublet model*, Phys. Lett. B751 (2015) 289–296, [arXiv:1509.06060].

[99] K. G. Klimenko, *On Necessary and Sufficient Conditions for Some Higgs Potentials to Be Bounded From Below*, Theor. Math. Phys. 62 (1985) 58–65. [Teor. Mat. Fiz.62,87(1985)].

[100] A. G. Akeroyd, A. Arhrib, and E.-M. Naimi, *Note on tree level unitarity in the general two Higgs doublet model*, Phys. Lett. B 490 (2000) 119–124, [hep-ph/0006035].

[101] G. Bhattacharyya and D. Das, *Scalar sector of two-Higgs-doublet models: A minireview*, Pramana 87 (2016), no. 3 40, [arXiv:1507.06424].

[102] H. E. Haber and A. Pomarol, *Constraints from global symmetries on radiative corrections to the Higgs sector*, Phys. Lett. B302 (1993) 435–441, [hep-ph/9207267].

[103] A. Pomarol and R. Vega, *Constraints on CP violation in the Higgs sector from the rho parameter*, Nucl. Phys. B413 (1994) 3–15, [hep-ph/9305272].

[104] R. Barbieri, L. J. Hall, and V. S. Rychkov, *Improved naturalness with a heavy Higgs: An Alternative road to LHC physics*, Phys. Rev. D74 (2006) 015007, [hep-ph/0603188].

[105] J. M. Gerard and M. Herquet, *A Twisted custodial symmetry in the two-Higgs-doublet model*, Phys. Rev. Lett. 98 (2007) 251802, [hep-ph/0703051].

[106] B. Grzadkowski, M. Maniatis, and J. Wudka, *The bilinear formalism and the custodial symmetry in the two-Higgs-doublet model*, JHEP 11 (2011) 030, [arXiv:1011.5228].

[107] H. E. Haber and D. O'Neil, *Basis-independent methods for the two-Higgs-doublet model III: The CP-conserving limit, custodial symmetry, and the oblique parameters S, T, U*, Phys. Rev. D83 (2011) 055017, [arXiv:1011.6188].

[108] T. Enomoto and R. Watanabe, *Flavor constraints on the Two Higgs Doublet Models of Z_2 symmetric and aligned types*, JHEP 05 (2016) 002, [arXiv:1511.05066].

[109] G. Arcadi, *2HDM portal for Singlet-Doublet Dark Matter*, Eur. Phys. J. C78 (2018), no. 10 864, [arXiv:1804.04930].

[110] G. Arcadi, A. Djouadi, and M. Raidal, *Dark Matter through the Higgs portal*, Phys. Rept. 842 (2020) 1–180, [arXiv:1903.03616].

[111] M. Cirelli, E. Del Nobile, and P. Panci, *Tools for model-independent bounds in direct dark matter searches*, JCAP 1310 (2013) 019, [arXiv:1307.5955].

[112] M. J. Dolan, F. Kahlhoefer, C. McCabe, and K. Schmidt-Hoberg, *A taste of dark matter: Flavour constraints on pseudoscalar mediators*, JHEP 03 (2015) 171, [arXiv:1412.5174]. [Erratum: JHEP07,103(2015)].

[113] C. Arina, E. Del Nobile, and P. Panci, *Dark Matter with Pseudoscalar-Mediated Interactions Explains the DAMA Signal and the Galactic Center Excess*, Phys. Rev. Lett. 114 (2015) 011301, [arXiv:1406.5542].

[114] A. L. Fitzpatrick, W. Haxton, E. Katz, N. Lubbers, and Y. Xu, *The Effective Field Theory of Dark Matter Direct Detection*, JCAP 1302 (2013) 004, [arXiv:1203.3542].

[115] A. L. Fitzpatrick, W. Haxton, E. Katz, N. Lubbers, and Y. Xu, *Model Independent Direct Detection Analyses*, [arXiv:1211.2818].

[116] J. B. Dent, L. M. Krauss, J. L. Newstead, and S. Sabharwal, *General analysis of direct dark matter detection: From microphysics to observational signatures*, Phys. Rev. D 92 (2015), no. 6 063515, [arXiv:1505.03117].

[117] R. J. Hill and M. P. Solon, *Standard Model anatomy of WIMP dark matter direct detection II: QCD analysis and hadronic matrix elements*, Phys. Rev. D 91 (2015) 043505, [arXiv:1409.8290].

[118] N. Anand, A. L. Fitzpatrick, and W. C. Haxton, *Weakly interacting massive particle-nucleus elastic scattering response*, Phys. Rev. C89 (2014), no. 6 065501, [arXiv:1308.6288].

[119] F. Bishara, J. Brod, B. Grinstein, and J. Zupan, *From quarks to nucleons in dark matter direct detection*, JHEP 11 (2017) 059, [arXiv:1707.06998].

[120] F. Bishara, J. Brod, B. Grinstein, and J. Zupan, *Renormalization Group Effects in Dark Matter Interactions*, JHEP 03 (2020) 089, [arXiv:1809.03506].

[121] N. F. Bell, G. Busoni, and I. W. Sanderson, *Loop Effects in Direct Detection*, JCAP 1808 (2018), no. 08 017, [arXiv:1803.01574]. [Erratum: JCAP1901, no. 01, E01(2019)].

[122] M. Freytsis and Z. Ligeti, *On dark matter models with uniquely spin-dependent detection possibilities*, Phys. Rev. D83 (2011) 115009, [arXiv:1012.5317].

[123] S. Ipek, D. McKeen, and A. E. Nelson, *A Renormalizable Model for the Galactic Center Gamma Ray Excess from Dark Matter Annihilation*, Phys. Rev. D90 (2014), no. 5 055021, [arXiv:1404.3716].

[124] G. Arcadi, M. Lindner, F. S. Queiroz, W. Rodejohann, and S. Vogl, *Pseudoscalar Mediators: A WIMP model at the Neutrino Floor*, JCAP 03 (2018) 042, [arXiv:1711.02110].

[125] T. Abe, M. Fujiwara, and J. Hisano, *Loop corrections to dark matter direct detection in a pseudoscalar mediator dark matter model*, JHEP 02 (2019) 028, [arXiv:1810.01039].

[126] F. Ertas and F. Kahlhoefer, *Loop-induced direct detection signatures from CP-violating scalar mediators*, JHEP 06 (2019) 052, [arXiv:1902.11070].

[127] T. Abe, M. Fujiwara, J. Hisano, and Y. Shoji, *Maximum value of the spin-independent cross section in the 2HDM+a*, JHEP 01 (2020) 114, [arXiv:1910.09771].

[128] **Fermi-LAT, DES** Collaboration, A. Albert et al., *Searching for Dark Matter Annihilation in Recently Discovered Milky Way Satellites with Fermi-LAT*, Astrophys. J. 834 (2017), no. 2 110, [arXiv:1611.03184].

[129] F. Kling, S. Su, and W. Su, *2HDM Neutral Scalars under the LHC*, JHEP 06 (2020) 163, [arXiv:2004.04172].

[130] **ATLAS** Collaboration, M. Aaboud et al., *Combination of searches for invisible Higgs boson decays with the ATLAS experiment*, Phys. Rev. Lett. 122 (2019), no. 23 231801, [arXiv:1904.05105].

[131] **ATLAS** Collaboration, *Search for invisible Higgs boson decays with vector boson fusion signatures with the ATLAS detector using an integrated luminosity of 139 fb^{-1}*, ATLAS-CONF-2020-008 (4, 2020).

[132] **ATLAS** Collaboration, *Combination of searches for invisible Higgs boson decays with the ATLAS experiment*, ATLAS-CONF-2020-052 (10, 2020).

[133] **ATLAS** Collaboration, M. Aaboud et al., *Search for dark matter produced in association with bottom or top quarks in $\sqrt{s} = 13$ TeV pp collisions with the ATLAS detector*, Eur. Phys. J. C78 (2018), no. 1 18, [arXiv:1710.11412].

[134] **CMS** Collaboration, A. M. Sirunyan et al., *Search for dark matter produced in association with a single top quark or a top quark pair in proton-proton collisions at $\sqrt{s} = 13$ TeV*, JHEP 03 (2019) 141, [arXiv:1901.01553].

[135] D. Dercks, N. Desai, J. S. Kim, K. Rolbiecki, J. Tattersall, and T. Weber, *CheckMATE 2: From the model to the limit*, Comput. Phys. Commun. 221 (2017) 383–418, [arXiv:1611.09856].

[136] **ATLAS** Collaboration, *Search for new phenomena in events with jets and missing transverse momentum in p p collisions at $\sqrt{s}$ = 13 TeV with the ATLAS detector*, ATLAS-CONF-2020-048 (8, 2020).

[137] J. Butterworth, M. Habedank, P. Pani, and A. Vaitkus, *A study of collider signatures for two Higgs doublet models with a Pseudoscalar mediator to Dark Matter*, [arXiv:2009.02220].

[138] F. D'Eramo, J. de Vries, and P. Panci, *A 750 GeV Portal: LHC Phenomenology and Dark Matter Candidates*, JHEP 05 (2016) 089, [arXiv:1601.01571].

[139] J. F. Gunion, H. E. Haber, G. L. Kane, and S. Dawson, *The Higgs Hunter's Guide*, vol. 80. 2000.

[140] J. Alwall, R. Frederix, S. Frixione, V. Hirschi, F. Maltoni, O. Mattelaer, H. S. Shao, T. Stelzer, P. Torrielli, and M. Zaro, *The automated computation of tree-level and next-to-leading order differential cross sections, and their matching to parton shower simulations*, JHEP 07 (2014) 079, [arXiv:1405.0301].

[141] V. Hirschi and O. Mattelaer, *Automated event generation for loop-induced processes*, JHEP 10 (2015) 146, [arXiv:1507.00020].

[142] G. Ossola, C. G. Papadopoulos, and R. Pittau, *CutTools: A Program implementing the OPP reduction method to compute one-loop amplitudes*, JHEP 03 (2008) 042, [arXiv:0711.3596].

[143] T. Peraro, *Ninja: Automated Integrand Reduction via Laurent Expansion for One-Loop Amplitudes*, Comput. Phys. Commun. 185 (2014) 2771–2797, [arXiv:1403.1229].

[144] A. Denner, S. Dittmaier, and L. Hofer, *Collier: a fortran-based Complex One-Loop LIbrary in Extended Regularizations*, Comput. Phys. Commun. 212 (2017) 220–238, [arXiv:1604.06792].

[145] J. Butterworth et al., *PDF4LHC recommendations for LHC Run II*, J. Phys. G43 (2016) 023001, [arXiv:1510.03865].

[146] A. Buckley, J. Ferrando, S. Lloyd, K. Nordström, B. Page, M. Rüfenacht, M. Schönherr, and G. Watt, *LHAPDF6: parton density access in the LHC precision era*, Eur. Phys. J. C75 (2015) 132, [arXiv:1412.7420].

[147] T. Sjöstrand, S. Ask, J. R. Christiansen, R. Corke, N. Desai, P. Ilten, S. Mrenna, S. Prestel, C. O. Rasmussen, and P. Z. Skands, *An Introduction to PYTHIA 8.2*, Comput. Phys. Commun. 191 (2015) 159–177, [arXiv:1410.3012].

[148] **DELPHES 3** Collaboration, J. de Favereau, C. Delaere, P. Demin, A. Giammanco, V. Lemaître, A. Mertens, and M. Selvaggi, *DELPHES 3, A modular framework for fast simulation of a generic collider experiment*, JHEP 02 (2014) 057, [arXiv:1307.6346].

[149] E. Conte and B. Fuks, *Confronting new physics theories to LHC data with MadAnalysis 5*, Int. J. Mod. Phys. A33 (2018), no. 28 1830027, [arXiv:1808.00480].

[150] E. Conte, B. Dumont, B. Fuks, and C. Wymant, *Designing and recasting LHC analyses with MadAnalysis 5*, Eur. Phys. J. C74 (2014), no. 10 3103, [arXiv:1405.3982].

[151] **CMS** Collaboration, A. M. Sirunyan et al., *Search for heavy Higgs bosons decaying to a top quark pair in proton-proton collisions at $\sqrt{s} = 13$ TeV*, JHEP 04 (2020) 171, [arXiv:1908.01115].

[152] **ATLAS** Collaboration, M. Aaboud et al., *Search for Heavy Higgs Bosons A/H Decaying to a Top Quark Pair in pp Collisions at $\sqrt{s} = 8$ TeV with the ATLAS Detector*, Phys. Rev. Lett. 119 (2017), no. 19 191803, [arXiv:1707.06025].

[153] T. Hahn, S. Heinemeyer, F. Maltoni, G. Weiglein, and S. Willenbrock, *SM and MSSM*

Higgs boson production cross-sections at the Tevatron and the LHC, in *TEV4LHC Workshop: 3rd Meeting Geneva, Switzerland, April 28-30, 2005*, 2006. [hep-ph/0607308].

[154] A. Djouadi, J. Kalinowski, and P. M. Zerwas, *Two and three-body decay modes of SUSY Higgs particles*, Z. Phys. C70 (1996) 435–448, [hep-ph/9511342].

[155] **ATLAS** Collaboration, M. Aaboud et al., *Search for an invisibly decaying Higgs boson or dark matter candidates produced in association with a Z boson in pp collisions at $\sqrt{s} = 13$ TeV with the ATLAS detector*, Phys. Lett. B776 (2018) 318–337, [arXiv:1708.09624].

[156] **CMS** Collaboration, A. M. Sirunyan et al., *Search for new physics events with a leptonically decaying Z boson and a large momentum imbalance in proton-proton collisions at $\sqrt{s} = 13$ TeV*, Eur. Phys. J. C78 (2018), no. 4 291, [arXiv:1711.00431].

[157] **CMS** Collaboration, A. M. Sirunyan et al., *Search for dark matter produced in association with a leptonically decaying Z boson in proton-proton collisions at $\sqrt{s} = 13$ TeV*, [arXiv:2008.04735].

[158] G. Cowan, *Discovery sensitivity for a counting experiment with background uncertainty*, . Available at https://www.pp.rhul.ac.uk/~cowan/stat/medsig/medsigNote.pdf.

[159] **CMS** Collaboration, *Projection of the Mono-Z search for dark matter to the HL-LHC*, CMS-PAS-FTR-18-007 (2018).

[160] X. Cid Vidal et al., *Report from Working Group 3: Beyond the Standard Model physics at the HL-LHC and HE-LHC*, CERN Yellow Rep. Monogr. 7 (2019) 585–865, [arXiv:1812.07831].

[161] **ATLAS** Collaboration, M. Aaboud et al., *Search for Dark Matter Produced in Association with a Higgs Boson Decaying to $b\bar{b}$ using 36 fb^{-1} of pp collisions at $\sqrt{s} = 13$ TeV with the ATLAS Detector*, Phys. Rev. Lett. 119 (2017), no. 18 181804, [arXiv:1707.01302].

[162] **CMS** Collaboration, A. M. Sirunyan et al., *Search for dark matter particles produced in association with a Higgs boson in proton-proton collisions at $\sqrt{s} = 13$ TeV*, JHEP 03 (2020) 025, [arXiv:1908.01713].

[163] R. Penco, *An Introduction to Effective Field Theories*, [arXiv:2006.16285].

[164] T. Cohen, *As Scales Become Separated: Lectures on Effective Field Theory*, PoS TASI2018 (2019) 011, [arXiv:1903.03622].

[165] M. Neubert, *Effective field theory and heavy quark physics*, in *Theoretical Advanced Study Institute in Elementary Particle Physics: Physics in $D \geqq 4$*, pp. 149–194, 12, 2005. [hep-ph/0512222].

[166] A. V. Manohar, *Effective field theories*, Lect. Notes Phys. 479 (1997) 311–362, [hep-ph/9606222].

[167] A. V. Manohar, *Introduction to Effective Field Theories*, Les Houches Lect. Notes 108 (2020) [arXiv:1804.05863].

[168] I. Z. Rothstein, *TASI lectures on effective field theories*, 8, 2003. [hep-ph/0308266].

[169] J. Polchinski, *Effective field theory and the Fermi surface*, in *Theoretical Advanced Study Institute (TASI 92): From Black Holes and Strings to Particles*, pp. 0235–276, 6, 1992. [hep-th/9210046].

[170] W. Skiba, *Effective Field Theory and Precision Electroweak Measurements*, in *Theoretical Advanced Study Institute in Elementary Particle Physics: Physics of the Large and the Small*, pp. 5–70, 2011. [arXiv:1006.2142].

[171] D. B. Kaplan, *Five lectures on effective field theory*, 10, 2005. [nucl-th/0510023].

[172] H. Georgi, *Effective field theory*, Ann. Rev. Nucl. Part. Sci. 43 (1993) 209–252.

[173] A. Pich, *Effective field theory: Course*, in *Les Houches Summer School in Theoretical Physics, Session 68: Probing the Standard Model of Particle Interactions*, pp. 949–1049, 6, 1998. [hep-ph/9806303].

[174] M. Neubert, *Les Houches Lectures on Renormalization Theory and Effective Field Theories*, Les Houches Lect. Notes 108 (2020) [arXiv:1901.06573].

[175] F. Goertz, *Warped Extra Dimensions: Flavor, Precision Tests and Higgs Physics*. PhD thesis, Mainz U., Inst. Phys., 2011. [arXiv:1112.6387].

[176] S. Weinberg, *Baryon and Lepton Nonconserving Processes*, Phys. Rev. Lett. 43 (1979) 1566–1570.

[177] W. Buchmuller and D. Wyler, *Effective Lagrangian Analysis of New Interactions and Flavor Conservation*, Nucl. Phys. B268 (1986) 621–653.

[178] B. Grzadkowski, M. Iskrzynski, M. Misiak, and J. Rosiek, *Dimension-Six Terms in the Standard Model Lagrangian*, JHEP 10 (2010) 085, [arXiv:1008.4884].

[179] R. Alonso, E. E. Jenkins, A. V. Manohar, and M. Trott, *Renormalization Group Evolution of the Standard Model Dimension Six Operators III: Gauge Coupling Dependence and Phenomenology*, JHEP 04 (2014) 159, [arXiv:1312.2014].

[180] B. Henning, X. Lu, T. Melia, and H. Murayama, *2, 84, 30, 993, 560, 15456, 11962, 261485, ...: Higher dimension operators in the SM EFT*, JHEP 08 (2017) 016, [arXiv:1512.03433]. [Erratum: JHEP 09, 019 (2019)].

[181] C. B. Marinissen, R. Rahn, and W. J. Waalewijn, *..., 83106786, 114382724, 1509048322, 2343463290, 27410087742, ... efficient Hilbert series for effective theories*, Phys. Lett. B 808 (2020) 135632, [arXiv:2004.09521].

[182] R. Cotta, J. Hewett, M. Le, and T. Rizzo, *Bounds on Dark Matter Interactions with Electroweak Gauge Bosons*, Phys. Rev. D 88 (2013) 116009, [arXiv:1210.0525].

[183] L. M. Carpenter, A. Nelson, C. Shimmin, T. M. Tait, and D. Whiteson, *Collider searches for dark matter in events with a Z boson and missing energy*, Phys. Rev. D 87 (2013), no. 7 074005, [arXiv:1212.3352].

[184] A. Crivellin, U. Haisch, and A. Hibbs, *LHC constraints on gauge boson couplings to dark matter*, Phys. Rev. D 91 (2015) 074028, [arXiv:1501.00907].

[185] J. Goodman, M. Ibe, A. Rajaraman, W. Shepherd, T. M. P. Tait, and H.-B. Yu, *Constraints on Dark Matter from Colliders*, Phys. Rev. D82 (2010) 116010, [arXiv:1008.1783].

[186] Q.-H. Cao, C.-R. Chen, C. S. Li, and H. Zhang, *Effective Dark Matter Model: Relic density, CDMS II, Fermi LAT and LHC*, JHEP 08 (2011) 018, [arXiv:0912.4511].

[187] M. Beltran, D. Hooper, E. W. Kolb, Z. A. C. Krusberg, and T. M. P. Tait, *Maverick dark matter at colliders*, JHEP 09 (2010) 037, [arXiv:1002.4137].

[188] M. Beltran, D. Hooper, E. W. Kolb, and Z. C. Krusberg, *Deducing the nature of dark*

matter from direct and indirect detection experiments in the absence of collider signatures of new physics, Phys. Rev. D 80 (2009) 043509, [arXiv:0808.3384].

[189] W. Shepherd, T. M. P. Tait, and G. Zaharijas, *Bound states of weakly interacting dark matter*, Phys. Rev. D79 (2009) 055022, [arXiv:0901.2125].

[190] J. Goodman, M. Ibe, A. Rajaraman, W. Shepherd, T. M. P. Tait, and H.-B. Yu, *Constraints on Light Majorana dark Matter from Colliders*, Phys. Lett. B695 (2011) 185–188, [arXiv:1005.1286].

[191] N. F. Bell, Y. Cai, J. B. Dent, R. K. Leane, and T. J. Weiler, *Dark matter at the LHC: Effective field theories and gauge invariance*, Phys. Rev. D92 (2015), no. 5 053008, [arXiv:1503.07874].

[192] M. Gaillard, *The Effective One Loop Lagrangian With Derivative Couplings*, Nucl. Phys. B 268 (1986) 669–692.

[193] O. Cheyette, *Effective Action for the Standard Model With Large Higgs Mass*, Nucl. Phys. B 297 (1988) 183–204.

[194] B. Henning, X. Lu, and H. Murayama, *One-loop Matching and Running with Covariant Derivative Expansion*, JHEP 01 (2018) 123, [arXiv:1604.01019].

[195] A. Drozd, J. Ellis, J. Quevillon, and T. You, *The Universal One-Loop Effective Action*, JHEP 03 (2016) 180, [arXiv:1512.03003].

[196] S. A. R. Ellis, J. Quevillon, T. You, and Z. Zhang, *Extending the Universal One-Loop Effective Action: Heavy-Light Coefficients*, JHEP 08 (2017) 054, [arXiv:1706.07765].

[197] B. Henning, X. Lu, and H. Murayama, *How to use the Standard Model effective field theory*, JHEP 01 (2016) 023, [arXiv:1412.1837].

[198] M. Jiang, N. Craig, Y.-Y. Li, and D. Sutherland, *Complete One-Loop Matching for a Singlet Scalar in the Standard Model EFT*, JHEP 02 (2019) 031, [arXiv:1811.08878].

[199] I. Low, J. Lykken, and G. Shaughnessy, *Singlet scalars as Higgs imposters at the Large Hadron Collider*, Phys. Rev. D84 (2011) 035027, [arXiv:1105.4587].

[200] B. Coleppa, K. Kumar, and H. E. Logan, *Can the 126 GeV boson be a pseudoscalar?*, Phys. Rev. D86 (2012) 075022, [arXiv:1208.2692].

[201] A. Azatov, R. Contino, A. Di Iura, and J. Galloway, *New Prospects for Higgs Compositeness in $h \to Z\gamma$*, Phys. Rev. D88 (2013), no. 7 075019, [arXiv:1308.2676].

[202] R. Contino, M. Ghezzi, C. Grojean, M. Muhlleitner, and M. Spira, *Effective Lagrangian for a light Higgs-like scalar*, JHEP 07 (2013) 035, [arXiv:1303.3876].

[203] A. Pomarol and F. Riva, *Towards the Ultimate SM Fit to Close in on Higgs Physics*, JHEP 01 (2014) 151, [arXiv:1308.2803].

[204] J. Elias-Miro, J. R. Espinosa, E. Masso, and A. Pomarol, *Higgs windows to new physics through d=6 operators: constraints and one-loop anomalous dimensions*, JHEP 11 (2013) 066, [arXiv:1308.1879].

[205] G. Belanger, V. Bizouard, and G. Chalons, *Boosting Higgs boson decays into gamma and a Z in the NMSSM*, Phys. Rev. D89 (2014), no. 9 095023, [arXiv:1402.3522].

[206] Y. Chen, A. Falkowski, I. Low, and R. Vega-Morales, *New Observables for CP Violation in Higgs Decays*, Phys. Rev. D90 (2014), no. 11 113006, [arXiv:1405.6723].

[207] C. Arina, V. Martin-Lozano, and G. Nardini, *Dark matter versus $h \to \gamma\gamma$ and $h \to \gamma Z$ with supersymmetric triplets*, JHEP 08 (2014) 015, [arXiv:1403.6434].

[208] D. Liu, I. Low, and Z. Yin, *Universal Relations in Composite Higgs Models*, JHEP 05 (2019) 170, [arXiv:1809.09126].

[209] A. Freitas and P. Schwaller, *Multi-Photon Signals from Composite Models at LHC*, JHEP 01 (2011) 022, [arXiv:1010.2528].

[210] J. S. Gainer, W.-Y. Keung, I. Low, and P. Schwaller, *Looking for a light Higgs boson in the $Z\gamma \to \ell\ell\gamma$ channel*, Phys. Rev. D86 (2012) 033010, [arXiv:1112.1405].

[211] **ATLAS** Collaboration, M. Aaboud et al., *Projections for measurements of Higgs boson cross sections, branching ratios, coupling parameters and mass with the ATLAS detector at the HL-LHC*, ATL-PHYS-PUB-2018-054 (Dec, 2018).

[212] M. Cepeda et al., *Report from Working Group 2: Higgs Physics at the HL-LHC and HE-LHC*, vol. 7, pp. 221–584. 12, 2019. [arXiv:1902.00134].

[213] **ATLAS** Collaboration, G. Aad et al., *A search for the $Z\gamma$ decay mode of the Higgs boson in pp collisions at $\sqrt{s}$ = 13 TeV with the ATLAS detector*, Phys. Lett. B 809 (2020) 135754, [arXiv:2005.05382].

[214] **ATLAS** Collaboration, M. Aaboud et al., *Searches for the $Z\gamma$ decay mode of the Higgs boson and for new high-mass resonances in pp collisions at $\sqrt{s} = 13$ TeV with the ATLAS detector*, JHEP 10 (2017) 112, [arXiv:1708.00212].

[215] **CMS** Collaboration, A. M. Sirunyan et al., *Search for the decay of a Higgs boson in the $\ell\ell\gamma$ channel in proton-proton collisions at $\sqrt{s}$ = 13 TeV*, JHEP 11 (2018) 152, [arXiv:1806.05996].

[216] **ATLAS** Collaboration, G. Aad et al., *CP Properties of Higgs Boson Interactions with Top Quarks in the $t\bar{t}H$ and tH Processes Using $H \to \gamma\gamma$ with the ATLAS Detector*, Phys. Rev. Lett. 125 (2020), no. 6 061802, [arXiv:2004.04545].

[217] **CMS** Collaboration, A. M. Sirunyan et al., *Measurements of $\mathrm{t\bar{t}}H$ production and the CP structure of the Yukawa interaction between the Higgs boson and top quark in the diphoton decay channel*, Phys. Rev. Lett. 125 (2020), no. 6 061801, [arXiv:2003.10866].

[218] **ATLAS** Collaboration, M. Aaboud et al., *Observation of Higgs boson production in association with a top quark pair at the LHC with the ATLAS detector*, Phys. Lett. B784 (2018) 173–191, [arXiv:1806.00425].

[219] **ATLAS** Collaboration, M. Aaboud et al., *Measurement of Higgs boson production in association with a $t\bar{t}$ pair in the diphoton decay channel using 139 fb^{-1} of LHC data collected at $\sqrt{s} = 13$ TeV by the ATLAS experiment*, ATLAS-CONF-2019-004 (2019).

[220] **CMS** Collaboration, A. M. Sirunyan et al., *Observation of $\mathrm{t\bar{t}}H$ production*, Phys. Rev. Lett. 120 (2018), no. 23 231801, [arXiv:1804.02610].

[221] F. Goertz, E. Madge, P. Schwaller, and V. T. Tenorth, *Discovering the $h \to Z\gamma$ decay in $t\bar{t}$ associated production*, Phys. Rev. D 102 (2020), no. 5 053004, [arXiv:1909.07390].

[222] J. de Blas, O. Eberhardt, and C. Krause, *Current and Future Constraints on Higgs Couplings in the Nonlinear Effective Theory*, JHEP 07 (2018) 048, [arXiv:1803.00939].

[223] J. Ellis, C. W. Murphy, V. Sanz, and T. You, *Updated Global SMEFT Fit to Higgs, Diboson and Electroweak Data*, JHEP 06 (2018) 146, [arXiv:1803.03252].

[224] A. Biekötter, T. Corbett, and T. Plehn, *The Gauge-Higgs Legacy of the LHC Run II*, SciPost Phys. 6 (2019) 064, [arXiv:1812.07587].

[225] D. de Florian et al., *Handbook of LHC Higgs Cross Sections: 4. Deciphering the Nature of the Higgs Sector*, [arXiv:1610.07922].

[226] **Particle Data Group** Collaboration, M. Tanabashi et al., *Review of Particle Physics*, Phys. Rev. D98 (2018), no. 3 030001.

[227] **ATLAS** Collaboration, G. Aad et al., *Search for $t\bar{t}H$ production in the $H \to \gamma\gamma$ channel at $\sqrt{s} = 8$ TeV with the ATLAS detector*, ATLAS-CONF-2013-080 (2013).

[228] M. Cacciari, G. P. Salam, and G. Soyez, *FastJet User Manual*, Eur. Phys. J. C72 (2012) 1896, [arXiv:1111.6097].

[229] M. Cacciari, G. P. Salam, and G. Soyez, *The anti-k_t jet clustering algorithm*, JHEP 04 (2008) 063, [arXiv:0802.1189].

[230] **CMS** Collaboration, A. M. Sirunyan et al., *Measurement of the associated production of a Higgs boson and a pair of top-antitop quarks with the Higgs boson decaying to two photons in proton-proton collisions at $\sqrt{s} = 13$* TeV, CMS-PAS-HIG-18-018 (2018).

[231] G. Cowan, K. Cranmer, E. Gross, and O. Vitells, *Asymptotic formulae for likelihood-based tests of new physics*, Eur. Phys. J. C 71 (2011) 1554, [arXiv:1007.1727]. [Erratum: Eur.Phys.J.C 73, 2501 (2013)].

[232] **FCC** Collaboration, A. Abada et al., *HE-LHC: The High-Energy Large Hadron Collider*, Eur. Phys. J. ST 228 (2019), no. 5 1109–1382.

[233] **FCC** Collaboration, A. Abada et al., *FCC-hh: The Hadron Collider*, Eur. Phys. J. ST 228 (2019), no. 4 755–1107.

[234] R. Contino et al., *Physics at a 100 TeV pp collider: Higgs and EW symmetry breaking studies*, CERN Yellow Rep. (2017), no. 3 255–440, [arXiv:1606.09408].

[235] Q.-H. Cao, H.-R. Wang, and Y. Zhang, *Probing $HZ\gamma$ and $H\gamma\gamma$ anomalous couplings in the process $e^+e^- \to H\gamma$*, Chin. Phys. C39 (2015), no. 11 113102, [arXiv:1505.00654].

[236] J. M. No and M. Spannowsky, *A Boost to $h \to Z\gamma$: from LHC to Future e^+e^- Colliders*, Phys. Rev. D95 (2017), no. 7 075027, [arXiv:1612.06626].

[237] G. Durieux, C. Grojean, J. Gu, and K. Wang, *The leptonic future of the Higgs*, JHEP 09 (2017) 014, [arXiv:1704.02333].

[238] S. Bruggisser, F. Riva, and A. Urbano, *The Last Gasp of Dark Matter Effective Theory*, JHEP 11 (2016) 069, [arXiv:1607.02475].

[239] J. Alwall, P. Schuster, and N. Toro, *Simplified Models for a First Characterization of New Physics at the LHC*, Phys. Rev. D79 (2009) 075020, [arXiv:0810.3921].

[240] A. De Simone, G. F. Giudice, and A. Strumia, *Benchmarks for Dark Matter Searches at the LHC*, JHEP 06 (2014) 081, [arXiv:1402.6287].

[241] M. R. Buckley, D. Feld, and D. Goncalves, *Scalar Simplified Models for Dark Matter*, Phys. Rev. D91 (2015) 015017, [arXiv:1410.6497].

[242] P. Harris, V. V. Khoze, M. Spannowsky, and C. Williams, *Constraining Dark Sectors at Colliders: Beyond the Effective Theory Approach*, Phys. Rev. D91 (2015) 055009, [arXiv:1411.0535].

[243] A. De Simone and T. Jacques, *Simplified models vs. effective field theory approaches in dark matter searches*, Eur. Phys. J. C76 (2016), no. 7 367, [arXiv:1603.08002].

[244] E. Morgante, *Simplified Dark Matter Models*, Adv. High Energy Phys. 2018 (2018) 5012043, [arXiv:1804.01245].

[245] T. Alanne and F. Goertz, *Extended Dark Matter EFT*, Eur. Phys. J. C 80 (2020), no. 5 446, [arXiv:1712.07626].

[246] M. Duerr, P. Fileviez Pérez, and J. Smirnov, *Scalar Dark Matter: Direct vs. Indirect Detection*, JHEP 06 (2016) 152, [arXiv:1509.04282].

[247] E. Morgante, *On the validity of the effective field theory for dark matter searches at the LHC*, Nuovo Cim. C 38 (2015), no. 1 32, [arXiv:1409.6668].

[248] A. Ismail, W.-Y. Keung, K.-H. Tsao, and J. Unwin, *Axial vector Z' and anomaly cancellation*, Nucl. Phys. B918 (2017) 220–244, [arXiv:1609.02188].

[249] K. Hagiwara, S. Ishihara, R. Szalapski, and D. Zeppenfeld, *Low-energy effects of new interactions in the electroweak boson sector*, Phys. Rev. D48 (1993) 2182–2203.

[250] S. Adhikari, I. M. Lewis, and M. Sullivan, *Beyond the Standard Model Effective Field Theory: The Singlet Extended Standard Model*, [arXiv:2003.10449].

[251] J. F. Kamenik, B. R. Safdi, Y. Soreq, and J. Zupan, *Comments on the diphoton excess: critical reappraisal of effective field theory interpretations*, JHEP 07 (2016) 042, [arXiv:1603.06566].

[252] R. Franceschini, G. F. Giudice, J. F. Kamenik, M. McCullough, F. Riva, A. Strumia, and R. Torre, *Digamma, what next?*, JHEP 07 (2016) 150, [arXiv:1604.06446].

[253] B. Gripaios and D. Sutherland, *An operator basis for the Standard Model with an added scalar singlet*, JHEP 08 (2016) 103, [arXiv:1604.07365].

[254] A. Carmona, F. Goertz, and A. Papaefstathiou, *Uncovering the relation of a scalar resonance to the Higgs boson*, Phys. Rev. D 95 (2017), no. 9 095022, [arXiv:1606.02716].

[255] M. Bauer, A. Butter, J. Gonzalez-Fraile, T. Plehn, and M. Rauch, *Learning from a Higgs-like scalar resonance*, Phys. Rev. D 95 (2017), no. 5 055011, [arXiv:1607.04562].

[256] G. D'Ambrosio, G. F. Giudice, G. Isidori, and A. Strumia, *Minimal flavor violation: An Effective field theory approach*, Nucl. Phys. B645 (2002) 155–187, [hep-ph/0207036].

[257] M. Pospelov and T. ter Veldhuis, *Direct and indirect limits on the electromagnetic form-factors of WIMPs*, Phys. Lett. B 480 (2000) 181–186, [hep-ph/0003010].

[258] V. Barger, W.-Y. Keung, and D. Marfatia, *Electromagnetic properties of dark matter: Dipole moments and charge form factor*, Phys. Lett. B 696 (2011) 74–78, [arXiv:1007.4345].

[259] B. J. Kavanagh, P. Panci, and R. Ziegler, *Faint Light from Dark Matter: Classifying and Constraining Dark Matter-Photon Effective Operators*, JHEP 04 (2019) 089, [arXiv:1810.00033].

[260] C. Arina, A. Cheek, K. Mimasu, and L. Pagani, *Light and Darkness: consistently coupling dark matter to photons via effective operators*, [arXiv:2005.12789].

[261] T. Robens and T. Stefaniak, *Status of the Higgs Singlet Extension of the Standard Model after LHC Run 1*, Eur. Phys. J. C75 (2015) 104, [arXiv:1501.02234].

[262] A. Falkowski, C. Gross, and O. Lebedev, *A second Higgs from the Higgs portal*, JHEP 05 (2015) 057, [arXiv:1502.01361].

[263] H. Bélusca-Maïto, A. Falkowski, D. Fontes, J. C. Romão, and J. P. Silva, *Higgs EFT for 2HDM and beyond*, Eur. Phys. J. C77 (2017), no. 3 176, [arXiv:1611.01112].

[264] T. Alanne, G. Arcadi, F. Goertz, V. Tenorth, and S. Vogl, *Model-independent constraints with extended dark matter EFT*, JHEP 10 (2020) 172, [arXiv:2006.07174].

[265] F. Goertz, K. Tame-Narvaez, and V. T. Tenorth, *Di-jet/e^+e^- + MET to Probe Z_2-Odd Mediators to the Dark Sector*, Eur. Phys. J. C79 (2019), no. 10 860, [arXiv:1906.08007].

[266] G. Arcadi, A. Bally, F. Goertz, K. Tame-Narvaez, V. Tenorth, and S. Vogl, *EFT Interpretation of XENON1T Electron Recoil Excess: Neutrinos and Dark Matter*, [arXiv:2007.08500].

[267] G. Steigman, B. Dasgupta, and J. F. Beacom, *Precise Relic WIMP Abundance and its Impact on Searches for Dark Matter Annihilation*, Phys. Rev. D86 (2012) 023506, [arXiv:1204.3622].

[268] K. Griest and D. Seckel, *Three exceptions in the calculation of relic abundances*, Phys. Rev. D43 (1991) 3191–3203.

[269] G. Belanger, F. Boudjema, A. Pukhov, and A. Semenov, *micrOMEGAs3: A program for calculating dark matter observables*, Comput. Phys. Commun. 185 (2014) 960–985, [arXiv:1305.0237].

[270] G. Bélanger, F. Boudjema, A. Goudelis, A. Pukhov, and B. Zaldivar, *micrOMEGAs5.0 : Freeze-in*, Comput. Phys. Commun. 231 (2018) 173–186, [arXiv:1801.03509].

[271] C. Cheung, L. J. Hall, D. Pinner, and J. T. Ruderman, *Prospects and Blind Spots for Neutralino Dark Matter*, JHEP 05 (2013) 100, [arXiv:1211.4873].

[272] P. Huang and C. E. M. Wagner, *Blind Spots for neutralino Dark Matter in the MSSM with an intermediate m_A*, Phys. Rev. D90 (2014), no. 1 015018, [arXiv:1404.0392].

[273] A. Berlin, S. Gori, T. Lin, and L.-T. Wang, *Pseudoscalar Portal Dark Matter*, Phys. Rev. D92 (2015) 015005, [arXiv:1502.06000].

[274] A. Choudhury, K. Kowalska, L. Roszkowski, E. M. Sessolo, and A. J. Williams, *Blind Spots for Direct Detection with Simplified DM Models and the LHC*, Universe 3 (2017), no. 2 41, [arXiv:1705.04230].

[275] A. Djouadi, *The Anatomy of electro-weak symmetry breaking. I: The Higgs boson in the standard model*, Phys. Rept. 457 (2008) 1–216, [hep-ph/0503172].

[276] M. Cacciari and G. P. Salam, *Dispelling the N^3 myth for the k_t jet-finder*, Phys. Lett. B641 (2006) 57–61, [hep-ph/0512210].

[277] A. L. Read, *Presentation of search results: The CL(s) technique*, J. Phys. G28 (2002) 2693–2704. [,11(2002)].

[278] T. Sjostrand, S. Mrenna, and P. Z. Skands, *PYTHIA 6.4 Physics and Manual*, JHEP 05 (2006) 026, [hep-ph/0603175].

[279] T. Sjostrand, S. Mrenna, and P. Z. Skands, *A Brief Introduction to PYTHIA 8.1*, Comput. Phys. Commun. 178 (2008) 852–867, [arXiv:0710.3820].

[280] M. Spira, A. Djouadi, D. Graudenz, and P. Zerwas, *Higgs boson production at the LHC*, Nucl. Phys. B 453 (1995) 17–82, [hep-ph/9504378].

[281] S. Dawson, C. Englert, and T. Plehn, *Higgs Physics: It ain't over till it's over*, [arXiv:1808.01324].

[282] **ATLAS** Collaboration, M. Aaboud et al., *Search for heavy particles decaying into top-quark pairs using lepton-plus-jets events in proton–proton collisions at $\sqrt{s} = 13\,TeV$ with the ATLAS detector*, Eur. Phys. J. C78 (2018), no. 7 565, [arXiv:1804.10823].

[283] **ATLAS** Collaboration, M. Aaboud et al., *Searches for heavy ZZ and ZW resonances in the $\ell\ell qq$ and $\nu\nu qq$ final states in pp collisions at $\sqrt{s} = 13$ TeV with the ATLAS detector*, JHEP 03 (2018) 009, [arXiv:1708.09638].

[284] **ATLAS** Collaboration, M. Aaboud et al., *Search for WW/WZ resonance production in $\ell\nu qq$ final states in pp collisions at $\sqrt{s} = 13$ TeV with the ATLAS detector*, JHEP 03 (2018) 042, [arXiv:1710.07235].

[285] **ATLAS** Collaboration, M. Aaboud et al., *Search for heavy resonances decaying into WW in the $e\nu\mu\nu$ final state in pp collisions at $\sqrt{s} = 13$ TeV with the ATLAS detector*, Eur. Phys. J. C78 (2018), no. 1 24, [arXiv:1710.01123].

[286] **ATLAS** Collaboration, M. Aaboud et al., *Search for new phenomena in high-mass diphoton final states using 37 fb^{-1} of proton–proton collisions collected at $\sqrt{s} = 13$ TeV with the ATLAS detector*, Phys. Lett. B775 (2017) 105–125, [arXiv:1707.04147].

[287] **CMS** Collaboration, A. M. Sirunyan et al., *Search for physics beyond the standard model in high-mass diphoton events from proton-proton collisions at $\sqrt{s} = 13$ TeV*, Phys. Rev. D98 (2018), no. 9 092001, [arXiv:1809.00327].

[288] **CMS** Collaboration, A. M. Sirunyan et al., *Search for $Z\gamma$ resonances using leptonic and hadronic final states in proton-proton collisions at $\sqrt{s} = 13$ TeV*, JHEP 09 (2018) 148, [arXiv:1712.03143].

[289] **ATLAS** Collaboration, M. Aaboud et al., *Search for heavy resonances decaying to a photon and a hadronically decaying $Z/W/H$ boson in pp collisions at $\sqrt{s} = 13$ TeV with the ATLAS detector*, Phys. Rev. D98 (2018), no. 3 032015, [arXiv:1805.01908].

[290] **CMS** Collaboration, A. M. Sirunyan et al., *Search for narrow and broad dijet resonances in proton-proton collisions at $\sqrt{s} = 13$ TeV and constraints on dark matter mediators and other new particles*, JHEP 08 (2018) 130, [arXiv:1806.00843].

[291] **ATLAS** Collaboration, M. Aaboud et al., *Search for pair production of Higgs bosons in the $b\bar{b}b\bar{b}$ final state using proton-proton collisions at $\sqrt{s} = 13$ TeV with the ATLAS detector*, JHEP 01 (2019) 030, [arXiv:1804.06174].

[292] **CMS** Collaboration, A. M. Sirunyan et al., *Search for nonresonant Higgs boson pair production in the $\mathrm{b\bar{b}b\bar{b}}$ final state at $\sqrt{s} = 13$ TeV*, JHEP 04 (2019) 112, [arXiv:1810.11854].

[293] **ATLAS** Collaboration, M. Aaboud et al., *Search for Higgs boson pair production in the $b\bar{b}WW^*$ decay mode at $\sqrt{s} = 13$ TeV with the ATLAS detector*, JHEP 04 (2019) 092, [arXiv:1811.04671].

[294] **ATLAS** Collaboration, M. Aaboud et al., *Search for resonant and non-resonant Higgs boson pair production in the $b\bar{b}\tau^+\tau^-$ decay channel in pp collisions at $\sqrt{s} = 13$ TeV with the ATLAS detector*, Phys. Rev. Lett. 121 (2018), no. 19 191801, [arXiv:1808.00336]. [Erratum: Phys. Rev. Lett.122,no.8,089901(2019)].

[295] **ATLAS** Collaboration, M. Aaboud et al., *Search for Higgs boson pair production in the $\gamma\gamma WW^*$ channel using pp collision data recorded at $\sqrt{s} = 13$ TeV with the ATLAS detector*, Eur. Phys. J. C78 (2018), no. 12 1007, [arXiv:1807.08567].

[296] **ATLAS** Collaboration, M. Aaboud et al., *Search for Higgs boson pair production in the $\gamma\gamma b\bar{b}$ final state with 13 TeV pp collision data collected by the ATLAS experiment*, JHEP 11 (2018) 040, [arXiv:1807.04873].

[297] **CMS** Collaboration, A. M. Sirunyan et al., *Combination of searches for Higgs boson*

pair production in proton-proton collisions at $\sqrt{s} = 13$ TeV, Phys. Rev. Lett. 122 (2019), no. 12 121803, [arXiv:1811.09689].

[298] **ATLAS** Collaboration, G. Aad et al., *Combination of searches for Higgs boson pairs in pp collisions at $\sqrt{s} = 13$ TeV with the ATLAS detector*, [arXiv:1906.02025].

[299] **LEP Working Group for Higgs boson searches, ALEPH, DELPHI, L3, OPAL** Collaboration, R. Barate et al., *Search for the standard model Higgs boson at LEP*, Phys. Lett. B 565 (2003) 61–75, [hep-ex/0306033].

[300] **DELPHI** Collaboration, P. Abreu et al., *Search for low mass Higgs bosons produced in Z0 decays*, Z. Phys. C 51 (1991) 25–36.

[301] **LHCb** Collaboration, R. Aaij et al., *Differential branching fraction and angular analysis of the $B^+ \to K^+\mu^+\mu^-$ decay*, JHEP 02 (2013) 105, [arXiv:1209.4284].

[302] **Belle** Collaboration, J.-T. Wei et al., *Measurement of the Differential Branching Fraction and Forward-Backword Asymmetry for $B \to K^{(*)}\ell^+\ell^-$*, Phys. Rev. Lett. 103 (2009) 171801, [arXiv:0904.0770].

[303] L. Lopez-Honorez, T. Schwetz, and J. Zupan, *Higgs portal, fermionic dark matter, and a Standard Model like Higgs at 125 GeV*, Phys. Lett. B716 (2012) 179–185, [arXiv:1203.2064].

[304] G. Busoni et al., *Recommendations on presenting LHC searches for missing transverse energy signals using simplified s-channel models of dark matter*, [arXiv:1603.04156].

[305] Y. Mambrini, G. Arcadi, and A. Djouadi, *The LHC diphoton resonance and dark matter*, Phys. Lett. B755 (2016) 426–432, [arXiv:1512.04913].

[306] A. Angelescu and G. Arcadi, *Dark Matter Phenomenology of SM and Enlarged Higgs Sectors Extended with Vector Like Leptons*, Eur. Phys. J. C77 (2017), no. 7 456, [arXiv:1611.06186].

[307] M. Backovic, A. Mariotti, and D. Redigolo, *Di-photon excess illuminates Dark Matter*, JHEP 03 (2016) 157, [arXiv:1512.04917].

[308] A. Falkowski, O. Slone, and T. Volansky, *Phenomenology of a 750 GeV Singlet*, JHEP 02 (2016) 152, [arXiv:1512.05777].

[309] J. Ellis, A. Fowlie, L. Marzola, and M. Raidal, *Statistical Analyses of Higgs- and Z-Portal Dark Matter Models*, Phys. Rev. D97 (2018), no. 11 115014, [arXiv:1711.09912].

[310] M. Pospelov, A. Ritz, and M. B. Voloshin, *Secluded WIMP Dark Matter*, Phys. Lett. B662 (2008) 53–61, [arXiv:0711.4866].

[311] M. Pospelov and A. Ritz, *Astrophysical Signatures of Secluded Dark Matter*, Phys. Lett. B671 (2009) 391–397, [arXiv:0810.1502].

[312] K. Huitu, N. Koivunen, O. Lebedev, S. Mondal, and T. Toma, *Probing pseudo-Goldstone dark matter at the LHC*, Phys. Rev. D100 (2019), no. 1 015009, [arXiv:1812.05952].

[313] **ATLAS** Collaboration, G. Aad et al., *Search for new phenomena in events with at least three photons collected in pp collisions at $\sqrt{s} = 8$ TeV with the ATLAS detector*, Eur. Phys. J. C76 (2016), no. 4 210, [arXiv:1509.05051].

[314] P. Tunney, J. M. No, and M. Fairbairn, *A Novel LHC Dark Matter Search to Dissect the Galactic Centre Excess*, [arXiv:1705.09670].

[315] M. A. Fedderke, J.-Y. Chen, E. W. Kolb, and L.-T. Wang, *The Fermionic Dark Matter Higgs Portal: an effective field theory approach*, JHEP 08 (2014) 122, [arXiv:1404.2283].

[316] J. Diaz-Cruz, U. Saldana-Salazar, K. Tame-Narvaez, and V. Tenorth, *Natural 2HDMs without FCNCs*, [arXiv:2010.05923].

[317] **ATLAS** Collaboration, M. Aaboud et al., *Search for squarks and gluinos in final states with jets and missing transverse momentum using 36 fb^{-1} of $\sqrt{s} = 13$ TeV pp collision data with the ATLAS detector*, Phys. Rev. D97 (2018), no. 11 112001, [arXiv:1712.02332].

[318] R. Contino, A. Falkowski, F. Goertz, C. Grojean, and F. Riva, *On the Validity of the Effective Field Theory Approach to SM Precision Tests*, JHEP 07 (2016) 144, [arXiv:1604.06444].

[319] C. Degrande, C. Duhr, B. Fuks, D. Grellscheid, O. Mattelaer, and T. Reiter, *UFO - The Universal FeynRules Output*, Comput. Phys. Commun. 183 (2012) 1201–1214, [arXiv:1108.2040].

[320] A. Alloul, N. D. Christensen, C. Degrande, C. Duhr, and B. Fuks, *FeynRules 2.0 - A complete toolbox for tree-level phenomenology*, Comput. Phys. Commun. 185 (2014) 2250–2300, [arXiv:1310.1921].

[321] N. D. Christensen, P. de Aquino, C. Degrande, C. Duhr, B. Fuks, M. Herquet, F. Maltoni, and S. Schumann, *A Comprehensive approach to new physics simulations*, Eur. Phys. J. C71 (2011) 1541, [arXiv:0906.2474].

[322] **ATLAS** Collaboration, G. Aad et al., *Search for high-mass dilepton resonances using 139 fb^{-1} of pp collision data collected at $\sqrt{s}$ =13 TeV with the ATLAS detector*, [arXiv:1903.06248].

[323] The ATLAS Collaboration, *ATL-PHYS-PUB-2018-043*, tech. rep., CERN, Geneva, Dec, 2018.

[324] A. Robson, P. N. Burrows, N. Catalan Lasheras, L. Linssen, M. Petric, D. Schulte, E. Sicking, S. Stapnes, and W. Wuensch, *The Compact Linear e^+e^- Collider (CLIC): Accelerator and Detector*, [arXiv:1812.07987].

[325] J. de Blas et al., *The CLIC Potential for New Physics*, [arXiv:1812.02093].

[326] J.-J. Blaising, M. Battaglia, J. Marshall, J. Nardulli, M. Thomson, A. Sailer, and E. van der Kraaij, *Physics performances for Scalar Electrons, Scalar Muons and Scalar Neutrinos searches at CLIC*, [arXiv:1201.2092].

[327] **XENON** Collaboration, E. Aprile et al., *First Dark Matter Search Results from the XENON1T Experiment*, Phys. Rev. Lett. 119 (2017), no. 18 181301, [arXiv:1705.06655].

[328] **LUX, LZ** Collaboration, M. Szydagis, *The Present and Future of Searching for Dark Matter with LUX and LZ*, PoS ICHEP2016 (2016) 220, [arXiv:1611.05525].

[329] **DARWIN** Collaboration, J. Aalbers et al., *DARWIN: towards the ultimate dark matter detector*, JCAP 1611 (2016) 017, [arXiv:1606.07001].

[330] **XENON** Collaboration, E. Aprile et al., *Observation of Excess Electronic Recoil Events in XENON1T*, [arXiv:2006.09721].

[331] C. Boehm, D. G. Cerdeno, M. Fairbairn, P. A. Machado, and A. C. Vincent, *Light new physics in XENON1T*, [arXiv:2006.11250].

[332] D. Aristizabal Sierra, V. De Romeri, L. Flores, and D. Papoulias, *Light vector mediators facing XENON1T data*, [arXiv:2006.12457].

[333] A. N. Khan, *Can nonstandard neutrino interactions explain the XENON1T spectral excess?*, [arXiv:2006.12887].

[334] S.-F. Ge, P. Pasquini, and J. Sheng, *Solar Neutrino Scattering with Electron into Massive Sterile Neutrino*, [arXiv:2006.16069].

[335] W. Chao, Y. Gao, and M. j. Jin, *Pseudo-Dirac Dark Matter in XENON1T*, [arXiv:2006.16145].

[336] Y. Gao and T. Li, *Lepton Number Violating Electron Recoils at XENON1T by the $U(1)_{B-L}$ Model with Non-Standard Interactions*, [arXiv:2006.16192].

[337] K. Babu, S. Jana, and M. Lindner, *Large Neutrino Magnetic Moments in the Light of Recent Experiments*, [arXiv:2007.04291].

[338] I. M. Shoemaker, Y.-D. Tsai, and J. Wyenberg, *An Active-to-Sterile Neutrino Transition Dipole Moment and the XENON1T Excess*, [arXiv:2007.05513].

[339] O. Miranda, D. Papoulias, M. Tórtola, and J. Valle, *XENON1T signal from transition neutrino magnetic moments*, [arXiv:2007.01765].

[340] M. Lindner, Y. Mambrini, T. B. de Melo, and F. S. Queiroz, *XENON1T Anomaly: A Light Z'*, [arXiv:2006.14590].

[341] A. Bally, S. Jana, and A. Trautner, *Neutrino self-interactions and XENON1T electron recoil excess*, [arXiv:2006.11919].

[342] F. Takahashi, M. Yamada, and W. Yin, *XENON1T anomaly from anomaly-free ALP dark matter and its implications for stellar cooling anomaly*, [arXiv:2006.10035].

[343] G. Alonso-Álvarez, F. Ertas, J. Jaeckel, F. Kahlhoefer, and L. Thormaehlen, *Hidden Photon Dark Matter in the Light of XENON1T and Stellar Cooling*, [arXiv:2006.11243].

[344] I. M. Bloch, A. Caputo, R. Essig, D. Redigolo, M. Sholapurkar, and T. Volansky, *Exploring New Physics with O(keV) Electron Recoils in Direct Detection Experiments*, [arXiv:2006.14521].

[345] N. Okada, S. Okada, D. Raut, and Q. Shafi, *Dark Matter Z' and XENON1T Excess from $U(1)_X$ Extended Standard Model*, [arXiv:2007.02898].

[346] H.-J. He, Y.-C. Wang, and J. Zheng, *EFT Analysis of Inelastic Dark Matter for Xenon Electron Recoil Detection*, [arXiv:2007.04963].

[347] K. Kannike, M. Raidal, H. Veermäe, A. Strumia, and D. Teresi, *Dark Matter and the XENON1T electron recoil excess*, [arXiv:2006.10735].

[348] B. Fornal, P. Sandick, J. Shu, M. Su, and Y. Zhao, *Boosted Dark Matter Interpretation of the XENON1T Excess*, [arXiv:2006.11264].

[349] L. Su, W. Wang, L. Wu, J. M. Yang, and B. Zhu, *Atmospheric Dark Matter from Inelastic Cosmic Ray Collision in Xenon1T*, [arXiv:2006.11837].

[350] Q.-H. Cao, R. Ding, and Q.-F. Xiang, *Exploring for sub-MeV Boosted Dark Matter from Xenon Electron Direct Detection*, [arXiv:2006.12767].

[351] H. Alhazmi, D. Kim, K. Kong, G. Mohlabeng, J.-C. Park, and S. Shin, *Implications of the XENON1T Excess on the Dark Matter Interpretation*, [arXiv:2006.16252].

[352] K. Harigaya, Y. Nakai, and M. Suzuki, *Inelastic Dark Matter Electron Scattering and the XENON1T Excess*, [arXiv:2006.11938].

[353] N. F. Bell, J. B. Dent, B. Dutta, S. Ghosh, J. Kumar, and J. L. Newstead, *Explaining the XENON1T excess with Luminous Dark Matter*, [arXiv:2006.12461].

[354] H. M. Lee, *Exothermic Dark Matter for XENON1T Excess*, [arXiv:2006.13183].

[355] J. Bramante and N. Song, *Electric But Not Eclectic: Thermal Relic Dark Matter for the XENON1T Excess*, [arXiv:2006.14089].

[356] S. Baek, J. Kim, and P. Ko, *XENON1T excess in local Z_2 DM models with light dark sector*, [arXiv:2006.16876].

[357] D. McKeen, M. Pospelov, and N. Raj, *Hydrogen portal to exotic radioactivity*, [arXiv:2006.15140].

[358] L. Zu, G.-W. Yuan, L. Feng, and Y.-Z. Fan, *Mirror Dark Matter and Electronic Recoil Events in XENON1T*, [arXiv:2006.14577].

[359] Y. Jho, J.-C. Park, S. C. Park, and P.-Y. Tseng, *Gauged Lepton Number and Cosmic-ray Boosted Dark Matter for the XENON1T Excess*, [arXiv:2006.13910].

[360] P. Ko and Y. Tang, *Semi-annihilating Z_3 Dark Matter for XENON1T Excess*, [arXiv:2006.15822].

[361] G. Cacciapaglia, C. Cai, M. T. Frandsen, M. Rosenlyst, and H. H. Zhang, *XENON1T solar axion and the Higgs boson emerging from the dark*, [arXiv:2006.16267].

[362] G. Paz, A. A. Petrov, M. Tammaro, and J. Zupan, *Shining dark matter in Xenon1T*, [arXiv:2006.12462].

[363] D. G. Cerdeño, M. Fairbairn, T. Jubb, P. A. N. Machado, A. C. Vincent, and C. Bœ hm, *Physics from solar neutrinos in dark matter direct detection experiments*, JHEP 05 (2016) 118, [arXiv:1604.01025]. [Erratum: JHEP 09, 048 (2016)].

[364] E. Vitagliano, I. Tamborra, and G. Raffelt, *Grand Unified Neutrino Spectrum at Earth*, [arXiv:1910.11878].

[365] J. N. Bahcall, *Gallium solar neutrino experiments: Absorption cross-sections, neutrino spectra, and predicted event rates*, Phys. Rev. C 56 (1997) 3391–3409, [hep-ph/9710491].

[366] **XENON** Collaboration, E. Aprile et al., *Observation of two-neutrino double electron capture in ^{124}Xe with XENON1T*, Nature 568 (2019), no. 7753 532–535, [arXiv:1904.11002].

[367] B. Roberts, V. Flambaum, and G. Gribakin, *Ionization of atoms by slow heavy particles, including dark matter*, Phys. Rev. Lett. 116 (2016), no. 2 023201, [arXiv:1509.09044].

[368] B. Roberts, V. Dzuba, V. Flambaum, M. Pospelov, and Y. Stadnik, *Dark matter scattering on electrons: Accurate calculations of atomic excitations and implications for the DAMA signal*, Phys. Rev. D 93 (2016), no. 11 115037, [arXiv:1604.04559].

[369] B. Roberts and V. Flambaum, *Electron-interacting dark matter: Implications from DAMA/LIBRA-phase2 and prospects for liquid xenon detectors and NaI detectors*, Phys. Rev. D 100 (2019), no. 6 063017, [arXiv:1904.07127].

[370] N. Bernal, M. Heikinheimo, T. Tenkanen, K. Tuominen, and V. Vaskonen, *The Dawn of*

FIMP Dark Matter: A Review of Models and Constraints, Int. J. Mod. Phys. A 32 (2017), no. 27 1730023, [arXiv:1706.07442].

[371] S. Knapen, T. Lin, and K. M. Zurek, *Light Dark Matter: Models and Constraints*, Phys. Rev. D 96 (2017), no. 11 115021, [arXiv:1709.07882].

[372] **Borexino** Collaboration, M. Agostini et al., *Limiting neutrino magnetic moments with Borexino Phase-II solar neutrino data*, Phys. Rev. D 96 (2017), no. 9 091103, [arXiv:1707.09355].

[373] A. Beda, V. Brudanin, V. Egorov, D. Medvedev, V. Pogosov, E. Shevchik, M. Shirchenko, A. Starostin, and I. Zhitnikov, *Gemma experiment: The results of neutrino magnetic moment search*, Phys. Part. Nucl. Lett. 10 (2013) 139–143.

[374] D. Hanneke, S. Fogwell, and G. Gabrielse, *New measurement of the electron magnetic moment and the fine structure constant*, Physical Review Letters 100 (Mar, 2008).

[375] G. Giudice, P. Paradisi, and M. Passera, *Testing new physics with the electron g-2*, JHEP 11 (2012) 113, [arXiv:1208.6583].

[376] R. Jackiw and S. Weinberg, *Weak interaction corrections to the muon magnetic moment and to muonic atom energy levels*, Phys. Rev. D 5 (1972) 2396–2398.

[377] E. Hardy and R. Lasenby, *Stellar cooling bounds on new light particles: plasma mixing effects*, JHEP 02 (2017) 033, [arXiv:1611.05852].

[378] F. Capozzi and G. Raffelt, *Axion and neutrino red-giant bounds updated with geometric distance determinations*, [arXiv:2007.03694].

[379] J. Khoury and A. Weltman, *Chameleon fields: Awaiting surprises for tests of gravity in space*, Phys. Rev. Lett. 93 (2004) 171104, [astro-ph/0309300].

[380] A. Joyce, B. Jain, J. Khoury, and M. Trodden, *Beyond the Cosmological Standard Model*, Phys. Rept. 568 (2015) 1–98, [arXiv:1407.0059].

[381] W. DeRocco, P. W. Graham, and S. Rajendran, *Exploring the robustness of stellar cooling constraints on light particles*, [arXiv:2006.15112].

[382] G. Raffelt, *Stars as laboratories for fundamental physics*. 5, 1996.

[383] C.-Y. Chen, J. Kozaczuk, and Y.-M. Zhong, *Exploring leptophilic dark matter with na64*, Journal of High Energy Physics 2018 (Oct, 2018).

[384] J. M. Berryman, A. De Gouvêa, K. J. Kelly, and Y. Zhang, *Lepton-Number-Charged Scalars and Neutrino Beamstrahlung*, Phys. Rev. D 97 (2018), no. 7 075030, [arXiv:1802.00009].

[385] S. Shalgar, I. Tamborra, and M. Bustamante, *Core-collapse supernovae stymie secret neutrino interactions*, [arXiv:1912.09115].

[386] E. W. Kolb and M. S. Turner, *Supernova SN 1987a and the Secret Interactions of Neutrinos*, Phys. Rev. D 36 (1987) 2895.

[387] R. H. Cyburt, B. D. Fields, K. A. Olive, and T.-H. Yeh, *Big Bang Nucleosynthesis: 2015*, Rev. Mod. Phys. 88 (2016) 015004, [arXiv:1505.01076].

[388] M. Archidiacono and S. Hannestad, *Updated constraints on non-standard neutrino interactions from Planck*, JCAP 07 (2014) 046, [arXiv:1311.3873].

[389] M. Carena, Z. Liu, and Y. Wang, *Electroweak Phase Transition with Spontaneous Z_2-Breaking*, [arXiv:1911.10206].

[390] M. Quiros, *Finite temperature field theory and phase transitions*, in *ICTP Summer School*, pp. 187–259, 1, 1999. [hep-ph/9901312].

[391] J. Brehmer, K. Cranmer, G. Louppe, and J. Pavez, *A Guide to Constraining Effective Field Theories with Machine Learning*, Phys. Rev. D 98 (2018), no. 5 052004, [arXiv:1805.00020].

[392] J. Brehmer, K. Cranmer, G. Louppe, and J. Pavez, *Constraining Effective Field Theories with Machine Learning*, Phys. Rev. Lett. 121 (2018), no. 11 111801, [arXiv:1805.00013].

[393] C. K. Khosa, V. Sanz, and M. Soughton, *WIMPs or else? Using Machine Learning to disentangle LHC signatures*, [arXiv:1910.06058].

[394] https://iminuit.readthedocs.io/en/latest/index.html.